Low Temperature Kerr Effect Study of Magnetic Topological Insulators and Other Magnetic Structures

Jieyi Liu

Fitzwilliam College
University of Cambridge

This dissertation is submitted for the degree of Doctor of Philosophy

June 2019

DECLARATION

This thesis is the result of my own work and includes nothing which is the outcome of work done in collaboration except as declared in the Preface and specified in the text. It is not substantially the same as any that I have submitted, or, is being concurrently submitted for a degree or diploma or other qualification at the University of Cambridge or any other University or similar institution except as declared in the Preface and specified in the text. I further state that no substantial part of my thesis has already been submitted, or, is being concurrently submitted for any such degree, diploma or other qualification at the University of Cambridge or any other University or similar institution except as declared in the Preface and specified in the text. It does not exceed the prescribed word limit for the relevant Degree Committee.

Jieyi Liu
June 2019

Low Temperature Kerr Effect Study of Magnetic Topological Insulators and Other Magnetic Structures

Jieyi Liu

Spintronic technology utilises the spin of electrons as an extra degree of freedom to store and process information in microelectronic devices. Of special interest among all spintronic materials are topological insulators (TIs), which have insulating bulk but conductive surface states. In this thesis, a comprehensive study of various TI and non-TI spintronic systems is presented, with an emphasis on the magneto-optic Kerr effect (MOKE) characterisation. The design and construction of a MOKE microscope is described, for simultaneous magneto-optical and magneto-transport measurements in an applied field of up to 9 T at temperatures from 1.5 to 300 K. This microscope is used to study Cr:Sb_2Te_3, (Cr,V):Sb_2Te_3, EuS/Bi_2Se_3, and [Cr:Sb_2Te_3/Dy:Bi_2Te_3]$_{10}$ magnetic TI thin films. A good agreement is established between the electrical transport and MOKE results of the Cr:Sb_2Te_3 films. However, in (Cr,V):Sb_2Te_3, a discrepancy is found between the two measurement techniques, indicating the presence of the Cr_2Te_3 secondary phase in the sample. For EuS/Bi_2Se_3, its interface-induced perpendicular magnetisation is successfully verified using the MOKE microscope. Regarding the ferromagnet/paramagnet [Cr:Sb_2Te_3/Dy:Bi_2Te_3]$_{10}$ superlattice film, unexpected exchange bias is observed in the material with an exchange field of up to 0.15 T at 10 K. This finding is supported by a density-functional-theory calculation. Apart from TIs, several ferromagnet/semiconductor heterostructures are investigated for spin transport experiments, including $L1_0$-FePt/MgO/GaAs and [Co/Pt]$_n$/GaAs. None of them show promising magnetisation features for the further pursuit of spin injection into semiconductors. Finally, the surface science of a few magnetic and non-magnetic materials is investigated using low energy electron microscopy (LEEM). A new approach is established to de-oxidise the surface of W(110) substrates at 1800 K, a temperature considerably lower than in the standard W(110) cleaning procedure (2100 K). LEEM also reveals the high-temperature dynamics of the Pt-Si alloy on Si(100) substrates. Following the temperature increment, the Pt-Si alloy goes through the phases of nanowires, islands, and eutectic droplets. This research paves the way towards the future energy-efficient spintronic devices.

ACKNOWLEDGEMENTS

First and foremost, I must thank my supervisor, Professor Crispin Barnes, for admitting me to TFM, and his continuous encouragement and support for almost 5 years. The weekly meetings with Crispin are not only fruitful but also fun. It is hard to say goodbye to him and to this group. I would thank Professor Richard Phillips, who devoted so much of his effort into the construction of the MOKE probe. I also acknowledge Professor Thorsten Hesjedal from Oxford, who provided enormous support on topological insulator projects. I must also thank Professor Wen-Xin Tang from Chongqing, who accommodated me in his group for two months and taught me about the low energy electron microscope.

I wish to mention a few people in the department that I feel grateful to: Justin, for introducing me to MOKE and teaching me the experiments from the basics; Adrian, for teaching me and helping me on so many things hand-by-hand; Angadjit, for bringing me to the field of topological insulator and together we worked on so many projects; Dr. Stuart Holmes, for helping on the cryostat and semiconductor knowledges; Professor Chris Ford, who always inspire me with his brilliant experimental skills and deep exploration into science. Not to mention Mu, Jung-Wei, Razan, David, Matthew, Peter, Chris, Ankita, Cheng, Jinggao, Ke-Xin, Jun-Young, Michael, Baodan, Dawei, and Debi, who helped my work and and made the lab an enjoyable place to work. I thank the Cavendish Workshop especially Chris and Gary for so much support on constructing the MOKE probe. I also express my appreciation to the team in Chongqing, including Yu Lei, Li Meng, Zhu Lin, Yang Xiaodong, and Shen Mengqiu, who kindly accepted me into the group, worked on my project day and night, and selflessly taught me so many things. I thank Professor Stephane Mangin and Thibaud from Nancy, for giving me the first co-authored paper. I also thank Professor Christian Back from Regensburg, for showing me his world-class MOKE setup. Special thanks to Adrian, Peter and Justin for proofreading my thesis.

I must acknowledge the Cambridge Philosophical Society and Fitzwilliam College for financial support during my PhD.

During these 5 years I had so much happiness, due to my friends in the college and in Cambridge: Juan, Max, Freya, Winnie, Sabrina, Florence, Niclas, Yiran, and so many others. I am truly grateful to have the Cambridge journey with them.

I cannot express how grateful I am to my parents. The unconditional love, trust, tolerance and support are what I owe beyond a lifetime. They have never been aboard, nor received good education, but they always make their best effort to educate me, comfort me and protect me. They always welcome me home and they always care about my well being, although I live thousands of miles away, and I can only visit them once or twice a year.

I wish to leave the last paragraph for my wife, Luyao, who has been together with me for over 8 years. I hope she will not regret her decision to marry me. Despite the continuous long distance, she is always so brave, so determined, and so devoted to our relationship. My PhD life would collapse without her standing by my side. I am looking forward to settling down with her somewhere in this world.

PUBLICATIONS

[1] **J. Liu**, A. Singh, J. Llandro, L. B. Duffy, M. R. Stanton, S. N. Holmes, M. J Applegate, R. T. Phillips, T. Hesjedal, and C. H. W. Barnes. A low-temperature Kerr effect microscope for the simultaneous magneto-optic and magneto-transport study of magnetic topological insulators. *Measurement Science and Technology* (under review).

[2] T. Fache, H. S. Tarazona, **J. Liu**, G. L'vova, M. J. Applegate, J. C. Rojas-Sanchez, S. Petit-Watelot, C. V. Landauro, J. Quispe-Marcatoma, R. Morgunov, C. H. W. Barnes, and S. Mangin. Nonmonotonic aftereffect measurements in perpendicular synthetic ferrimagnets. *Physical Review B*, **98**, 064410 (2018).

[3] A. Singh, V. S. Kamboj, **J. Liu**, J. Llandro, L. B. Duffy, S. P. Senanayak, H. E. Beere, A. Ionescu, D. A. Ritchie, T. Hesjedal, and C. H. W. Barnes. Systematic study of ferromagnetism in $Cr_xSb_{2-x}Te_3$ topological insulator thin films using electrical and optical techniques. *Scientific Reports*, **8**, 17024 (2018).

CONTENTS

Declaration **I**

Abstract **II**

Acknowledgements **IV**

Pulications **VI**

Contents **VIII**

List of Figures **IX**

List of Abbreviations **XVII**

1 Overview and Introduction **1**
1.1 Thesis Structure 1
1.2 Magneto-optic Kerr Effect 2
1.3 Exchange Bias 3
1.4 Hall Effects 5
1.5 Topological Insulator 11

2 Experimental Techniques **15**
2.1 Molecular Beam Epitaxy 15
2.2 Magnetron Sputtering 17
2.3 X-ray Diffraction and X-ray Reflectivity 18
2.4 Transmission Electron Microscope 20
2.5 Device Fabrication 22

3 Low Temperature Focused Scanning Polar MOKE Microscope **25**
3.1 Theoretical and Experimental Background 25
3.2 Construction of the Low Temperature MOKE Probe 29
3.2.1 Cryostat 29
3.2.2 MOKE Probe: Overall Layout 31
3.2.3 MOKE Probe: Optical Table Part 33
3.2.4 MOKE Probe: Room Temperature Part 35
3.2.5 MOKE Probe: Low Temperature Part 38
3.3 Experiment: 2D Scan of Magnetic Micro-patterns 41

3.4 Experiment: Temperature dependent magnetisation in (Ga,Mn)(As,P) 44
3.5 Summary and Discussion 47

4 Exchange Bias in Topological Insulator Superlattices 49
4.1 Rare-earth Doping of Topological Insulators 49
4.2 $[Cr:Sb_2Te_3/Dy:Bi_2Te_3]_{10}$ Superlattice: Growth and Structural Characterisation 54
4.3 $[Cr:Sb_2Te_3/Dy:Bi_2Te_3]_{10}$ Superlattice: Magnetic Measurements 56
4.4 $[Cr:Sb_2Te_3/Dy:Bi_2Te_3]_{10}$ Superlattice: First Principle Calculation . . . 63
4.5 Summary and Conclusion 66

5 MOKE Study of Various Magnetic Topological Insulator Systems 67
5.1 $Cr:Sb_2Te_3$ Single-doped Thin Films 67
5.2 $(Cr,V):Sb_2Te_3$ Co-doped Thin Films 72
5.3 EuS/Bi_2Se_3 Heterostructures 78

6 Towards Perpendicular Spin Transport in Ferromagnet / Semiconductor Heterostructures 81
6.1 Background 81
6.2 Growth and Characterisation of $L1_0$-FePt Alloy 84
6.3 Growth and Characterisation of FePt/MgO/GaAs Structures 87
6.4 Growth and Characterisation of $[Co/Pt]_n$/GaAs Sturctures 90
6.5 Non-monotonic After-effect Measurements in Pt/Co/Ir/Co/Pt Perpendicular Synthetic Ferrimagnets 92

7 Low Energy Electron Microscopy Study of Metal Structures 97
7.1 Low Energy Electron Microscopy 97
7.2 $L1_0$-FePt Heat-assisted Magnetic Recording 100
7.3 W(110) Surface Cleaning with Reduced Temperatures 102
7.4 Pt-Si Surface Dynamics on Si(100) 105
7.4.1 Pt-Si Dynamics: Background 105
7.4.2 Pt-Si Dynamics: Nanowires 106
7.4.3 Pt-Si Dynamics: Droplets 112
7.4.4 Pt-Si Dynamics: Summary and Discussion 116

8 Summary and Outlook 117
8.1 Research Summary 117
8.2 Future Work 120

Bibliography 121

LIST OF FIGURES

1.1 Three common MOKE geometries. 2
1.2 Phenomenological model of exchange bias in a FM/AFM system, illustrating a lateral offset in the hysteresis loop. The magnitude of the exchange bias field H_E and coercive field H_c are defined in the figure. Figure adapted from ref.[1] 4
1.3 Schematics of the anolamous Hall effect (AHE) and spin Hall effect (SHE). $N_{\text{spin-up}}$ and $N_{\text{spin-down}}$ stand for the number of spin-polarised electrons in up and down directions, and V_{xy} stands for the transverse voltage. Figure adapted from ref.[2]. 6
1.4 (a) Schematic of the Landau levels and Fermi energy in a two-dimensional electron gas (2DEG) system under a strong magnetic field. Here, E_F stands for Fermi energy. (b) Schematic showing the localised cyclotron orbits in the bulk and chiral conduction in the edge in a 2DEG system. Figure adapted from ref.[3]. 7
1.5 Schematics of the quantum Hall effect (QHE) and quantum spin Hall effect (QSHE). (a) In QHE, two spinless conduction channels for opposite directions are spatially separated to the upper and lower edges of the sample. This is illustrated by the symbolic equation: $2 = 1 + 1$. (b) In QSHE, four spinful conduction channels are also spatially separated to the upper and lower edges of the sample, with each edge containing two channels opposite in both spins and directions. This is illustrated by the symbolic equation: $4 = 2 + 2$. Figure adapted from ref.[4] 8
1.6 The two possible pathways of backscattering from an impurity in the edge states of a quantum Spin Hall system. The difference in the Berry phase between the two paths is 2π. Figure adapted from ref.[4]. 9
1.7 (a) The simplified model of CdTe/HgTe/CdTe quantum wells below and above the critical thickness. The bands are respectively Γ_8 (red) and Γ_6 (blue). (b) The corresponding energy spectra of the quantum wells. The normal band has an insulating gap, while the inverted band has linear edge states (red and blue lines). (c) The corresponding longitudinal resistance. Different colours represent different devices. Figure adapted from ref.[4]. 10
1.8 Schematic diagrams of the band inversion in a 3D TI. (a) The p-band is split due to SOC. (b) The normal band and inverted band crosses at the interface. Here, E_F is the Fermi energy 12

1.9 (a) Bulk and surface bands of a Bi_2Se_3 TI sample, revealed by ARPES. Figure adapted from ref.[5]. 12
1.10 QAHE in a Cr:$(Bi,Sb)_2Te_3$ film at 30 mK. (a) The measurement geometry. (b) Hall resistivity versus magnetic field under different gate voltages (V_g). Figure adapted from [6]. 13

2.1 Three primary modes of thin film growth. 16
2.2 Photograph of the TI MBE system at Oxford. 16
2.3 Schematic diagram of a magnetron sputtering system. Figure adapted from ref.[7]. 17
2.4 Schematic diagram of the X-ray diffraction 18
2.5 A typical X-ray reflectivity spectrum. Figure adapted from ref.[8]. . . . 19
2.6 Schematic diagram of the transmission electron microscopy (TEM). Left: imaging mode; right: diffraction mode. Figure adapted from [9]. 21
2.7 Optical micrograph of a (Ga,Mn)(As,P) Hall bar. 23
2.8 Optical microgrpah of the pattern 'CAMBRIDGE'. The stroke width is 5 μm, and the area of this graph is 350 μm × 50 μm. 24

3.1 Schematic of the room temperature MOKE microscope designed by Flajsman *et al.* Figure adapted from ref.[10]. 27
3.2 (a) Schematic of the Regensburg MOKE microscope. Figure adapted from ref.[11]. (b) Photograph of the MOKE microscope. (c)(d) Close-ups of this instrument. 28
3.3 Photograph of the cryostat lab at the Bragg Building 162A. 30
3.4 Diagram of the MOKE probe (not to scale) with the optical components as follows: (1) photodetector, (2) photoelastic modulator (PEM), (3) polariser at 45°, (4) fibre-coupled 850-nm laser, (5) polariser at 0°, (6) beamsplitter, (7) camera, (8) imaging lens, (9) 45° mirror, (10) LED bulb, (11) collimation lens, (12) beamsplitter, (13) cryostat window, (14) objective lens, and (15) sample on piezoelectric stage. 32
3.5 (a) Photograph of the laser stabilization and coupling system on the optical table. (b) Photograph of the controllers for the laser diode on the optical table. 34
3.6 (a) Photograph of the room temperature part of the MOKE probe. The numbering of the optical components is identical to Figure 3.4. (c) Photograph of the entire MOKE probe. The height of the room temperature (RT) part is 0.5 m and that of the low temperature (LT) part 1.2 m. . 36
3.7 (a) Photograph of the hollow cone (the one next to N6 in the MOKE probe) used to eliminate back reflection of the laser. This photo was taken under room light when the cone was placed on a standard black breadboard. Note the black colour inside the cone is significantly darker than the outside due to the multiple light reflections within the inner surface. (b) Photograph of the cryostat window assembly. The tilted window is highlighted in a red circle which prevents back reflection of the illumination light from entering the CCD camera. 37

3.8 Photograph of the bottom end of the MOKE probe, with numbered components listed as follow: (14) objective lens in a cage plate, (15) cryogenic sample holder, (16) Attocube piezoelectric steppers, (17) titanium tubes winded by cooper wires. 39
3.9 The cryogenic sample holder designed by E-tec. 40
3.10 Screenshot of the Nanoposition program for automatic control of two-dimensional MOKE scanning. 41
3.11 (a) Two-dimensional MOKE scan of the ferromagnetic pattern 'CAMBRIDGE' at 6 K, fabricated from a $[CoFeB/Pt]_n$ multilayer film with out-of-plane anisotropy. The letter stroke width is 5 μm and the scanning step size is 1 μm. An optical micrograph of the same area is shown at the top left corner. (b) Magnetic hysteresis loops of three different spots on or next to the 'CAMBRIDGE' pattern. (c) The photovoltage recorded (in blue) and its derivative, i.e., the laser profile (in red), when the laser scans across a knife edge. The yellow shaded area represents full width at half maximum (FWHM) of the laser spot. 43
3.12 Out-of-plane magnetic hysteresis loops of the (Ga,Mn)(As,P) film at different temperatures 45
3.13 Temperature-dependent spontaneous magnetisation of the (Ga,Mn)(Ga,P) film 46
3.14 Electrical transport results of the (Ga,Mn)(As,P) film. (a) Temperature-dependent longitudinal resistance. (b) Hall resistance at 6 K. 46

4.1 Lattice structure of RE:Bi_2Te_3. (a) Unit cell consisting of 3 QLs, separated by van der Waals gaps. (b) A QL without doping, showing the Te-Bi-Te-Bi-Te layered structure. (c) A QL with RE doping, showing the Te-Bi-Te-Re-Te layered structure. Figure adapted from ref.[12]. . . 50
4.2 In-plane magnetisation measurements of $(RE_xBi_{1-x})_2Te_3$ films using SQUID at low temperatures. Figure adapted from ref.[12]. 51
4.3 Doping-concentration-dependent magnetic moment of the $(RE_xBi_{1-x})_2Te_3$ films at low temperatures. Figure adapted from ref.[12]. 52
4.4 Band structures along $\Gamma - K$ and corresponding energy distributions along $k_{//} = 0$ for the $(Dy_xBi_{1-x})_2Te_3$ TI films at certain temperatures T. (a) $x = 0.055, T = 20$ K; (b) $x = 0.113, T = 20$ K; (c) $x = 0.055, T = 300$ K; (d) $x = 0.113, T = 300$ K. Results are obtained using APRES. Figure adapted from [13]. 53
4.5 Schematic of the $[Cr:Sb_2Te_3/Dy:Bi_2Te_3]_{10}$ TI superlattice (not to scale). 54
4.6 Cross-sectional TEM images of the $[Cr:Sb_2Te_3/Dy:Bi_2Te_3]_{10}$ TI superlattice with different magnifications. 55
4.7 XRD spectrum of the $[Cr:Sb_2Te_3/Dy:Bi_2Te_3]_{10}$ TI superlattice. Inset: superlattice peaks around (0 0 15). 56

4.8 Magnetic hysteresis loops of the $[Cr:Sb_2Te_3/Dy:Bi_2Te_3]_{10}$ TI superlattice at 10 K, obtained from from anomalous Hall effect (AHE) measurements (top row) and MOKE measurements (bottom row). All the measurements were taken after zero-field-cooling from 300 K. Different settings of the field sweep were applied during the measurements: (a)(b) sweep within ±0.6 T; (c)(d) preset to +2.0 T, then sweep within ±0.6 T; (e)(f) preset to −2.0 T, then sweep within ±0.6 T; (g)(h) sweep within ±2.0 T. 58
4.9 (a) Transport hysteresis loops of the $[Cr:Sb_2Te_3/Dy:Bi_2Te_3]_{10}$ superlattice at 10 K under various ranges of field sweep. (b) Corresponding MOKE hysteresis loops at 10 K. (c) Summary of the covercivities obtained under various ranges of field sweep. 60
4.10 (a) Exchange-biased hysteresis loops of $[Cr:Sb_2Te_3]$ at different temperatures, measured by electrical transport. (b) Corresponding hysteresis loops measured by MOKE. (c) Remanent magnetisation (M_r) and exchange bias field (H_{HB}) obtained from transport and MOKE measurements. Insert: Remanence and coercivity obtained in the 'no-bias' case. 61
4.11 Magnetisation of the $[Cr:Sb_2Te_3/Dy:Bi_2Te_3]_{10}$ film after field cooling. (a) MOKE Hysteresis loops of the TI superlattice at 10 K, after field-cooling from different temperatures. (b) Corresponding exchange bias field at 10 K obtained after field-cooling from temperature t. 62
4.12 Configurations of the following TI structures, optimised using DFT calculations: (a) Sb_2Te_3, (b) Bi_2Te_3, (c) Sb_2Te_3 / Bi_2Te_3, (d) $Cr_{0.33}Sb_{1.67}Te_3$ / $Dy_{0.33}Bi_{1.67}Te_3$, (e) $Cr_{0.33}Sb_{1.67}Te_3$ / $Dy_{0.67}Bi_{1.33}Te_3$. 64
4.13 Possible spin configurations of (a) Cr-Dy and (b) Cr-Dy-Dy. 65

5.1 Temperature-dependent AHE and polar MOKE results of $Cr_xSb_{2-x}Te3$ thin films with respect to magnetic field. Doping levels are $x = 0.76$ and $x = 0.58$. (a,e) MR ratios. (b,f) Hall resistance R_{xx} hysteresis loops. (c,g) Kerr angle θ_K hysteresis loops. (d,h) Comparison between AHE and MOKE hysteresis loops at 10 K and 50 K. 69
5.2 (a,c) Zero-field anomalous Hall conductivity σ_{xy}^A and Kerr angle θ_K versus temperature of $x = 0.76$ and $x = 0.58$ films. (b) Coercivity H_c versus laser power by MOKE measurement of $x = 0.76$ film at 10 K. The red dashed line represents a power law fit. (d) Coercivity H_c versus temperature of $x = 0.76$ film by electrical transport and MOKE measurements. 71
5.3 XRD spectra of the $(V,Cr):Sb_2Te_3$ (in blue) and $Cr:Sb_2Te_3$ (in red) MTI thin films. 73
5.4 Two-dimensional reflectivity map of a $(Cr.V):Sb_2Te_3$ Hall bar. The blue parts are the bare substrates with low reflectivity, green part is the Hall bar which is moderately reflective, and red parts are highly-reflective Au contacts. 74

5.5 Temperature-dependent magnetic hysteresis loops of (a) (Cr,V):Sb_2Te_3 and (b) Cr:Sb_2Te_3 films obtained from MOKE measurements. (d,e) Corresponding hysteresis loops obtained from AHE electrical transport measurements. (c,f) Temperature-dependent coercivity and saturation magnetisation values extracted from MOKE and transport measurements for the two films. 75
5.6 (a) Temperature-dependent MR of the (Cr,V):Sb_2Te_3 film from 5 K to 100 K. (b) Close-up of the MR above 60 K, with arrows indicating the direction of the magnetic field sweeps. (c) Comparison between the magnetic fields obtained from the resistance peaks in the MR measurements (R_{xx}), and the coercive fields obtained from MOKE and R_{xy}. (d,e,f) Corresponding results for the Cr:Sb_2Te_3 film. 76
5.7 Out-of-plane magnetic hysteresis loops of EuS/Bi_2Se_3 bilayer film . . . 79
5.8 Out-of-plane magnetic hysteresis loops of EuS single-layer film 80

6.1 Top: microscopy photograph showing the Fe/GaAs device. Bottom: Spin transport in the Fe/GaAs heterostructure imaged by polar MOKE at 4 K. Figure adapted from ref.[14]. 82
6.2 Top: Schematic graph showing the FeCo/GaAs device and the MOKE microscope objective. Bottom: Cross-sectional spin drift image in the Fe/GaAs heterostructure by polar MOKE at 10 K. Figure adapted from ref.[15]. 83
6.3 Unit cells of FCC (left) and the $L1_0$ phase (right). Different coloured balls represent different atoms. In $L1_0$ phase (001) planes are formed by two different elements which are stacked alternately. 85
6.4 Room-temperature polar MOKE hysteresis loops of $L1_0$-FePt/MgO(001) films grown at different temperatures. 86
6.5 XRD spectrum of the $L1_0$FePt/MgO film grown at 500°C. Clear peaks of $L1_0$-FePt (001) and $L1_0$-FePt (002) confirm the presence of $L1_0$ order. 86
6.6 Out-of-plane hysteresis loops of the $L1_0$-FePt/MgO/GaAs and $L1_0$-FePt/MgO films at room temperature. 88
6.7 Cross-sectional TEM images of the $L1_0$-FePt/MgO/GaAs structure. . . 89
6.8 Out-of-plane hysteresis loops of the $[Co/Pt]_n$/GaAs multilayer films at room temperature. S1 & S2: Pt(4)/Co(0.5)/Pt(1)/Co(0.7)/GaAs(001&111); S3 & S4: Pt(4)/Co(0.5)/Pt(1)/Co(0.5)/Pt(0.5)/GaAs(001&111); S5 & S6: Pt(4)/Co(0.5)/Pt(1)/Co(0.5)/Pt(0.7)/GaAs(001&111). Thicknesses in nm. 91
6.9 Hysteresis loop of the Pt(3) / Co(0.95) / Ir(1.4)/ Co(1) / Pt(3) (unit: nm) film at 232 K. The two following switching fields matches closely: one is AP^+ to P^- during downsweep (blue curve), the other being P^- to AP^- during upsweep (red curve). 93
6.10 Local magnetic relaxation curve of the Pt(3) / Co(0.95) / Ir(1.4)/ Co(1) / Pt(3) (unit: nm) film at 232 K, under an applied field of -870 Oe. . . 94

6.11 Domain wall movements in the Pt(3.2) / Co(1) / Ir(1.4) / Co(9) / Pt(3) multilayer film at room temperature with an applied field of -600 Oe. Photographs taken with a time interval of 20 seconds. The light, mid and dark grey colours represent P^- $\downarrow\downarrow$, AP^+ $\downarrow\uparrow$ and AP^- $\uparrow\downarrow$ domains, respectively. The greyscale contrast may not be very clear on the printed version of this thesis. 95

7.1 Schematic diagram of the AC-LEEM at Chongqing University. Phase I is the current AC-LEEM, Phase II is a spin-polarised electron gun system under development, and Phase III is a femtosecond laser system under development. Abbreviations are listed as follow. FEG: field emission gun, D: deflector, Stig: stigmator, CL: condenser lens, MPA: magnetic prism array, ETL: electrostatic transfer lens, MTL: magnetic transfer lens, TL: transfer lens, P: projector lens. Figure adapted from ref.[16]. . 98
7.2 Photograph of the AC-LEEM/PEEM/HT-STM platform at Chongqing University. Figure adapted from ref.[16]. 99
7.3 Left: schematic of HAMR. Right: close-up schematic of the NFT coupling to the $L1_0$-FePt granular media layer. Figure adapted from ref.[17]. 101
7.4 LEEM/LEED images of the oxygen-covered W(100) surface. (a) Bright-field LEEM at 14 eV with 7 μm field-of-view (FOV). (b) LEED pattern at 24 eV. (c,d) Dark-field LEEM images from two half-order LEED spots at 14 eV with 7 μm FOV, showing reversed bright/dark contrast. . . . 103
7.5 PEEM/LEEM/LEED images of the W(100) surface after ion sputtering and 1300 K flashing. (a) PEEM image with 100 μm FOV. (b,c) μLEED patterns of the areas shown under PEEM. (d) Bright-field LEEM image of the middle area at 16 eV. 105
7.6 LEED/LEEM images of the Si(100) surface after degassing and flashing at 1200 °C. (a) LEED pattern at 17 eV. (b) Bright-field LEEM image at 2 eV with a tilted beam, showing (2×1) and (1×2) Si(100) domains. The FOV is 10 μm. 107
7.7 Bright-field LEEM images showing the formation of Pt-Si NWs on Si(100), with 10 μm FOV at 720°C. (a)-(g) were recorded with a time interval of 50 seconds, and (g)-(l) with an interval of 100 seconds. The view had a small lateral drift induced by the high temperature of the chamber. . . 109
7.8 LEED and dark-field LEEM images of the Si(100) surface with Pt-Si NWs. (a) LEED pattern at 14 eV. showing $c(4 \times 6)$ phase. (b,c) Dark-field LEEM images at 4 eV, from spot A and B in the LEED pattern respectively. 111
7.9 μLEED patterns at 14 eV on 4 Pt-Si NWs. NWs are along the [011] direction in (a) and (b), and along $[0\bar{1}1]$ in (c) and (d). 112
7.10 Bright-field LEEM images with 10 μm FOV at 9 eV on the Pt-Si(100) surface, taken at the following temperatures: (a) 770 °C, (b) 810 °C, and (c) 860 °C. 114

7.11 Slightly-tilted bright-field LEEM images showing the Pt-Si droplets on Si(100) at 1040°C. The FOV is 10 μm the electron energy is 2 eV. Time interval is 50 seconds. 115

LIST OF ABBREVIATIONS

2DEG	Two-dimensional electron gas
AC	Aberration-corrected
AFM	Antiferromagnet
AHE	Anomalous Hall effect
AMR	Anisotropic magnetoresistence
ARPES	Angle resolved photoemission spectroscopy
BCC	Body-centred-cubic
CCD	Charge-coupled device
DFT	Density functional theory
DMS	Dilute magnetic semiconductor
EB	Exchange bias
FC	Field cooling
FCC	Face-centred cubic
FI	Ferrimagnet
FM	Ferromagnet
FMI	Ferromagnetic insulator
FOV	Field of view
FWHM	Full width at half maximum
GGA	Generalised gradient approximation
HAMR	Heat-assisted magnetic recording
HCP	Hexagonal close-packed
LC	Left circular

LCC	Leadless chip carrier
LEED	Low energy electron diffraction
LEEM	Low energy electron microscope
MBE	Molecular beam epitaxy
ML	Monolayer
MOKE	Magneto-optic Kerr effect
MR	Magnetoresistance
MTI	Magnetic topological insulator
NA	Numerical aperture
NW	Nanowire
PEEM	Photoemission electron microscopy
PEM	Photoelastic modulator
PM	Paramagnet
PMR	Perpendicular magnetic recording
QAHE	Quantum anomalous Hall effect
QHE	Quantum Hall effect
QL	Quintuple layer
QSHE	Quantum spin Hall effect
RC	Right circular
RE	Rare earth
RHEED	Reflection high-energy electron diffraction
RKKY	Ruderman–Kittel–Kasuya–Yosida
SOC	Spin-orbit coupling
SHE	Spin Hall effect
TEM	Transmission electron microscope
THE	Topological Hall effect
TI	Topological insulator

TRS	Time-reversal symmetry
TSS	Topological surface state
UHV	Ultra high vacuum
vdW	van der Waals
WAL	Weak antilocalisation
XRD	X-ray diffraction
XRR	X-ray reflectivity
ZFC	Zero-field cooling

CHAPTER 1

OVERVIEW AND INTRODUCTION

1.1 Thesis Structure

This thesis consists of eight chapters. Chapter 1 introduces the concepts and research background of the magneto-optic Kerr effect (MOKE), exchange bias, Hall effects, and topological insulators (TIs). Chapter 2 lists out the experimental techniques used in this thesis, including molecular beam epitaxy (MBE), magnetron sputtering, X-ray diffraction (XRD), X-ray reflectivity (XRR), transmission electron microscopy (TEM), and device fabrication. Chapter 3 gives a detailed description of the design and construction of a low temperature polar MOKE microscope, with a base temperature of 1.6 K and a magnetic field of up to 9 T. Two experiments are used to verify the scanning and measurement capabilities of the apparatus: one is on $[CoFeB/Pt]_n$ micro-structures, the other on (Ga,Mn)(As,P) films and Hall bars. Chapter 4 provides a systematic structural, magneto-optic and magneto-transport study of $[Cr:Sb_2Te_3/Dy:Bi_2Te_3]_{10}$ TI superlattices, revealing an unexpected exchange bias effect in this heterostructure. The experimental results are supported by density functional theory (DFT) calculations. Chapter 5 demonstrates the study of various other TI thin film systems, including singled-doped $Cr:Sb_2Te_3$, co-doped $(Cr,V):Sb_2Te_3$, and proximity-coupled EuS/Bi_2Se_3 films. Chapter 6 illustrates the efforts towards an out-of-plane spin transport device in ferromagnet/semiconductor systems. Two structures are used to investigate the spin transport, including $L1_0$-FePt/GaAs, and $[Co/Pt]_n$/GaAs. The non-monotonic spin relaxation in Pt/Co/Ir/Co/Pt perpendicularly magnetic multilayers is also described in this chapter. Chapter 7 shows the study of the W(110) surfaces and Pt dynamics on Si(100) substrates using a novel low energy electron microscope (LEEM). Finally, Chapter 8 concludes this thesis and points out the direction for future work.

1.2 Magneto-optic Kerr Effect

The magneto-optical Kerr effect (MOKE) describes the changes of the reflected light, usually laser light, from a spin polarised surface. Microscopically, this effect originates from the interaction between the electric field of the light and the electron spins of the material due to spin-orbit coupling. Macroscopically it can be explained by the presence of antisymmetric, off-diagonal elements in the dielectric tensor [18, 19]. MOKE is a non-invasive magnetisation measurement technique that combines the advantages of μm-sized lateral resolution and surface sensitivity, due to the controlled spatial laser profile and its limited penetration depth into a sample (∼20 nm for metals) [19, 20, 21], making it a powerful tool to investigate magnetic thin films and micro-structures. In contrast, many other magnetometers, such as superconducting quantum interference device (SQUID) and vibrating sample magnetometer (VSM) based techniques, are sensitive to bulk materials only. MOKE microscopy has been used to resolve the spin Hall effect in metals and semiconductors [22, 23, 24], to map spin injection and drift in ferromagnet/semiconductor heterostructures [14, 15], and to verify ferromagnetism in two-dimensional van der Waals crystals [25, 26].

MOKE can be further categorised by the direction of the magnetisation vector in the material with respect to the reflecting surface and the plane of incidence, shown in Figure 1.1. In a polar MOKE geometry the magnetisation vector is perpendicular to the reflecting surface and parallel to the plane of incidence; in a longitudinal MOKE geometry the magnetisation vector is parallel to both the reflecting surface and the plane of incidence; and finally, in a transverse MOKE geometry the magnetisation vector is parallel to the reflecting surface and perpendicular to the plane of incidence. In the first two cases the incident light undergoes changes both in the polarisation angle and

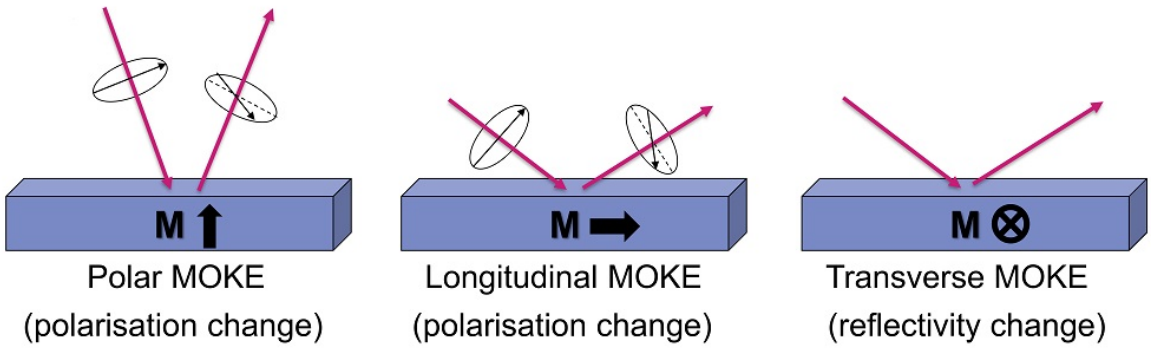

Figure 1.1: Three common MOKE geometries.

ellipticity, while in the last case the light undergoes a change in the reflectivity. This makes the transverse geometry less favourable in experiments, due to the difficulty to precisely track variations in the light intensity compared to polarisation changes.

Many materials for which MOKE studies are of interest need to be measured at low temperatures, e.g. due to low Curie temperatures or temperature-dependent spin lifetimes required to resolve spin distributions spatially [14, 15, 22, 24]. Although a room temperature MOKE microscope is a common apparatus in magnetism research facilities [10, 27, 28], due to the challenges associated with incorporating optical instruments into cryogenic systems, it is not common to find low temperature microscopes that combine the virtues of high sensitivity, high spatial resolution, high magnetic field, and electrical measurement capability. Most low-temperature MOKE magnetometers are designed with optic-purpose cryostats in mind, allowing the specimen to be placed on a cold-finger close to a transparent window, while all optical components of the Kerr microscope can stay at ambient conditions [14, 15, 22, 24]. This is not a feasible approach for users of conventional non-optical cryostats. It is therefore beneficial to develop optical instruments which are compatible with many non-optical cryostats to measure the Kerr effect simultaneously with other important electrical transport characteristics.

1.3 Exchange Bias

The exchange bias effect, also called the exchange anisotropy, is a magnetic phenomena due to interface exchange coupling. This effect leads to a shift of the magnetic hysteresis loop after field cooling (FC) opposite the direction of the previously applied field, or/and increased coercivity in the field-cooled hysteresis compared to zero-field-cooled (ZFC) hysteresis [29, 30]. The difference of the coercive fields between the two sides of a shifted loop is called the exchange bias field (H_{EB}). Sometimes exchange bias is accompanied by the training effect, which is the gradual reduction in H_{EB} following the repeated cycling of hysteresis loops [31]. Exchange bias originates from the interface between two magnetic materials, commonly between one ferromagnetic (FM) and one antiferromagnetic (AFM) material. Other cases do exist, such as FM / paramagnet (PM) [32], AFM / PM [33], AFM / ferrimagnet (FI) [34, 35, 36], and FM / FM [37, 38, 39], to name a few. Exchange bias was first discovered in 1956 by Meiklejohn and Bean in Co/CoO nanoparticles [40], where Co is ferromagnetic and CoO is antiferromagnetic. In 1991 Dieny *et al.* demonstrated the application of exchange bias

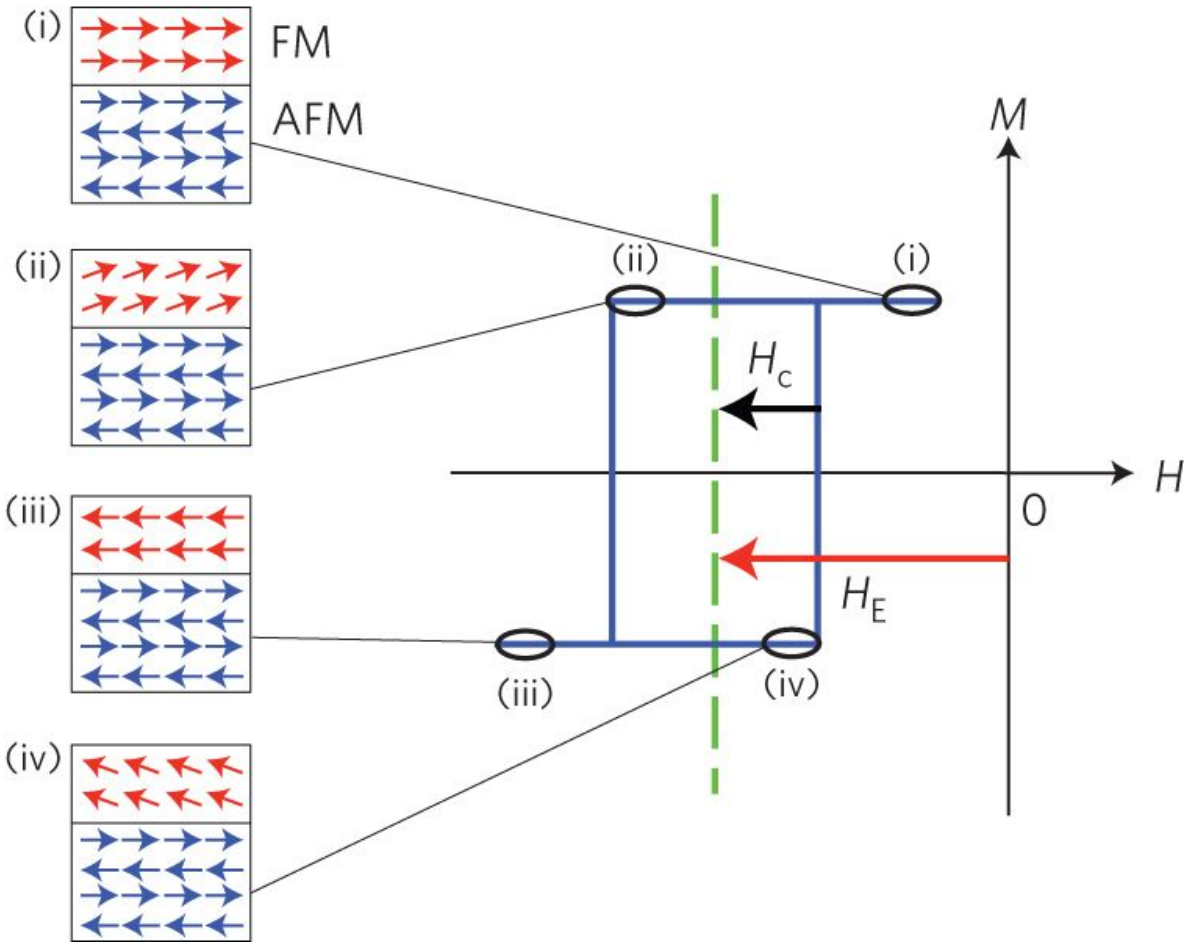

Figure 1.2: Phenomenological model of exchange bias in a FM/AFM system, illustrating a lateral offset in the hysteresis loop. The magnitude of the exchange bias field H_E and coercive field H_c are defined in the figure. Figure adapted from ref.[1]

in NiFe/Cu/NiFe/FeMn spin valve structures [41], opening the pathway to magnetic hard disk storage. Now exchange bias is widely utilised to stabilise the soft ferromagnetic layers in spin valve readback heads and magneto-resistive random-access memory (MRAM) devices [42].

The phenomenological model of exchange bias in a FM/AFM system is illustrated in Figure 1.2. Suppose the FM layer is in close contact to the AFM layer, and the Curie temperature (T_C) of the FM is larger than the Neél temperature (T_N) of the AFM. Starting at temperature T that is between T_C and T_N, an external field in the positive direction is applied to this sample, which aligns the spins of the FM along the field. Meanwhile the AFM is in a paramagnetic state as the temperature is above T_N. The sample is then field-cooled to below T_N, when AFM ordering takes place. Due to the

exchange coupling at the FM/AFM interface, the uppermost monolayer of the AFM will align in the same or the opposite direction of the FM layer depending on the exchange constant between them. Then the second monolayer of the AFM material will align antiparallel to the first one due to AFM ordering, and so on. Now, if the external field is reversed to the negative direction and exceeds the coercivity of the FM layer, the FM spins are supposed to flip along with the field. However due to the pinning by the AFM spins, more Zeeman energy and therefore a higher magnetic field is required to flip the FM spins. When the field goes from the negative back to positive direction, less Zeeman energy is required to recover the FM spins back to the initial state (positively aligned). What is shown in the hysteresis loop is therefore a horizontal shift from the centre towards the negative field direction. It should be mentioned that this model is only a phenomenological approximation and it does not quantitatively match the exchange bias field obtained in experiments [43, 44].

1.4 Hall Effects

The classical Hall effect is named after Edwin H. Hall for his discovery in 1879, who observed a voltage transverse to the direction of a current flow in a gold leaf strip, once an electrical magnet was turned on [45]. This effect was explained by the Lorentz force acting on the moving electrons in a magnetic field. A few years later, Hall discovered that in a ferromagnetic material the transverse voltage can be observed without an external magnetic field, providing the material keeps its remnant magnetisation [46]. In this case the spin-up and spin-down electrons accumulate on the two sides of the conducting sample, showing a net Hall voltage due to the imbalance in the number of spin-polarised electrons. This effect is called the anomalous Hall effect (AHE). The spin-orbit coupling (SOC) is widely believed to be the cause of AHE, however the exact mechanism of this effect is still under debate. Intrinsic deflection, side jump and skew scattering are proposed the main possible mechanisms [47]. Following this argument, in a non-ferromagnetic material, electrons of opposite spins can also deflect due to SOC, which is called the spin Hall effect (SHE) [48]. Since the number of spin-up and spin-down electrons are equal, there is no net Hall voltage in the SHE. The experimental observations of SHE have been reported in GaAs and Ge using low temperature MOKE measurements [22, 24]. Figure 1.3 demonstrates the difference between AHE and SHE.

The quantum Hall effect (QHE), i.e. the Hall effect with quantised conductivity, was

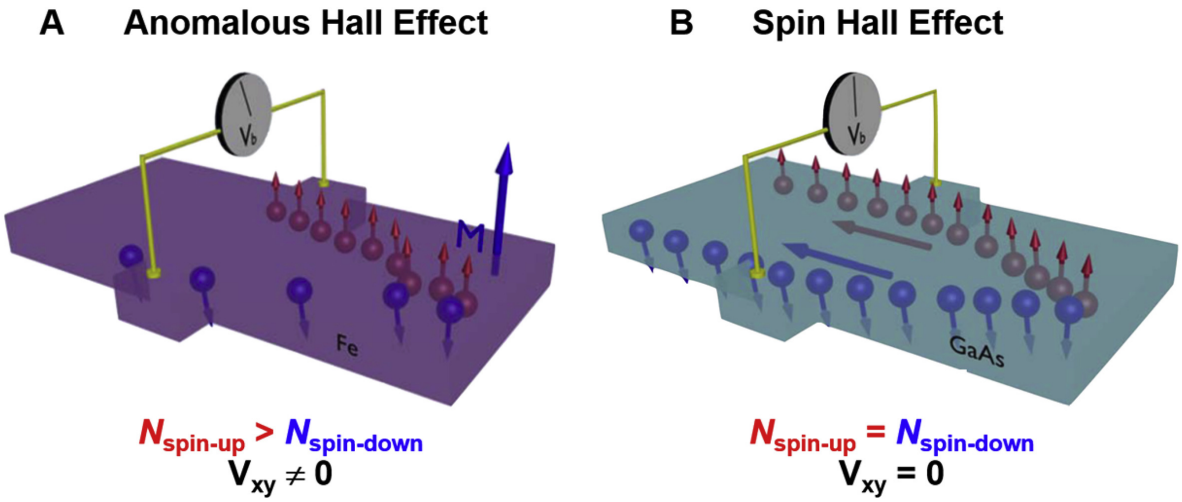

Figure 1.3: Schematics of the anolamous Hall effect (AHE) and spin Hall effect (SHE). $N_{\text{spin-up}}$ and $N_{\text{spin-down}}$ stand for the number of spin-polarised electrons in up and down directions, and V_{xy} stands for the transverse voltage. Figure adapted from ref.[2].

discovered in two-dimensional electron gas (2DEG) systems [49]. In 2DEG the electrons are confined in the z-direction, and an out-of-plane magnetic field B causes the electrons to move in cycles in the $x-y$ plane, with a cyclotron frequency at $\omega_c = \frac{eB}{m}$, where e is electron charge, and m is electron mass. Under a sufficiently large magnetic field, the Hamiltonian of the electrons is described by:

$$[-\frac{\hbar^2}{2m}\nabla^2 + m{\omega_c}^2(x^2+y^2) - i\hbar\omega_c(x\frac{\partial}{\partial y} + y\frac{\partial}{\partial x})]\phi = E\phi$$

where $\hbar$ is the reduced Planck constant, ϕ is electron wavefunction, and E is electron energy. It can be found that the electrons will behave like simple harmonic oscillators, with energy levels described by:

$$E_n = E_0 + (n+\frac{1}{2})\hbar\omega_c$$

where E_n is the n-th energy level, called the Landau level, and E_0 is the ground state energy determined by the confinement in the z-direction. By changing the external magnetic field, the longitudinal conductivity σ_{xx} of this system will oscillate, and the Hall conductivity σ_{xy} will change in steps of $\frac{e^2}{h}$. This phenomenon can be explained by the simplified model shown in Figure 1.4 [3]. As it is shown in Figure 1.4(a), the bulk part of the material has discrete Landau levels, but due to the boundary condition of the device, the energy levels go upwards to meet the continuity of the energy barrier. In this way, the Landau levels that are below the Fermi energy (E_F) in the bulk, which

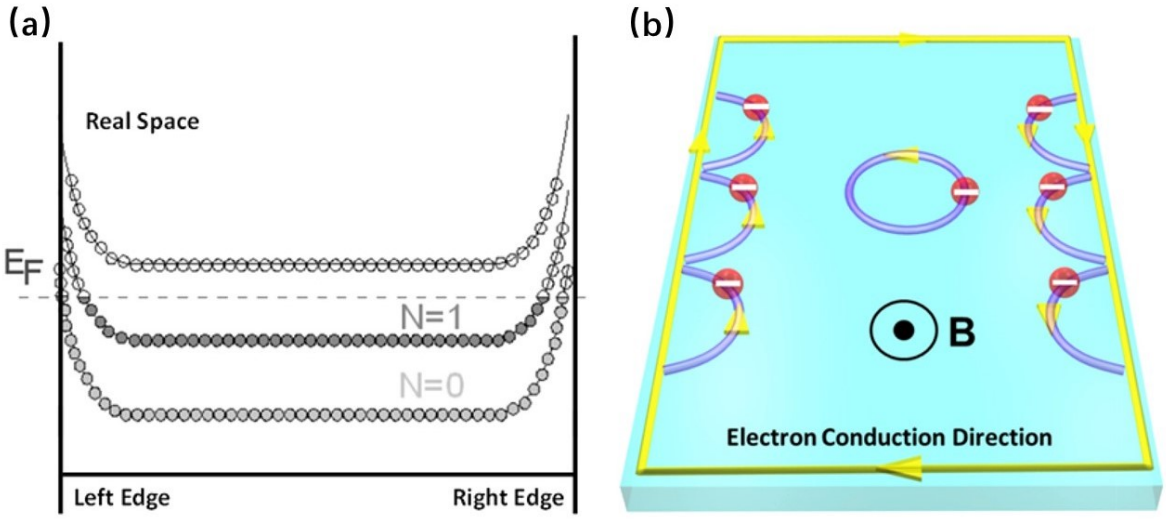

Figure 1.4: (a) Schematic of the Landau levels and Fermi energy in a two-dimensional electron gas (2DEG) system under a strong magnetic field. Here, E_F stands for Fermi energy. (b) Schematic showing the localised cyclotron orbits in the bulk and chiral conduction in the edge in a 2DEG system. Figure adapted from ref.[3].

are occupied by electrons, must cross the Fermi energy at the edge, forming conductive edge states. When the Fermi energy is located between two neighbouring Landau levels, electrons in the bulk will be localised in cyclotron motion and therefore showing insulating behaviour, while the edges states are conducting in the ballistic regime, as shown in Figure 1.4(b). When the external magnetic field changes, the Fermi level will move across different Landau levels, resulting in an oscillation in the longitudinal resistance. The ballistic edge state has a conductivity of $\frac{e^2}{h}$, so that the Hall resistance will reach a plateau when the Fermi energy is between two neighbouring Landau levels, and move to another plateau when the Fermi energy crosses a Landau level.

Most materials that have been investigated including the 2DEG systems have a common parabolic $E(k)$ band structure. In recent years, QHE has also been realised in other novel materials with a linear $E(k)$ band structure, such as graphene [50, 51]. Graphene is a monolayer of carbon atoms arranged into a hexagonal lattice structure. The first Brillouin zone of this structure is also hexagonal. By applying a tight binding model with nearest-neighbour interactions, one can find that the conduction and valence band touch at six points (K points) of the Brillouin zone boundary, forming a Dirac cone. The energy at the K points depends linearly on the momentum, in the same manner as the Dirac equation for a massless relativistic fermion in quantum field theory [52]. The

$E(k)$ relation at K points is described by the following equation:

$$E = \pm\hbar v_F \sqrt{k_x^2 + k_y^2}$$

where v_F is the Fermi velocity, and k_x and k_y are reciprocal space vectors. By applying an out-of-plane magnetic field, Landau levels come into formation and the Hall conductance is quantised, described by:

$$\sigma_{xy} = \pm 4(n + \frac{1}{2})\frac{e^2}{h}$$

The physical importance of the Dirac cone will be further elaborated below. The dissipationless edge currents can be useful for electronic industry, however the strong magnetic field required to induce the QHE limits the application of this phenomenon.

The next Hall effect which does not require an external magnetic field is the quantum spin Hall effect (QSHE) [53, 54], which preserves time-reversal symmetry (TRS) due

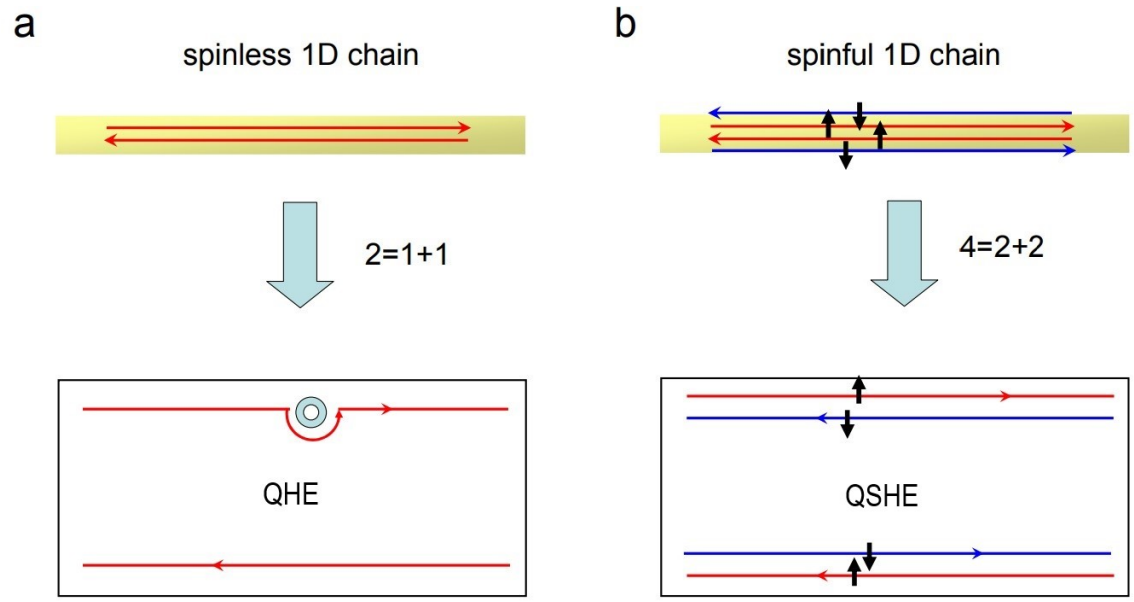

Figure 1.5: Schematics of the quantum Hall effect (QHE) and quantum spin Hall effect (QSHE). (a) In QHE, two spinless conduction channels for opposite directions are spatially separated to the upper and lower edges of the sample. This is illustrated by the symbolic equation: $2 = 1 + 1$. (b) In QSHE, four spinful conduction channels are also spatially separated to the upper and lower edges of the sample, with each edge containing two channels opposite in both spins and directions. This is illustrated by the symbolic equation: $4 = 2 + 2$. Figure adapted from ref.[4]

to the lack of a net magnetisation. Figure 1.5 shows the difference between QHE and QSHE. One of the very interesting aspects of QSHE is spin-momentum locking [4]. The large SOC in some materials renders the spin of a surface electron locked to its momentum, therefore producing two spin-polarised conduction channels at each edge. Here a quantum mechanical term is introduced, called the Berry phase or geometrical phase [55]. When a quantum system undergoes adiabatic evolution in the parameter space of a Hamiltonian and eventually comes back to its original position, this system will acquire an extra phase which is dependent on the closed trajectory of the evolution. Once a conduction electron encounters a non-magnetic impurity on a QSHE edge, due to time-reversal invariance, it has an equal probability to back scatter with the spin rotating either clockwise or anticlockwise, as shown in Figure 1.6. Each of the spins in the two paths accumulates a phase of π in opposite directions, resulting in a net phase difference of 2π. Since electrons are fermions, the wavefunction of an electron gains a minus sign upon changing the spin phase by 2π, leading to destructive interference between the two backscattering channels. In this way, TRS protects the edge conduction and eliminates backscattering. QSHE systems have the potential to implement this 'spin highway' in future electronic devices [56].

The QSHE was first predicted and experimentally observed in CdTe/HgTe/CdTe quantum wells [56, 57], with the structure shown in Figure 1.7(a). CdTe has a common band

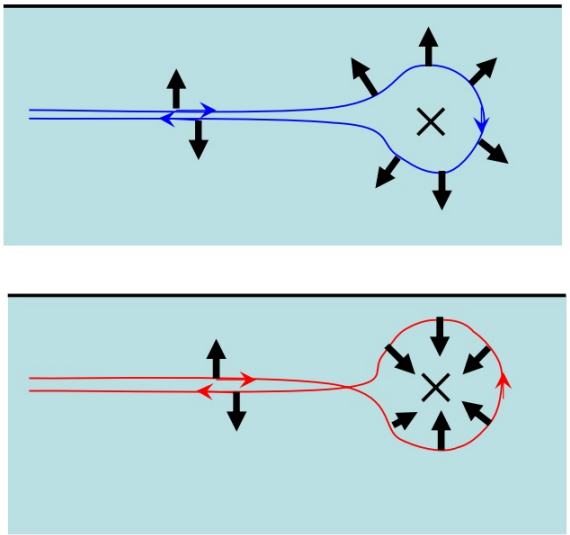

Figure 1.6: The two possible pathways of backscattering from an impurity in the edge states of a quantum Spin Hall system. The difference in the Berry phase between the two paths is 2π. Figure adapted from ref.[4].

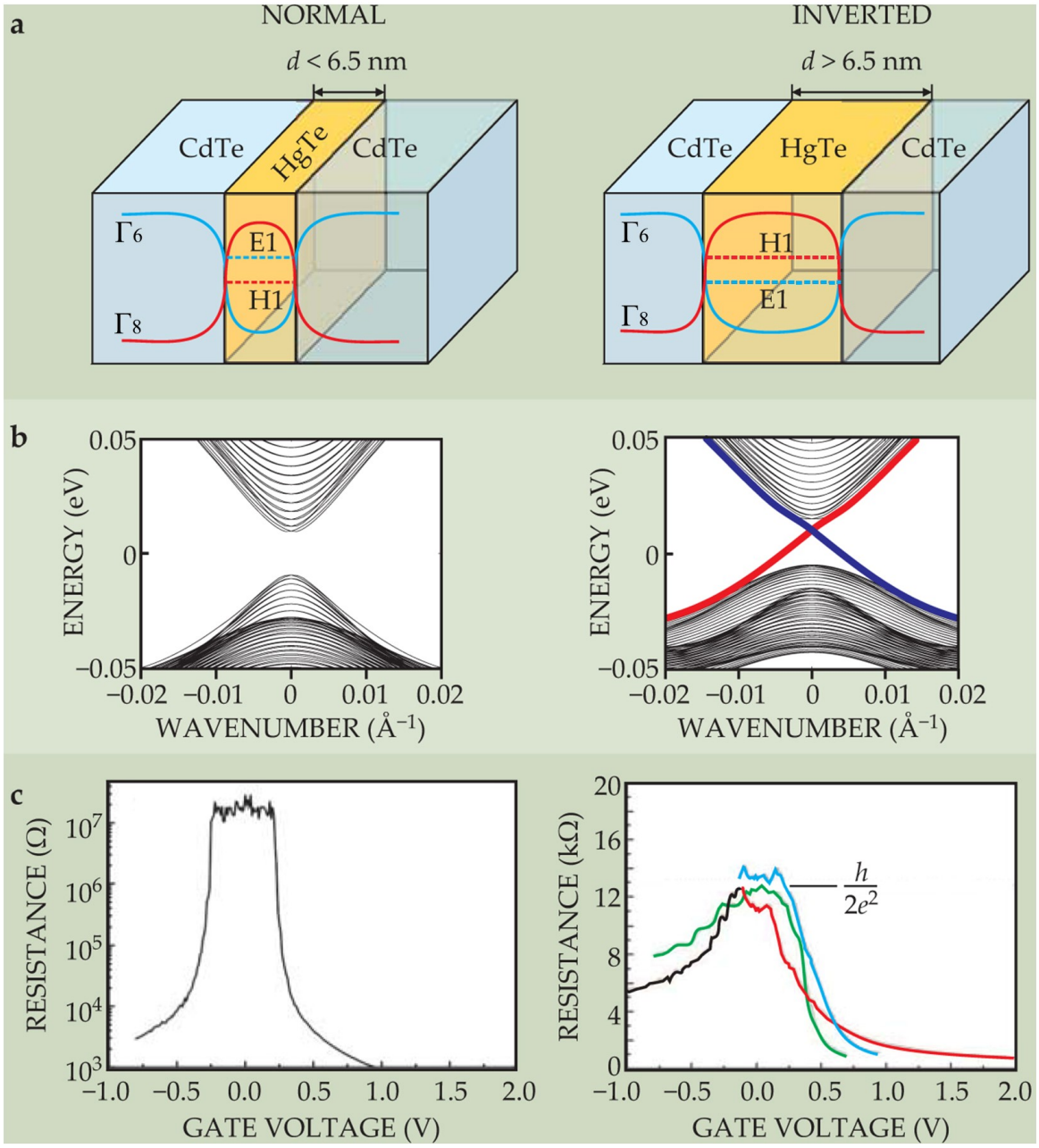

Figure 1.7: (a) The simplified model of CdTe/HgTe/CdTe quantum wells below and above the critical thickness. The bands are respectively Γ_8 (red) and Γ_6 (blue). (b) The corresponding energy spectra of the quantum wells. The normal band has an insulating gap, while the inverted band has linear edge states (red and blue lines). (c) The corresponding longitudinal resistance. Different colours represent different devices. Figure adapted from ref.[4].

structure with an s-type Γ_8 band (red in the figure) below a p-type Γ_6 band (blue in the figure). HgTe, on the other side, has a strong SOC that pushes the Γ_8 band to above the Γ_6 band. Due to the band continuity at the interface, below a critical thickness ($d_c = 6.5$ nm) the HgTe band has Γ_8 below Γ_6, but above d_c the electronic band structure of HgTe itself becomes dominating and the band is inverted (Γ_8 above Γ_6). As shown in Figure 1.7(b), the bulk is insulating as a band gap is present, however, the 2D inverted band yields a pair of 1D edge states crossing at the Dirac point, similar to the K point in graphene. The two conduction channels carry electrons of opposite spins due to spin-momentum locking, and backscattering is prohibited as the Berry phase difference of the two backscattering channels is 2π. Figure 1.7(c) reveals that different devices (coloured in the graph) with inverted bands all reached a longitudinal resistance plateau at $\frac{h}{2e^2}$ due to the edge states, and those with normal bands were strongly insulating.

A main difference between QSHE and QHE is that, the QHE requires a large magnetic field to break the TRS. By applying a perpendicular magnetic field to the HgTe quantum well, it was found that the Hall resistance rose from 0 Ω at 0 T to $\frac{e^2}{h}$ at 1 T, and the longitudinal resistance fell to almost 0, showing a transition from QSHE to QHE regime [56].

1.5 Topological Insulator

Topological insulators (TIs) refer to materials with electrically insulating bulk, but conducting, topologically protected surface states [58]. The HgTe quantum well is the first discovered 2D TI system with 1D surface states. The Dirac nature of the band structure can also be extended to 3D systems, which occupy 2D surface states. Take the 3D TI material Bi_2Se_3 for example [59]. The strong SOC in Bi_2Se_3 lifts the degeneracy of the p-wave valence band and splits it into the $j = \frac{3}{2}$ and $j = \frac{1}{2}$ bands. The $j = \frac{3}{2}$ can go above the s-state, as shown in Figure 1.8(a). When placed next to the vacuum or a topologically trivial material, 'normal' and 'inverted' band configurations must have a crossing point at the interface, giving rise to a topological surface state, as is shown in Figure 1.8(b).

A typical band diagram of Bi_2Se_3 is shown in Figure 1.9, measured by angle resolved photoemission spectroscopy (ARPES) [5]. The bulk shows a classical parabolic band

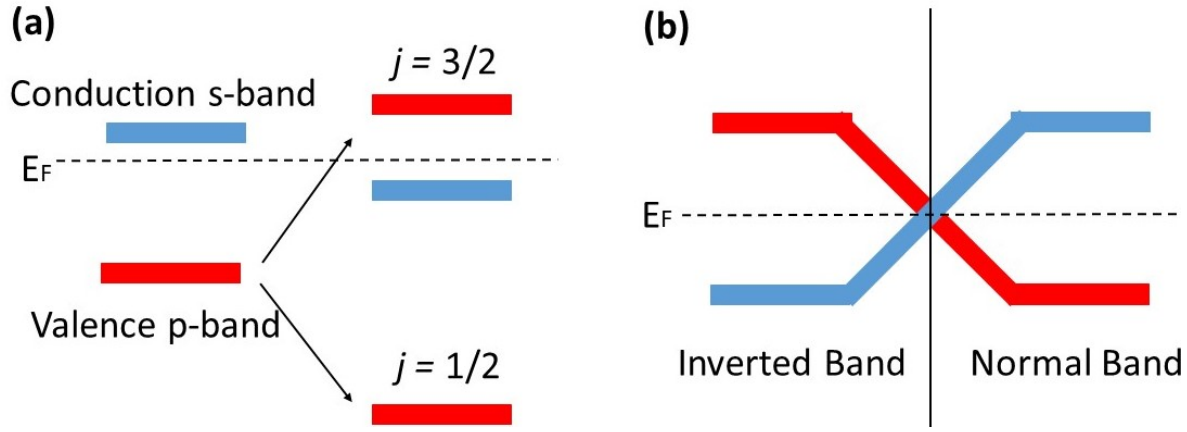

Figure 1.8: Schematic diagrams of the band inversion in a 3D TI. (a) The p-band is split due to SOC. (b) The normal band and inverted band crosses at the interface. Here, E_F is the Fermi energy

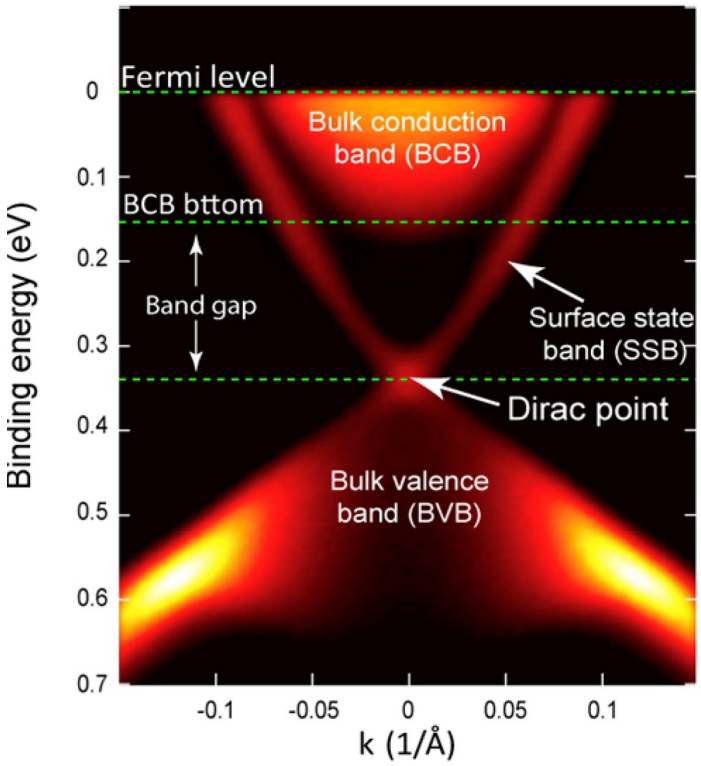

Figure 1.9: (a) Bulk and surface bands of a Bi_2Se_3 TI sample, revealed by ARPES. Figure adapted from ref.[5].

with a band gap of 0.2 eV, while the surface shows a linear $E(k)$ relation with a TR-invariant Dirac point, similar to graphene and HeTe quantum well. This indicates that the electrons in the surface states can be regarded as massless Dirac fermions, moving in the ballistic regime. As mentioned beforehand, what makes a TI more interesting is the

spin-momentum locking. Both Bi and Se are heavy elements and hence the large SOC in Bi_2Se_3 renders the spin of a surface electron locked to its momentum. Therefore, TI has the potential to implement spin as an extra degree of freedom and to realise the 'spin highway' in electronic devices.

Magnetic doping in 3D TIs can break the TRS, induce a band gap in the surface states, and give rise to the quantum anomalous Hall effect (QAHE) at low temperatures [60]. A QAHE system possesses one dissipationless conduction channel in each surface with a defined spin polarisation. The analogy between QAHE and QSHE can be understood as follows: the QSHE regime has two QAHE channels with opposite chirality and the QAHE happens when one of the spin conduction channels is suppressed, sometimes due to ferromagnetic ordering [61].

The QAHE was first experimentally realised in 2013 by Chang *et al.* in 5 nm thick MBE-grown Cr-doped $(Bi,Sb)_2Te_3$ magnetic TI (MTI) films at 30 mK [6]. The schematic of the device is shown in Figure 1.8(a), and the Hall measurement results are illustrated in Figure 1.10(b). By tuning the voltage of the back gate (V_g), the Fermi level resides in the surface band gap and the Hall resistivity can reach the quantised value of $\frac{h}{e^2}$.

Since the discovery of QAHE in Cr-doped $(Bi,Sb)_2Te_3$ and afterwards in V-doped $(Bi,Sb)_2Te_3$ TI thin films below 100 mK [62], many attempts have been made to increase the realisation temperature of the QAHE, mostly by changing the doping scheme in the $(Bi,Sb)_2(Te,Se)_3$ family [63, 64, 65, 66, 67]. Even though the crystal structure

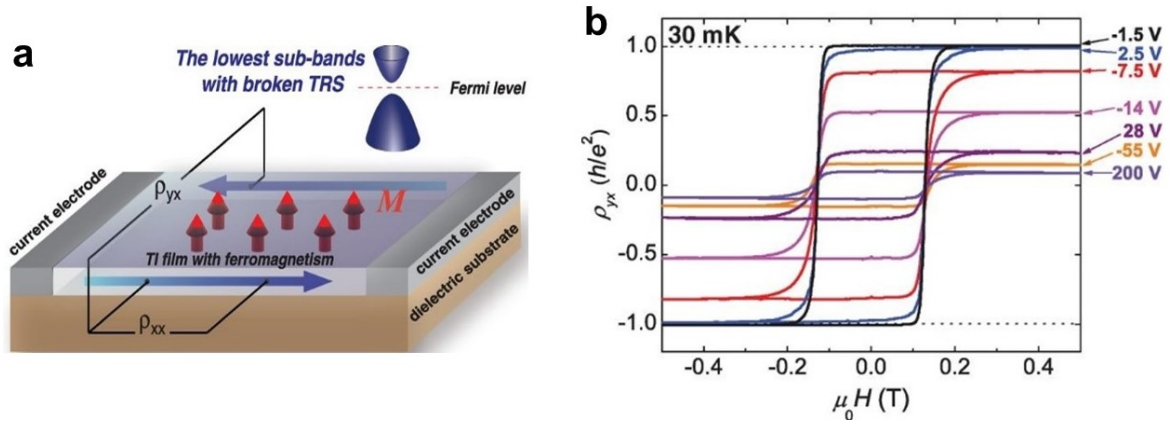

Figure 1.10: QAHE in a Cr:$(Bi,Sb)_2Te_3$ film at 30 mK. (a) The measurement geometry. (b) Hall resistivity versus magnetic field under different gate voltages (V_g). Figure adapted from [6].

of $(Bi,Sb)_2(Te,Se)_3$ remain unaltered moderate Cr doping levels and long-range ferromagnetic order can be establilised above 100 K [68], the QAHE is restricted to the mK regime due to the large Dirac-mass disorder [69]. In 2017, Ou *et al.* showed that, by co-doping $(Bi,Sb)_2Te_3$ with both Cr and V simultaneously, the Hall conductance of the material can stay close to the quantum regime up to 1.5 K [67]. They suggested that the co-doping provides the combined effect of a large magnetic moment (from Cr) and a strong perpendicular anisotropy (from V), overall resulting in a large out-of-plane magnetic moment in the host material. The band gap can therefore be sustained to a higher temperature, since the size of the gap is directly related to the magnitude of the out-of-plane magnetic moment. Another way to increase the QAHE operating temperature is modulation doping, that is, periodically inserting a heavily-doped $Cr:(Bi,Sb)_2Te_3$ layer (1 nm thick) during the growth of non-doped $(Bi,Sb)_2Te_3$ films [66]. The modulation doping scheme is a establised technique in $GaAs/Al_xGa_{1-x}As$ heterostructures to achieve a high carrier mobility [70]. Here the modulation doping in $Cr:(Bi,Sb)_2Te_3$ induces a large mass-gap due to the high Cr concentration, while it preserves the conduction channel in the surface states due to the reduced impurity scattering [71]. As a result the QAHE temperature was lifted to 1 K.

CHAPTER 2

EXPERIMENTAL TECHNIQUES

2.1 Molecular Beam Epitaxy

Molecular Beam Epitaxy (MBE) is an atomic-level deposition technique under ultra-high vacuum (UHV) conditions, generally with a pressure not larger than 10^{-9} mbar [72]. This technique was initially developed for the production of III-V semiconductor superlattices [73]. In MBE the elemental sources are directly co-evaporated into gas phase. These gaseous particles travel through the chamber as a non-interacting molecular beam, and get deposited onto the substrate purely as a surface reaction. It is known that the mean free path (λ) of a single molecule in an ideal gas is given by:

$$\lambda = \frac{RT}{\sqrt{2}\pi N_A P d^2}$$

where R is the Rydberg constant, T is the temperature, N_A is the Avogadro constant, P is the gas pressure, and d is the diameter of the molecule. Considering the room air which are mostly N_2 and O_2 diatomic molecules, the mean free path in a 10^{-9} mbar environment at the room temperature will be about 10^5 m, greatly exceeding the dimension of the growth chamber. In this way the gas particles can be regarded as travelling in a straight line to the substrate without collision. The deposition rate of the individual elements can be precisely tuned by changing the source temperature, and the growth condition of the substrate can be controlled by changing the substrate temperature during and before/after and growth. MBE is a non-equilibrium method allowing the films to be grown at lower temperatures. This non-equilibrium nature allows the incorporation of dopants at high concentration without inducing secondary phases in the film. As a result, MBE has become the most popular approach to grow doped TI materials.

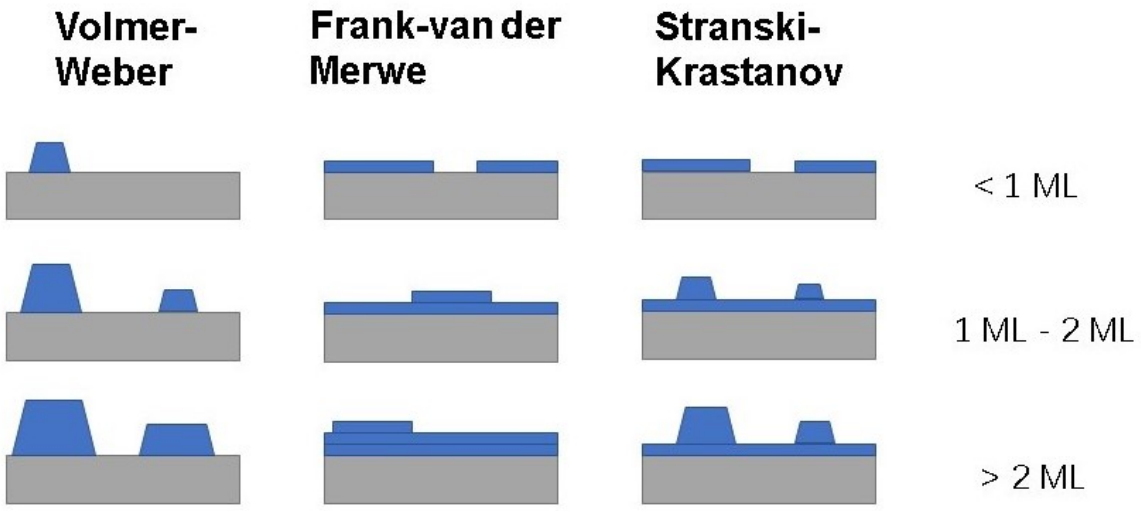

Figure 2.1: Three primary modes of thin film growth.

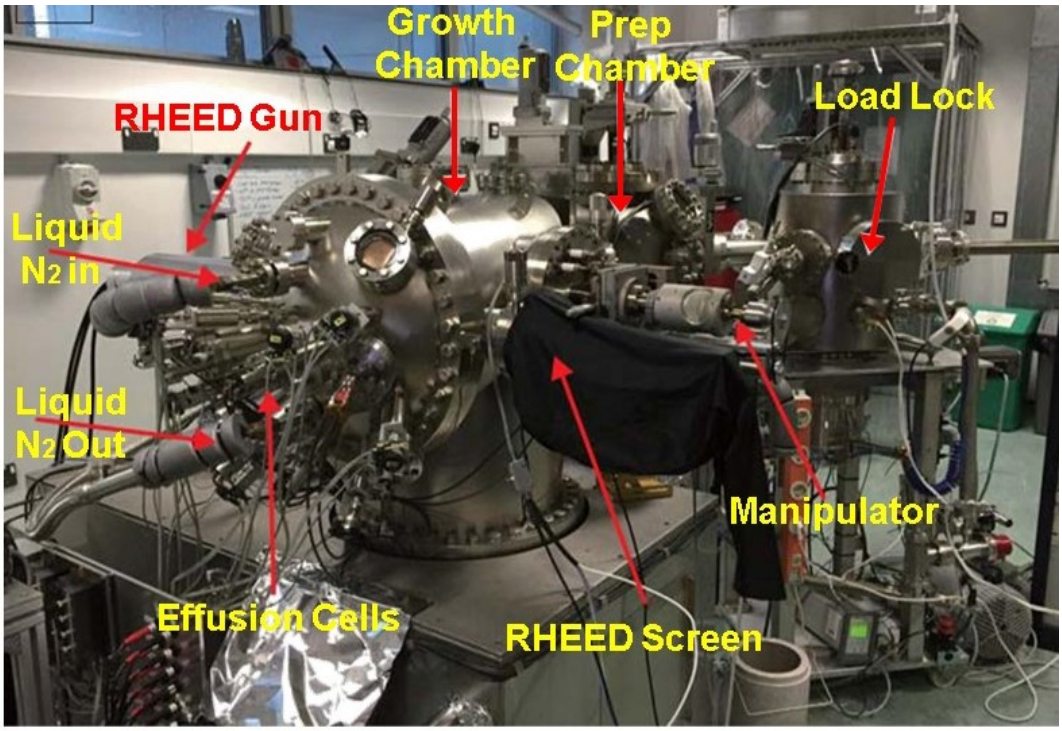

Figure 2.2: Photograph of the TI MBE system at Oxford.

Ideally the MBE films are grown layer by layer: the second monolayer is not deposited until the substrate is fully covered by the first monolayer, and same goes for the higher order monolayers. This is called the Frank-van der Merwe growth. However, depending on the strain and chemical potential of the film surface, new layers may be grown in islands instead of a uniform monolayer, which is called the Volmer-Weber growth. A

hybrid of the two modes can also happen, which involves the first one or few monolayers in a layer-by-layer fashion, then the island mode appears after a critical thickness. This hybrid mode is called the Stranski-Krastanov growth. These three primary MBE growth modes are summarised in Figure 2.1 [74].

Most of the TI films featured in this thesis were grown in the TI MBE chamber at the Rutherford Appleton Laboratory (Didcot), operated by Professor Thorsten Hesjedal and his group members from the University of Oxford. Figure 2.2 shows a photograph of this MBE system. It is composed of 3 interconnected chambers: the loading chamber, the prep chamber and the main growth chamber. There are 8 effusion cells on the side of the growth chamber, equipped with TI elemental sources (Bi, Sb, Te etc) and dopants (Cr, V, Dy etc) of the highest purity, mostly between 4N and 6N. There is also a reflection high-energy electron diffraction (RHEED) gun and screen to *in situ* to observe the growth mode of the films.

2.2 Magnetron Sputtering

Magnetron sputtering is an another popular technique to produce magnetic thin films [75]. Figure 2.3 shows the schematic of a magnetron sputtering system. Noble gases such as Ar are ionised into plasma due to the passage of free electrons, a process called glow discharge. Positively charged Ar^+ accelerates under a high voltage and bombards

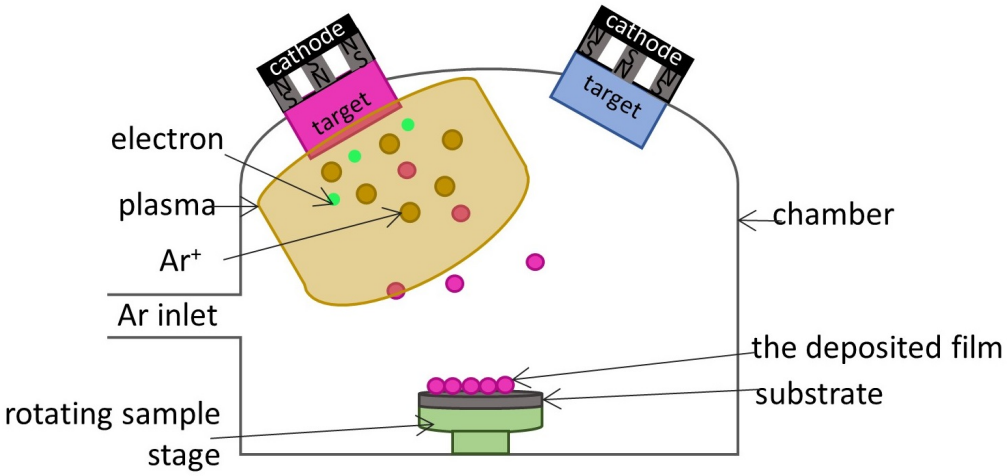

Figure 2.3: Schematic diagram of a magnetron sputtering system. Figure adapted from ref.[7].

onto the target material. This transfers momentum to the target upon collision, causing the outer layer of the material to be sputtered into the chamber and condensed on the sample stage. In the meantime, the secondary electrons generated during the bombardment will collide with more Ar atoms and create more Ar^+ ions. This process sustains the production of the Ar plasma so the film deposition on the sample stage is continuous. Moreover, in a magnetron sputtering system there are permanent magnets placed behind the target, which confines the trajectory of the secondary electrons close to the target due to the Lorentz force. In this way the secondary electrons have a higher probability to collide with Ar atoms and create stronger plasma close to the target, which increases the deposition rate. After several collisions, the secondary electrons will only have a small kinetic energy when they eventually escapes from the dense plasma area and reaches the sample stage under an applied electric field. This small energy has a minimal effect on increasing the temperature of the sample stage, and therefore reduces the possible damage and contamination to the grown film. Apart from Ar, sometimes N_2 and O_2 are used in the chamber to grow oxide and nitride films. In this thesis, the $[Co/Pt]_n$, $[CoFeB/Pt]_n$ and $L1_0$-FePt films were grown using magnetron sputtering at Cambridge and Nottingham.

2.3 X-ray Diffraction and X-ray Reflectivity

X-ray diffraction (XRD) and x-ray reflectivity (XRR) are widely used to study the structure of thin films [76]. Most of the X-ray studies reported in this thesis were conducted by Dr. Adrian Ionescu (TFM Group) using a Bruker D8 Discover diffractometer. In this diffractometer, accelerated electrons hit a Cu target and generate heat and radiation. The typical radiation is Cu-K_α which has a wavelength of $\lambda = 1.5418$ Å, in the same order of magnitude as atomic lattices. The principle of XRD is the constructive

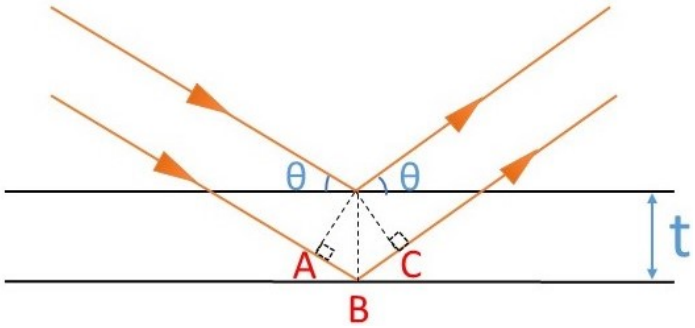

Figure 2.4: Schematic diagram of the X-ray diffraction

interference of reflected light from the surface of the material, shown in Figure 2.3. Since the difference in the travelling distance of the two beams is $AB + BC = 2d \sin\theta$, The constructive interference occurs only when the following condition is met:

$$2t \sin\theta = n\lambda$$

where t is the lattice spacing, θ is the incident angle to the film plane, and λ is the wavelength of the X-ray. This formula is called Bragg's law. The diffraction peaks at certain θ in an XRD spectrum give out the information of the out-of-plane lattice parameter, film strain and identification of the phases.

In X-ray reflectivity (XRR), the X-ray beam is incident on the film at a grazing angle and the reflectance is monitored [76]. A typical XRR spectrum is shown in Figure (2.5). XRR complies with the principle of total external reflection, which has a critical angle (θ_c) of less than 0.3° in most materials. X-ray is reflected both at the surface and the interfaces of different materials due to the difference in electron densities between the different layers in a thin film or heterostructure. The critical angle θ_c is used to infer

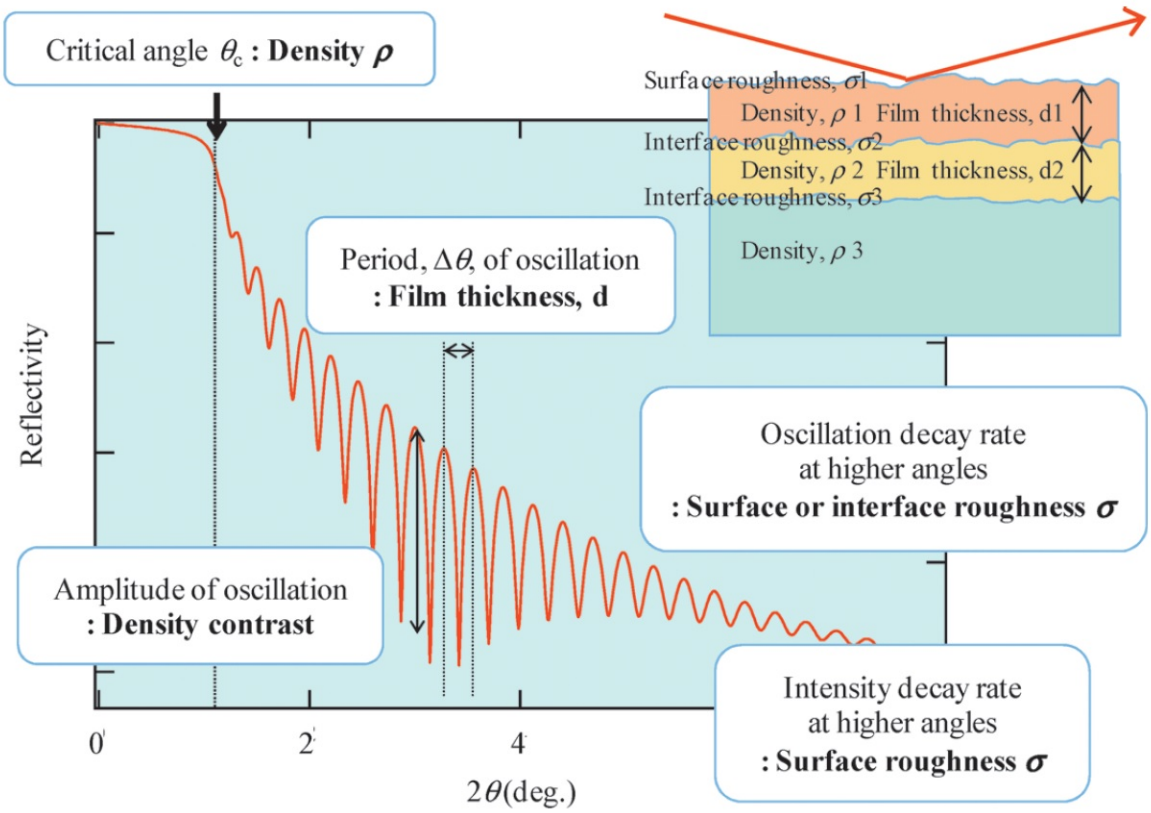

Figure 2.5: A typical X-ray reflectivity spectrum. Figure adapted from ref.[8].

the density ρ of the sample. When the incidence angle exceeds θ_c, the reflected beam from different interfaces creates an oscillation pattern in the XRR spectrum, called the Kiessig fringes. The film thickness d can be inferred using the following equation:

$$d = \frac{\lambda}{2\Delta\theta}$$

where λ is the wavelength of the X-ray, and $\Delta\theta$ is the spacing between the Kiessig fringes. Also the amplitude of the oscillation is directly related to the density contrast between the different layers. Finally, the decay of both the oscillation and the overall intensity reflect the interface roughness of the sample.

2.4 Transmission Electron Microscope

Some samples featured in this thesis were examined under the FEI Tecnai F20 transmission electron microscope (TEM) at the Cavendish Laboratory. TEM is a microscopy instrument in which a beam of electrons is transmitted through a specimen and form a magnified image [77]. Here electrons instead of visible light are used due to the stronger resolving power. A human eye has a resolution of 0.2 mm, and an advanced optical microscope can have a resolution of 200 nm. This is because of the wave nature of light, where the resolving power is limited by diffraction. The Abbe diffraction limit states that the minimum resolvable distance of a microscope is

$$d = \frac{\lambda}{2\mathrm{NA}}$$

where d is the resolvable distance, λ is the wavelength of light, and NA is the numerical aperture which can have a value of 1.5 in modern instruments. As a result the minimum d of an optical microscope is 200 nm considering the visible wavelength is 380 - 740 nm. This is 1000 times higher than the resolution of a human eye. Electromagnetic waves of smaller wavelengths, such as X-ray, are difficult to focus or deflect using optical components. However, the de Broglie wavelength of the electrons can be much smaller than the visible region, for example, electrons accelerated though 20 kV have a wavelength of 0.01 nm. This means a microscope that utilises the electron beam can have a sub-nm spatial resolution. Also, as electrons are charged particles, the trace of an electron beam can be manipulated by an electric field or magnetic field (Lorentz force), making it possible to focus or deflect the electron beam with electrostatic and magnetic lenses.

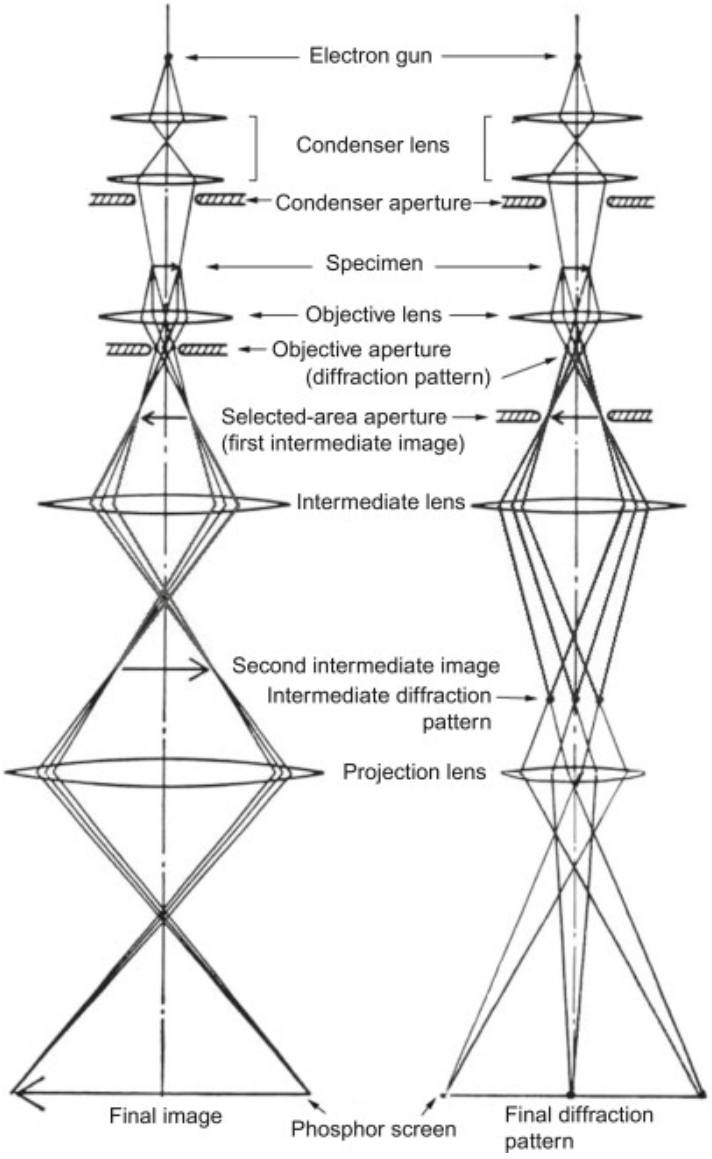

Figure 2.6: Schematic diagram of the transmission electron microscopy (TEM). Left: imaging mode; right: diffraction mode. Figure adapted from [9].

Figure 2.6 shows the schematic diagram of a TEM system under imaging mode (left) and diffraction mode (right). In the imaging mode, the electron beam is first ejected from the electron gun and accelerated by a high voltage, then collimated by the condenser lens system. This parallel beam then transmits through the thin specimen. Part of the beam is not scattered, and part is scattered due to the interaction between the electrons and the specimen. Afterwards there is an objective lens to focus the beam and generate a magnified image. Since both scattered and non-scattered electrons exist, a

diffraction pattern is formed at the back focal plane of the objective lens, which contains the structural information of the specimen. An objective aperture is therefore placed at this back focal plane, to select between the non-scattered and scattered beams, which respectively forms the bright-field and dark-field images. Below the objective lens there is an intermediate lens placed at the image plane of the objective lens, and a projection lens is placed further below them. This three-lens combination is used to provide a two-stage magnified image with a tunable magnification ratio. Finally this image is collected at the bottom screen or camera. In the diffraction mode, the objective aperture is removed, and the intermediate lens is at the back focal plane of the objective lens. The strength of the intermediate lens is adjusted, so that the intermediate lens produces a magnified image of the diffraction pattern. This pattern is then further magnified by the projection lens and finally collected by the screen or camera. In this mode a selected-area aperture is placed before the intermediate lens to determine which part of the specimen is displaced on the screen.

2.5 Device Fabrication

The micro-devices featured in this thesis were fabricated in the Cavendish SP and TFM cleanrooms using standard photolithography and wet/dry etching techniques. The topological insulator devices were fabricated by Dr. Angadjit Singh, and other devices were fabricated by the author of this thesis. In this section the processing of a (Ga,Mn)(As,P) dilute magnetic semiconductor (DMS) film is described as an example. The epitaxial film is 25 nm thick, on a semi-insulating GaAs(100) substrate. The film was first cleaved into 5 mm $\times$ 5 mm in dimension using a microscope scriber in the SP cleanroom. Then the chip was put on a spinner and a few drops of Shipley 1813 positive photoresist was dispensed on the chip. The chip was spun at 5500 rounds-per-minute for 30 seconds, then baked on a 110 °C hotplate for 1 minute. Afterwards the chip was inserted into an aligner and aligned with a pre-designed Hall bar pattern, and exposed to ultraviolet light for 6.5 seconds. Then the pattern was developed in the MF-319 developer for 30 seconds and rinsed in DI water and blown dry by N_2. The quality of the pattern was checked under an optical microscope with ultraviolet filter to prevent further exposure. The next step was wet etching. The chip was immersed in an acid solution for 20 seconds with composition ratio H_3PO_4 : H_2SO_4(95 %) : H_2O_2 : H_2O = 1:1:1:12, then rinsed in DI water and blown dry by N_2 again. An etching depth of 180 nm was confirmed by the Dektak. Afterwards the photoresist was removed in acetone,

rinsed in isopropanol and blown with N_2.

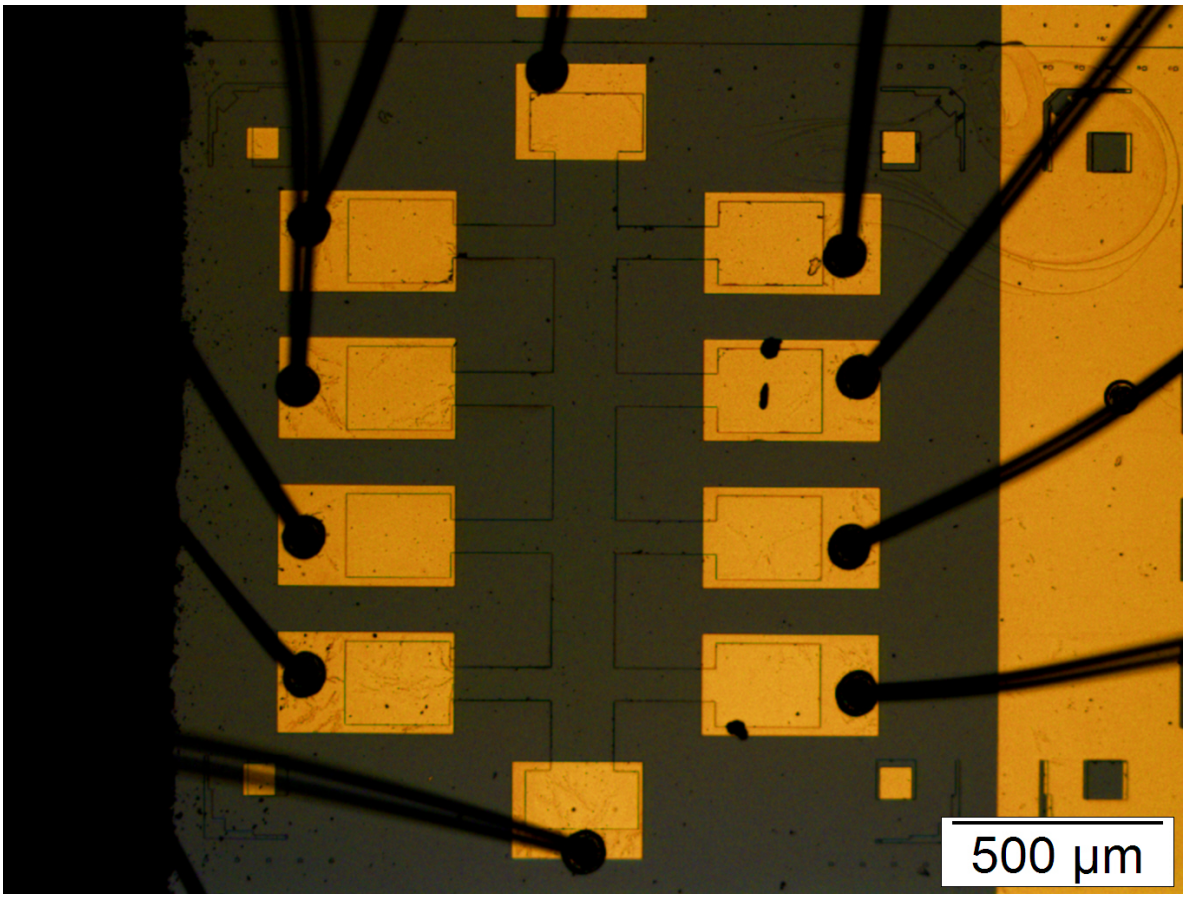

Figure 2.7: Optical micrograph of a (Ga,Mn)(As,P) Hall bar.

The next step was to add ohmic contacts to the pattern. The chip was again spin coated with Shipley 1813 photoresist, baked at 90 °C for 2 minutes, aligned to the contacts pattern and exposed under ultraviolet light. The chip was then immersed in chlorobenzene for 2 minutes and afterwards in MF-319 developer for 2 minutes. The chip was rinsed, blown dry and the pattern was inspected under the optical microscope. Residues were cleaned off from the chip in a RF asher, and afterwards the oxides were removed by dipping into HCl (10%). The contact layer was added to the chip by thermal evaporation. 20-nm-thick Ti were first evaporated onto the chip, followed by 80-nm-thick Au. The chip was then immersed in acetone to lift off the metal layer, while gentle brushing was applied to speed up this process. Finally, individual Hall bars were scribed off from the chip, glued to standard 20-pin leadless chip carriers using Ge varnish, and wire bonded using a ball bonder. A photograph of the packaged (Ga,Mn)(As,P) device is shown in Figure 2.7.

Figure 2.8: Optical microgrpah of the pattern 'CAMBRIDGE'. The stroke width is 5 μm, and the area of this graph is 350 μm × 50 μm.

The fabrication procedure of other micro-structures may vary from the one listed above. For instance, a $[CoFeB/Pt]_n$ micro-pattern on Si(100) was made to verify the two-dimensional magnetic scanning capability of the MOKE probe, which is shown in Figure 2.8. In this case the micro-pattern was a one-off design, so a MicroWriter (Durham Magneto Optics) instead of mask/aligner was used to directly write the pattern onto the film, using a 405-nm continuous-wave laser focused to a spot size of 0.6 μm in diameter. The negative photoresist scheme was used for this process to save the time of laser scanning, that is, the areas unexposed to light are dissolved by the developer. Before exposure, a layer of HMDS primer was first spin-coated onto the film for better adhesion between the film and the photoresist, then Ma-N 1410 negative photoresist was spin coated to the film. Instead of using wet etching, the $[CoFeB/Pt]_n$ multilayer sample was loaded into a sputter chamber and the pattern was etched out by Ar^+ ion milling.

CHAPTER 3

LOW TEMPERATURE FOCUSED SCANNING POLAR MOKE MICROSCOPE

3.1 Theoretical and Experimental Background

In 1877, John Kerr discovered the magneto-optical effect, in which light changes its polarisation due to the presence of magnetisation in a medium [78]. When the light is reflected from a magnetic material it is known as the magneto-optical Kerr effect (MOKE), analogous to the Faraday effect which describes the changes of the transmitted light. On the microscopic scale, MOKE originates from the spin-orbit coupling (SOC) of the electrons in the magnetic medium, contributing to a change of the polarisation angle or ellipticity in the reflected beam, that is proportional to a first order to the magnetisation of the material [18, 19]. Higher order magneto-optic effects, such as the Voigt effect, are beyond the scope of this thesis [79].

A full explanation of MOKE requires quantum mechanical perturbation theory which has been developed by Hulme, Kittel and Argyres [18]. However, a semi-classical picture can be used to understand MOKE following the arguments listed below. An electron with spin $\boldsymbol{s}$ and momentum $\boldsymbol{p}$ moving through potential $\boldsymbol{V}$ in a magnetic material has a Hamiltonian term arising from the SOC:

$$H_{SOC} = \frac{1}{2m_e^2c^2} \cdot (\nabla \boldsymbol{V} \times \boldsymbol{p}) \cdot \boldsymbol{s}$$

This perturbation Hamiltonian which connects the spin and momentum of the electron changes the wavefunction of the system, resulting in the Kerr effect. The incident light

contributes an extra electric field $\boldsymbol{E}$ to the material and induces a current density $\boldsymbol{j}$, part of which, $\boldsymbol{j_{SOC}}$, is perpendicular to both $\boldsymbol{E}$ and $\boldsymbol{s}$ due to its SOC origin. This $\boldsymbol{j_{SOC}}$ has two opposite directions corresponding to two different spin polarisations, so that the Kerr effect is not observed in a non-magnetic medium with zero net spin. Semi-classically, $\boldsymbol{j_{SOC}}$ can be described as an effective displacement field $\boldsymbol{D}$. Since only the first order magneto-optical effects are discussed, $\boldsymbol{D}$ can be written as a 3×3 tensor, given as

$$\boldsymbol{D} = \epsilon(\boldsymbol{E} + i\boldsymbol{Q} \times \boldsymbol{E})$$

where ϵ is the linear permittivity of the material, and $\boldsymbol{Q} = Q \cdot \boldsymbol{M} = (Q_x, Q_y, Q_z)$ is the Voigt vector aligned along the magnetisation through a Voigt constant Q, a material-dependent magneto-optic parameter. In another way, the displacement field can be expressed as $\boldsymbol{D} = \boldsymbol{\epsilon} \cdot \boldsymbol{E}$ using the complex dielectric tensor $\boldsymbol{\epsilon}$, which has the form [19]:

$$\boldsymbol{\epsilon} = \epsilon \begin{pmatrix} 1 & iQ_z & -iQ_y \\ -iQ_z & 1 & iQ_x \\ iQ_y & -iQ_x & 1 \end{pmatrix}$$

For an electromagnetic wave travelling in direction $\hat{\boldsymbol{k}}$, the complex tensor can be diagonalised, which gives two complex eigenvalues:

$$\epsilon_{\pm} = \epsilon(1 \pm \boldsymbol{Q} \cdot \hat{\boldsymbol{k}})$$

The two eigenfunctions correspond to the propagations of left-circular (LC) and right-circular (RC) polarised beams. In principle any electromagnetic wave of a certain polarisation can be decomposed into LC and RC parts, for instance, linearly polarised light contains these two components of equal magnitudes. In a magnetic material LC and RC will experience different permittivities (ϵ_+ and ϵ_-), and therefore have different velocities (imaginary part of the permittivity) and attenuations (real part) in the reflected beam. The difference in velocities gives a phase in the reflected beam which is the Kerr angle, and the difference in attenuations makes the amplitudes of LC and RC different, resulting in the Kerr ellipticity [19]. A similar analysis on the transmitted wave can explain the Faraday effect. In practice, the magnitudes of the Kerr angle and Kerr ellipticity depend on many factors, such as the material being measured, wavelength of the light and the experimental geometry.

Although the main aim of this chapter is to demonstrate the construction of the low temperature Kerr probe, it is still important to discuss on the development of the room

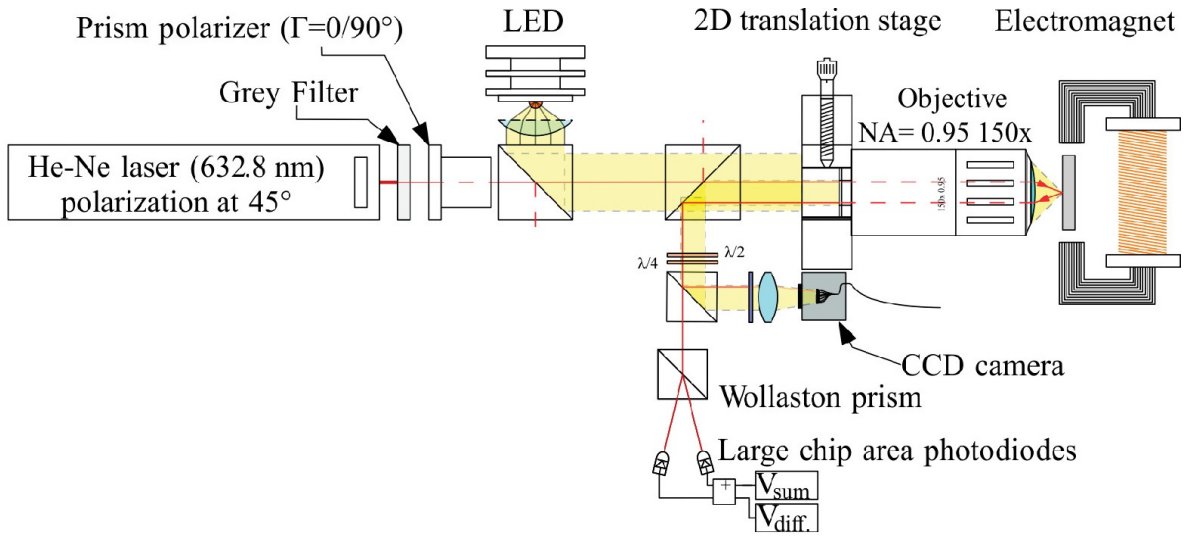

Figure 3.1: Schematic of the room temperature MOKE microscope designed by Flajsman *et al.* Figure adapted from ref.[10].

temperature Kerr instruments, which involves advanced optical designs and measurement schemes that the low temperature research field can learn from.

A state-of-the-art room temperature MOKE magnetometer has been presented by Flajsman *et al* [10]. This Kerr magnetometer has a sensitivity of 5×10^{-7} rad and a spatial resolution of 600 nm. The optical diagram is shown in Figure 3.1. A He-Ne laser is attenuated and polarised by passing through a grey filter and prim polariser. The light is then focused by a high numerical aperture (NA) objective (NA = 0.95, 150 times magnification) onto the sample with a 600 nm spot size. The electromagnet is specially designed to allow the sample to be very close to the objective to accommodate its short working distance. The reflected beam then passes through a rotatable half-wave plate, whose orientation is set to eliminate the unwanted polarisation noise. Afterwards there is a quarter-wave plate used for measuring the Kerr ellipticity. This plate is removed when the Kerr angle is to be measured. Finally the light is split into two cross-polarised parts by a Wollaston prism and collected by a balanced photodetector with two diode sensors. An LED light source and a charge-coupled device (CCD) camera are used to take optical photographs simultaneously with the Kerr measurements.

A unique feature of this Kerr microscope is that both the in-plane and out-of-plane magnetisations can be measured without alternating the optical layout, making this apparatus a vectorial magnetometer. This is because the lateral position of the mi-

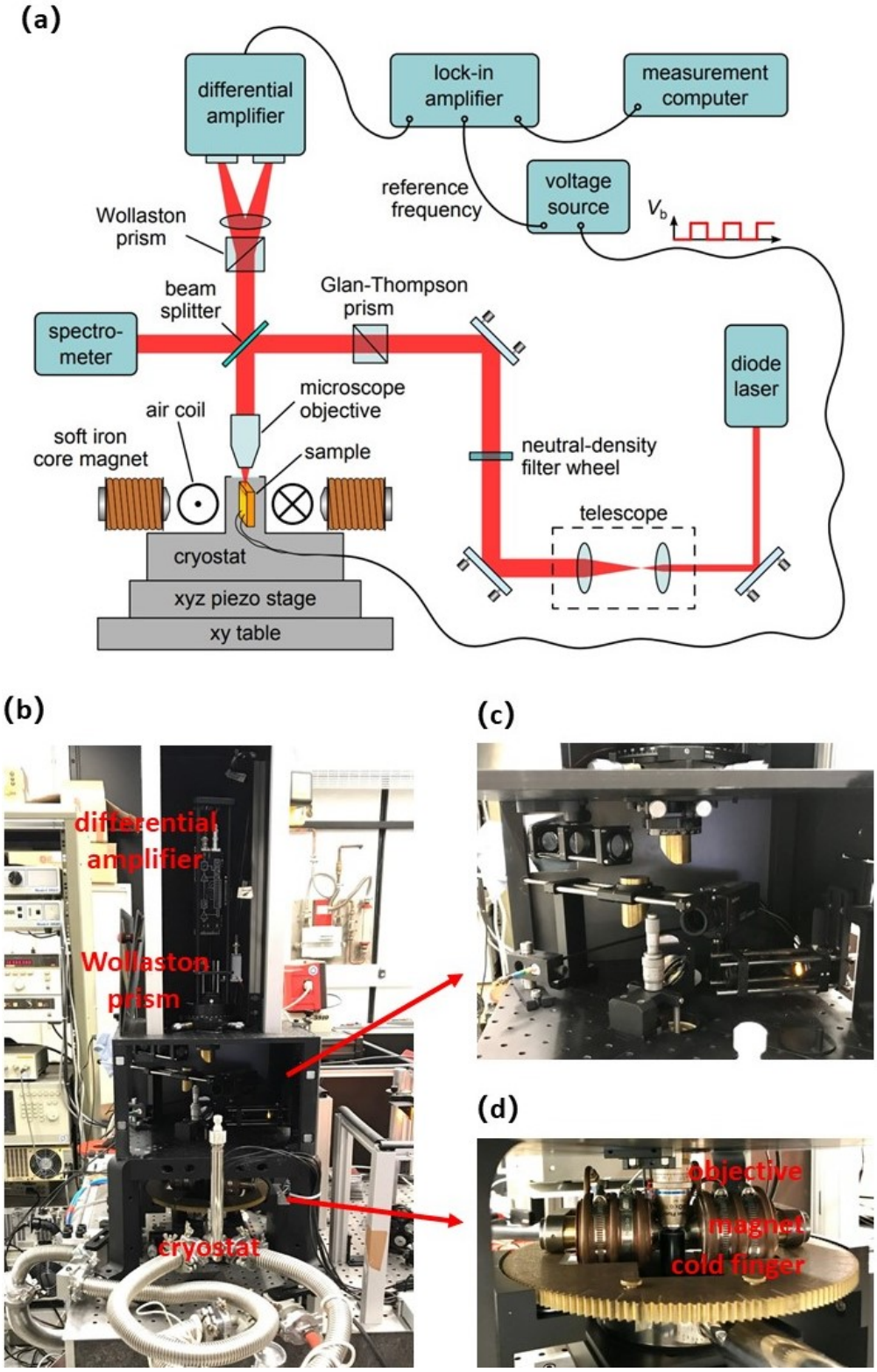

Figure 3.2: (a) Schematic of the Regensburg MOKE microscope. Figure adapted from ref.[11]. (b) Photograph of the MOKE microscope. (c)(d) Close-ups of this instrument.

croscope objective can be precisely controlled on a two-dimensional translation stage, which can deterministically manipulate the direction of the light propagation when it incidents at a certain place of the wide aperture. The user can therefore conduct three measurements in series and obtain the magnetisations of the sample in x, y, and z directions [80].

Regarding the low temperature instruments, the polar MOKE microscope in the research group of Professor Christian H. Back (University of Regensburg, Germany), is known as a high standard He-4 magneto-optic system. The Regensburg microscope has been utilised to image the spin transport at a cross-section of FeCo/GaAs heterostrcutres and other ferromagnet/semiconductor devices [15, 81, 82]. Figure 3.2 shows the schematic diagram and photos of this system, which were taken during a visit to the lab in September 2017. All optical components are fixed in a three-floor aluminium house on a vibration-damped optical table in the ambient environment. The overall optical layout of this system is similar to the one presented by Flajsman [10], both consisting a polariser, a Wollaston prism and a balanced photodetctor. There is a telescope placed in the incoming beam path to expand the beam diameter in order to create a sharp focal spot. The sample is mounted on a He cold finger with optical access through a transparent window. A commercial microscope objective with a working distance of 2.5 mm (NA = 0.7, 60 times magnification) is placed right on top of the cold finger which focuses the laser to 1.6 μm in diameter. Due to the geometrical restriction from the cryostat, the objective cannot have a very large aperture, and therefore the incident beam can only be perpendicular to the cryostat window, i.e. polar MOKE.

3.2 Construction of the Low Temperature MOKE Probe

3.2.1 Cryostat

Figure 3.3 shows a photograph of the cryostat lab at the Bragg Building 162A of the Cavendish Laboratory. In the middle of lab, there is a two-metre-tall Oxford Instruments continuous-flow He-4 cryostat with 1.5 K base temperature, used for low temperature MOKE and transport measurements. It is equipped with a 4.2 K liquid He bath that houses a 9 T perpendicular field superconducting coil. A 77 K liquid N_2 jacket surrounds the He bath, to reduce the He loss due to blackbody radiation between the

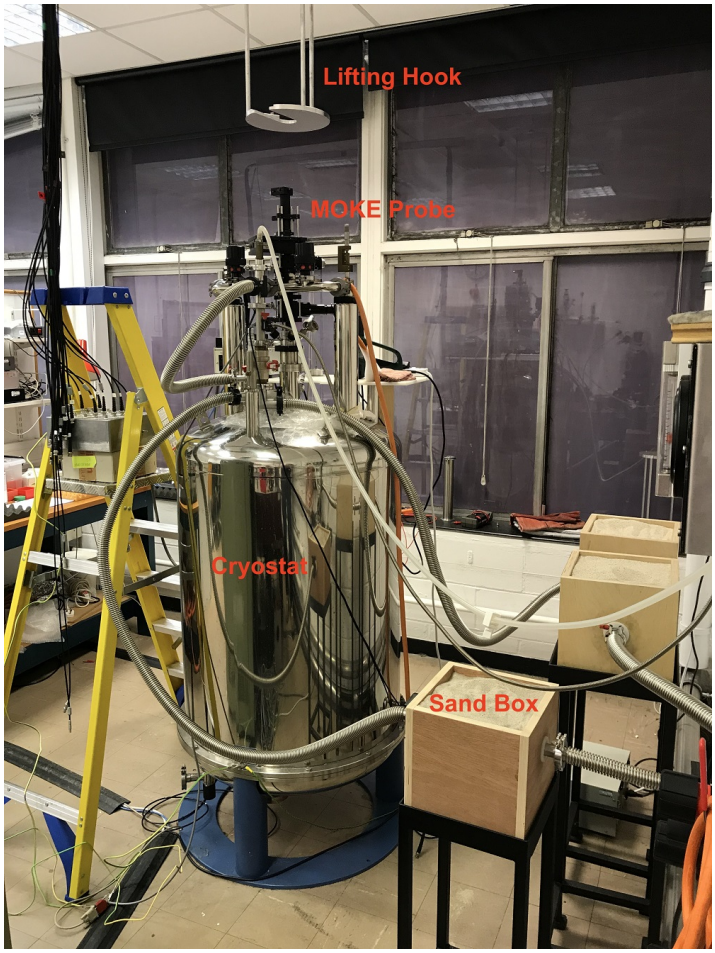

Figure 3.3: Photograph of the cryostat lab at the Bragg Building 162A.

bath and the ambient environment. Both the He bath and the N_2 jacket are further isolated from the cryostat's shell by an outer vacuum chamber with a pressure of less than 1×10^{-6} mbar. The cylindrical sample space is 1.5 m deep and over 2 inch wide, accessible from a top port with a KF-50 vacuum flange. The sample is normally located 1078 mm below the flange, which is the geometrical centre of the superconducting magnet so the field is the strongest and spatially uniform. The is a lifting hook above the cryostat to mechanically lift up (lower down) the MOKE probe from (into) the sample space. The sample temperature in this cryostat can be stabilised anywhere between 1.5 K and 290 K, by carefully tuning both the needle valve that connects the He bath and the sample space, and the power of a heater built in the sample space close to the centre of the magnet. The base temperature can be reached when the pressure of the sample space is kept at about 6 mbar, and the heater is turned off.

The low He pressure (6 - 10 mbar during operation) in the sample space is achieved by

pumping through a rotary vacuum pump connected via a transfer tube system, which is part of the departmental He recycle line. During the initial test of the MOKE system in the cryostat, mechanical vibration from the rotary pump was found to be the major noise source. For this reason an edge-welded bellow was inserted between the rotary pump and the transfer tube, and heavy sandboxes were added between the transfer tube and the helium bath for two-stage vibration isolation. The sandboxes can also be seen in Figure 3.3.

3.2.2 MOKE Probe: Overall Layout

Figure 3.4 shows the schematic diagram (not to scale) of the MOKE probe, an optical system based on standard commercial components. Light from a continuous-wave diode laser operated at 850 nm with stabilised optical output power and temperature is coupled into a polarisation-maintaining (PM) single-mode fibre [labelled as Number 4 in Figure 3.4, abbreviated as N4 in the text]. This cleans the spatial mode from the laser, and the exiting light is collimated at the entry to the MOKE head to produce a free-space beam with a Gaussian transverse profile, which has a beam-waist parameter of about 1 mm. The Rayleigh range of this beam exceeds the path length within the apparatus, so the beam profile is almost constant except where focussed. The collimated laser light then passes through a Glan-Taylor polariser (N5) at 0° to ensure a high degree of controlled linear polarisation. This is deflected by the non-polarising beamsplitter (N6) into the main optical axis of the probe. For the MOKE measurement, the light passes through a fused silica window into the cryostat, and down to the objective (N14). This is a moulded aspherical lens with a numerical aperture of 0.5, optimised to produce a spot of less than 2 μm in diameter. The light reflected from the sample is re-collimated by the objective lens (N14) and exits the cryostat through the same optical path, passing through the cube beamsplitter (N6), a photoelastic modulator (PEM, N3), and another Glan-Taylor polariser (N2) that is aligned at 45° to the initial polarisation. Finally the beam hits a biased Si photodiode, which converts the photocurrent to a usable voltage by a transimpedance amplifier.

Initial alignment is greatly facilitated by the inclusion of two removable elements in the MOKE head: a Köhler illuminator (N10 - N12) and camera system focussed on infinity (N7 - N8) fed by an additional beamsplitter (N9). This provides an image of the sample with 20 μm spatial resolution when these elements are inserted into the main beam path. This function is particularly useful as a pre-positioning before measuring

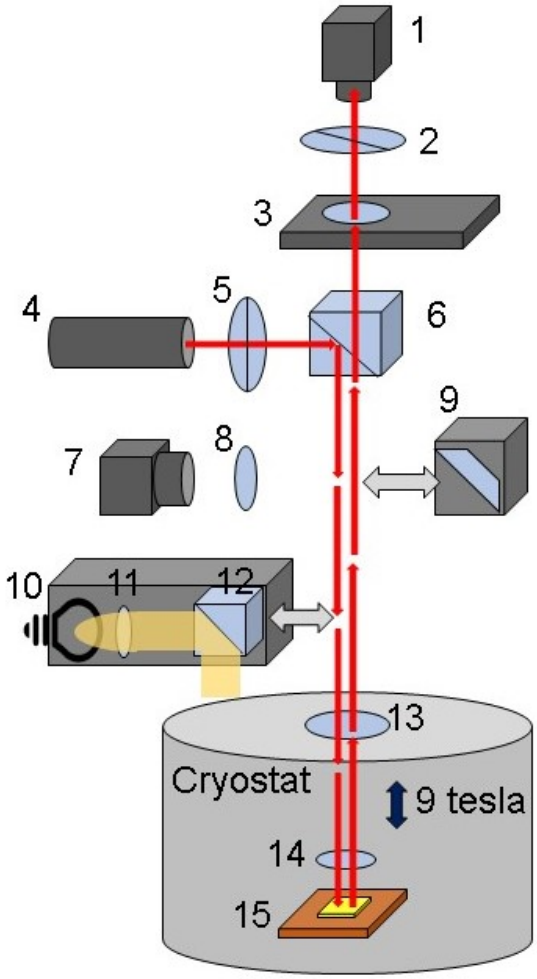

Figure 3.4: Diagram of the MOKE probe (not to scale) with the optical components as follows: (1) photodetector, (2) photoelastic modulator (PEM), (3) polariser at 45°, (4) fibre-coupled 850-nm laser, (5) polariser at 0°, (6) beamsplitter, (7) camera, (8) imaging lens, (9) 45° mirror, (10) LED bulb, (11) collimation lens, (12) beamsplitter, (13) cryostat window, (14) objective lens, and (15) sample on piezoelectric stage.

the Kerr response of a specific area of the material. To control the area of the sample examined by MOKE, there is a stick-slip XYZ stage with resistive position readout at the bottom of the MOKE probe, permitting the sample mounted on the top to be placed with precision of about 50 nm. There are 20 electrical contacts wired on the sample holder to support magneto-transport measurements.

The polarisation of the light is modulated by the PEM utilising the photoelastic effect. In the PEM there is a piezoelectric transducer that compresses and stretches a fused

silica window at its resonant frequency (50 kHz). This induces birefringence in the window that modulates the transmitted light of a certain wavelength between left- and right-circular polarisation at 50 kHz. In our optical geometry, the Kerr rotation angle and ellipticity can be derived using the following equations [83, 84]:

$$\theta_K = \frac{\sqrt{2}}{4J_2(a)}\frac{V_{2f}}{V_{dc}}$$

$$\epsilon_K = \frac{\sqrt{2}}{4J_1(a)}\frac{V_f}{V_{dc}}$$

where J_1 and J_2 are the first and second order Bessel functions of the tunable retardation phase a of the PEM, and V_f, V_{2f} and V_{dc} are the photovoltages at 50 kHz, 100 kHz and DC, respectively. In this way both the Kerr rotation and ellipticity of the reflected beam can be detected simultaneously.

3.2.3 MOKE Probe: Optical Table Part

The 850-nm laser, fibre coupler and their supporting system are mounted on an metric breadboard on top of a vibration-damped optical table, shown in Figure 3.5(a). A 850 nm continous wave TO can laser diode (Thorlabs L850P010, 10 mW, class 3B) is housed in a Thorlabs L850P010 diode mount. The wavelength of the laser diode was chosen to be 850 nm because the Kerr microscope was firstly intended to use for ferromagnet/GaAs spin transport and GaAs spin Hall experiments, and 850 nm is close to the bandgap of GaAs to ensure a substantial Kerr angle to be detected [14, 15, 22]. The diode mount is electrically connected to a diode current controller (Thorlabs LDC205C) and a temperature controller (Thorlabs TED200C), which provide precise regulations on the power and wavelength of the laser diode. These controllers are shown in Figure 3.5(b). The temperature controller employs a thermistor sensor which has a resistance of 10.000 kΩ at the default operation condition of the diode laser. By changing the stabilization temperature, the wavelength of the diode can be tuned by ±20 nm. An aspheric singlet lens (Thorlabs AL108-B, 8.0 mm focal length) with Near-infared antireflection coating is housed at the end of a silvery stick-out tube and positioned in front of the diode to collimate its output light. A selection of neutral density filters can be placed at the exit of this mounting assembly to further reduce the light intensity.

The collimated laser beam passes through a Faraday isolator (Thorlabs IO-850-VLP,

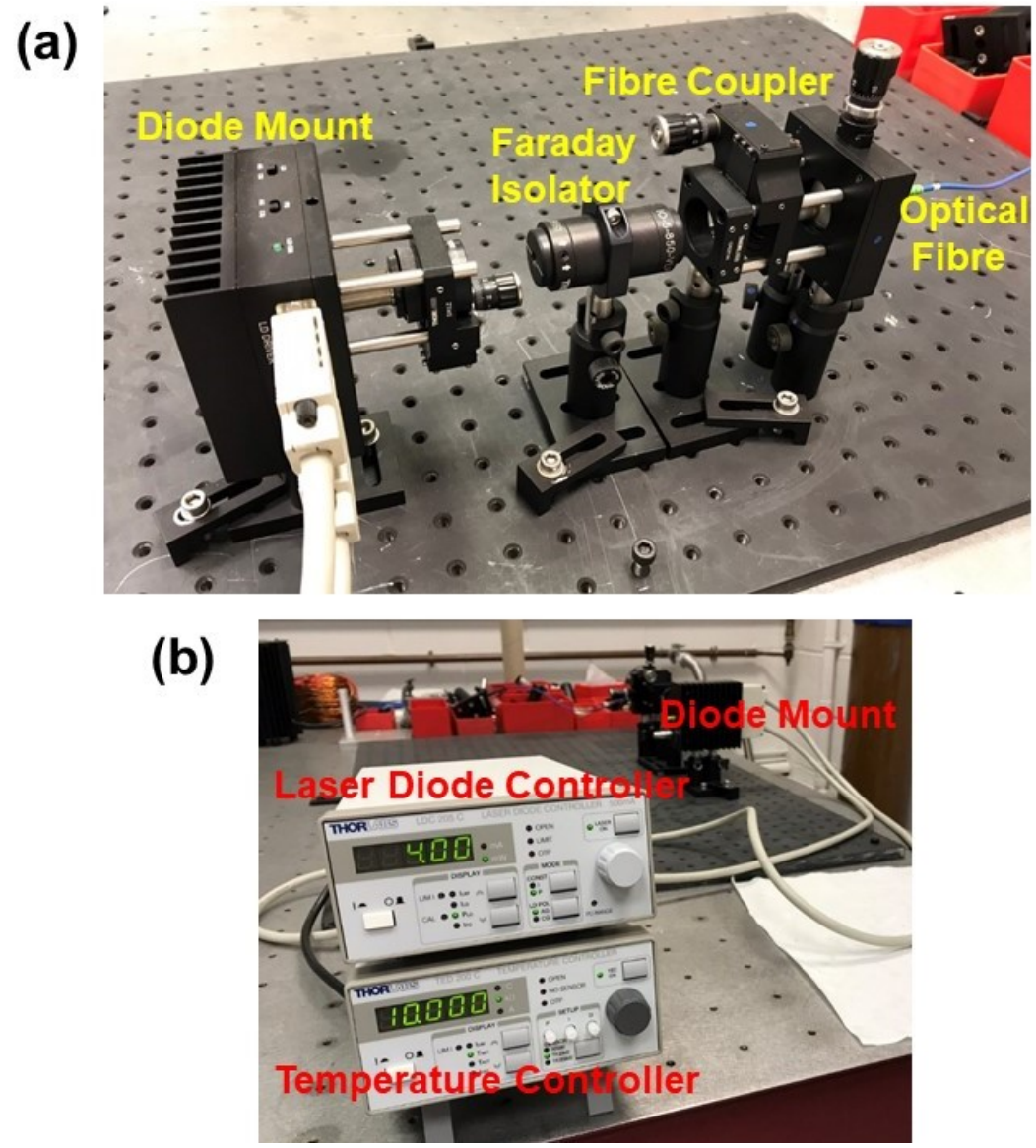

Figure 3.5: (a) Photograph of the laser stabilization and coupling system on the optical table. (b) Photograph of the controllers for the laser diode on the optical table.

830 - 870 nm) and couples into the PM fibre through another identical aspheric lens. The Faraday isolator is made of an three parts: input polariser at a certain polarisation direction, a Faraday rotator surrounded by a built-in permanent ferromagnet, and an output analyser 45° off the input polariser direction. Light of a certain wavelength that enters the input port will convert to linearly polarised light, and then rotated by 45° through the Faraday rotator, which matches the polarisation direction of output polariser. In this way the intensity of the output light will only be slightly less than the input. However, if the light travels back from the output to the input side, then due to

the nature of the Faraday rotation the light polarisation will be rotated by further 45°, resulting in cross-polarisation to the input port. This practically eliminates any back reflection of the laser.

A three-axis mechanical fibre-coupling system (Thorlabs KT310) is used to couple the laser from freespace into the PM fibre, that is, a 5-metre-long FC/APC PM patch cable (Thorlabs P5-780-FC-5). This coupler houses an aspheric coupling lens and precisely tunes the XYZ positions of the lens for optimal coupling efficiency. Regarding the PM patch cable, the APC patch has an 8° angle off the central axis which is designed to reduce back reflection commonly induced at the interface between the freespace and the fibre. This patch design, other with the Faraday isolator, has been proven effective in stabilizing the laser diode and reducing the noise during early-stage tests. It is noted that the majority part of the 5-metre fibre will be hung in mid-air in order to guide the laser wavefront from the coupler to the MOKE probe sitting in the cryostat, and therefore the fibre may be subject to mechanical distortions, such as bending or twisting, or other environmental noises. Apart from a PM fibre, a single mode fibre can also preserve the intensity of the transmitted light when it is subject to mechanical distortions, but the polarisation status will be altered randomly by the time the light reaches the other end of the cable, and as a result the light intensity will fluctuate after passing through the first polariser (N7). Due to the reason listed above, a PM fibre is used to transport the laser light from the optical table to the MOKE probe.

3.2.4 MOKE Probe: Room Temperature Part

The room temperature part of the MOKE probe is shown in Figure 3.6(a), while a full-body photograph of the probe is displayed in Figure 3.6(b). The total height of the probe is 1.7 m, with the room temperature (RT) part taking up 0.5 m and the low temperature (LT) part taking up 1.2 m. The light that exits from the PM cable (N4) enters the MOKE probe through a side-arm and is decoupled into freespace by a compact decoupler (Thorlabs PAFA-X-4-B). This free beam passes through the polariser (N5, Thorlabs GT10-B) to become a linearly polarised light at 0°. The rotation of N5 is mechanically controlled by a cage rotation mount with a micrometre drive (Thorlabs CRM1P/M). The light then goes into a 50:50 cube beamsplitter (N6, Thorlabs CM1-BS014). A home-made silvery hollow cone with black painting inside is placed at the opposite side of the cube beamsplitter, working as a light absorber. As is shown in Figure 3.7(a), light that transmits into this hollow cone will go through multi-

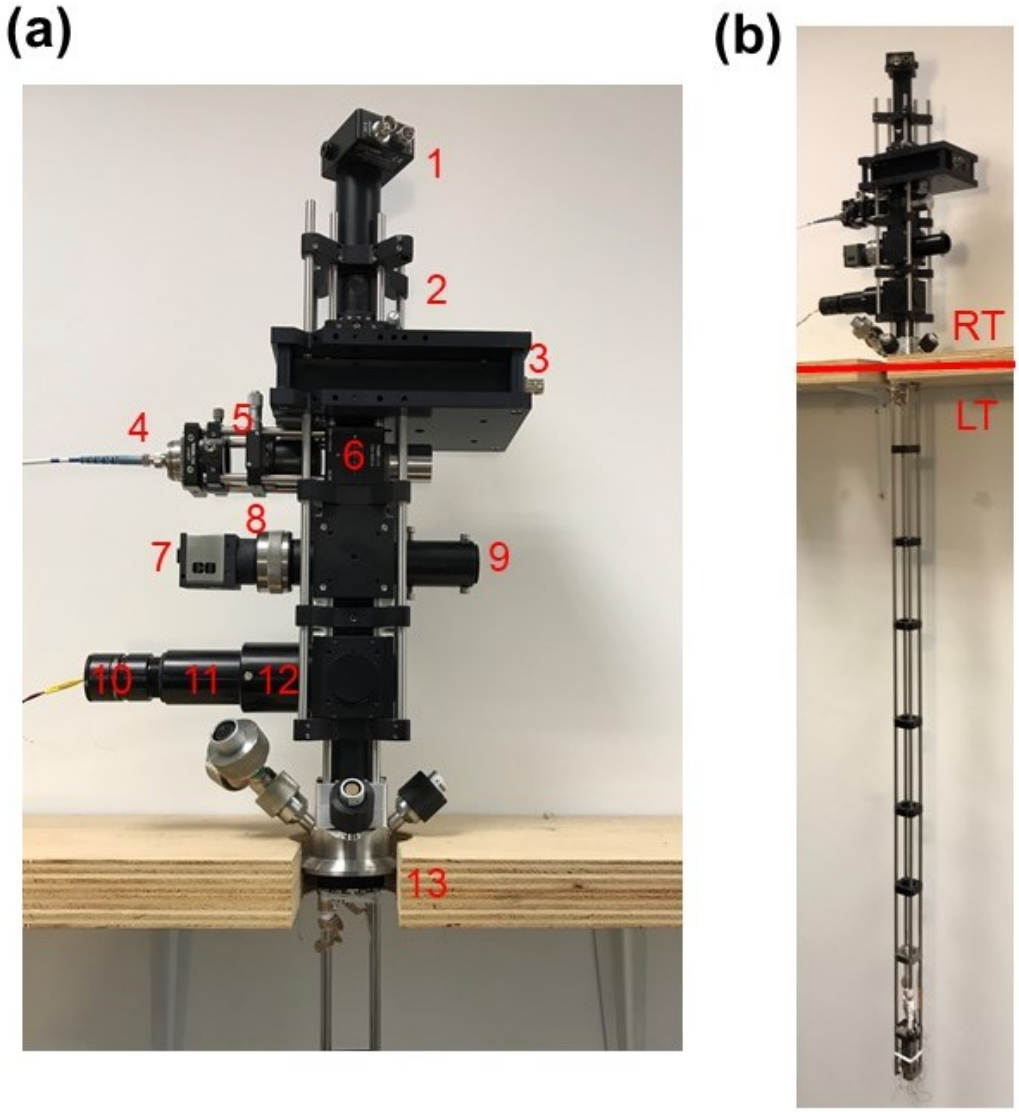

Figure 3.6: (a) Photograph of the room temperature part of the MOKE probe. The numbering of the optical components is identical to Figure 3.4. (c) Photograph of the entire MOKE probe. The height of the room temperature (RT) part is 0.5 m and that of the low temperature (LT) part 1.2 m.

ple reflections on the black-painted surface and therefore most of the back reflection is eliminated. The other half of the laser light is reflected into the vertical main beam path.

After passing through the two optical photography blocks (N7 - N12), the laser beam goes into the cryostat through a fused silica window (N13, UQG Optics FVI-302C) which is 1 inch in diameter. This window is housed in the middle of an aluminium KF-50 flange with 4 electrical connection ports. The upper photography block has two

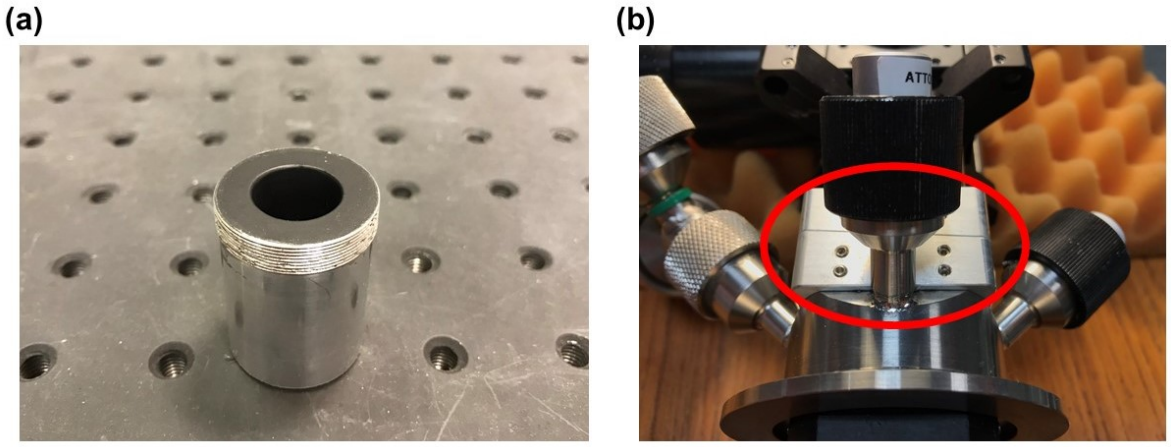

Figure 3.7: (a) Photograph of the hollow cone (the one next to N6 in the MOKE probe) used to eliminate back reflection of the laser. This photo was taken under room light when the cone was placed on a standard black breadboard. Note the black colour inside the cone is significantly darker than the outside due to the multiple light reflections within the inner surface. (b) Photograph of the cryostat window assembly. The tilted window is highlighted in a red circle which prevents back reflection of the illumination light from entering the CCD camera.

side arms. One arm has a slide-in tube with a right-angle prism dielectric mirror (N9, Thorlabs MRA12-E03) at the end. The other arm contains an aspheric focusing lens (N8, Thorlabs ASL10142-B, 79 mm focal length), a ring-shaped silvery high-precision mechanical zoom housing (Thorlabs SM1ZM, 4 mm travel), and a CCD monochrome USB camera (N7, Edmund Optics EO-0813M). When the optical photography is required, the prism mirror will be slid into the vertical optical path to reflect the real time image of the sample into the camera. This image is focused through a plano-convex lens (N11), and the zoom housing is used to position the camera to the focal spot. The lower photography block with another slide-in arm is built for light illumination on the sample. This arm contains a white LED bulb (N10), an iris diaphragm (between N10 and N11), a collimation lens (N11, Thorlabs LA1131-A, 50 mm focal length), and a 50:50 pellicle beamsplitter (N12, Thorlabs BP154B1). When both the N9 arm and the N12 arm are pushed into the vertical beam path, collimated white light will be reflected into the cryostat and illuminate the sample. The returning light will transmit through the pellicle beamsplitter and be reflected by the prism mirror into the CCD camera. The cryostat window is tilted by 3° to prevent the back reflection of the illumination light from entering the CCD camera. The window is inserted between two aluminium plates and vacuum sealed using two o-rings. The pressure from the o-rings should be

light to prevent any stress-induced birefringence (i.e. polarisation-dependent refractive index) in the window. Figure 3.7(b) shows a close-up of the aluminium plates around N13, in which there is clearly a tilt.

A PEM (N3, Hinds Instruments I/FS50, 50 kHz) aligned along 0° is located above the N6 beamsplitter. The working principle of a PEM is the photoelastic effect, in which a mechanical stress or stretch induces birefringence in a material whose magnitude is proportional to the resulting strain. In this PEM a transparent fused silica bar has a natural resonant frequency of about 50 kHz. A quartz piezoelectric transducer is attached to the transparent bar to sustain its vibration at this frequency. At the centre of the transmission window (part of the fused silica bar) the birefringence oscillates at 50 kHz to provide polarisation modulation on the transmitted light. Above this PEM block in the MOKE probe, there is a second polariser (N2) aligned at 45°, equipped with an identical micrometre rotation mechanism as N5. This polariser translates the modulated polarisation into an oscillation in the intensity of the transmitted light. Finally a gain-tunable silicon amplified photodetector (N1, Thorlabs PDA100A-EC) is positioned at the very top end of the MOKE probe, which proportionally converts the laser power to photovoltage. The whole room-temperature part of MOKE probe is based on a Thorlabs 30 mm and 60 mm hybrid cage system, with 4 cage adapter plates (Thorlabs LCP02/M) and 27 aluminium tubes providing extra mechanical assurance.

3.2.5 MOKE Probe: Low Temperature Part

The main material used to construct the low temperature part of the MOKE probe is grade 2 titanium. Compared to other materials such as aluminium and stainless steel, titanium combines the virtues of the low thermal expansion coefficient, low magnetic susceptibility, lightness and strength, making it a popular material in cryogenic magnetic applications. The design of the low temperature part of the MOKE probe resembles a Thorlabs 30 mm cage system. By referring back to Figure 3.6(b), it can be seen that there are four titanium tubes (Ti-shop, 1.2 m long, 6.1 mm in diameter) making up a square-shaped main frame. The separations between the nearest tubes are 30 mm. Eight SM-1 threaded 30 mm black cage plates are placed evenly along the tubes for mechanical support. Figure 3.8 shows a close-up of the sample holder. An aspheric singlet lens (N14, Thorlabs AL108-B, 10.0 mm in outer diameter, 8.0 mm focal length) working as the objective lens is housed in the middle of a cage plate right above the sample holder, which focuses the laser to a spot of less than 3 μm in diameter. The reason to use an aspheric lens instead of a spheric lens as the objective is to reduce the

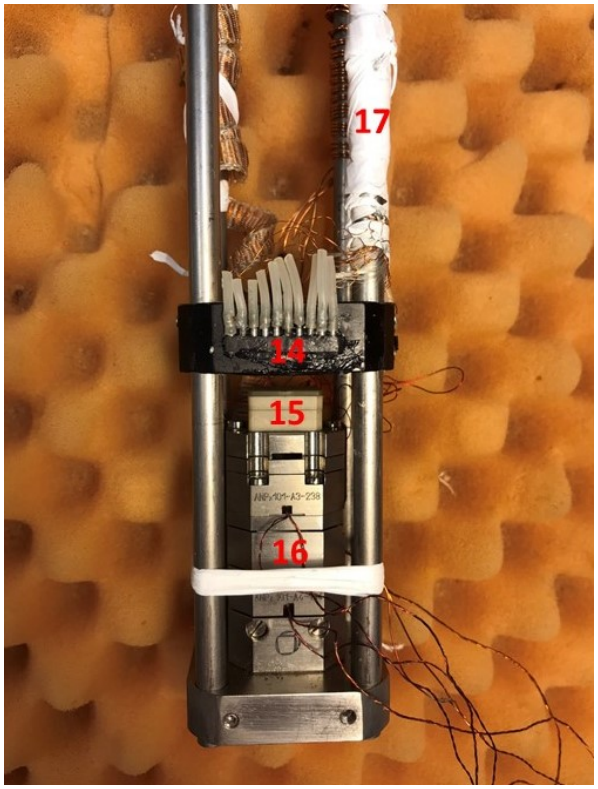

Figure 3.8: Photograph of the bottom end of the MOKE probe, with numbered components listed as follow: (14) objective lens in a cage plate, (15) cryogenic sample holder, (16) Attocube piezoelectric steppers, (17) titanium tubes winded by cooper wires.

spherical aberration [85]. Most simple spheric lenses use part of a sphere as its surface profile, and the light rays that strike near the centre and near the edge of the lens will go through different magnitudes of refraction, resulting in the spherical aberration. On the contrary, an aspheric lens has a more complex surface profile, which significantly reduces the spherical aberration and other optical aberrations (e.g. astigmatism), and therefore can generate a sharper focal spot.

There is a home-made titanium base at the very bottom end of the MOKE probe. Three attocube piezoelectric steppers (N16), responsible for Z, Y, and X movements respectively, are bottom-to-top stacked on this base, controlling the sample position using closed-loop with a resistive encoder. Each of these steppers (ANPz101, ANPx101 and ANPx101) has 4 mm travel and 100 nm resolution. A custom-designed cryogenic sample holder (N15) compatible with a 20-pin leadless chip carrier (LCC) is attached to the top of the X stepper with the help of a titanium adapter plate (between N15 and N16). The engineering drawing of this sample holder is shown in Figure 3.9. The main

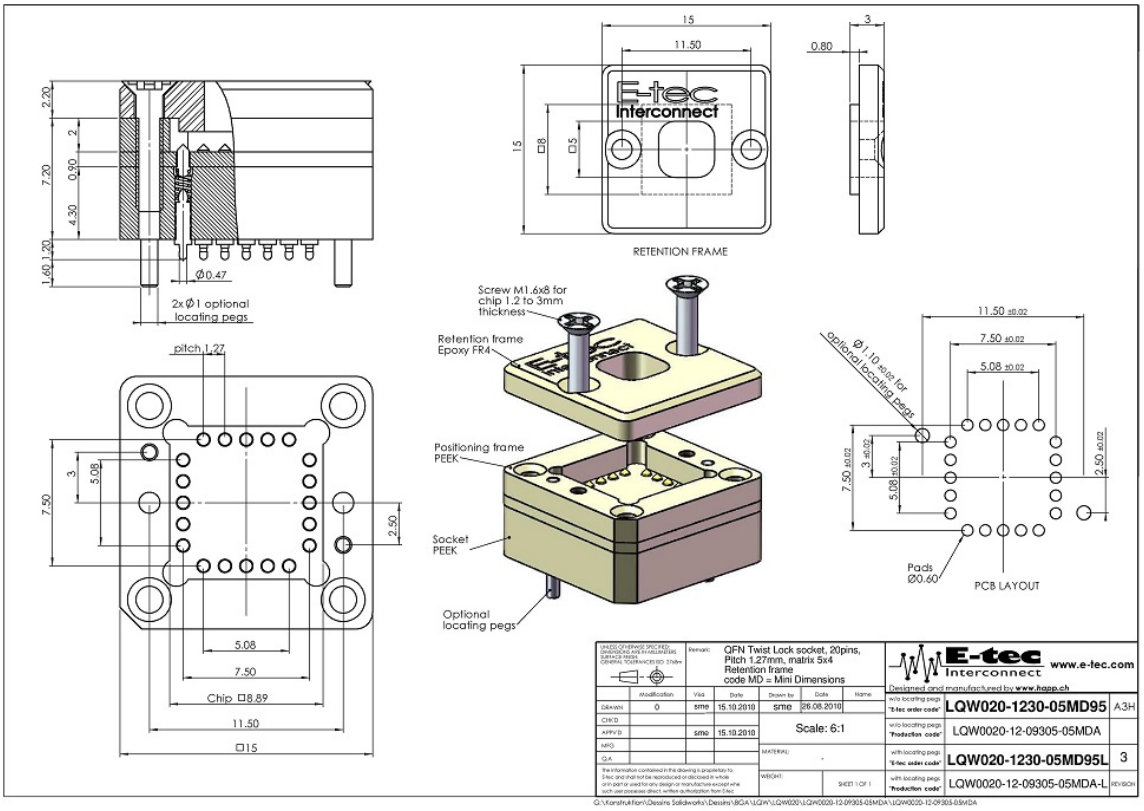

Figure 3.9: The cryogenic sample holder designed by E-tec.

body of this sample holder is a polyether ether ketone (PEEK) sink with 20 copper pins at the bottom. A hollow fibreglass cap with two titanium countersink screws are used to press down a 20-pin LCC into the PEEK sink. The zero-insertion-force design of this sample holder provides a low profile socket that could survive multiple thermal cycles without the pins breaking. This design helps avoid the problems happening to the normal chip carrier sockets, which need quite a bit of force to load the sample and especially to remove it, and the added fatigue from the thermal cycling tends to make the pins fail quite quickly. 12-pair copper woven looms are soldered to the back of the PEEK holder and inserted into one of the titanium tubes through a opening close to the lowest cage plate. These wires come out at the cryostat flange, enter one of the electric connection ports, and connect to a circular Fischer connector sealed by an o-ring. Back to the bottom end, there are 15 connection pins glued by silicone rubber compound to the sides of the lowest cage plate (N14). Attocube steppers (5 wires each) are first electrically connected to these pins, and then connected to another port next to the flange through the second titanium tube, in the same manner as the connections for the sample holder. Finally, a calibrated 4-lead resistance temperature sensor (Lakeshore

Cernox, AA package) is glued to the sample adapter plate (between N15 and N16) using the Araldite rapid adhesive, and further connected to another port next to the flange using four thin copper wires buried in the third titanium tube. All wires are wound around the tubes next to the lowest cage plate (N14) to dissipate heat transferred from the room temperature environment.

3.3 Experiment: 2D Scan of Magnetic Micro-patterns

A perpendicularly magnetised micro-pattern was used to verify the two-dimensional scanning capability of the MOKE probe at low temperatures. The $[CoFeB/Pt]_n$ multilayers have out-of-plane anisotropy originating from interface exchange coupling [86, 87]. The $Pt(2)/[CoFeB(0.55)/Pt(0.7)]_4/CoFeB(0.55)/Pt(2)/Ta(2)$ (thicknesses in nm) multilayer structure was grown on a Si substrate using magnetron sputtering. After the

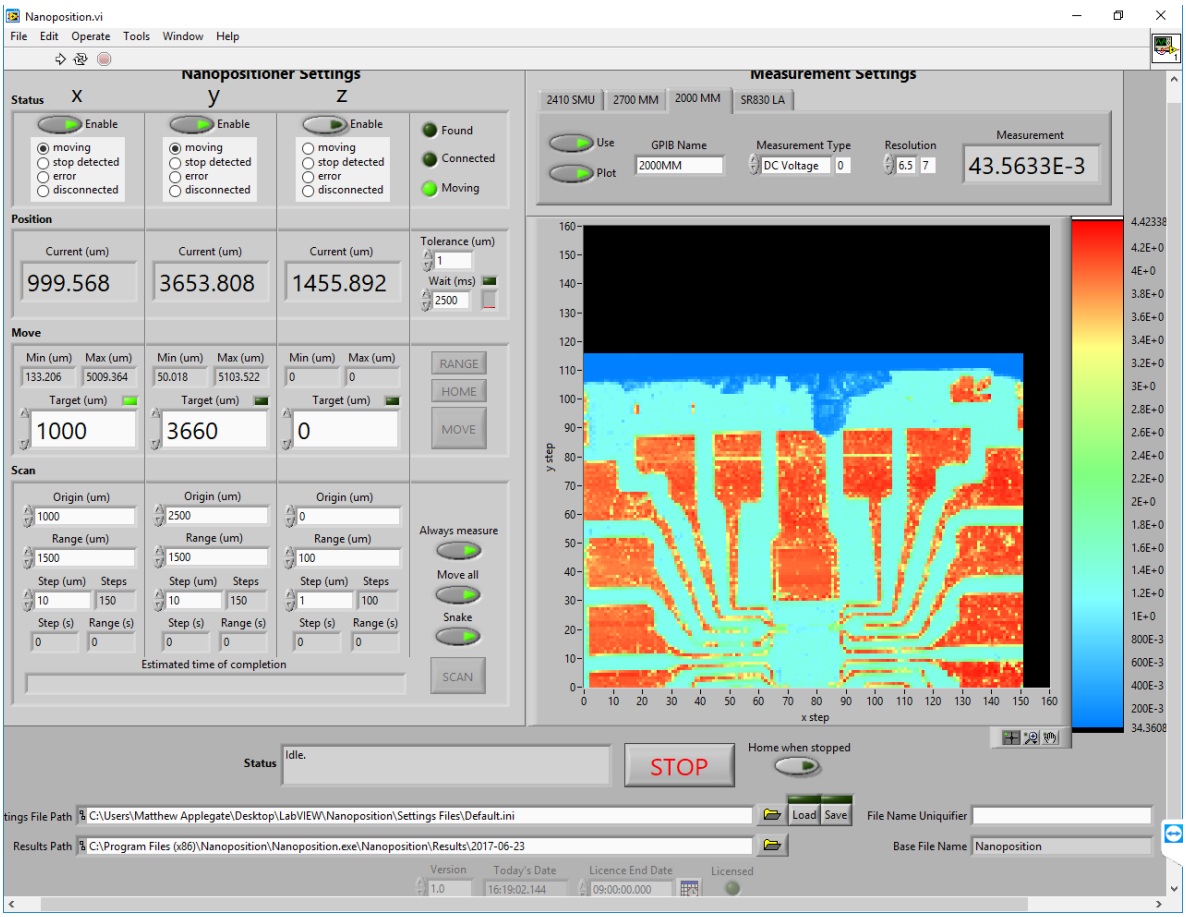

Figure 3.10: Screenshot of the Nanoposition program for automatic control of two-dimensional MOKE scanning.

initial deposition of the Ta buffer layer on the Si(100) substrate, Pt and CoFeB were alternately sputtered from individual targets onto the film. The substrate was kept at room temperature and the chamber pressure was at 7.1×10^{-3} mbar throughout the deposition. After growth the sample was taken out and its perpendicular magnetic anisotropy at the ambient conditions was confirmed using NanoMOKE 3 (Durham Magneto Optics). This multilayer sample was then fabricated into pre-designed structures by standard optical lithography and Ar^+ dry etching techniques. First, negative photoresist was spin-coated onto the film, followed by patterning and exposure using a MicroWriter (Durham Magneto Optics). Afterwards, the pattern was etched using Ar^+ milling and a standard lift-off process. Finally the wafer was loaded into the low temperature MOKE probe and cooled to 6 K. A two-dimensional magnetisation scan was recorded using a LabView program developed by Dr. Matthew J. Applegate. A screenshot of the program is shown in Figure 3.10.

Figure 3.11(a) shows a two-dimensional MOKE scan at 6 K of the micro-pattern, comprising the word 'CAMBRIDGE' formed in capitals with 5 μm-wide strokes of a magnetic $[CoFeB/Pt]_n$ multilayer structure, on a bare Si(100) substrate. An out-of-plane magnetic field of +0.5 T was first applied and then removed so that the magnetisation of the multilayer stays at the positive remanence. The laser was scanned across an area of 350 μm × 50 μm with 1 μm step size, and both the AC Kerr angle and DC reflectance were recorded. On this map every character can be clearly recognised with moderately sharp edges. The gradual magnetisation change at the edges of those letters is perhaps due to the resolution limit of the focused laser spot. The small horizontal lines in the map arise from position readout errors. Another Kerr scan at remanence, but after applying a -0.5 T preset field, revealed an identical magnetisation distribution with opposite rotation angles (not shown here), proving that the Kerr signal does originate from the $[CoFeB/Pt]_n$ structure. As a reference, an image of the text taken from an optical microscope is displayed at the top left corner of the Kerr map.

To examine further the magnetisation at individual x-y coordinates, the hysteresis loops were measured when focusing the laser at Spot S1 on letter D, S2 in the hollow part of letter D, and S3 off the letter. The results are shown in Figure 3.11(b) after subtracting a linear background arising from Faraday rotation in the objective lens. Spot S1 has a square-shaped loop indicating the magnetic easy axis is perpendicular to the film. The hysteresis loop at Spot S2 shows the same coercivity as S1 but the magnetisation is smaller. This small but existing magnetic response is perhaps due to a fraction of the

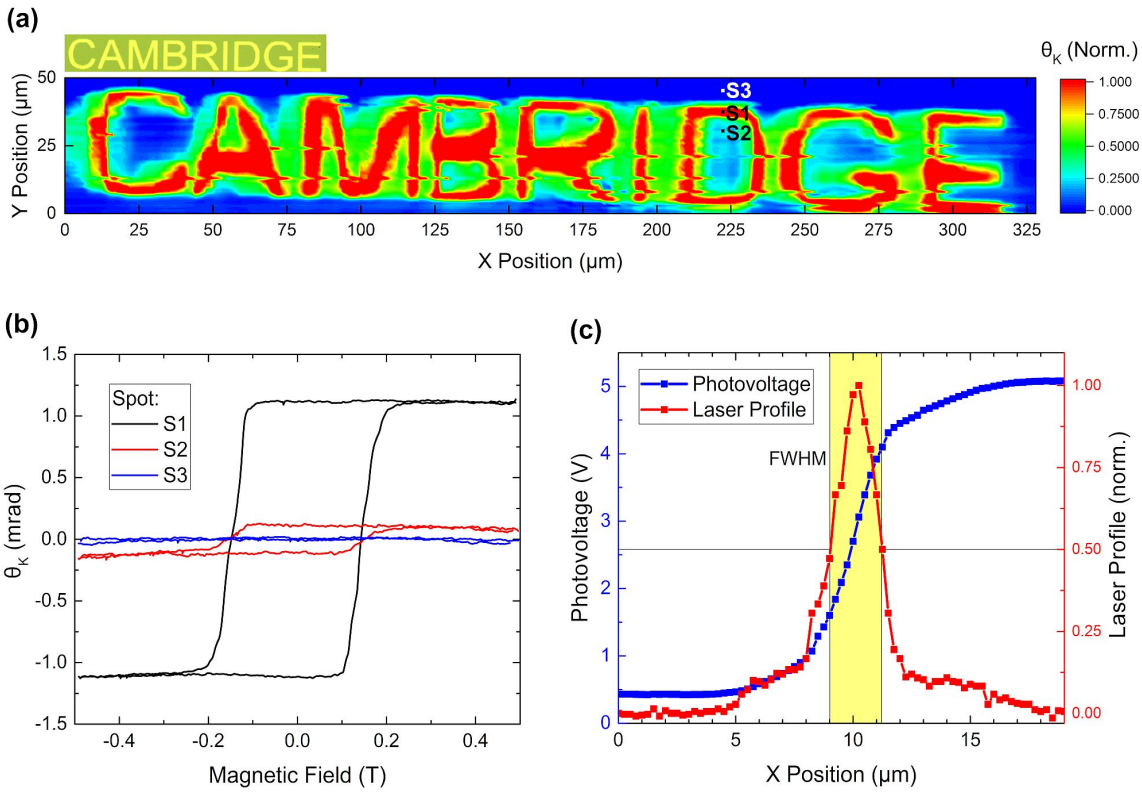

Figure 3.11: (a) Two-dimensional MOKE scan of the ferromagnetic pattern 'CAMBRIDGE' at 6 K, fabricated from a $[CoFeB/Pt]_n$ multilayer film with out-of-plane anisotropy. The letter stroke width is 5 μm and the scanning step size is 1 μm. An optical micrograph of the same area is shown at the top left corner. (b) Magnetic hysteresis loops of three different spots on or next to the 'CAMBRIDGE' pattern. (c) The photovoltage recorded (in blue) and its derivative, i.e., the laser profile (in red), when the laser scans across a knife edge. The yellow shaded area represents full width at half maximum (FWHM) of the laser spot.

light reflected from the magnetic letters nearby. In comparison, no magnetic response was found on Spot S3 which is away from the letters. Close examination of the hysteresis loops shows the noise level is less than 10 μrad at 6 K.

Finally, the focused laser was scanned across a knife edge with a step size of 0.25 μm. The intensity of the reflected light and its differentiation at each step are illustrated in Figure 3.11(c). The laser profile is close to a Gaussian with 2.2 μm full width at half maximum (FWHM, shaded in yellow in the figure). The minimum spot size of a laser is given approximately by the beam waist $w_0 = \frac{\lambda}{\pi \mathrm{NA}}$, where w_0 is the radius at the point

where intensity falls to $\frac{1}{e^2}$ of the maximum value, and NA is the numerical aperture. This gives a value slightly smaller than that determined experimentally.

3.4 Experiment: Temperature dependent magnetisation in (Ga,Mn)(As,P)

This experiment on (Ga,Mn)(As,P) is used to verify the temperature-dependent optical and electrical measurement capability of the MOKE probe. (Ga,Mn)As as a III-V dilute-magnetic semiconductor (DMS) has been a material of scientific interest, due to its tunable magnetic properties under changes of epitaxial strain and Mn doping concentration [88, 89, 90]. When a (Ga,Mn)As thin film is grown directly on a GaAs substrate with a Mn concentration higher than 2%, the film experiences compressive strain, resulting a magnetic easy axis lying in-plane [89, 90]. In 2008, Rushforth *et al* at the University of Nottingham experimentally demonstrated the out-of-plane magnetic anisotropy in MBE grown (Ga,Mn)(As,P) [91]. They found annealed $Ga_{0.94}Mn_{0.06}As_{1-y}P_y$ ($y \leqslant 0.3$) thin films on GaAs substrates are metallic and perpendicularly magnetised due to tensile strain, and the magnetisation increases as P concentration increases [92]. They found the magnetic easy axis of the $Ga_{0.94}Mn_{0.06}As_{0.9}P_{0.1}$ goes from in-plane to out-of-plane by post-growth annealing at 180 °C for 48 hours, due to out-diffusion of interstitial Mn and therefore increased tensile strain. Several research projects have been developed based on this out-of-plane DMS structure, including spin-orbit-driven ferromagnetic resonance [93], and controlling the mobility of domain walls with piezoelectricity [94].

A 25-nm-thick $Ga_{0.94}Mn_{0.06}As_{0.94}P_{0.06}$ film grown by Dr. Richard Campion at Nottingham was used in Cambridge to test the MOKE probe. The sample was grown using MBE co-evaporation on a semi-insulating GaAs (100) substrate. The detailed growth and calibration procedure has been described in previous publications [91, 95]. A 50-nm-thick $GaAs_{0.94}P_{0.06}$ buffer layer was grown at 580 °C, before the deposition of the ferromagnetic layer. Finally the sample was annealed in an oven at 180 °C for 48 hours immediately before the MOKE measurements to diffuse out interstitial Mn.

Figure 3.12 shows the magnetic hysteresis loops of the (Ga,Mn)(As,P) film at different temperatures. All results are obtained after averaging over three repeats. The signal is very clean, and the noise level is less than 10 μrad. The square-shaped loops

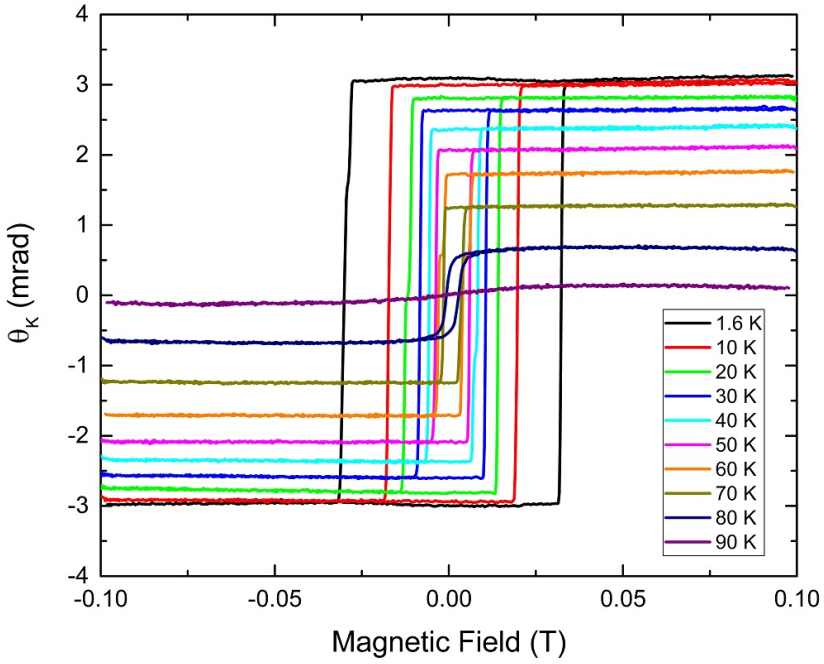

Figure 3.12: Out-of-plane magnetic hysteresis loops of the (Ga,Mn)(As,P) film at different temperatures

indicate strong out-of-plane anisotropy. The relationship between spontaneous magnetisation and temperature is shown in Figure 3.13. The convex curvature is common in ferromagnetic materials, which can be explained by the mean field theory, i.e. in a many-body system all interactions on one body are approximated by an effective field (molecular field) [96]. From both graphs the Curie temperature of this film is estimated to be 85 - 90 K.

To verify the electrical transport capability of the MOKE probe, the (Ga,Mn)(As,P) film was fabricated into Hall bar devices of dimensions 1400 μm × 150 μm. A detailed description of the fabrication process can be found in Chapter 2. The measurement was completed using a standard four-terminal AC lock-in scheme with an input current of 1 μA at 77 Hz. The change of the longitudinal resistance (R_{xx}) during cooling is illustrated in Figure 3.14(a). The resistance first increases following the temperature decrement, reaching maximum at 90 K. Afterwards the resistance starts decreasing, with a small tail below 15 K. The insulating-to-metallic transition at 90 K matches the Curie temperature of the material, when long-range ferromagnetic ordering is established. This indicates a good consistency between the magneto-optic and magneto-transport results. Figure 3.14(b) shows the Hall resistance of the device at 6 K. The presence of the anomalous Hall effect (AHE) with square-shaped hysteresis loop confirms the

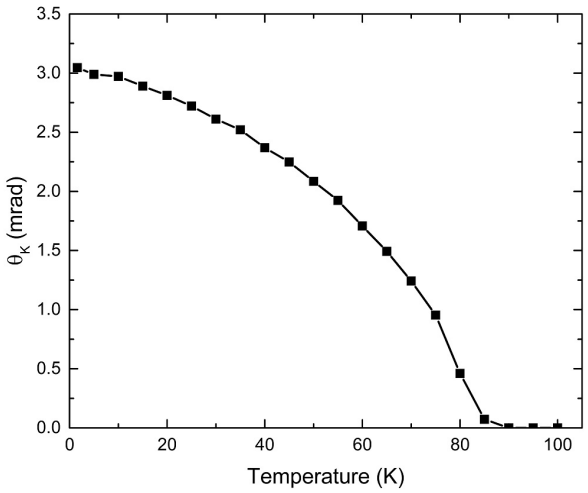

Figure 3.13: Temperature-dependent spontaneous magnetisation of the (Ga,Mn)(Ga,P) film

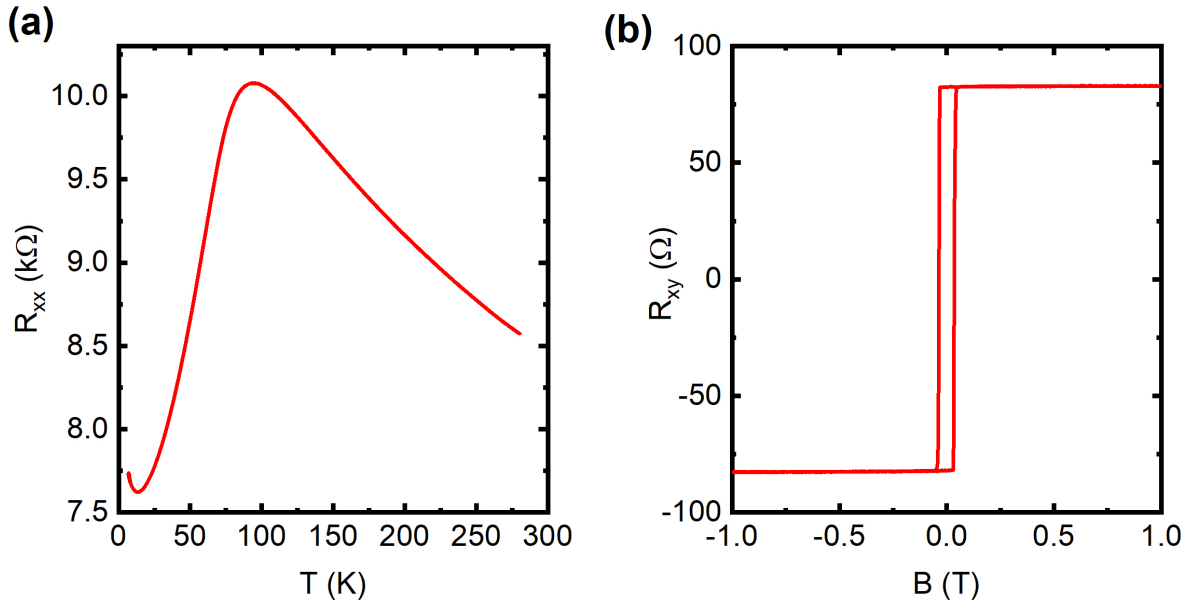

Figure 3.14: Electrical transport results of the (Ga,Mn)(As,P) film. (a) Temperature-dependent longitudinal resistance. (b) Hall resistance at 6 K.

out-of-plane ferromagnetism.

In summary, this experiment demonstrates the capability of the MOKE probe on temperature-dependent magneto-optical and magneto-electrical measurements.

3.5 Summary and Discussion

This chapter presented the design and demonstrated the performance of a low temperature focused polar MOKE microscope for use under applied magnetic fields of up to 9 T and with a base temperature of 1.5 K. Instead of using a cold-finger with a transparent window, the Kerr magnetometer is integrated into a conventional cryostat, demonstrating a practical approach to set up low-temperature microscopy instrumentation for non-optical cryostat users. The laser travels as a free-space beam in the cryostat, and the polarisation modulation at 100 kHz is achieved by employing a PEM. A two-dimensional Kerr scan at 6 K was performed on ferromagnetic $[CoFeB/Pt]_n$ multilayer microstructures with perpendicular interfacial anisotropy. A clearly resolved word pattern with 5 μm stroke width confirms the capability of micro-scale magnetisation mapping. Another scan across a knife edge reveals a focal spot size of 2.2 μm FWHM, close to the predicted diffraction limit. In addition, measurements on the (Ga,Mn)(As,P) films and micro-devices prove the electrical transport capability of the MOKE probe. Since the optical design must comprise the geometry of the large non-optical cryostat, this MOKE probe is outperformed by other world-class MOKE systems, such as the Regensburg MOKE, in both the sensitivity and spatial resolution.

A few alternative design options have been considered during constructing the MOKE probe. For example, light transmission could be in an optical fibre instead of freespace, which provides more geometrical flexibility in the limited cryostat space. However, the extinction ratio (light intensity difference between the wanted polarisation and its orthogonal polarisation) of a Glan-Taylor polariser is 10^5, but for a PM fibre it is only 10^3.

To obtain better laser focusing and optical photography capabilities, a compact mutlilens objective has been considered to replace the aspheric singlet as the objective lens. However, a common refractive objective has multiple lens cemented to a metal housing which seals air in the middle. Under the condition of low temperature vacuum, the objective components are very fragile and holes must be drilled on the objective housing to balance the air pressure. Besides, lenses and metal housing have different thermal expansion coefficients and the cement may not adhere them at low temperature. In this way the housing will shrink more than the lenses inside, resulting in mechanical failure. Attocube can offer expensive cryogenic refractive objectives with titanium housing and cryo-epoxy glue, which can be considered as an upgrade option to current MOKE probe in the future. Another option that has been considered is the reflective objective, made

up of two metal mirrors and a metal housing. Both components have similar thermal expansion ratios. Thorlabs can provide a cryogenic version of this objective by using cryo-epoxy to glue the conponents, which is another expensive alternative to the current singlet lens.

Apart from using the photoelastic effect of a PEM, another common modulation scheme in a MOKE microscope is the differential detection. In this scheme the reflected beam is split into two cross-polarised beams and collected by a differential photodetector with two balanced photodiodes [10, 28, 97], as is shown in previous sections. Here the PEM modulation scheme is employed because it has a better tolerance to misalignment, as the reflected light always stays in the central optical path without splitting.

CHAPTER 4

EXCHANGE BIAS IN TOPOLOGICAL INSULATOR SUPERLATTICES

4.1 Rare-earth Doping of Topological Insulators

Since the discovery of QAHE in Cr-doped $(Bi,Sb)_2Te_3$ and afterwards in V-doped $(Bi,Sb)_2Te_3$ TI thin films below 100 mK [6, 62], many attempts have been made to increase the realisation temperature of QAHE [66, 67]. Due to the direct dependence of the band gap to the magnetic moment in the TRS-broken TI materials, doping with rare-earth (RE) elements which have large atomic moments can be an alternative approach to raise the QAHE temperature. For instance, Dy and Ho in the lanthanide series have an effective magnetic moment of up to 10.5 μ_B. Although up to now there is still no evidence of QAHE in RE-doped TIs, novel electronic and magnetic properties have been demonstrated in these materials. Gd-doped $(Bi,Sb)_2(Te,Se)_3$ was found to transform from a paramagnetic to antiferromagnetic phase upon cooling, a phenomenon explained by Gd-Gd exchange coupling through Te ions [98, 99, 100]. In the meanwhile, Sm-doped Bi_2Se_3 can exhibit ferromagnetism up to 52 K [101]. Recently, Sm-doped Bi_2Se_3 has also been proposed as a possible magnetic axion insulator to realise chiral hinge states and surface QAHE [102].

In order to raise the QAHE temperature in TI materials, Professor Thorsten Hesjedal and his colleagues at the University of Oxford have been investigating RE doping in $(Bi,Sb)_2(Se,Te)_3$ thin films in the past few years [13, 103, 104, 105]. Figure 4.1 shows the unit cell of RE-doped Bi_2Se_3. The material forms a tetradymite structure consisting of quintuple layers (QLs), with RE atoms expected to replace Bi through substitutional doping. A QL is made up of five atomic layers: Te-Bi-Te-Bi-Te, while adjacent QLs are weakly bounded by van der Waals (vdW) force between Te atoms.

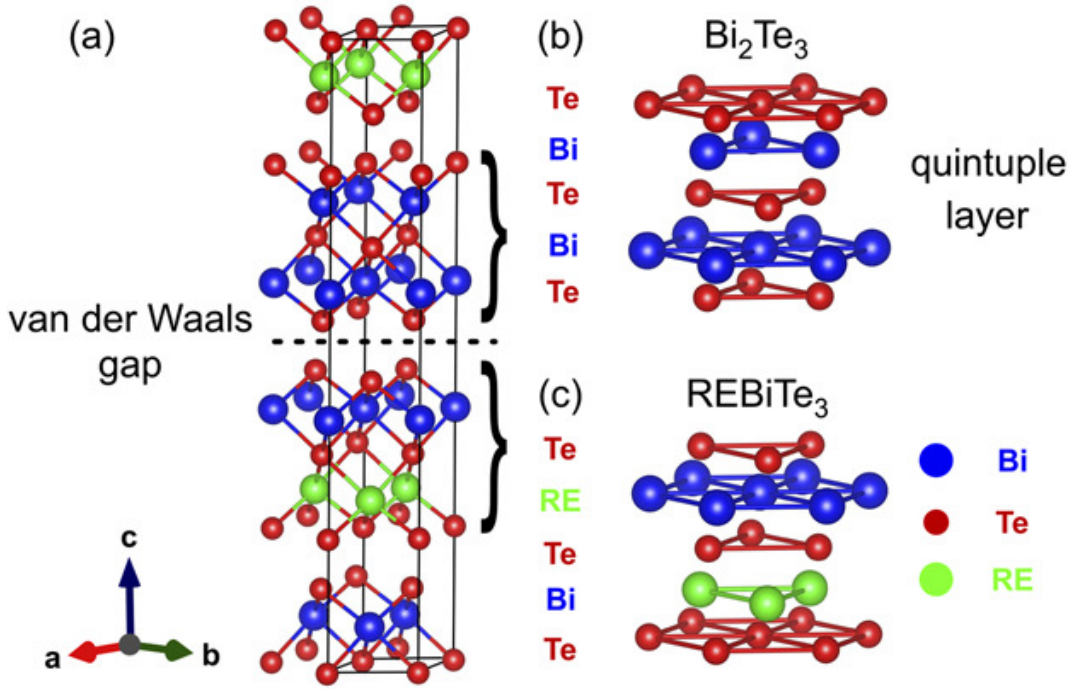

Figure 4.1: Lattice structure of RE:Bi_2Te_3. (a) Unit cell consisting of 3 QLs, separated by van der Waals gaps. (b) A QL without doping, showing the Te-Bi-Te-Bi-Te layered structure. (c) A QL with RE doping, showing the Te-Bi-Te-Re-Te layered structure. Figure adapted from ref.[12].

Gd-, Ho- and Dy-doped Bi_2Te_3 films of 50 - 120 nm thick were grown in Professor Hesjedal's group using MBE co-deposition on $c-$plane sapphire substrates, and analysed via various structural, electronic and magnetic characterisation techniques. The presence of single crystalline, rhomebohedral thin films with substitutional doping was confirmed for $(RE_xBi_{1-x})_2Te_3$ with doping concentration was up to $x = 0.355$, using XRD and Rutherford backscattering spectrometry (RBS). Their magentisations were measured using a SQUID magnetometer. Figure 4.2 shows the low temperature in-plane hysteresis of various $(RE_xBi_{1-x})_2Te_3$ films [12]. All the films show a similar paramagnetic response. The magnetic moments are saturated to above 4 μ_B at a high field, proving the high magnetic moment of the RE elements. Neither a hysteresis loop nor remanence was observed in these samples, indicating the absence of long-range ferromagnetic order. A very similar paramagnetic response was also observed in all samples when the field was applied perpendicular to the film plane (not shown here). It is generally understood that $4f$ electrons in the RE series are well shielded by the outer orbitals. Individual RE ions in a host material may behave like isolated magnetic

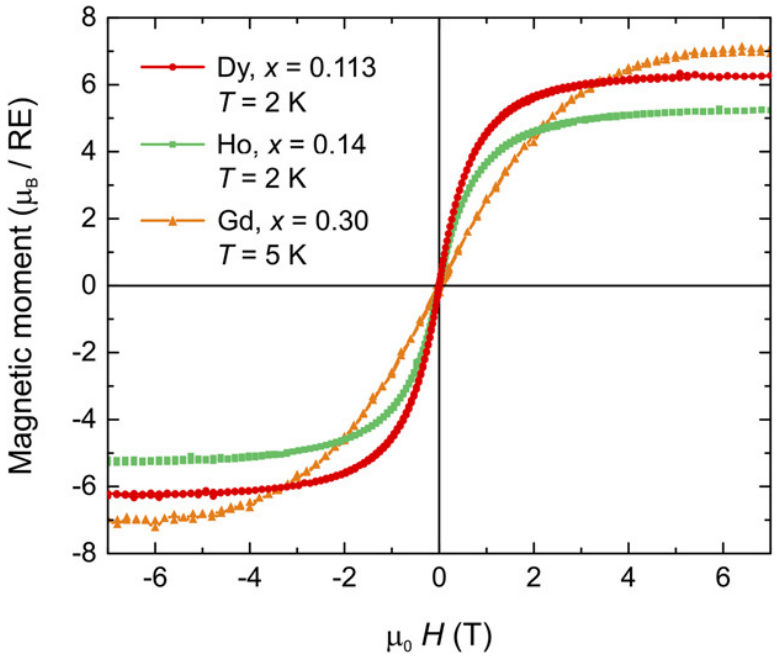

Figure 4.2: In-plane magnetisation measurements of $(RE_xBi_{1-x})_2Te_3$ films using SQUID at low temperatures. Figure adapted from ref.[12].

moments without much overlap in the wave functions, which hence promotes paramagnetism.

Figure 4.3 shows the relationship between the magnetic moment per atom and the doping concentration of the $(RE_xBi_{1-x})_2Te_3$ films. These results were also obtained using SQUID at 2 - 5 K. In this figure, the Gd and Ho doping show a constant atomic moment, but the Dy-doped film unexpectedly exhibits a steady decrease in the atomic moment following an increase in the doping concentration, from 12.6 μ_B at $x = 0.023$ to 4.3 μ_B at $x = 0.335$. The decrease in atomic moment may come from the rise of antiferromagnetic ordering, which has been found in other Dy compounds such as Dy_2Te_3 with a Néel temperature of 4.1 K [106]. A similar doping dependence was also observed in Cr:Sb_2Se_3 TI films [107], which was explained by the possible formation of antiferromagnetic compounds and a loss of crystallinity (as indicated by XRD). In the context of Dy:Bi_2Te_3, no secondary phase was found in the XRD spectra including the higher doped film. The magnetic moment at the lowest doping has exceeded the theoretical prediction by the Hund's rule of 10.6 μ_B. This may be explained by the possible induced polarisation of the Bi_2Te_3 matrix by Dy. A similar polarisation effect in the host material has been reported in other RE-doped systems, such as Gd-doped and Eu-doped GaN [108, 109].

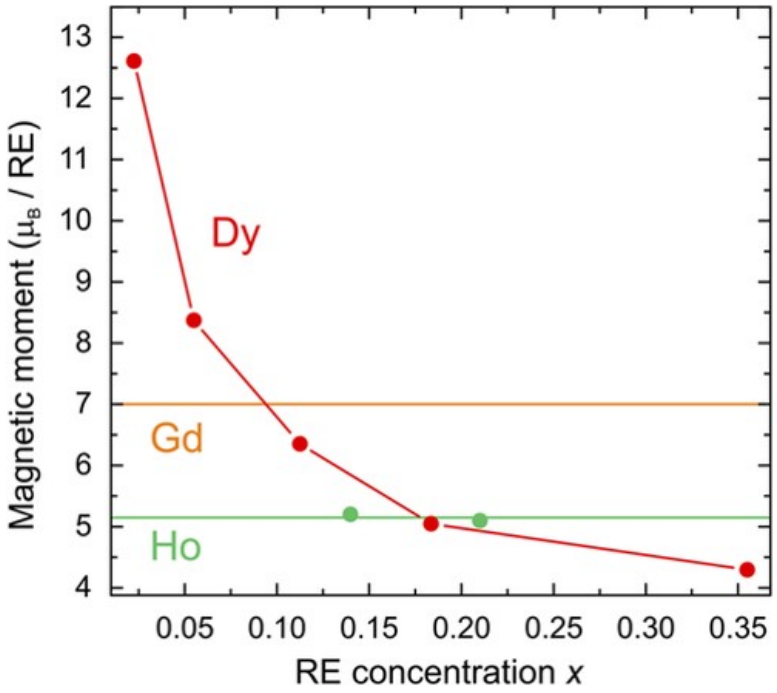

Figure 4.3: Doping-concentration-dependent magnetic moment of the $(RE_xBi_{1-x})_2Te_3$ films at low temperatures. Figure adapted from ref.[12].

ARPES results showed a Dirac cone in the Ho- and Gd-doped films, confirming the preservation of the gapless topological surface states (TSS) upon doping. Interestingly, despite the absence of ferromagnetic ordering, a gap opening was observed in the $(Dy_xBi_{1-x})_2Te_3$ films when the doping concentration reached $x = 0.113$. The resolved band structures along the $\Gamma - K$ direction and the corresponding energy distribution curves along $k_{//} = 0$ are shown in Figure 4.4. When the doping was low ($x = 0.055$), at both 20 K (Figure 4.4(a)) and 300 K (Figure 4.4(c)), a linear dispersion of the energy band with a high brightness was found at the Dirac point. A high intensity peak at the corresponding location of the energy dispersion curve indicates the band is continuous. This is similar to a TRS-protected surface state in pristine Bi_2Te_3 [110]. However, when the doping was high ($x = 0.133$), at 20 K (Figure 4.4(b)) a reduced brightness was observed at the Dirac point, and a small dip was found in the energy dispersion curve, indicating a gap opened at the Dirac point. A close examination of the dip tells that the band gap is about 85 meV. Noticeably, the band gap was preserved when the sample reached room temperature (Figure 4.4(d)).

The co-existence of a surface band gap and paramagnetism in Dy-doped Bi_2Te_3 is un-

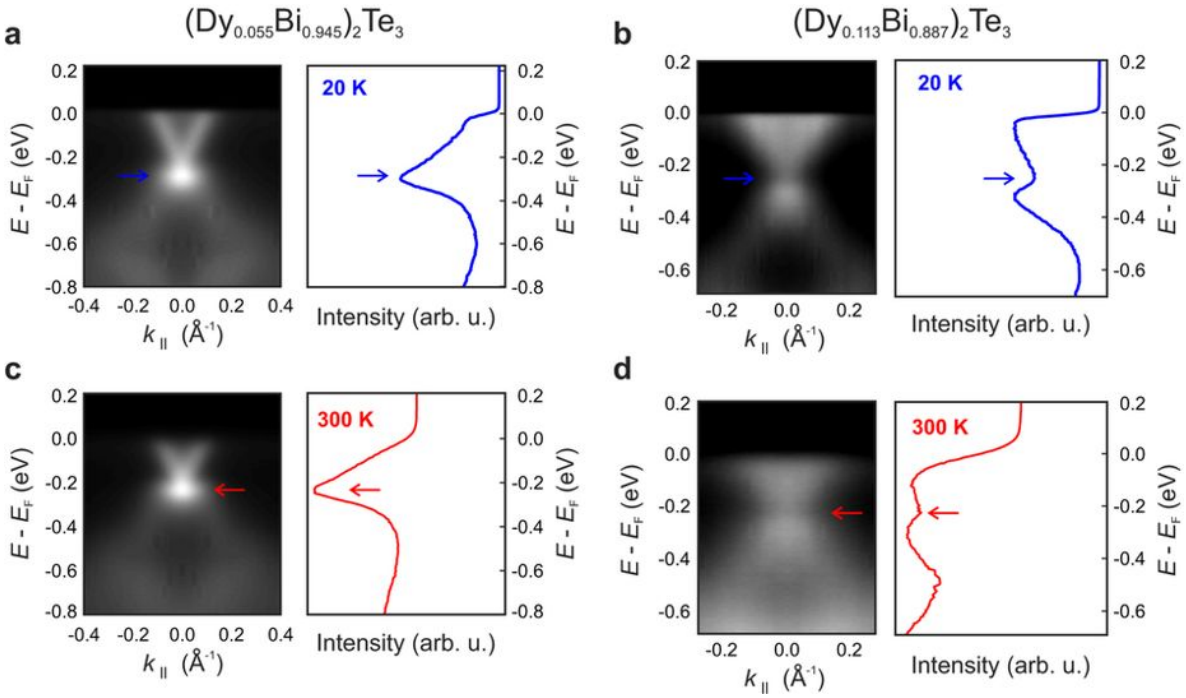

Figure 4.4: Band structures along $\Gamma - K$ and corresponding energy distributions along $k_{//} = 0$ for the $(Dy_xBi_{1-x})_2Te_3$ TI films at certain temperatures T. (a) $x = 0.055, T = 20$ K; (b) $x = 0.113, T = 20$ K; (c) $x = 0.055, T = 300$ K; (d) $x = 0.113, T = 300$ K. Results are obtained using APRES. Figure adapted from [13].

expected but not unprecedented. A gap in the surface state was found in Cr:Bi_2Se_3 TI films above the Curie temperature [111], when the ferromagnetic ordering disappeared. The reason of the gapped surface state was the short-range magnetic order coming from the inhomogeneous Cr doping and the formation of Cr clusters in the host material. However, in the context of Dy:Bi_2Te_3, it is not clear if the inhomogeneous doping is the reason for the surface band gap, since Dy-doped films show very similar structural and magnetic properties as Ho- and Gd-doped films. What makes Dy different to other RE elements is a question not yet answered.

The presence of a surface gap has made Dy an interesting dopant to further investigate in the TI films. A set of detailed studies was carried out on Dy:Bi_2Te_3 using X-ray magnetic circular dichroism, polarised neutron reflectometry, muon-spin rotation and resonant photoemission [112, 113]. Despite Dy:Bi_2Te_3 films being macroscopically paramagnetic, short-range and inhomogeneous magnetic order was found in these films, which can generate a large effective magnetisation. Also possible antiferromagnetic coupling was discovered when a Co layer is placed next to a Dy:Bi_2Te_3 layer. In the mean-

while, Cr:Sb_2Te_3, who has a similar lattice structure to Dy:Bi_2Te_3, is a well-studied ferromagnetic TI material with a magnetic easy axis pointing out-of-plane [68, 114]. A systematic study of Cr:Sb_2Te_3 can be found in Chapter 5. In an attempt to establish the magnetic ordering in Dy:Bi_2Te_3 by proximity coupling, Professor Hesjedal's group created a TI heterostructure, that is, a $[Cr:Sb_2Te_3/Dy:Bi_2Te_3]_{10}$ superlattice [115]. The study of this superlattice is the main focus of this chapter.

4.2 $[Cr:Sb_2Te_3/Dy:Bi_2Te_3]_{10}$ Superlattice: Growth and Structural Characterisation

The $[Cr:Sb_2Te_3/Dy:Bi_2Te_3]_{10}$ superlattice films were grown by Dr. Liam Duffy on a *c*-plane sapphire substrate using the Oxford TI MBE chamber, with a base pressure of 1×10^{-10} mbar. A detailed description of the MBE chamber can be found in Chapter 2. The layered model of the superlattice is shown in Figure 4.5. Prior to growth the substrate was cleaned in solvent and rinsed in DI water *ex situ*, degassed overnight in the preparation chamber, and annealed at 450 °C for 10 minutes in the growth chamber. Bi, Sb and Te elements of 6N purity were evaporated from standard effusion cells, while Cr and Dy elements of 4N purity were evaporated from high temperature cells. A beam flux ratio of 1:10:100 for (Cr+Dy):(Bi+Sb):Te was maintained throughout the growth. The overpressure of Te helps reduce vacancies and anti-site defects commonly seen in the $(Bi,Sb)_2Te_3$ system [116]. Firstly, a 3-nm-thick Bi_2Te_3 seed layer was deposited on the sapphire substrate at 250 °C, then the film was annealed at 300 °C under an over-flux of Te. Starting with a 5-nm-thick Dy:Bi_2Te_3 layer then a 10-nm-thick Cr:Sb_2Te_3 layer, 10 repeats of the Cr:Sb_2Te_3/Dy:Bi_2Te_3 bilayer structure were built up from the

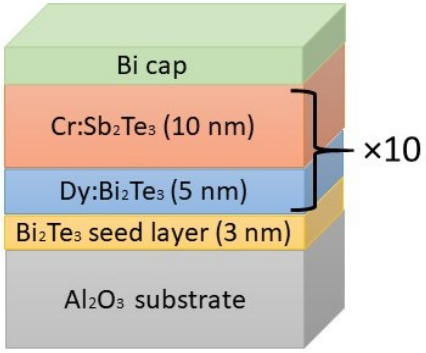

Figure 4.5: Schematic of the $[Cr:Sb_2Te_3/Dy:Bi_2Te_3]_{10}$ TI superlattice (not to scale).

Bi_2Te_3 seed layer at a substrate temperature of 300 °C. Streaky patterns can be observed throughout the growth using *in situ* reflection high-energy electron diffraction (RHEED, not shown here), indicating the growth was epitaxial and two-dimensional. The nominal composition of the superlattice is $[Cr_{0.41}Sb_{1.59}Te_3/Dy_{0.62}Bi_{1.38}Te_3]_{10}$. Finally an amorphous Bi layer was capped on the heterostructure to prevent the sample from oxidation or environmental contamination. The overall thickness of the superlattice (excluding the seed layer and the capping layer) is about 150 nm.

In order to investigate the structural quality of the TI superlattice, Dr. Barat Kurbanjan at the University of York prepared the specimen for transmission electron microscopy (TEM) using focused ion milling, and took cross-sectional TEM images of the sample using a JEOL 2200 system.The TEM images are shown in Figure 4.6. In this figure, the thinner, bright layer are the Dy:Bi_2Te_3, and the thicker, dark layers are Cr:Sb_2Te_3. According to Figure 4.6(a) the thickness of the individual layers are well maintained with smooth interfaces throughout the stack. A close-up of this film (Figure 4.6(b)) clearly shows the quintuple layers (QLs), confirming the superlattice is a TI. The atomic inter-diffusion at the interfaces is around 1 QL.

X-ray diffraction (XRD) was used to investigate the structure of the $[Cr:Sb_2Te_3/Dy:Bi_2Te_3]_{10}$

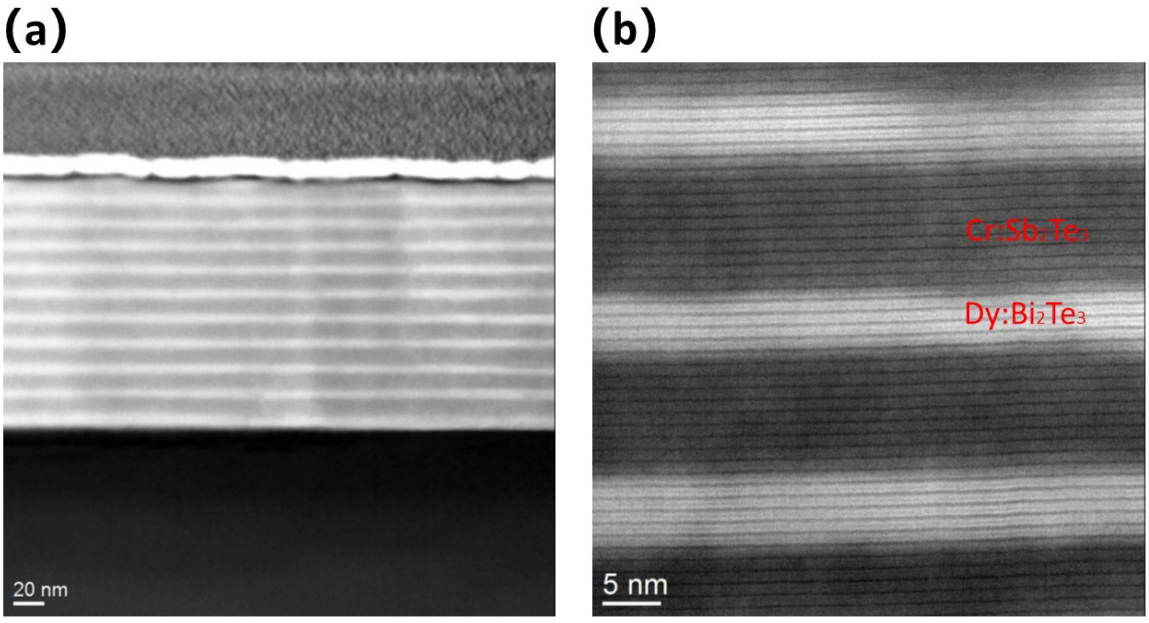

Figure 4.6: Cross-sectional TEM images of the $[Cr:Sb_2Te_3/Dy:Bi_2Te_3]_{10}$ TI superlattice with different magnifications.

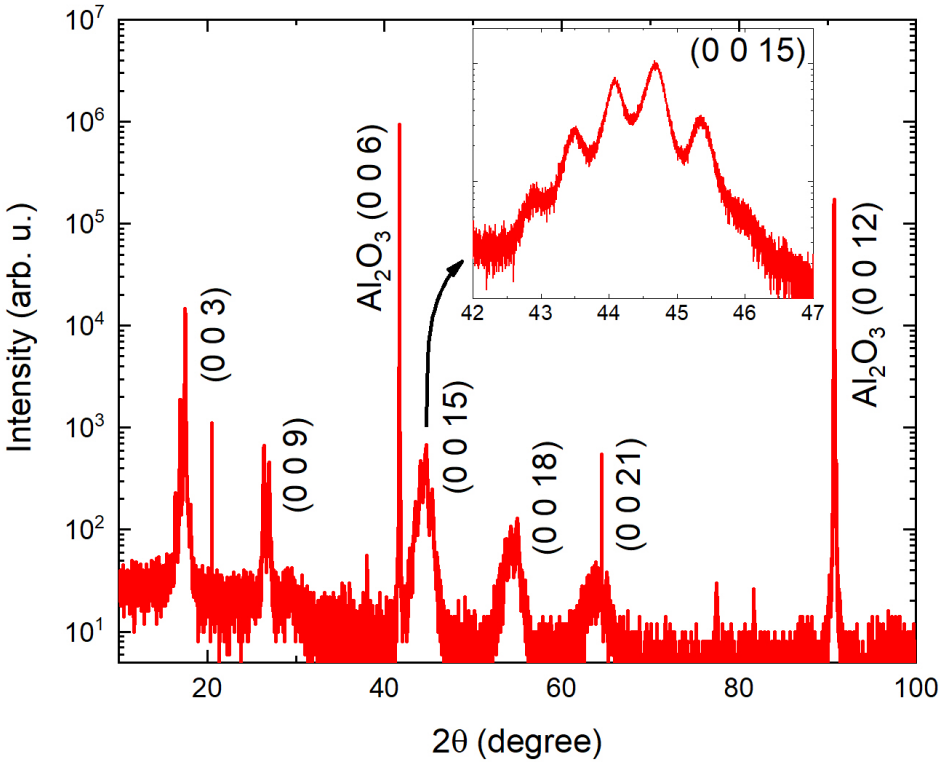

Figure 4.7: XRD spectrum of the $[Cr:Sb_2Te_3/Dy:Bi_2Te_3]_{10}$ TI superlattice. Inset: superlattice peaks around (0 0 15).

superlattice. Figure 4.7 shows the XRD spectrum of the sample. The presence of several (0 0 l) peaks indicates that the sample is epitaxial and has good crystallinity. It is not possible to distinguish between Sb_2Te_3 and Bi_2Te_3 peaks in the spectrum since the lattice constants are similar. The superlattice peaks around (0 0 15) (shown in the inset) suggests a well-ordered multilayer structure with smooth interfaces. This result is similar to the XRD spectrum of doped Sb_2Te_3/Bi_2Te_3 heterostructures published earlier [113].

4.3 $[Cr:Sb_2Te_3/Dy:Bi_2Te_3]_{10}$ Superlattice: Magnetic Measurements

For the MOKE measurements, the $[Cr:Sb_2Te_3/Dy:Bi_2Te_3]_{10}$ thin film was cleaved to less than 3 mm × 3 mm in dimension, placed onto the MOKE probe and cooled down in the cryostat. For the electrical transport measurements, the film was fabricated into Hall bars of 1400 μm ×150 μm in dimension using optical lithography and Ar^+ ion milling,

following the process described in Chapter 2. The micro-devices were placed onto the sample holder of the TFM transport probe and loaded into the cryostat. Magneto-electric properties of the micro-devices were measured using a standard four-terminal AC lock-in scheme with an input current of 1 μA at a frequency of 77 Hz. Fabrication and transport measurements of the sample were performed by Dr. Angadjit Singh.

The $[Cr:Sb_2Te_3/Dy:Bi_2Te_3]_{10}$ film was cooled to 10 K without a magnetic field, then after reaching 10 K the hysteresis loops of the material were recorded, under various field settings. The results are shown in Figure 4.8. The hysteresis loops in the top row are obtained from the electrical transport measurements which are sensitive to the bulk of the material, and those in the bottom row are from the MOKE measurements which are sensitive to the surface layers, due to the limited penetration depth of the laser (∼20 nm). Square-shaped loops were observed using both techniques when the field was swept within ±0.6 T (blue curves), proving the existence of long-range ferromagnetic ordering with an out-of-plane easy axis. This magnetic response is similar to the $Cr:Sb_2Te_3$ single-layer film (shown in Chapter 5). The quantitative match between the coercive field of the two loops ($H_c = 0.18$ T) not only confirms the consistency between the two measurement techniques, but also reflects the uniformity in the superlattice between the top layers and the bulk. However, when the magnetic field was first preset at +2.0 T and then swept within ±0.6 T, both AHE and MOKE loops experienced a lateral shift toward the negative direction (red curves). This indicates a +2.0 T field is adequate to induce an exchange bias at the interface between $Cr:Sb_2Te_3$ and $Dy:Bi_2Te_3$ at 10 K. Similarly a preset field of −2.0 T will cause an opposite shift to the AHE and the MOKE loops (magenta curves). The exchange bias field (H_{EB}) in the MOKE loop and AHE loop can reach up to 0.15 T and 0.08 T respectively. This favours the potential applications of high-stability magnetic memory devices, which require a high H_{EB} against the environmental stray fields. It was also found that, by ±2.0 T field-cooling from 300 K to 10 K, exchange-biased loops can also appear, which are identical to the red and magenta curves. Finally, hysteresis loops under a sweep of ±2.0 T at 10 K did not show a lateral shift but showed higher coercive fields on both sides (orange curves), another common feature of exchange bias. The ascending and descending branches of these curves are similar to the respective branches in red and magenta curves. These results further prove that, at 10 K a +2.0 T field can fully polarise this exchange-biased TI system, and then a −2.0 T field can fully reverse the polarisation to the opposite direction. By comparing the Kerr angle (θ_K) and the Hall resistance (R_{xy}), it is obvious to find that the magnetisations match quantitatively under different field sweeps.

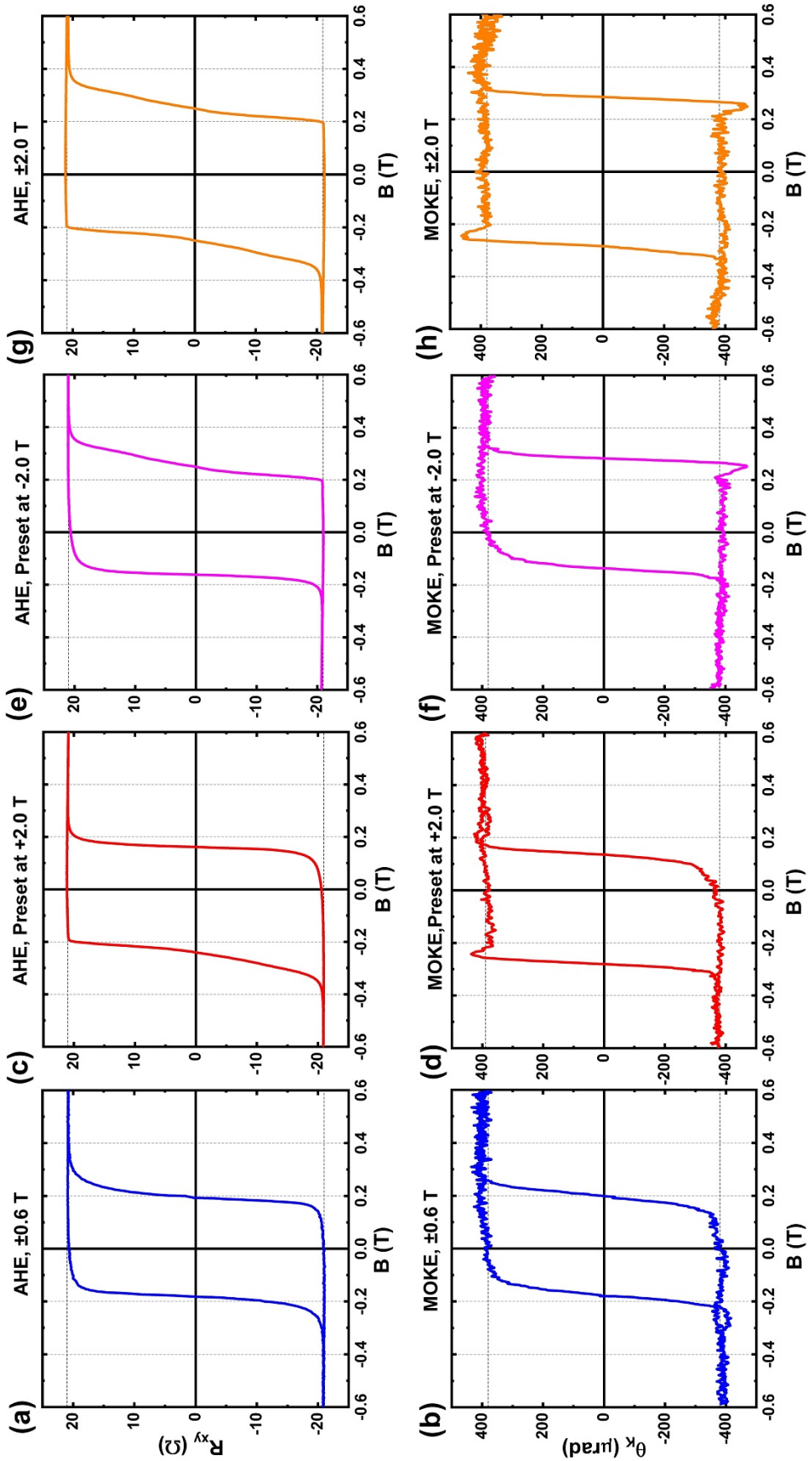

Figure 4.8: Magnetic hysteresis loops of the $[Cr:Sb_2Te_3/Dy:Bi_2Te_3]_{10}$ TI superlattice at 10 K, obtained from from anomalous Hall effect (AHE) measurements (top row) and MOKE measurements (bottom row). All the measurements were taken after zero-field-cooling from 300 K. Different settings of the field sweep were applied during the measurements: (a)(b) sweep within ±0.6 T; (c)(d) preset to +2.0 T, then sweep within ±0.6 T; (e)(f) preset to −2.0 T, then sweep within ±0.6 T; (g)(h) sweep within ±2.0 T.

The next experiment was used to clarify the effect of the sweep range on the coercivity of the superlattice, and to find out if any magnetic transition exists at a high field. The sample was zero-field-cooled from 300 K to 10 K, and then MOKE and electrical transport measurements were carried out with a progressively increasing field range. At first, the field went up from 0 to +0.1 T, then down to −0.1 T, and then repeated the ±0.1 T cycle 3 times. After the final cycle the field went up to +0.2 T. In this way the measurement range was increased after every 3 full loops, up to ±8 T. It was found that the hysteresis loops started to appear from ±0.3 T. Figure 4.9(a) and (b) demonstrate the hysteresis loops obtained from transport and MOKE measurements respectively. For the presentation purpose the field range in the figures is limited to ±0.6 T. No other magnetic switching was observed outside this range even in the measurement of the highest field (±8 T). It can be seen that all the loops show symmetric coercive fields in both directions. The coercivity increased gradually when the sweep range was ramped up from ±0.3 T to ±2 T. When the field direction reversed to negative and reached the same magnitude as the positive side, the exchange coupling between the Cr-doped and Dy-doped layers was also flipped. The hysteresis loops obtained from higher field ranges (after the ±2 T sweep) showed identical pattern as the ±2 T result. This means a 2 T field is strong enough to fully polarise the Cr:Sb_2Te_3/Dy:Bi_2Te_3 system. All hysteresis loops have the same height, which rules out the presence of a minor loop, something that can be mistaken as the exchange bias effect [117]. Figure 4.9(c) summarises the difference of coercvities (H_c) between the two measurement schemes at different temperatures. The coercivities of the MOKE measurements are again larger than the transport measurements. What contributes to this difference is a question not yet answered..

The temperature dependence of the exchange bias effect in the [Cr:Sb_2Te_3/Dy:Bi_2Te_3]$_{10}$ superlattice is illustrated in Figure 4.10. The sample was zero-field-cooled from 300 K to 1.6 K, and then at 1.6 K a preset field of +2.0 T was applied. Afterwards the hysteresis loops were recorded when the field was swept within ±0.6 T. After this measurement at 1.6 K, the sample temperature was increased and the field sweep was kept within ±0.6 T. Figure 4.10(a)(b) demonstrate the temperature-dependent transport and MOKE loops of the superlattice, from 1.6 K to 150 K. Both probing methods reveal a decreasing magnetisation and coercivity following the temperature increase, with the exchange bias effect vanishing at around 100 K and the remanance disappearing before 150 K. To quantitatively track the changes of the magnetisation in the superlattice, the rema-

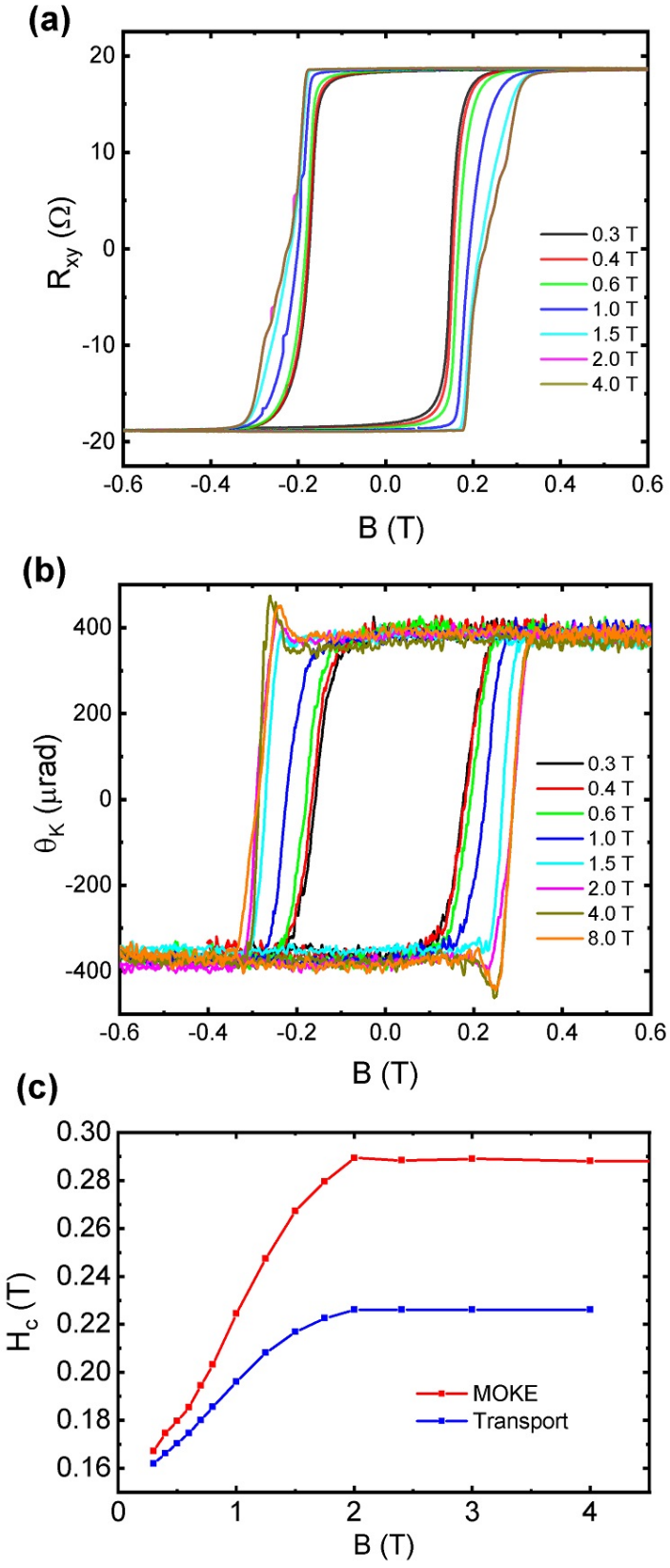

Figure 4.9: (a) Transport hysteresis loops of the $[Cr:Sb_2Te_3/Dy:Bi_2Te_3]_{10}$ superlattice at 10 K under various ranges of field sweep. (b) Corresponding MOKE hysteresis loops at 10 K. (c) Summary of the covercivities obtained under various ranges of field sweep.

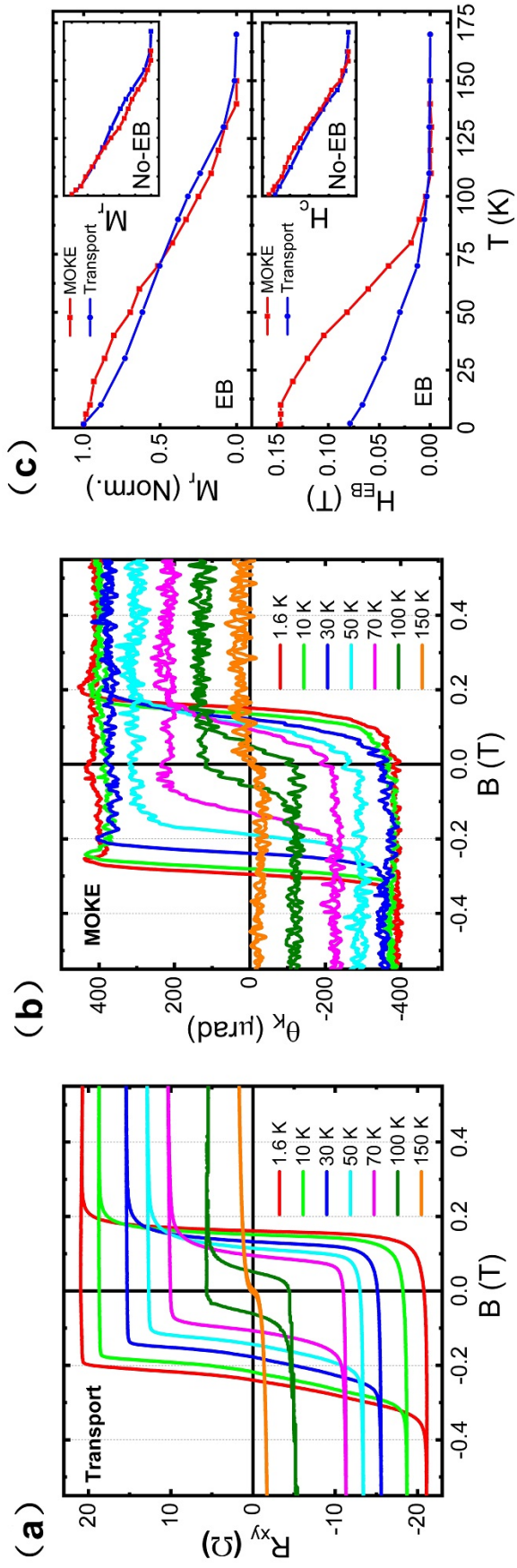

Figure 4.10: (a) Exchange-biased hysteresis loops of [Cr:Sb_2Te_3] at different temperatures, measured by electrical transport. (b) Corresponding hysteresis loops measured by MOKE. (c) Remanent magnetisation (M_r) and exchange bias field (H_{HB}) obtained from transport and MOKE measurements. Insert: Remanence and coercivity obtained in the 'no-bias' case.

nent magnetisation (M_r) and exchange bias field (H_{EB}) versus the temperature were plotted, shown in Figure 4.10(c). The overall trend of M_r matches well between the transport and MOKE results. Again this suggests not only a consistency between the two measurement schemes, but also a good uniformity of the magnetisation between the top layers and the bulk of the superlattice stack. A decline in H_{EB} is also observed as the sample warms up, which approaches zero at 100 K according to both the transport and MOKE curves (Figure 4.10(c) lower), implying that the exchange bias effect can persist up to 100 K in the $[Cr:Sb_2Te_3/Dy:Bi_2Te_3]_{10}$ system. However, a considerable difference in H_{EB} is noticed between the two probing methods. For reference, the same temperature-dependent magnetisation measurements were repeated but without a +2.0 T preset field. As a result, no horizontal bias appeared in the hysteresis loops (not shown here). In this case good similarities in both M_r and H_c were established, as is shown in the insert of Figure 4.10(c).

To further explore the temperature dependence of exchange bias in the superlattice, especially to link the field cooling process to the establishment of the exchange bias effect, the following MOKE experiment was conducted. The sample was zero-field-cooled from 300 K to a certain temperature, marked as t. At this temperature, a +2 T

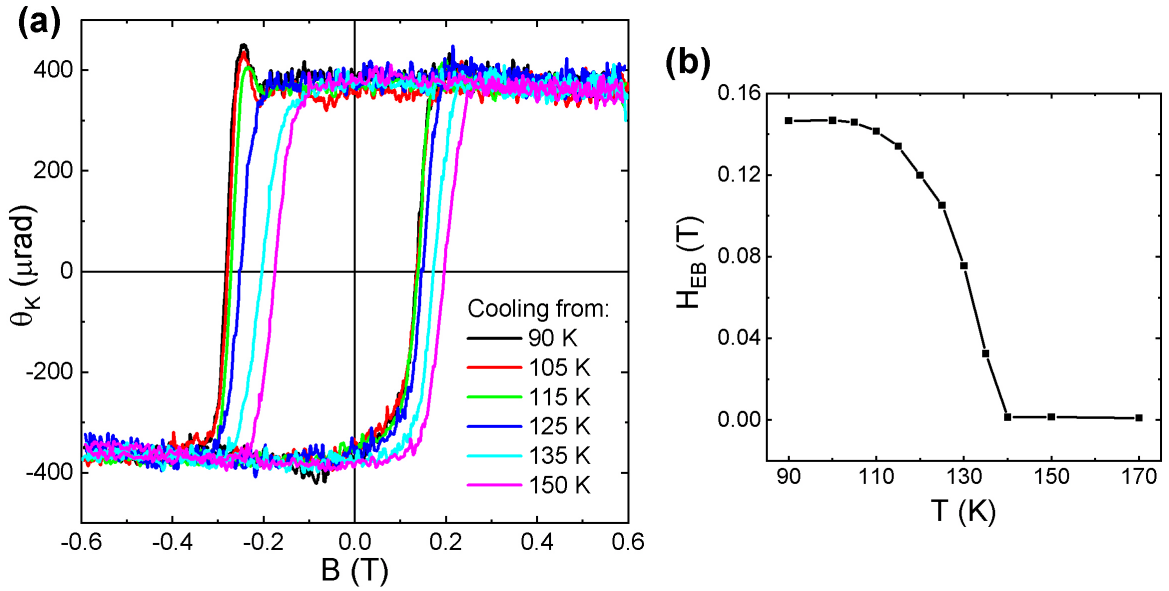

Figure 4.11: Magnetisation of the $[Cr:Sb_2Te_3/Dy:Bi_2Te_3]_{10}$ film after field cooling. (a) MOKE Hysteresis loops of the TI superlattice at 10 K, after field-cooling from different temperatures. (b) Corresponding exchange bias field at 10 K obtained after field-cooling from temperature t.

field was applied to the film then the field went back to 0 T. Afterwards the film was zero-field-cooled to 10 K, and the MOKE hysteresis loops were recorded under a ±0.6 T sweep. The MOKE loops with different temperatures t are shown in Figure 4.11(a), and the corresponding exchange bias field is plotted in Figure 4.11(b). Clearly when t increases from 90 K to 150 K the hysteresis loops gradually change from the 'maxi-bias' case to the 'mini-bias' case. The results obtained by cooling above 140 K are identical to zero-field-cooling from 300 K, and the results from cooling below 100 K is identical to the +2 T field cooling. This means, a +2 T field cannot induce the exchange bias effect in the $[Cr:Sb_2Te_3/Dy:Bi_2Te_3]_{10}$ superlattice at 140 K, while at 100 K the exchange bias can be fully induced. In combination with the previous experiments, it can be inferred that, the ferromagnetic layers in the superlattice has a Curie temperature of about 140 K, and the effectively antiferromagnetic layers, if they exist, have a Néel temperature of about 100 K.

4.4 $[Cr:Sb_2Te_3/Dy:Bi_2Te_3]_{10}$ Superlattice: First Principle Calculation

To better understand the experimental results of the $[Cr:Sb_2Te_3/Dy:Bi_2Te_3]_{10}$ superlattice, density functional theory (DFT) calculation was implemented by Mr. Yu Yang Liu (TCM Group), using the Vienna ab initio Simulation Package (VASP) [118, 119, 120]. The Perdew-Burke-Ernzerhof generalized gradient approximation (PBE-GGA) was applied for the exchange correlation functional [121]. The projector augmented wave (PAW) method was employed, together with the plane wave basis set which had a kinetic energy cut-off of 520 eV. The structure relaxation was performed under the conjugated gradient optimization method, using the following convergence criteria: the residual forces must be less than 5×10^{-4} eV/Å, and the total energy must be converged to 1×10^{-5} eV. A dense k-point grid was applied to compute the Brillouin-zone integrals, for example, a Γ-centred $6 \times 6 \times 1$ grid was used for the calculations of a 30-atom cell.

The calculated structures of the TI material are shown in Figure 4.12. In this figure, (a)(b)(c) show the optimised configurations of bulk Sb_2Te_3, Bi_2Te_3 and the Sb_2Te_3 / Bi_2Te_3 heterostructure, respectively. It is known that the nominal composition of the TI superlattice is $Cr_{0.41}Sb_{1.59}Te_3/Dy_{0.62}Bi_{1.38}Te_3$. To simulate the doped heterostructure within a reasonable computation time, the following two doping concentrations

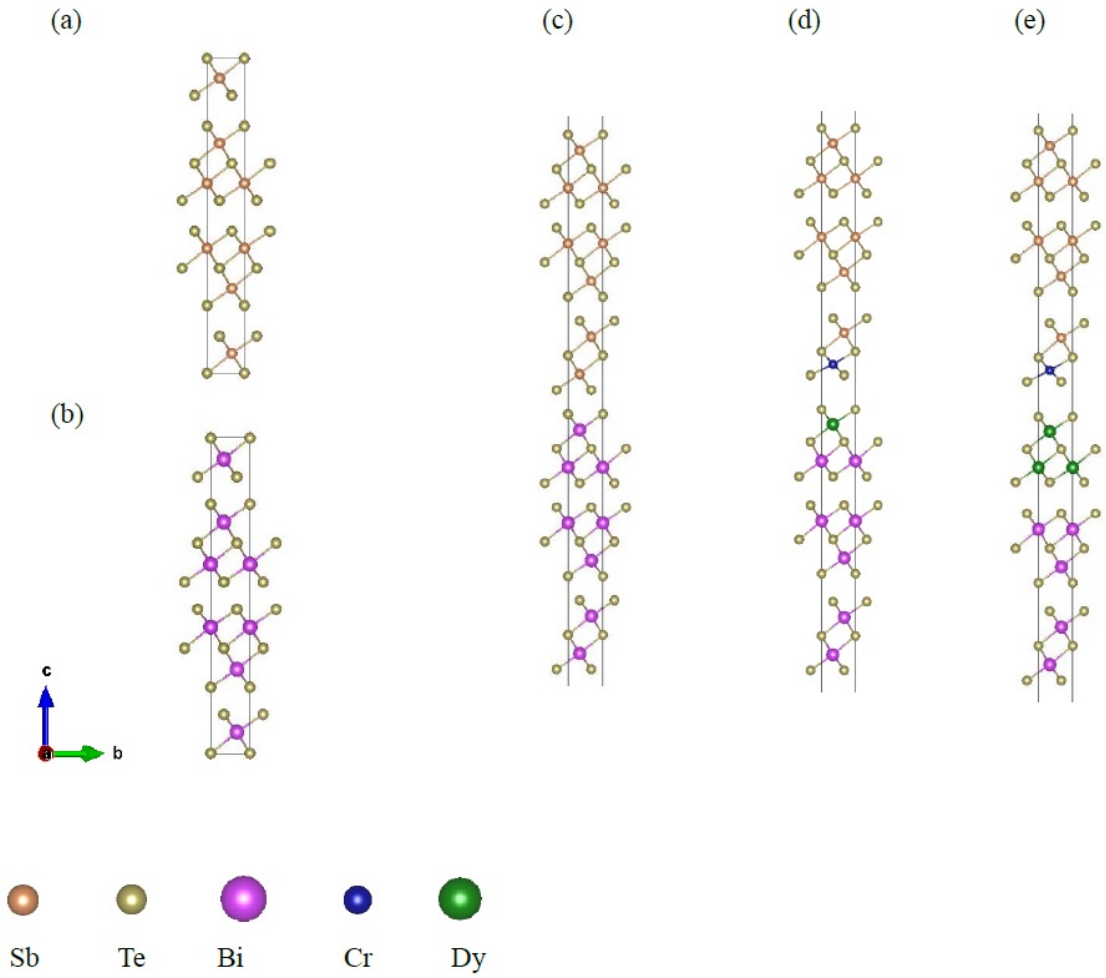

Figure 4.12: Configurations of the following TI structures, optimised using DFT calculations: (a) Sb_2Te_3, (b) Bi_2Te_3, (c) Sb_2Te_3 / Bi_2Te_3, (d) $Cr_{0.33}Sb_{1.67}Te_3$ / $Dy_{0.33}Bi_{1.67}Te_3$, (e) $Cr_{0.33}Sb_{1.67}Te_3$ / $Dy_{0.67}Bi_{1.33}Te_3$.

were investigated: $Cr_{0.33}Sb_{1.67}Te3/Dy_{0.33}Bi_{1.67}Te_3$ and $Cr_{0.33}Sb_{1.67}Te_3/Dy_{0.67}Bi_{1.33}Te_3$. Their optimised configurations are shown in Figure 4.12(d)(e). In Figure 4.12(d), one Cr/Dy atom replaces one Sb/Bi atom near the interface, and in Figure 4.12(e), one Cr atom replaces one Sb atom, while two Dy atoms replaces two Bi atoms near the interface.

The DFT calculation showed that all the above structures are relaxed. The bulk hexagonal Sb_2Te_3 has the lattice constants of $a = 4.33$ Å and $c = 31.34$ Å, and the bulk hexagonal Bi_2Te_3 has the lattice constants of $a = 4.44$ Å and $c = 31.91$ Å. These values are sightly larger than the lattice constants estimated from experiments, that is,

hexagonal lattice constants are $a = 4.26$ Å and $c = 30.49$ Å for Sb_2Te_3, and $a = 4.38$ Å and $c = 30.49$ Å for Bi_2Te_3 [122]. The overestimation of the bond length by GGA is a general phenomenon, which arises from the underestimation of the energies of virtual Kohn-Sham states relative to the occupied states [123]. Although both materials have very similar lattice constants, atoms in the Sb_2Te_3/Bi_2Te_3 heterostructure change their positions slightly compared to the bulk materials, due to the lattice mismatch between the two systems. The DFT calculation revealed that this heterostructure has lattice constants of $a = 4.39$ Å and $c = 63.49$ Å. To mimic the layer repeats of the superlattice sample, in the calculation a periodic boundary condition was applied along the $c-$axis.

To investigate the magnetic properties of the doped superlattice, atomic magnetic moments were assigned to Cr and Dy, but not to Bi, Sb or Te. In the $Cr_{0.33}Sb_{1.67}Te_3$ / $Dy_{0.33}Bi_{1.67}Te_3$ model, where only one monolayer (ML) of Dy was considered in the calculation, the atomic magnetic moment of Dy was found to be 4.8 μ_B and Cr was 3.4 μ_B. If the Cr spin is pre-biased to the 'up' direction, the Dy moment can be either 'up' or 'down', as shown in Figure 4.13(a). It turned out that the parallel alignment at the interface has a higher energy than the antiparallel alignment, indicating that the antiferromagnetic coupling is a more energy-favoured state for Cr-Dy. Meanwhile, in the $Cr_{0.33}Sb_{1.67}Te_3$ / $Dy_{0.67}Bi_{1.33}Te_3$ model, which has two MLs of Dy near the interface, the Dy and Cr atoms showed magnetic moments of 4.7 μ_B and 3.4 μ_B respectively, matching the experimental results in previous publications [13, 68]. If the Cr spin is pre-biased to the 'up' direction, the alignment of two Dy spins can have four configurations, as shown in Figure 4.13(b). It was found that the most stable state was the

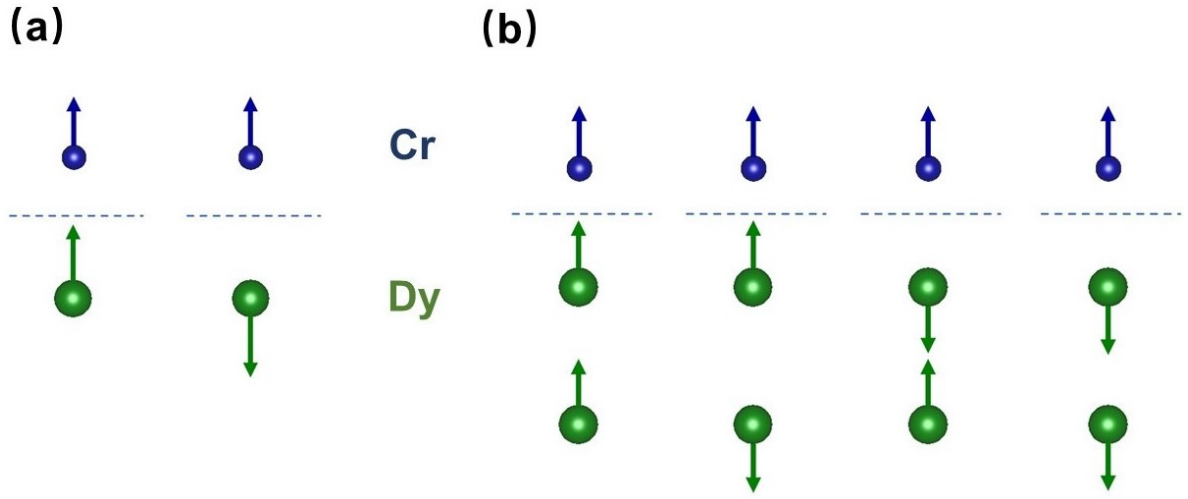

Figure 4.13: Possible spin configurations of (a) Cr-Dy and (b) Cr-Dy-Dy.

'up-down-up' configuration for Cr-Dy-Dy. This means the two MLs of Dy tend to form an antiferromagnetic pouch, making the Cr-doped/Dy-doped heterostructure effectively an FM/AFM system at the interface, a common spin configuration to induce exchange bias. It should be mentioned that these calculated results are still preliminary and more detailed analysis will be conducted in the near future.

4.5 Summary and Conclusion

In summary, this chapter has demonstrated a systematic structural and magnetic study of the ferromagnet/paramagnet $[Cr:Sb_2Te_3/Dy:Bi_2Te_3]_{10}$ TI superlattice system. Ordered crystal structure of the film with smooth interfaces was confirmed using TEM and XRD. The temperature-dependent magnetisation of the film was probed using MOKE and electrical transport techniques, which are sensitive to the surface layers and the bulk, respectively. A good qualitative agreement is established between the two probing methods. The film shows out-of-plane ferromagnetism up to 150 K, and an exchange bias effect up to 100 K. An exchange bias field of up to 0.15 T is observed at 10 K. According to the preliminary results of the DFT calculation, when the Cr-doped layer is ferromagnetically ordered, the two Dy spins close to the interface are more stable in the antiferromagnetic alignment, making the Cr-doped/Dy-doped heterostructure effectively an FM/AFM system. This experiment indicates the possible proximity-induced antiferromagnetism in rare-earth-doped TI materials, providing a new pathway in the growing field of topological antiferromagnetic spintronics [124, 125, 126, 127].

CHAPTER 5

MOKE STUDY OF VARIOUS MAGNETIC TOPOLOGICAL INSULATOR SYSTEMS

This chapter describes various collaboration projects on magnetic topological insulators that the MOKE measurements have made substantial contribution.

5.1 Cr:Sb_2Te_3 Single-doped Thin Films

MOKE has been applied to study magnetism on various doped topological insulator (TI) materials [61, 128, 129, 130]. The recent discovery of the topological Hall effect (THE) in TI heterostructures highlights the virtue of a combined technique of MOKE and electrical transport [131, 126]. In this case the magnitude of the THE can be derived from a direct subtraction of the anomalous Hall effect (AHE) results by the Kerr responses [132, 133]. It is therefore important to examine systematically the consistency between data obtained from anomalous Hall effect (AHE) and MOKE in various magnetic TI (MTI) materials. In light of this, a systematic study of magnetically doped $Cr_xSb_{2-x}Te_3$ topological insulator thin films is demonstrated using electrical transport and MOKE measurements, with Cr concentration varying from $x = 0.15$ to $x = 0.76$. The temperature-dependent magnetisation, coercivity and the Curie temperature agree well between the two measurement schemes. This project was lead by Dr. Angadjit Singh in TFM Group. The author of this thesis did the MOKE measurements, and collectively developed the analysis of carrier-dependent mechanism of magnetisation with Dr. Singh. Most of this work has been recently published on Scientific Reports [114].

Cr-doped Sb_2Te_3 films with 20 nm thickness were grown on *c*-plane sapphire substrates in the Oxford TI MBE chamber, with a base pressure of $1 \times 10^{-}10$ mbar. The growth follows the standard recipe as for the $[Cr:Sb_2Te_3/Dy:Bi_2Te_3]_10$ sample in Chapter 3, and therefore a detailed description is omitted here. To achieve a range of Cr doping concentrations, the temperature of the Cr evaporation cell was adjusted, while its beam flux was monitored. Finally, a 3-nm-thick amorphous Te capping layer was deposited at room temperature and then the film was taken out from the chamber. Another 20-nm-thick Sb_2Te_3 film without Cr doping was also grown as reference. For MOKE measurements, the TI films were cut to less than 4 mm × 4 mm in size, mounted onto the polar MOKE probe and dipped into the He-4 cryostat. For electrical transport measurements, the micro Hall bars with 800 μm length and 200 μm width were fabricated in SP cleanroom using standard photolithography and dry etching techniques, similar to the process described in Chapter 3. The devices were then mounted on an electrical measurement probe, dipped into the same cryostat, and measured using a standard AC four-terminal scheme with 1 μA excitation current at 77 Hz.

Cr doping concentration was confirmed by X-ray photoelectron spectroscopy (XPS) using a Thermo Fisher Scientific Kα x-ray photoelectron spectrometer. The doping concentrations of the four $Cr_xSb_{2-x}Te_3$ samples were found to be $x = 0.15, 0.41, 0.58, 0.76$. XRD confirmed the tetradymite structure in all samples. No secondary phase other than Sb_2Te_3 was found even in the highest doped sample. Temperature-dependent magneto-transport and MOKE measurements confirmed all four Cr-doped films have out-of-plane ferromagnetic order, with similar features in anisotropic magnetoresistence (AMR), Hall loops and MOKE loops. Results of the two highest-doped samples are shown in Figure 5.1. All respective parameters are the same as used in the superlattice experiment in Chapter 3. Figure 5.1(a,e) shows the temperature-dependent MR ratio $\frac{\delta\rho}{\rho} = \frac{\rho_{xx}(B)-\rho_{xx}(0)}{\rho_{xx}(0)}$ with respect to magnetic field. When the temperature is lower than a certain value (T_c) the MR trace is in a butterfly shape suggesting a negative MR, which originates from spin-dependent scattering of carriers when ferromagnetic long-range order exists [134, 135]. Figure 5.1(b,f) and (c,g) respectively describe magnetic hysteresis loops of various temperatures using magneto-transport and magneto-optic methods. The magnetisation was characterised by Hall resistance R_{xy} and polar Kerr angle θ_K respectively. These results clearly show the magnetic easy axis is out-of-plane. The coercive fields (H_c) from the transport data can quantitatively match the peaks in the MR graph. Figure 5.1(d,h) demonstrate a comparison between AHE (classical

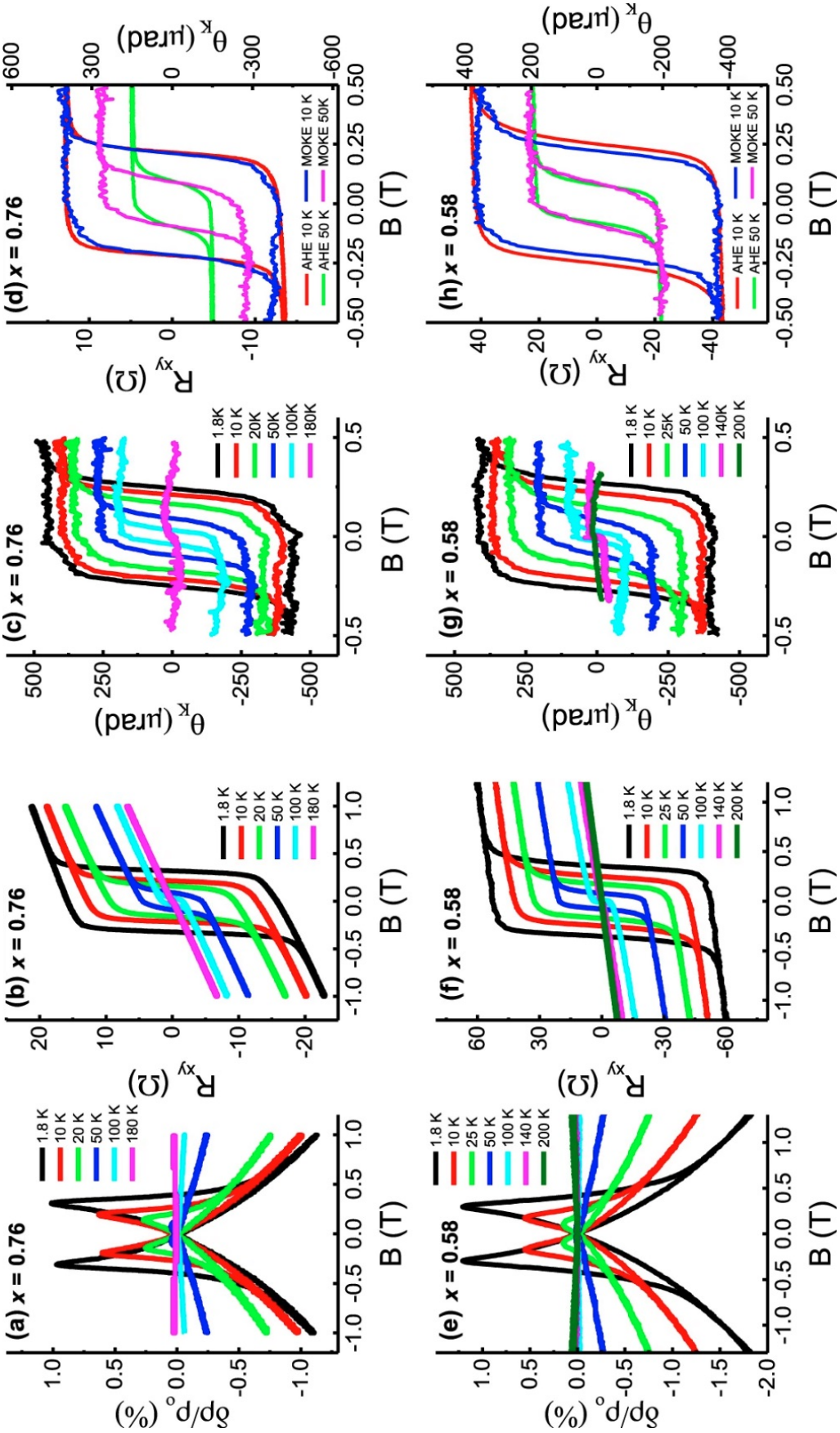

Figure 5.1: Temperature-dependent AHE and polar MOKE results of $Cr_xSb_{2-x}Te3$ thin films with respect to magnetic field. Doping levels are $x = 0.76$ and $x = 0.58$. (a,e) MR ratios. (b,f) Hall resistance R_{xx} hysteresis loops. (c,g) Kerr angle θ_K hysteresis loops. (d,h) Comparison between AHE and MOKE hysteresis loops at 10 K and 50 K.

Hall contribution is removed) and MOKE hysteresis loops at 10 K and 50 K. For the $x = 0.58$ sample, both the coercive field and saturation magnetisation have a good match. For the $x = 0.76$ sample, the coercive field matches well but an anomaly is found at the saturation magnetisation.

To further investigate the difference of magnetisation results between AHE and MOKE measurements, the Hall conductivity, σ_{xy}^{A}, the Kerr angle, θ_K, of the two high-doped samples are compared at different temperatures. The results are shown in Figure 5.2. From Figure 5.2(a,c) it is clear both curves decrease monotonically with increasing temperature, and approaches zero at similar temperatures (Curie temperature). The concave-shaped decreasing trend is similar to those obtained from transport measurements in various Cr-doped TI materials [68, 136]. The discrepancy between AHE and MOKE results may be partially due to the fact that, MOKE is a surface-sensitive technique with exponential intensity decay along the depth profile [21], while electrical transport probes the whole film including both the surface and the bulk. Magnetic properties of the magnetic TI films can also be affected by the laser illumination during MOKE measurements. When the laser was focused down to a 2 μm spot on the $x = 0.76$ sample at 10 K, the coercivity decreased with increasing laser power as is shown in Figure 5.2(b). This relation fits well to a power law (dashed line in the figure) at a photovoltage range from 0.1 V to 3 V, which corresponds to approximately 0.1 mW to 3 mW laser power incident on the film. This coercivity relation is likely a result of locally induced heat from the laser on the sample surface [130]. Below 0.05 mW laser power (0.05 V photovoltage) the coercivity reaches a plateau of 0.215 T, showing good agreement with AHE result at 10 K. This suggests laser power lower than 0.5 mW is less likely to affect the magnetic properties of Cr:Sb_2Te_3 film. Because of this, all MOKE measurements in this section were conducted at less than 0.5 mW laser power. This laser-power-dependent property has been used to non-invasively encode information at micron-sized spots on Cr:$(Bi,Sb)_2Te_3$ films [130]. Figure 5.2(d) shows good agreement of coercivities between AHE and MOKE results under 0.5 mW.

In summary, a systematic study of magnetism in Cr-doped Sb_2Te_3 MTI thin films were carried out using electrical transport and MOKE techniques. A good agreement was found among the two approaches regarding temperature-dependent magnetisation, coercivity and Curie temperature. Based on the investigations shown above, further electrical gating with ion gel, and Terahertz time-domain spectroscopy (THz-TDS) measurements were carried out on the Cr:Sb_2Te_3 films [137]. It was found that the

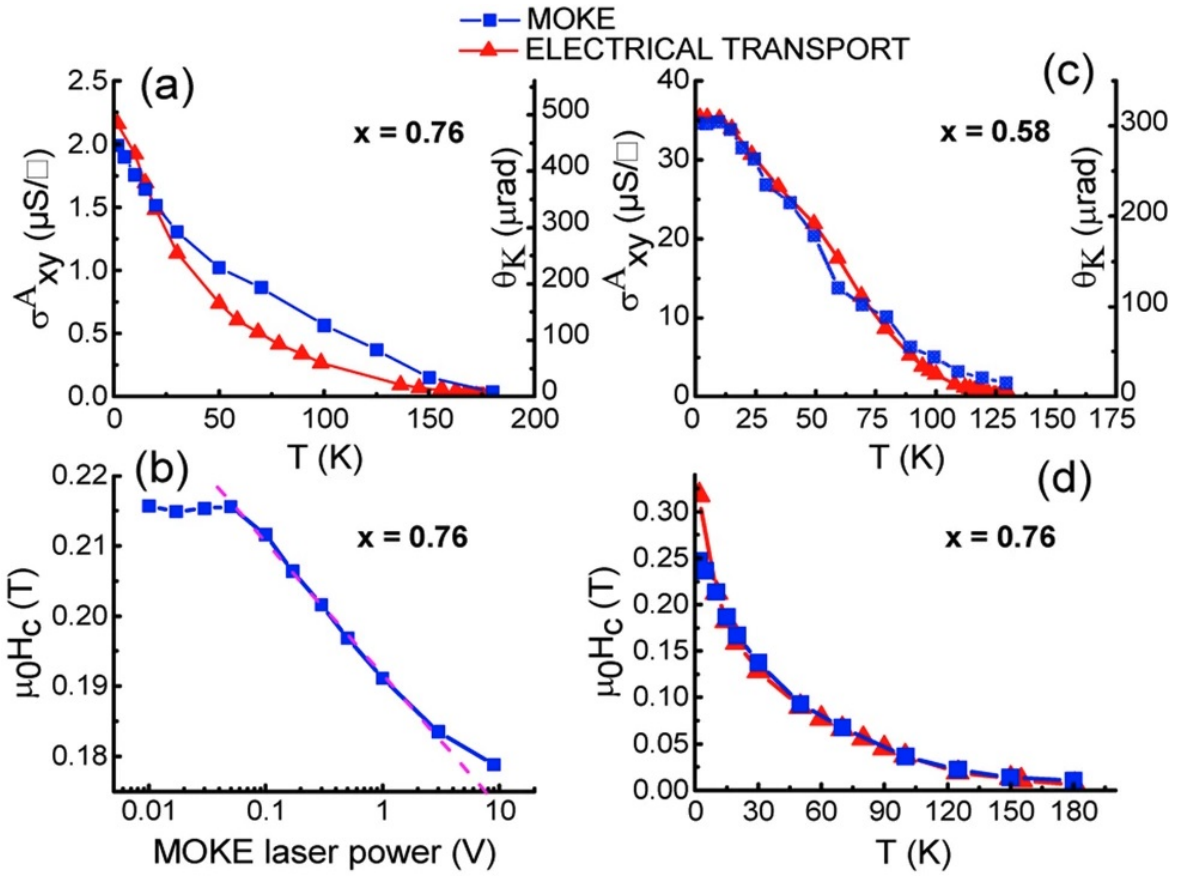

Figure 5.2: (a,c) Zero-field anomalous Hall conductivity σ^A_{xy} and Kerr angle θ_K versus temperature of $x = 0.76$ and $x = 0.58$ films. (b) Coercivity H_c versus laser power by MOKE measurement of $x = 0.76$ film at 10 K. The red dashed line represents a power law fit. (d) Coercivity H_c versus temperature of $x = 0.76$ film by electrical transport and MOKE measurements.

magnitude of AHE can be altered by 50 % by applying a gate voltage of ±3 V through ion gel DEME-TFSI, indicating the carrier-mediated RKKY interaction can be the major mechanism in establishing ferromagnetic ordering in Cr:Sb_2Te_3 material. This hypothesis is further supported by the linear correlation between $xp^{\frac{1}{3}}$ and T_c among all samples using transport and THz measurements, where x is the Cr doping concentration, and p is the carrier density. This relationship is characteristic in mean-field-theory ferromagnet systems [89]. These results can help people understand the magnetism in MTIs and paves the way to the further development of the TI electronic devices.

5.2 (Cr,V):Sb_2Te_3 Co-doped Thin Films

As was mentioned in Chapter 1, the quantum anomalous Hall effect (QAHE) was first observed in Cr-doped and V-doped $(Bi,Sb)_2Te_3$ epitaxial thin films below 100 mK [6, 62], then recently in Cr-V-co-doped $(Bi,Sb)_2Te_3$ at a higher temperature [67], showing a conductance value close to the quantum regime at 1.5 K. This finding brings scientific interest to pursue the co-doping of other compounds in the $(Bi,Sb)_2(Te,Se)_3$ family to realise the QAHE at elevated temperatures [138]. Here a simultaneous magneto-transport and magneto-optic study of co-doped (Cr,V):Sb_2Te_3 TI thin film is reported. A combination of weak antilocalization and anisotropic magnetoresistance effects were observed above 70 K. These results highlight the virtue of MOKE and electrical transport to optimise exotic topological magnetic materials. This project was lead by the author of this thesis, with contributions from Dr. Singh.

The 60-nm-thick (Cr,V):Sb_2Te_3 and Cr:Sb_2Te_3 TI thin films were grown on *c*-plane sapphire substrates by MBE co-deposition using the standard recipe at Oxford [68, 138]. Sb and Te elements were evaporated from 6N purity sources in standard effusion cells, while Cr and V elements were from 4N purity sources in high temperature cells. All beam fluxes were measured *in situ* by a beam flux monitor. The co-doped (Cr,V):Sb_2Te_3 sample was grown in a overpressure of Te, where the flux ratio (V+Cr+Sb):Te = 10:1 was maintained, which reduces Te vacancies and anti-site defects common in the Sb_2Te_3 system [116]. A flux ratio V:Cr = 1:5 was maintained for the growth of the co-doped layer. A single-doped Cr:Sb_2Te_3 thin film with identical Cr concentration was also grown using the same procedure but without V dopant. The nominal composition ratios of the two samples are $Cr_{0.41}V_{0.04}Sb_{1.65}Te_3$ and $Cr_{0.41}Sb_{1.69}Te_3$. Both films show streaky patterns by *in situ* reflection high energy electron diffraction throughout the deposition (not shown here), indicating a smooth two-dimensional growth mode. The structural property of the grown films was characterised *ex situ* by x-ray diffraction (XRD) in a Bruker D8 diffractometer.

The XRD spectra of the (Cr,V):Sb_2Te_3 (in blue) and Cr:Sb_2Te_3 (in red) thin films are illustrated in Figure 5.3. The (0 0 n) peaks of Sb_2Te_3 in the single-doped Cr:Sb_2Te_3 film indicate the presence of a well-ordered crystal structure, with the *c*-axis parallel to the surface normal. No secondary phases such as SbTe, $SbTe_2$ or Sb_2Te_5 can be found in this spectrum. The result indicates that the Sb_2Te_3 structure remains intact upon moderate Cr doping. The (Cr,V):Sb_2Te_3 sample, on the other hand, shows the

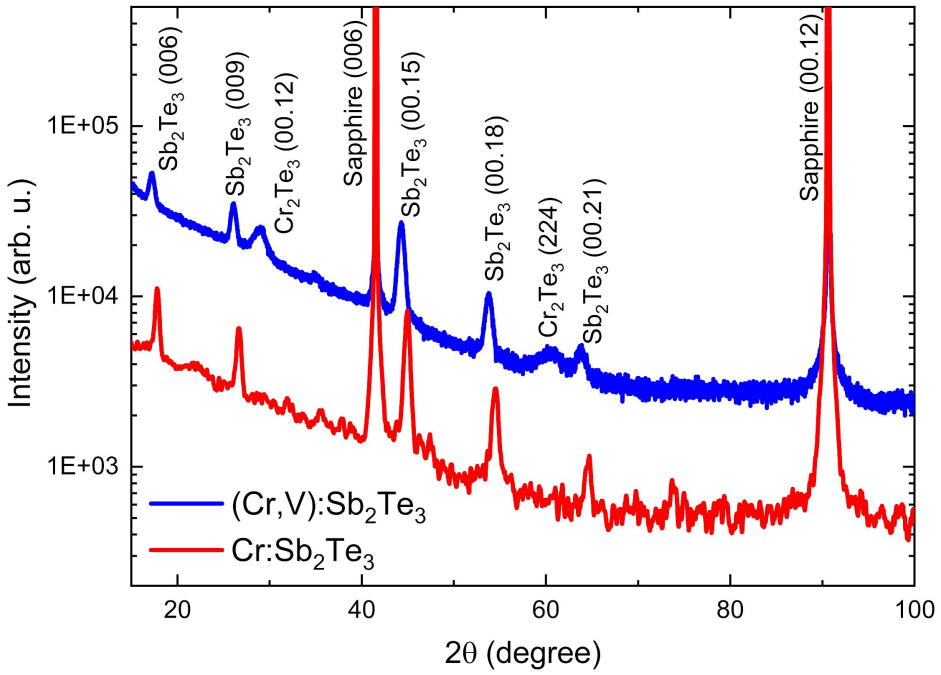

Figure 5.3: XRD spectra of the (V,Cr):Sb_2Te_3 (in blue) and Cr:Sb_2Te_3 (in red) MTI thin films.

presence of another phase, Cr_2Te_3, in addition to Sb_2Te_3. Diffraction peaks related to any V-Te compound were not found, such as VTe or V_3Te_4. The observation of Cr_2Te_3 is consistent with the previous finding that vanadium acts as a surfactant preventing Cr from substituting Sb in the co-doped (Cr,V):Sb_2Te_3 structure, forcing it to form Cr_2Te_3, which has similar crystallographic parameters to Sb_2Te_3 [138, 139].

For the electrical transport and MOKE measurements, the (Cr,V):Sb_2Te_3 and Cr:Sb_2Te_3 thin films were fabricated into Hall bar devices of dimensions 1400 μm ×150 μm in a similar way to the other TI devices featured in this thesis. The micro-devices were then glued and wire-bonded to a 20-pin leadless chip carrier and placed onto the sample holder of the MOKE probe before loading into the cryostat. The laser was scanned across the devices and their respective x-y coordinates were mapped out. Figure 5.4 shows a two-dimensional reflectivity map of a Hall bar. In this figure the blue parts are the bare substrates with low reflectivity, green part is the Hall bar which is moderately reflective, and red parts are highly-reflective Au contacts. In order to verify the planar magnetisation uniformity of both samples, the laser spot was moved to various places on the Hall bars. Variation of Kerr response at different locations was not significant. Finally the laser was focused to the geometrical centre of the Hall bars throughout the rest of the experiments. The electrical transport properties of the devices were mea-

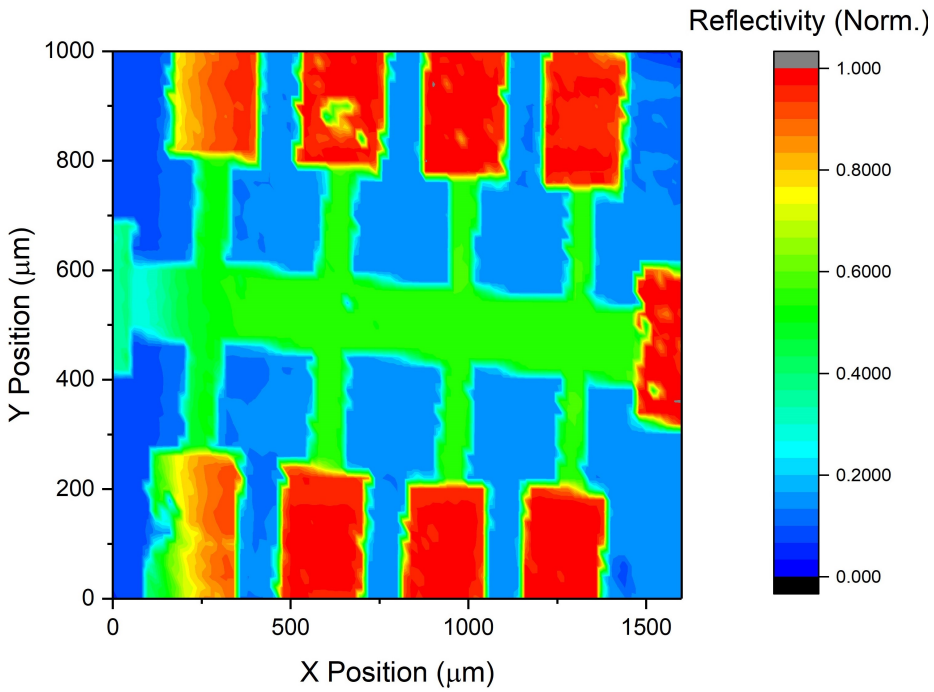

Figure 5.4: Two-dimensional reflectivity map of a (Cr.V):Sb_2Te_3 Hall bar. The blue parts are the bare substrates with low reflectivity, green part is the Hall bar which is moderately reflective, and red parts are highly-reflective Au contacts.

sured simultaneously with optical probing, using a standard four-terminal AC lock-in scheme with an input current of 1 μA at a frequency of 77 Hz.

Figures 5.5(a,d) illustrate the magnetic hysteresis loops of the (Cr,V):Sb_2Te_3 film at different temperatures ranging from 5 K to 100 K using combined optical and electrical techniques. The results obtained display the AHE effect, showing good consistency between the two measurement schemes. Figures 5.5(b,e) show corresponding results for the single-doped Cr:Sb_2Te_3 film. From the shape of the loops it can concluded that both materials establish a strong ferromagnetic order perpendicular to the film plane, with the magnitude of the remanence (M_r) at zero field close to the spontaneous magnetisation (M_s) at high fields. To compare better the results between the two samples, and also between the two measurement schemes, we plotted the coercivity (H_c) and remanent magnetisation (M_r) extracted from these four graphs in Figures 5.5(c,f). The electrically- and optically-obtained coercive fields of both samples match quantitatively across the whole temperature range. The remanent magnetisation, on the other hand, displays a concave-shaped trend in both materials following the temperature increment, consistent with observations in other magnetic-doped $(Bi,Sb)_2(Te,Se)_3$ TI

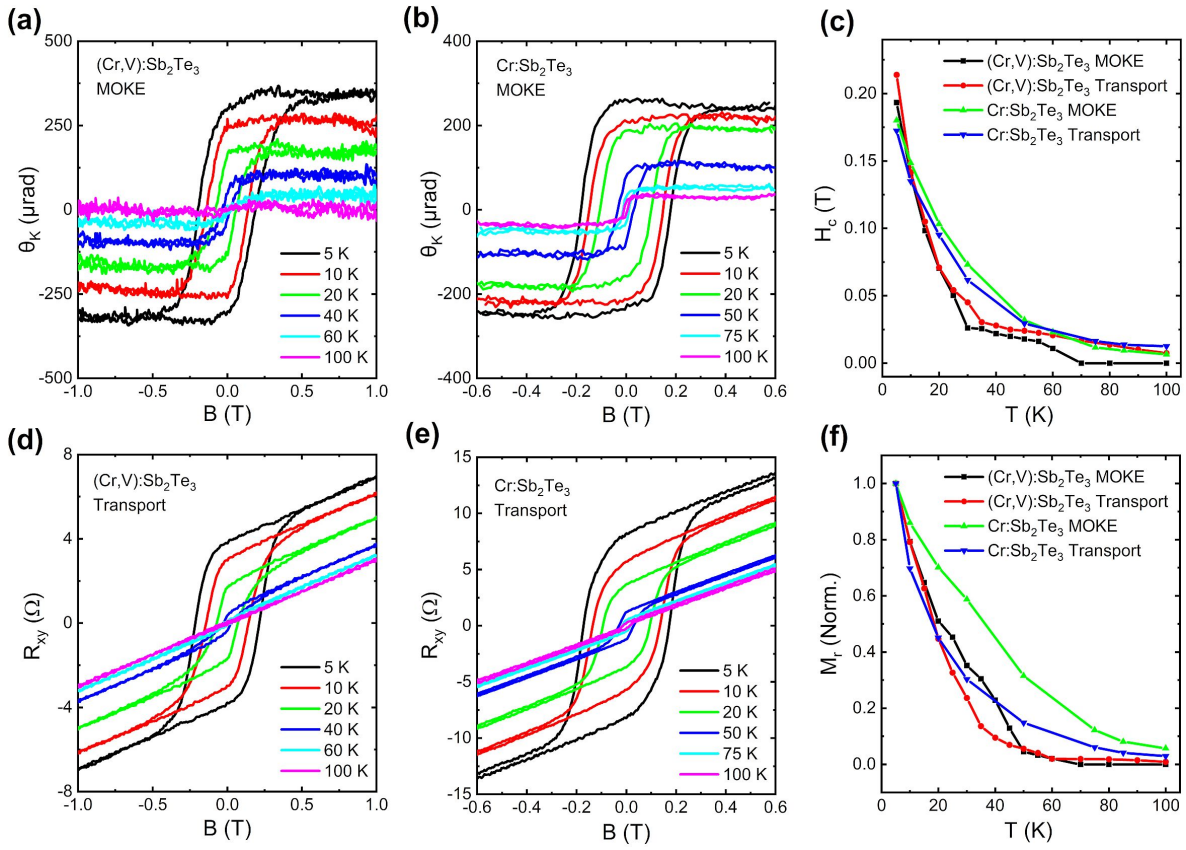

Figure 5.5: Temperature-dependent magnetic hysteresis loops of (a) (Cr,V):Sb_2Te_3 and (b) Cr:Sb_2Te_3 films obtained from MOKE measurements. (d,e) Corresponding hysteresis loops obtained from AHE electrical transport measurements. (c,f) Temperature-dependent coercivity and saturation magnetisation values extracted from MOKE and transport measurements for the two films.

systems [67, 68, 114]. In both samples, M_r sees a steeper decrease in the Hall resistance compared to the Kerr angle. Surface sensitivity of the Kerr measurement may account for the difference in M_r compared to transport measurement, which is bulk sensitive. The good consistency between the optically and electrically probed H_c and M_r may be relevant in the context of the recent discovery of the THE in TI heterostructures [131, 126], where the value of the THE can be obtained when the transport results are directly subtracted from the MOKE readings [132, 133].

Apart from the Hall resistance, longitudinal magnetoresistance (MR) has also been studied in the (Cr,V):Sb_2Te_3 and Cr:Sb_2Te_3 films. A signature effect found in MR results of many TI materials is the weak-antilocalisation (WAL) [140]. WAL can be observed in a system with strong spin-orbit coupling, as destructive interference is es-

tablished between two back-scattering channels when conduction carriers encounter a non-magnetic impurity, resulting in a minimum resistance at zero magnetic field [141]. WAL has been observed and investigated in various TI thin films [137, 142, 143, 144]. The exact origin of WAL in TIs is not completely clear, but many research groups have attributed this effect to spin-momentum-locked Dirac fermions in the topological surface states [142, 143]. Quantitative analysis can be conducted on WAL to further investigate this relationship, using the Hikami-Larkin-Nagaoka (HLN) theory to confirm the phase coherence length and type of localisation [144, 145].

The results MR (R_{xx}) measurements of the (Cr,V):Sb_2Te_3 and Cr:Sb_2Te_3 films at various temperatures are summarised in Figure 5.6. Figures 5(a-c) show the MR results of the of the co-doped (Cr,V):Sb_2Te_3 sample, and 5(d-f) show the results of the single-doped Cr:Sb_2Te_3 film. For presentation purposes, the field-dependent MR ratio $\Delta R_{xx}/R_{xx}$ is defined as $(R_{xx}(B) - R_{xx}(B_{max}))/R_{xx}(B_{max})$. The MR curves of

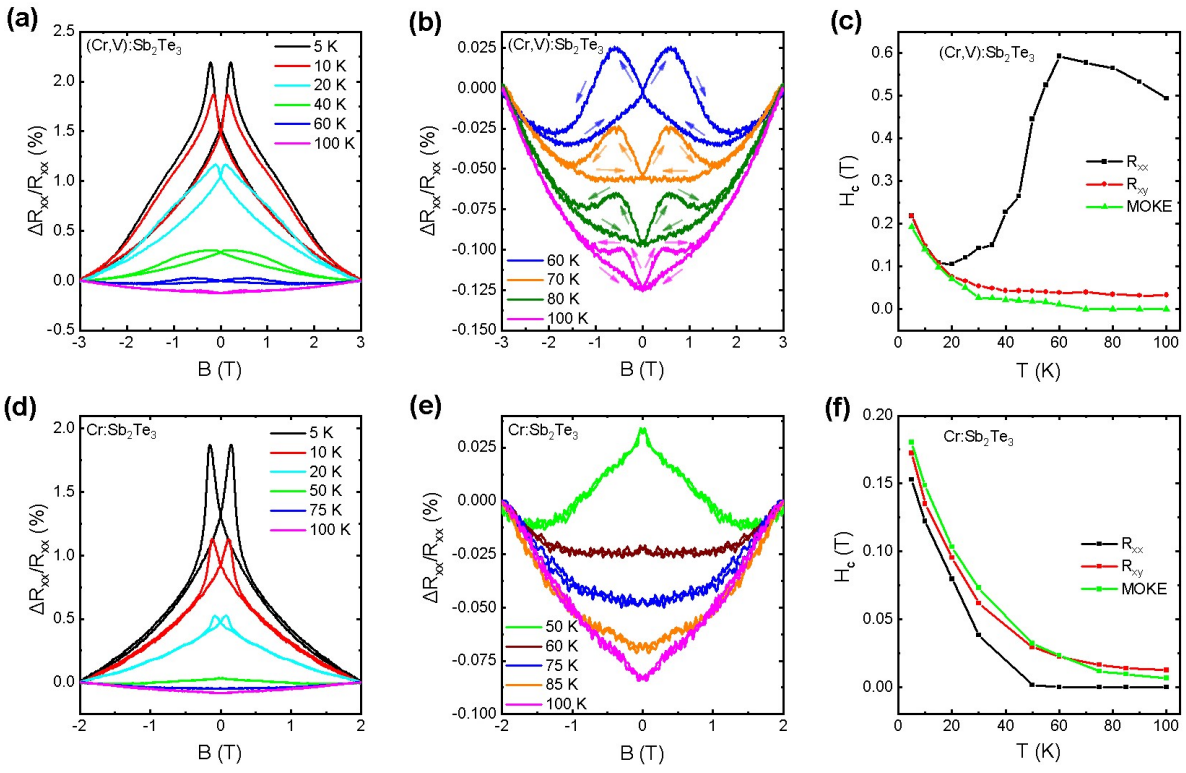

Figure 5.6: (a) Temperature-dependent MR of the (Cr,V):Sb_2Te_3 film from 5 K to 100 K. (b) Close-up of the MR above 60 K, with arrows indicating the direction of the magnetic field sweeps. (c) Comparison between the magnetic fields obtained from the resistance peaks in the MR measurements (R_{xx}), and the coercive fields obtained from MOKE and R_{xy}. (d,e,f) Corresponding results for the Cr:Sb_2Te_3 film.

(Cr,V):Sb_2Te_3 demonstrate the anisotropic magnetoresistance (AMR) below 60 K, shown in Figure 5.6(a), where the resistance reaches its maximum value during magnetisation reversal. Surprisingly, in the co-doped film above 70 K, the AMR feature still persists with flattened peaks, and a dip emerges in the resistance curve at zero magnetic field, hinting towards the presence WAL, as is shown in Figure 5.6(b). Above 70 K, the AMR effect is reduced with increasing temperature, and the dip feature becomes progressively dominant in the MR curve. This unusual response may arise from a joint effect of WAL from the Sb_2Te_3 phase and AMR from the Cr_2Te_3 phase — the latter being a ferromagnetic compound with a Curie temperature of over 100 K [139]. These results are consistent with the presence of the Cr_2Te_3 phase in the XRD spectrum of the co-doped sample. Figure 5.6(c) shows the difference of H_c extracted from R_{xx}, R_{xy} and the MOKE measurements. From 20 K to 60 K, the distance of the MR peaks corresponding to the coercive field for (Cr,V):Sb_2Te_3 (low T_C) show an increment. This is due to the gradual overshadowing of the Cr_2Te_3 (high T_C) ferromagnetic phase. On the contrary, the single-doped sample shows a clear transition from AMR to the dip feature above 50 K with matching coercivities among R_{xx}, R_{xy} and MOKE, as shown in Figure 5.6(d,e,f). This further proves that the inconsistency between the coercivity results in (Cr,V):Sb_2Te_3 come from the ferromagnetic Cr_2Te_3 secondary phase, which is not presented in the single-doped film. The arise of possible WAL at high temperatures has also been observed in $Cr_xBi_{1-x}Se_3$ (x = 0.13 and 0.23) films [146]. In that case there was no ferromagnetic order in the samples, and the MR curve experienced a transition from weak localisation (WL) to WAL following a temperature increase.

In summary, the MOKE probe has been utilised to carry out a simultaneous study of magneto-transport and magneto-optic effects on Cr:Sb_2Te_3 and co-doped (Cr,V):Sb_2Te_3 MTI thin films. Both materials show long-range ferromagnetic order at low temperature with the magnetic easy axis pointing out-of-plane. The consistency of the results obtained using the two measurement schemes is demonstrated for these MTI samples, with both the coercivity (H_c) and magnetisation (M_r) matching well. The appearance of a secondary Cr_2Te_3 phase in the co-doped sample is echoed by an unexpected MR response, as the coexistence of the two phases resulted in a combination of AMR and WAL effects above 70 K. The comparison of coercivities among the MOKE, R_{xx}, and R_{xy} results further confirms the presence of a secondary ferromagnetic phase. This study highlights the advantages of employing both magneto-optic and magneto-transport techniques to study MTI systems, providing a pathway to understand exotic topological materials for energy-dissipationless spintronic applications.

5.3 EuS/Bi_2Se_3 Heterostructures

In this section the interface-induced ferromagnetism is studied using the MOKE probe in a ferromagnetic insulator (FMI) / TI heterostructure, that is, EuS/Bi_2Se_3 thin film. This project came from collaboration with Ms. Ankita Anirban (SP Group), and the films were grown by Professor Jagadeesh Moodera at MIT (USA). On a TI surface, the TRS can be broken by magnetic doping into the bulk TI, or by proximity coupling to an adjacent magnetic material. Compared to magnetic doping, proximity coupling may have the advantages of inducing spatially uniform long-range ferromagnetic order, and avoiding scattering of surface electrons by impurities [147]. In 2013 researchers discovered the breaking of TRS in EuS/Bi_2Se_3 bilayer system [128, 147], where a canted magnetic moment with component perpendicular to the interface could be observed. On the other hand, an EuS thin film alone is a ferromagnetic insulator with only in-plane magnetic anisotropy, and its Curie temperature is about 16.6 K [148]. In 2016, Lee *et al* directly probed the magnetisation at the EuS/Bi_2Se_3 interface using second-harmonic generation (SHG) Faraday rotation technique [149], and Katmis *et al* successfully observed an interfacial ferromagnetic phase up to room temperature in the same material system using polarised neutron scattering [150]. It is clear the EuS/Bi_2Se_3 heterostructure is worth further investigation.

The bilayer film been studied is (from top to bottom) Al_2O_3 (2 nm) cap / EuS (4 nm) / Bi_2Se_3 (6QL) / Al_2O_3(0001) substrate, and the reference sample is Al_2O_3 (4 nm) cap / EuS (4 nm) / Si(001) substrate. Both samples were grown in MIT by MBE co-evaporation in the same way as described in previous publications [147, 149, 150]. The wafer was then cleaved to less than 3 mm $\times$ 3 mm shape, mounted onto the polar MOKE probe and cooled to helium temperature. The magnetic hysteresis loop of different temperatures of the bilayer sample are illustrated in Figure 5.7. The sample was cooled with zero magnetic field, and hysteresis loops were recorded while the out-of-plane magnetic field was swept within ± 4 T. No apparent feature can be observed outside the range of ± 0.5 T. Hysteresis loops can be observed below 15 K with monotonically decreasing magnetisation and coercivity, indicating the film is ferromagnetic with an out-of-plane component and the Curie temperature is approximately 15 K, close to T_c of bare EuS thin film. At 1.6 K the remanance is close to saturation magnetisation, which may imply the magnetic easy axis is out-of-plane. The Kerr angles are in the

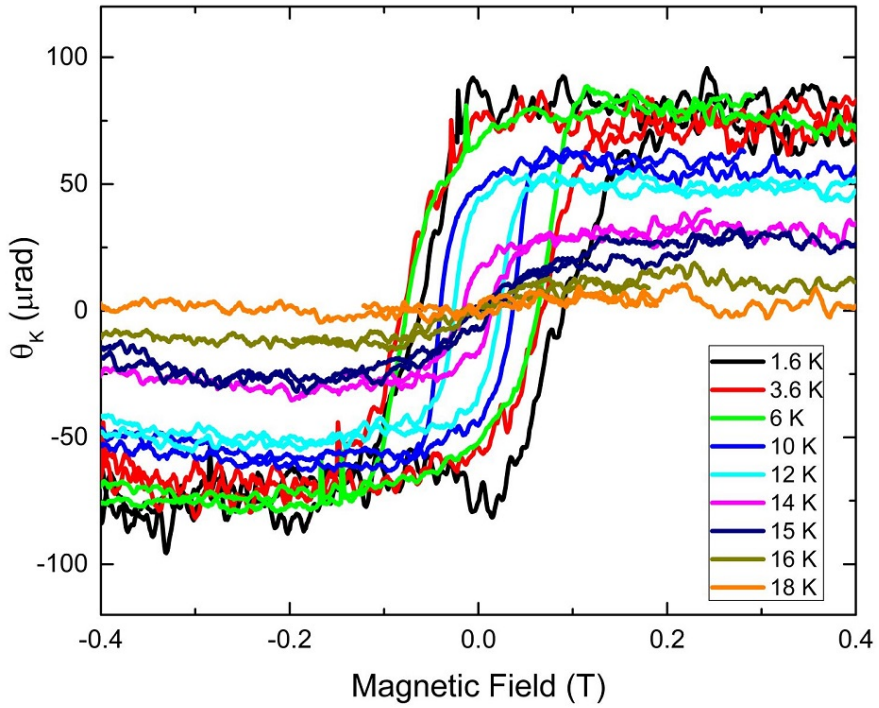

Figure 5.7: Out-of-plane magnetic hysteresis loops of EuS/Bi_2Se_3 bilayer film

same order of magnitude with the previous publication [128], at 100 μrad. To investigate whether field-cooling can have an impact onto the ferromagnetic ordering of this material, the film was also cooled from 130 K to 1.6 K under +6 T applied field, and the same MOKE measurement was conducted between ±0.5 T. No substantial difference can be found between FC and ZFC results (not shown here).

For reference, the same MOKE experiment was carried out on EuS film with ZFC and FC procedures. The ZFC hysteresis loop is shown in Figure 5.8. A small out-of-plane hysteresis loop can be found at 1.6 K, with saturation magnetisation at about 15 K, one order of magnitude smaller than the bilayer film. This small ferromagnetism disappears above 4 K. No significant difference can be found in FC results compared to ZFC.

In summary, low temperature out-of-plane magnetism was measured in EuS/Bi_2Se_3 bilayer and EuS single-layer films using the polar MOKE probe. In the bilayer sample an enhanced perpendicular anisotropy is observed persisting up to 15 K, matching the Curie temperature of EuS alone in which magnetisation commonly lies in plane. This indicates the existence of a canted magnetic moment due to proximity coupling at the interface between EuS and Bi_2Se_3. If time permits, a simultaneous transport and

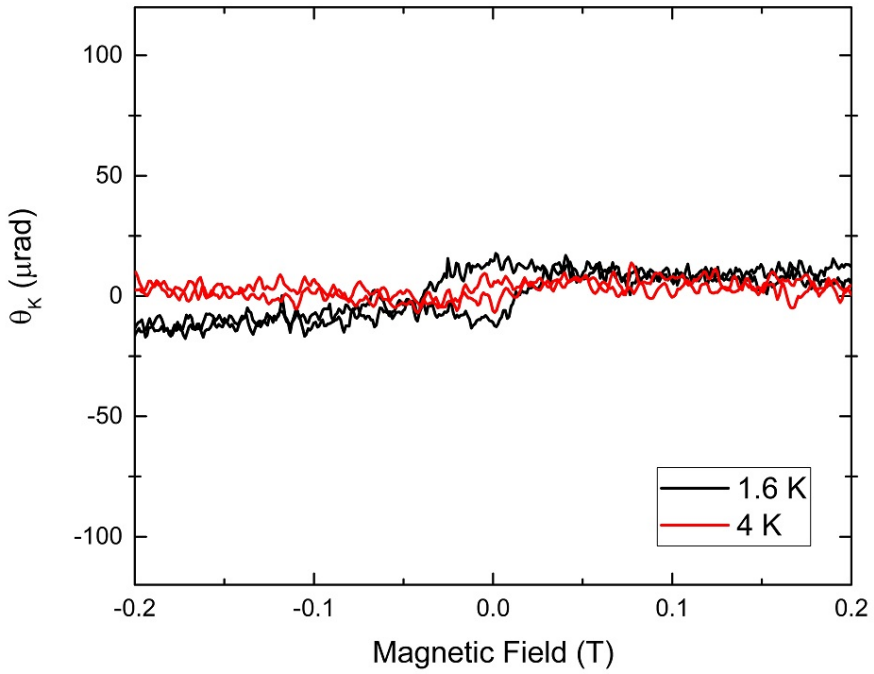

Figure 5.8: Out-of-plane magnetic hysteresis loops of EuS single-layer film

MOKE study will be performed on EuS/Bi_2Se_3 Hall bars after standard photolithography and wet etching, and the comparison of the Kerr signal will help elucidate possible effects of fabrication on the magnetic properties of FMI/TI systems.

CHAPTER 6

TOWARDS PERPENDICULAR SPIN TRANSPORT IN FERROMAGNET / SEMICONDUCTOR HETEROSTRUCTURES

6.1 Background

This section illustrates the efforts toward out-of-plane spin injection and transport in ferromagnet/semiconductor heterostructures [151], aiming to ultilise spin as an extra information carrier in electronic devices. In these heterostructures, spin-polarised electrons will be injected from an ferromagnetic contact (such as Fe) into a semiconductor (such as GaAs), and detected by a second ferromagnetic contact at the opposite end of the device. There are a few criteria to be met for a successful experimental realisation of this spin transport scheme. Firstly, the spins should have a long lifetime and therefore a long drift length before decoherence in the host material under an applied electric field, allowing for extended separation between the two magnetic contacts, for the convenience of the optically mapping the spin drift and manipulating spin orientation through gating. Secondly, the conductivity mismatch between the magnetic contacts and the host material must be small to provide a good spin injection efficiency [152]. Thirdly, the interface between the magnetic contacts and the host material should be smooth to reduce spin scattering. These criteria bring GaAs under the spotlight as the potential host material for the spin transport devices. In GaAs the spin lifetime can reach up to 200 ns at a doping concentration of 1×10^{-15} - 5×10^{-16} cm^{-3} at low temperatures [153, 154]. The lattice mismatch between the body-centred-cubic Fe(100) and the zinc-blende GaAs(100) is only 1%, providing the possibility to engineer Fe/GaAs

heterostructures with smooth interfaces. GaAs can also be heavily n-doped to reduce the conductivity mismatch with Fe and to increase the efficiency of spin injection.

In 2005, Crooker *et al.* demonstrated the optical imaging of spin drift in Fe/GaAs heterostructures using low temperature polar MOKE [14], with the results shown in Figure 6.1. A spin drift of up to 40 μm was detected at 4 K. Due to the anisotropy of the Fe contacts, the injected spins in GaAs lied in-plane with the sample, so a small transverse magnetic field of 3.6 G was applied to precess the spins to the out-of-plane direction (i.e. Hanle effect) for the magneto-optical imaging. The heterostructures were grown by MBE on semi-insulating GaAs(001) substrates. A 300-nm buffer layer of undoped GaAs was first deposited, followed by 2000 nm of lightly Si-doped n-GaAs ($n = 2 \times 10^{16}$ cm^{-3}). The doping was then gradually increased from $n = 2 \times 10^{16}$ cm^{-3} to $n = 5 \times 10^{18}$ cm^{-3} over the next 15 nm, followed by a 15 nm layer of $n = 5 \times 10^{18}$ cm^{-3}. Finally 5 nm of Fe was deposited at 0 °C to reduce the interfacial roughness with

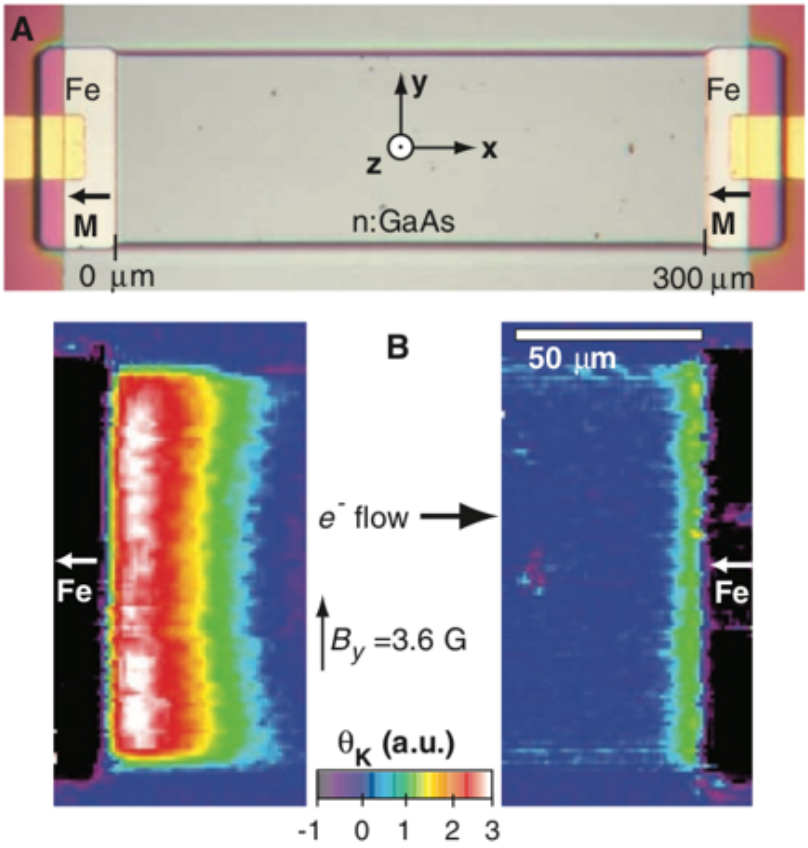

Figure 6.1: Top: microscopy photograph showing the Fe/GaAs device. Bottom: Spin transport in the Fe/GaAs heterostructure imaged by polar MOKE at 4 K. Figure adapted from ref.[14].

the GaAs layer, followed by a 2 nm cap of Al to prevent the sample from oxidation and air contamination. The presence of the light-doped GaAs layer ensures a long spin drift length while the heavy-doped layer helps to reduce the conductivity mismatch with Fe.

Professor Christian H. Back's group at the University of Regensburg further developed the Fe/GaAs heterostructure and successfully obtained a cross-sectional image of spin transport in GaAs in 2007 [15]. The results are shown in Figure 6.2. They scanned a cleaved edge of a FeCo/GaAs device at 10 K under a polar MOKE microscope so that the orientation of the spins is parallel to the laser beam. This GaAs has an identical doping profile to the work in 2005, except that here the light-doped layer has a thickness of 4 μm instead of 2 μm for the convenience of optical probing.

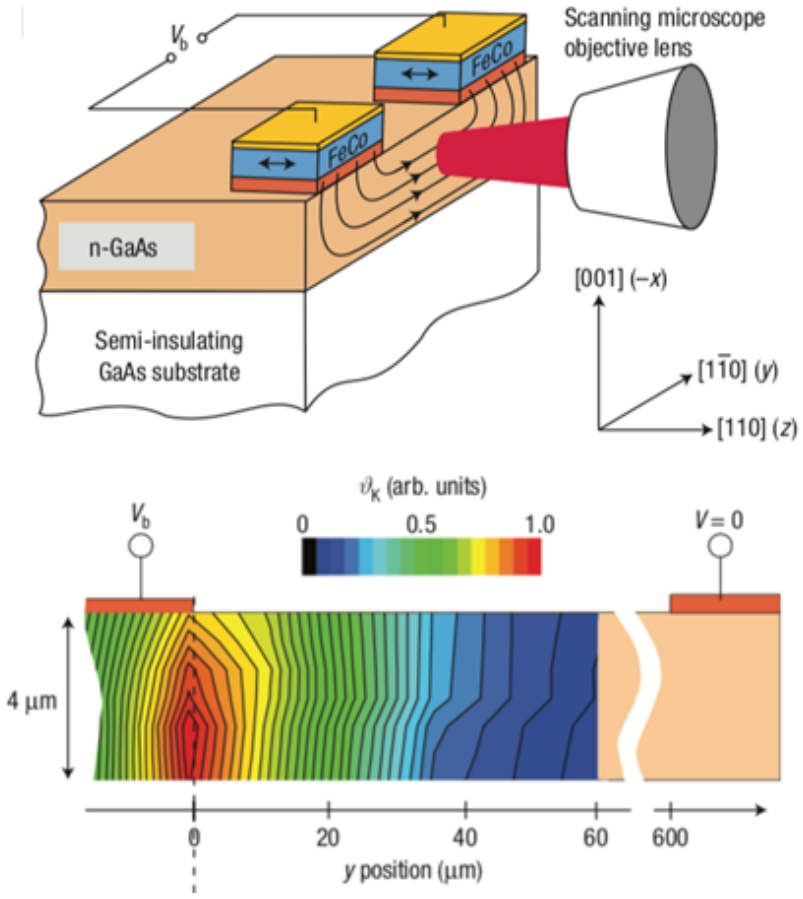

Figure 6.2: Top: Schematic graph showing the FeCo/GaAs device and the MOKE microscope objective. Bottom: Cross-sectional spin drift image in the Fe/GaAs heterostructure by polar MOKE at 10 K. Figure adapted from ref.[15].

Despite the demonstrations of the spin drift in Fe/GaAs, there are not many reports about the optical imaging of spin transport in ferromagnet/semiconductor heterostructures with the spin align perpendicular to the film plane. Perpendicular spin injection is often detected using polarised electroluminescence from GaAs or InGaAs quantum wells, with various our-of-plane ferromagnetic structures on top as the injection source, such as $[Tb/Fe]_n$, FePt/MgO and δ-MnGa [155, 156, 157]. Other perpendicular spin injection experiments are measured by electrical means on three-terminal multilayer devices, for example, Fe_3O_4/MgO/GaAs and TbFeCo/CoFeB/MgO/GaAs [158, 159]. It should be noted that out-of-plane magnetisation systems have strong potential in applications such as magnetic storage and magnetic tunnel junctions [160]. Recently, Ohsugi *et al.* showed promising results of out-of-plane spin transport in $L1_0$-FePt/MgO/GaAs trilayer systems, using a non-local electrical detection scheme and local MOKE probing next to the source contact [161]. The $L1_0$-FePt layer works as the source of perpendicular spins whose property will be discussed in the next section. The MgO tunnel barrier helps align the c-axis of the $L1_0$-FePt crystal perpendicular to the film due to its large lattice constant compared to FePt [162, 163], and acts as a tunnel barrier for spin injection. It is of scientific interest to further explore this trilayer system and attempt two-dimensional mapping of spin transport using the home-made cryogenic MOKE instrument.

6.2 Growth and Characterisation of $L1_0$-FePt Alloy

$L1_0$-FePt is a hard out-of-plane ferromagnetic material with a large perpendicular magneto-crystalline anisotropy between 7 J·cm^{-3} and 80 J·cm^{-3} [164, 165], which has about 0.5 meV anisotropy energy per 3d atom [166]. $L1_0$ is a crystallographic derivative structure of the face-centred-cubic (FCC), as Fe planes and Pt planes are stacked alternately in $L1_0$-FePt, as shown in Figure 6.3. $L1_0$-FePt is commonly grown my magnetron co-sputtering at elevated temperatures (above 400 °C) on a MgO single crystal seed layer or substrate. The 8% lattice mismatch between MgO and FePt creates tensile strain that promotes perpendicular magnetic anisotropy [166].

In order to find out the optimal deposition condition of $L1_0$-FePt, a set of growth trials was performed using magnetron sputtering on MgO(001) substrates, by Dr. Debi Pattnaik at the University of Nottingham. Before loading into the sputter chamber, the MgO(001) single crystal substrate was cut into 10 mm × 10 mm in dimension, and

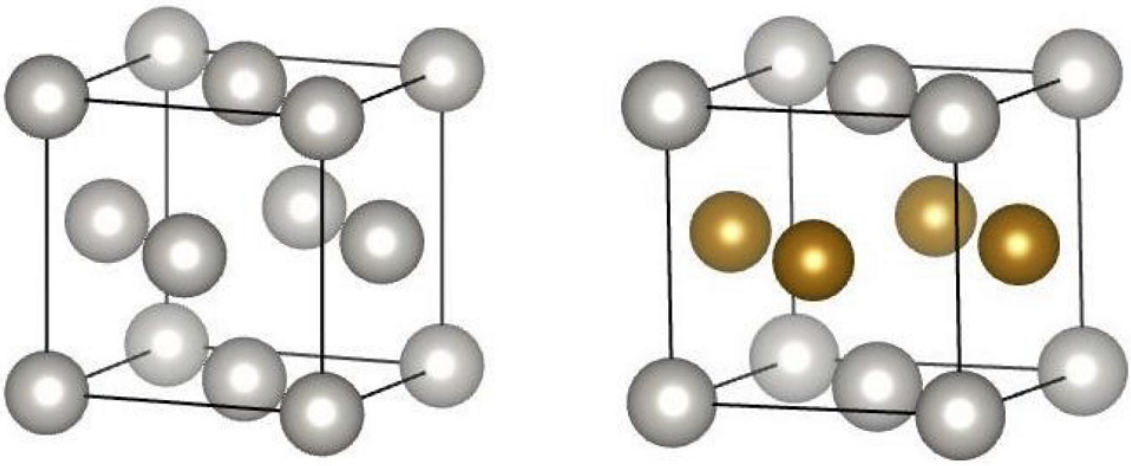

Figure 6.3: Unit cells of FCC (left) and the $L1_0$ phase (right). Different coloured balls represent different atoms. In $L1_0$ phase (001) planes are formed by two different elements which are stacked alternately.

cleaned using isopropanol in an ultrasonic bath for 2 minutes. A heater with a thermocouple is placed a few mm next to the sample holder, with the growth temperatures set to 400 °C, 500 °C, 600 °C and 700 °C. Since the thermocouple is at the hottest part during high temperature growth, and there exists a large temperature gradient between the thermocouple and the holder, the actual wafer temperature might be approximately 100 °C lower than the displayed value. Because of this, the growth temperatures in this thesis are noted as 300 °C, 400 °C, 500 °C, and 600 °C respectively. After loading into the main chamber, the MgO substrate was annealed for two hours at the temperatures mentioned above. Then Pt and Fe were co-sputtered at calibrated equal rates from individual targets whilst temperatures were kept at preset values. After 10 nm of FePt was grown, the sample was cooled back to room temperature, and finally 2 nm Pt was deposited as the capping layer.

The samples were sent to the TFM Group for structural and magnetic characterisations. The out-of-plane magnetisation was measured at room temperature using a Durham Magneto Optics (DMO) NanoMOKE 3 magnetometer equipped with a 632 nm He-Ne laser. The results shown in Figure 6.4. The square-shaped hysteresis loops above 500 °C indicate strong perpendicular anisotropy. These results align well with previous publications [164, 167, 168]. Out-of-plane X-ray diffraction (XRD) was applied to analyse the crystal structure of this film, and the spectrum is shown in Figure 6.5. Clear peaks of $L1_0$-FePt(001) and $L1_0$-FePt (002) confirm the presence of the $L1_0$ order.

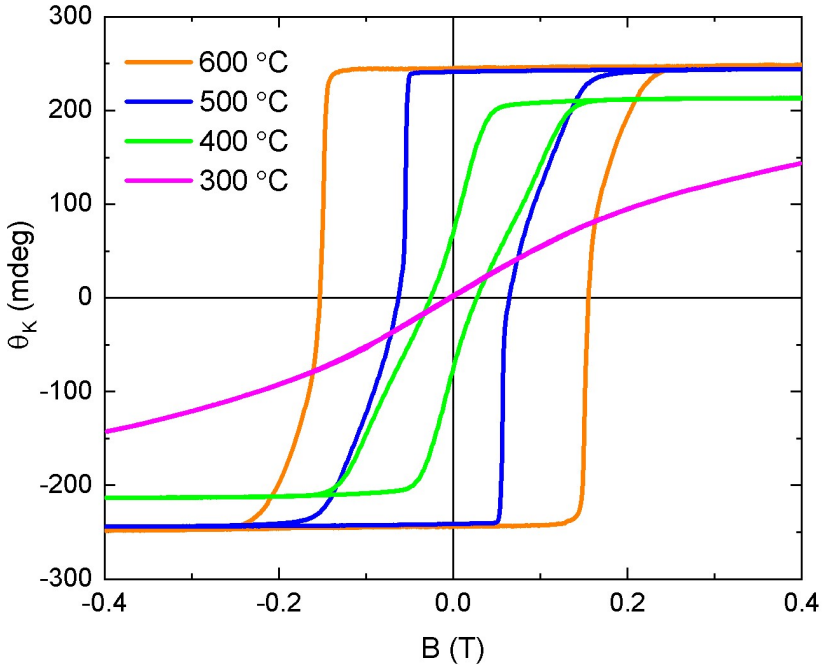

Figure 6.4: Room-temperature polar MOKE hysteresis loops of $L1_0$-FePt/MgO(001) films grown at different temperatures.

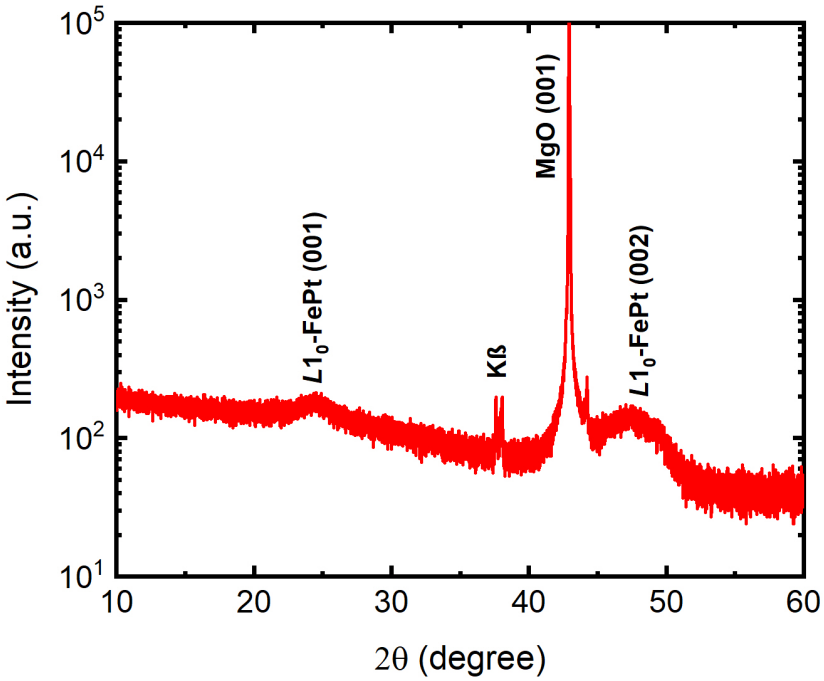

Figure 6.5: XRD spectrum of the $L1_0$FePt/MgO film grown at 500°C. Clear peaks of $L1_0$-FePt (001) and $L1_0$-FePt (002) confirm the presence of $L1_0$ order.

In summary, the optimal growth condition of the $L1_0$-FePt films has been found by magnetron co-sputtering at different temperatures. The presence of out-of-plane anisotropy is confirmed by room temperature MOKE measurements and the $L1_0$ phase is confirmed by XRD. This mini project paves way for the integration of $L1_0$-FePt into GaAs spin transport systems.

6.3 Growth and Characterisation of FePt/MgO/GaAs Structures

A GaAs (001) single crystal substrate was grown using MBE co-deposition by Dr. Harvey Beere in the V-Chamber of the Cavendish SP Group. The doping profile was identical to the work published by Crooker *et al.* [14], that is, a 2 μm thick n-doping (2×10^{16} cm^{-3}), then 15 nm of increased doping from 2×10^{16} cm^{-3} to 5×10^{18} cm^{-3} (marked as n^+), followed by 15 nm of n^+-doping. Finally, a few nm of amorphous arsenic was deposited to protect the film from air contamination. The substrate was then transferred through air into the M-Chamber of the TFM Group, where Dr. Peter Newton took charge of the MgO deposition with a single MgO source at room temperature. The arsenic cap was removed by evaporation at 500 °C in the preparation chamber, and then the sample was transferred to the main chamber without breaking the vacuum for the growth of MgO. No RHEED pattern was observed during the growth. After 2 nm of MgO was deposited at room temperature, the film was taken out from the chamber and immediately put into a vacuum desiccator, which was quickly pumped down to less than 10 mbar. One month later, the MgO/GaAs(001) film was taken out from the desiccator and immediately transferred into the sputter chamber at Nottingham, where Dr. Debi Pattnaik deposited 10 nm of $L1_0$-FePt at 500 °C. This moderate temperature was chosen because it was high enough to promote the $L1_0$ phase forming between Fe and Pt, while a higher temperature may induce interface mixing between MgO and GaAs [168]. Finally this trilayer film was capped with aluminium and shipped back to Cambridge for structural and magnetic characterisations.

Figure 6.6 shows the perpendicular hysteresis of the $L1_0$-FePt/MgO/GaAs film examined by NanoMOKE 3 at room temperature, in comparison to the 500 °C $L1_0$-FePt film described in the previous section. The Kerr angle of the trilayer sample is smaller than the reference sample by a order of magnitude, suggesting that only a small proportion of the Fe atoms are contributing to the ferromagnetism. The remanence of

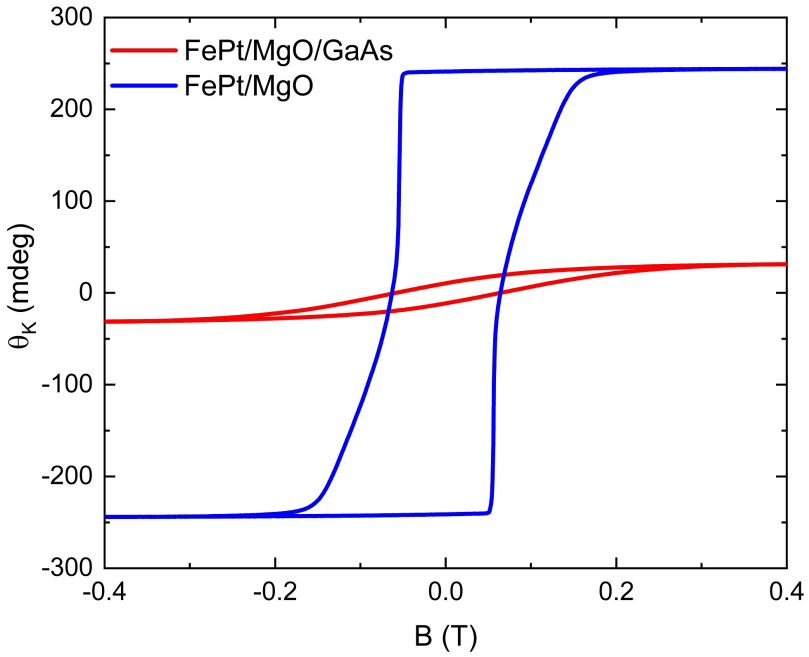

Figure 6.6: Out-of-plane hysteresis loops of the $L1_0$-FePt/MgO/GaAs and $L1_0$-FePt/MgO films at room temperature.

the trilayer sample at 0 field is less than half of its saturation at high field, indicating its magnetic easy axis is not perpendicular to the film plane. To find out the reason of this unexpected magnetic response, transmission electron microscopy (TEM) was employed to image the lattice and atomic arrangements at a cross section of the FePt/MgO/GaAs(001) film. The TEM specimen was prepared by Mr. Eric Tapley and the microscope was operated by Dr. Richard Langford of the Cavendish Lab. Figure 6.7 shows TEM images taken from various areas of the multilayer specimen. A well-ordered single crystal structure can be found in GaAs. However, the 2-nm MgO layer is mostly polycrystalline, with only a small part showing a single crystal phase. Finally, a mixture of different crystallographic orientations is observed in FePt. The absence of an perpendicular *c*-axis may explain the reduced out-of-plane anisotropy shown in the MOKE measurement. Both FePt/MgO and MgO/GaAs interfaces have a roughness of about 1 nm. By contrast, MgO deposited by Ohsugi et al. was in a single crystal phase and smooth interfaces were found at both FePt/MgO and MgO/GaAs [169]. It is highly possible that the interface roughness prevented FePt from forming an ordered $L1_0$ structure. Considering that a high temperature (> 300 °C) for MgO deposition is a standard recipe in MgO/GaAs(001) spin injection systems [170, 171], one reason that may explain the failure here to obtain a high-quality MgO tunnel barrier is that, the room-temperture growth in the M-Chamber reduces the mobility of atoms and de-

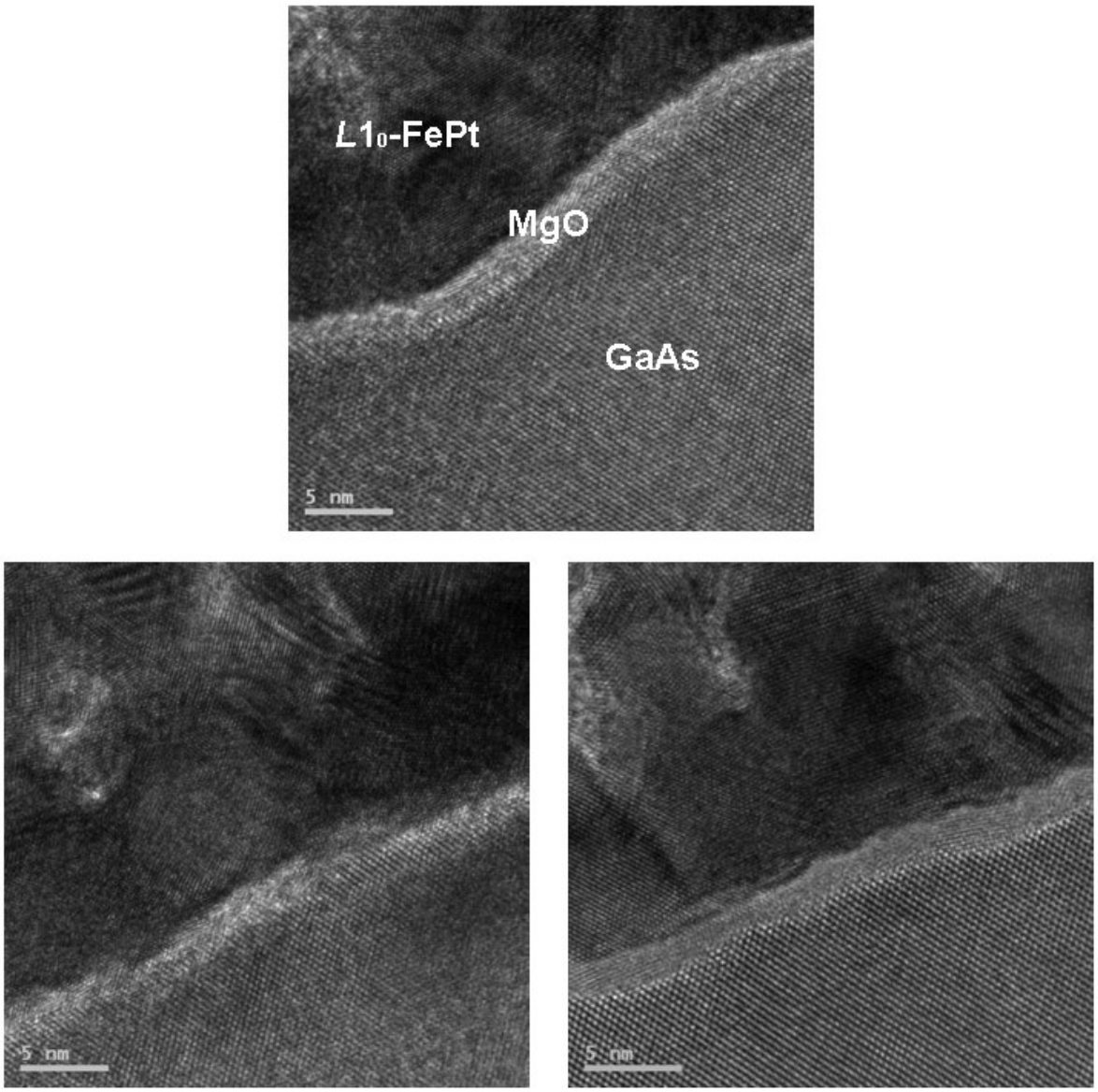

Figure 6.7: Cross-sectional TEM images of the $L1_0$-FePt/MgO/GaAs structure.

creases the chance to form an atomically flat interface.

In summary, attempts were made towards the realisation of out-of-plane spin transport devices in $L1_0$-FePt/MgO/GaAs trilayer structures. The thin film was grown using a three-step process including both MBE and magnetron sputtering. Ferromagnetic ordering was found in the film but the magnetic easy axis was not perfectly out-of-plane, and the total magnetisation was only 10 % compared to an ordered $L1_0$-FePt superlattice. TEM revealed that the MgO tunnel barrier is polycrystalline with 1 nm of interface roughness on both sides. It is highly possible that the growth parameters

of the MBE chamber was not optimised for the deposition of single-crystalline MgO. It is noted that, up to now there are only very few groups that have succeed in the magneto-optical imaging of spin transport in semiconductors [14, 15, 161]. In order to carry out a project of this kind, researchers are advised to use an MBE cluster system with UHV inter-connections, where each chamber is optimised for the growth of the respective materials.

6.4 Growth and Characterisation of $[Co/Pt]_n$/GaAs Sturctures

Apart from $L1_0$-FePt, $[Co/Pt]_n$ and $[CoFeB/Pt]_n$ multilayer structures also tend to exhibit strong out-of-plane magnetisation due to interface anisotropy and RKKY coupling between neighbouring layers [86, 87, 172, 173]. It is therefore obvious to try growing $[Co/Pt]_n$ or $[CoFeB/Pt]_n$ on top of GaAs(001) for spin injection into semiconductors. Several attempts were undertaken by the author of this thesis on such multilayer systems, and the results indicated that it is difficult to exhibit perpendicular anisotropy in $[CoFeB/Pt]_n$/GaAs(001) without a Ta seed layer. This seed layer introduces 2 more interfaces into this system and can severely reduce the spin injection efficiency into GaAs due to interface scattering. In light of this, this section mainly discusses the results obtained from $[Co/Pt]_n$/GaAs systems. Since the Co layer (0.5 nm) is thinner than the Pt layer (1.0 nm), it is more ideal to put Co adjacent to GaAs instead of Pt, in order to increase the spin injection efficiency from the Co/Pt interface.

The $[Co/Pt]_n$/GaAs multilayer films were grown using magnetron sputtering at room temperature with a base pressure of 6.0×10^{-8} mbar. GaAs(001) and GaAs(111) substrates were first ultra-sonicated in Semicoclean (semiconductor cleaning solution) for 12 minutes to remove oxide and other surface contaminations, and then ultra-sonicated in DI water for 3 minutes. Afterwards the substrates were quickly transferred under continuous dry N_2 blow into a magnetron sputtering chamber. At this moment two preparation approaches were employed: one with 15 s Ar ion milling to further clean the GaAs surface, and one without. It should be noted that there was no annealing process following the ion milling since the sputter chamber was not equipped with a heater. Alternating Co and Pt layers were deposited onto GaAs substrates from individual sputtering targets at room temperature. The chamber pressure during growth was kept at 7.1×10^{-3} mbar. After capping with 4 nm of Pt, the multilayer films were

taken out from the chamber, and their magnetisations were verified using NanoMOKE 3 at room temperature. It turns out that the grown films without ion milling exhibit no sign of perpendicular anisotropy. It is possible that oxidation on GaAs formed during transfer prevents proper seeding of $[Co/Pt]_n$. As a result, the rest of this section focuses on Ar^+-cleaned $[Co/Pt]_n$ films. The layout (top to bottom) of the six samples are listed as follows:
S1 and S2, Pt(4) / Co(0.5) / Pt(1) / Co(0.7) / GaAs (unit: nm);
S3 and S4, Pt(4) / Co(0.5) / Pt(1) / Co(0.5) / Pt(0.5) / GaAs;
S5 and S6, Pt(4) / Co(0.5) / Pt(1) / Co(0.5) / Pt(0.7) / GaAs.
S1, S3 and S5 are on GaAs(001) substrates, and S2, S4 and S6 are on GaAs(111) substrates.

The out-of-plane magnetisation of these films are shown in Figure 6.8. Samples S1 - S4 exhibit a paramagnetic response, while samples S5 and S6 display strong ferromagnetism with a magnetic easy axis perpendicular to the film plane. The $M - H$ curve between each pair of films [GaAs(001) and GaAs(111)] are almost identical, in-

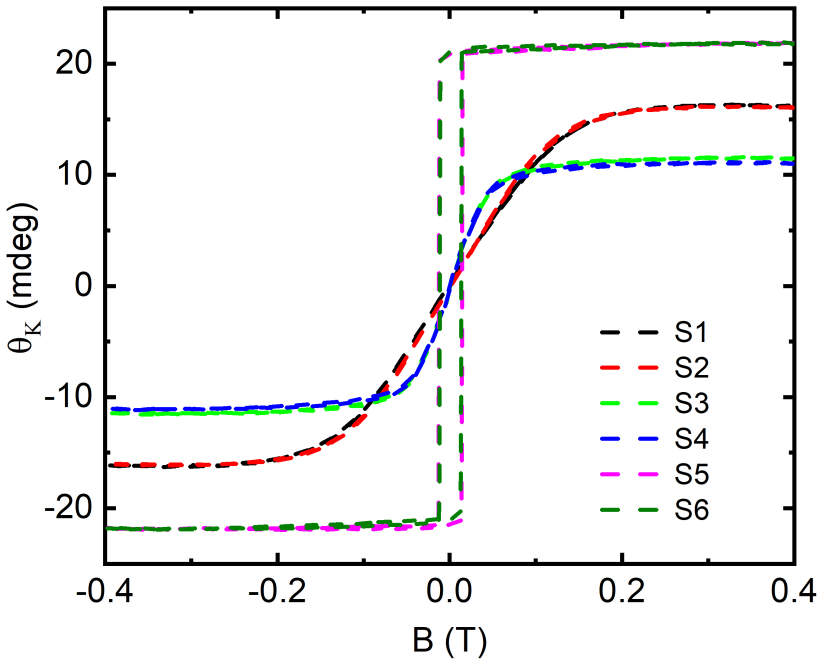

Figure 6.8: Out-of-plane hysteresis loops of the $[Co/Pt]_n$/GaAs multilayer films at room temperature.
S1 & S2: Pt(4)/Co(0.5)/Pt(1)/Co(0.7)/GaAs(001&111);
S3 & S4: Pt(4)/Co(0.5)/Pt(1)/Co(0.5)/Pt(0.5)/GaAs(001&111);
S5 & S6: Pt(4)/Co(0.5)/Pt(1)/Co(0.5)/Pt(0.7)/GaAs(001&111).
Thicknesses in nm.

dicating that the crystal orientation of the substrate has almost no influence on the magnetisation of the $[Co/Pt]_n$ multilayer. This implies that Co and Pt are not epitaxially grown on GaAs, and that the interface may be rough which can significantly reduce the efficiency of spin injection. S1 and S2 reveal that Co is not suitable to be the seed layer. The comparison between S3/4 and S5/6 shows that a Pt seed layer of over 0.5 nm is required to establish an out-of-plane ferromagnetic order, further proving that the Pt/GaAs interface is not very smooth. Considering all the factors listed above, it does not seem very promising to pursue perpendicular spin transport in these $[Co/Pt]_n$/GaAs films, and therefore this project was not proceeded any further.

6.5 Non-monotonic After-effect Measurements in Pt/Co/Ir/Co/Pt Perpendicular Synthetic Ferrimagnets

This section focuses on out-of-plane magnetised synthetic ferrimagnets with two antiferromagnetially coupled single layers. Many material combinations have been grown to realise an interlayer-spaced antiferromagnetic coupling between two ferromagnetic layers, such as $[Pt/Co]_n$/Ru/$[Co/Pt]_n$ [174], $[Pd/Co]_n$/Ru/$[Co/Pd]_n$ [175], CoFeB/Ta/CoFeB [176], CoFeB/MgO/CoFeB [177], Heusler-alloy/MnGa [178], and Fe/graphene/Co [179]. Synthetic ferrimagnets have potential applications in magnetic tunnel junctions and racetrack memories based on domain wall motion [180, 181, 182]. However, the magnetisation dynamics of the coupled ferromagnetic layers has not been heavily investigated. This section describes an unexpected non-monotonic magnetic relaxation in Pt/Co/Ir/Co/Pt multilayer systems. This project was lead by Mr. Thibaud Fache from The University of Lorraine (Nancy, France). The author of this thesis conducted the low temperature MOKE measurements and contributed to the paper writing. Most of this work is published in ref.[183].

The sample investigated under the low temperature MOKE microscope has the following structure (bottom to top): Si(001) substrate / Ta(3) / Pt(3) / Co(0.95) / Ir(1.4)/ Co(1) / Pt(3) (unit: nm). This multilayer film was deposited using magnetron sputtering at room temperature in Nancy. The thickness of the Ir spacer layer (1.4 nm) was calibrated to induce antiferromangetic coupling between the two Co layers, while maintaining smoothness of its upper and lower interfaces [184]. This sample has four possi-

ble magnetic states, namely P^+ (both Co layers pointing up), P^- (both layers pointing down), AP^+ (two layers couple antiferromangetically with a net magnetisation pointing up), and AP^- (reverse case of AP^+). By temperature-dependent measurements in the low temperature MOKE probe, a critical temperature of 232 K was found, when the two following switching fields matched closely: one is AP^+ to P^- during downsweep, the other being P^- to AP^- during upsweep. The hysteresis loop at 232 K is shown in Figure 6.9.

In the next experiment at 232 K, the magnetic field was first set to positive saturation at 10 kOe, then slowly decreased to -830 Oe, i.e. a value between the switching field of AP^+ to P^- during downsweep (-870 Oe), and P^- to AP^- during upsweep (-780 Oe). The magnetic field was held at -830 Oe and time evolution measurement of the magnetisation was performed. The result is shown in Figure 6.10, which displays a non-monotonic relaxation curve. The magnetic state remained at AP^+ for 40 seconds, then quickly dropped towards P^-. While approaching P^- the decrease slowed down

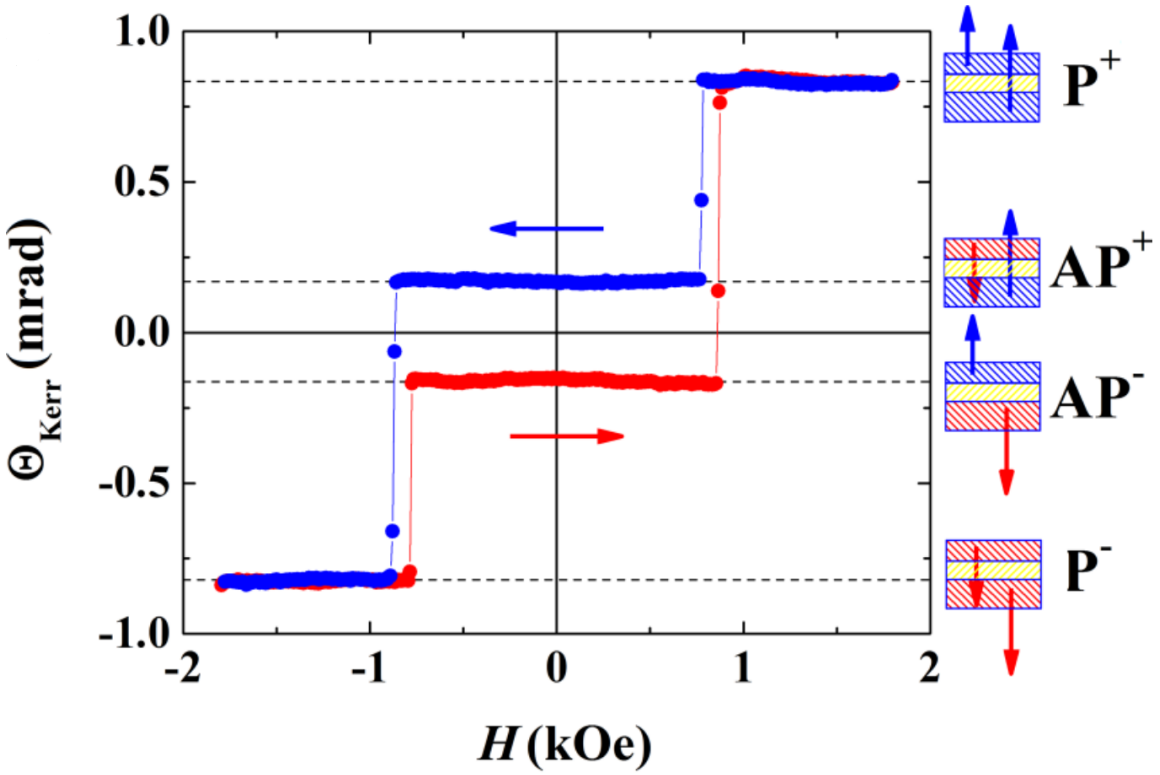

Figure 6.9: Hysteresis loop of the Pt(3) / Co(0.95) / Ir(1.4)/ Co(1) / Pt(3) (unit: nm) film at 232 K. The two following switching fields matches closely: one is AP^+ to P^- during downsweep (blue curve), the other being P^- to AP^- during upsweep (red curve).

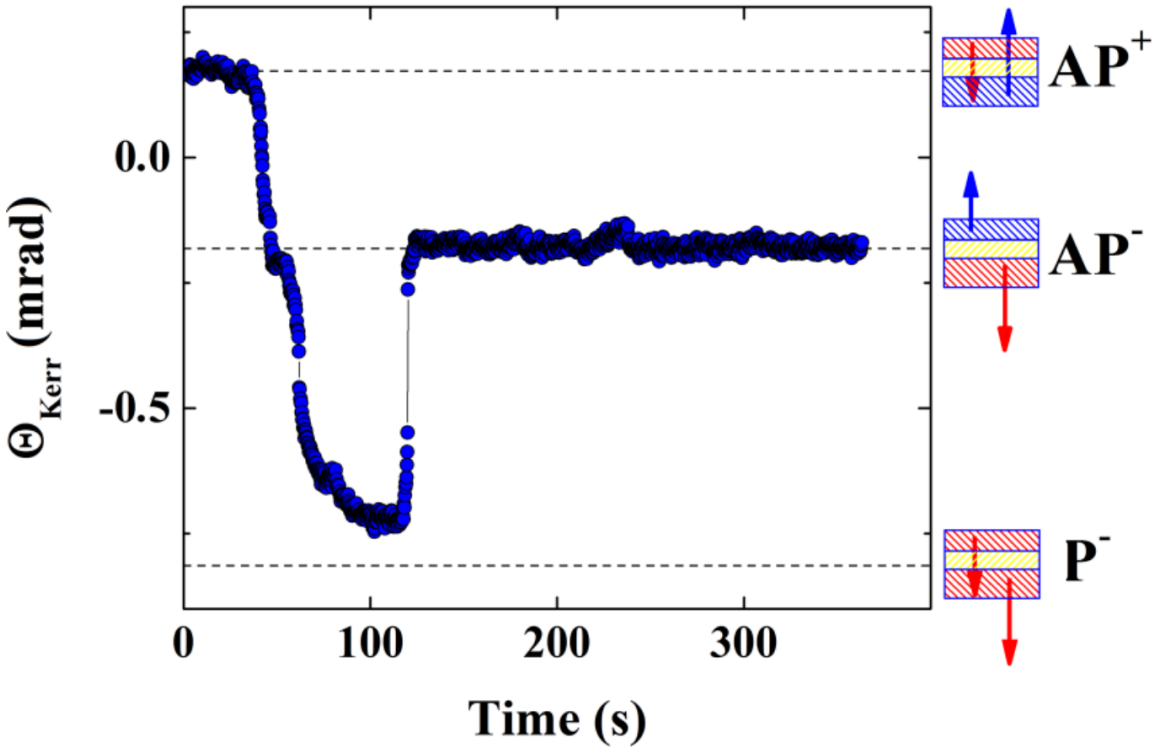

Figure 6.10: Local magnetic relaxation curve of the Pt(3) / Co(0.95) / Ir(1.4)/ Co(1) / Pt(3) (unit: nm) film at 232 K, under an applied field of -870 Oe.

and remained at a metastable state for 20 seconds, which is slightly higher than P^- in the figure. Finally, the magnetic state swiftly jumped back to AP^- within a few seconds, and stayed there for the rest of measurement (a few hours). This relaxation curve was also observed at other locations of the sample but with different time delays and slightly different shapes, which were later found to be related to the respective distances to the nucleation points and the propagation speed of the domain walls.

It should be noted that the low temperature MOKE probe only measures an area of 10 μm^2 and therefore it only reveals the magnetisation evolution at a local scale. SQUID measurements on two other Pt/Co/Ir/Co/Pt samples, which are Si(001) substrate / Ta(3) / Pt(3) / Co(0.7) / Ir(1.4)/ Co(1) / Pt(3) and Si(001) substrate / Ta(3) / Pt(3.2) / Co(1) / Ir(1.4)/ Co(0.9) / Pt(3), disclosed magnetic evolutions in the magnetisation curve, indicating the same non-monotonic spin relaxation happens not only at a local scale but through the whole wafer. The last sample showed a similar hysteresis loop at room temperature and therefore its magnetic domain movement was examined using a commercial room-temperature MOKE projection microscope (Evico Magnetics).

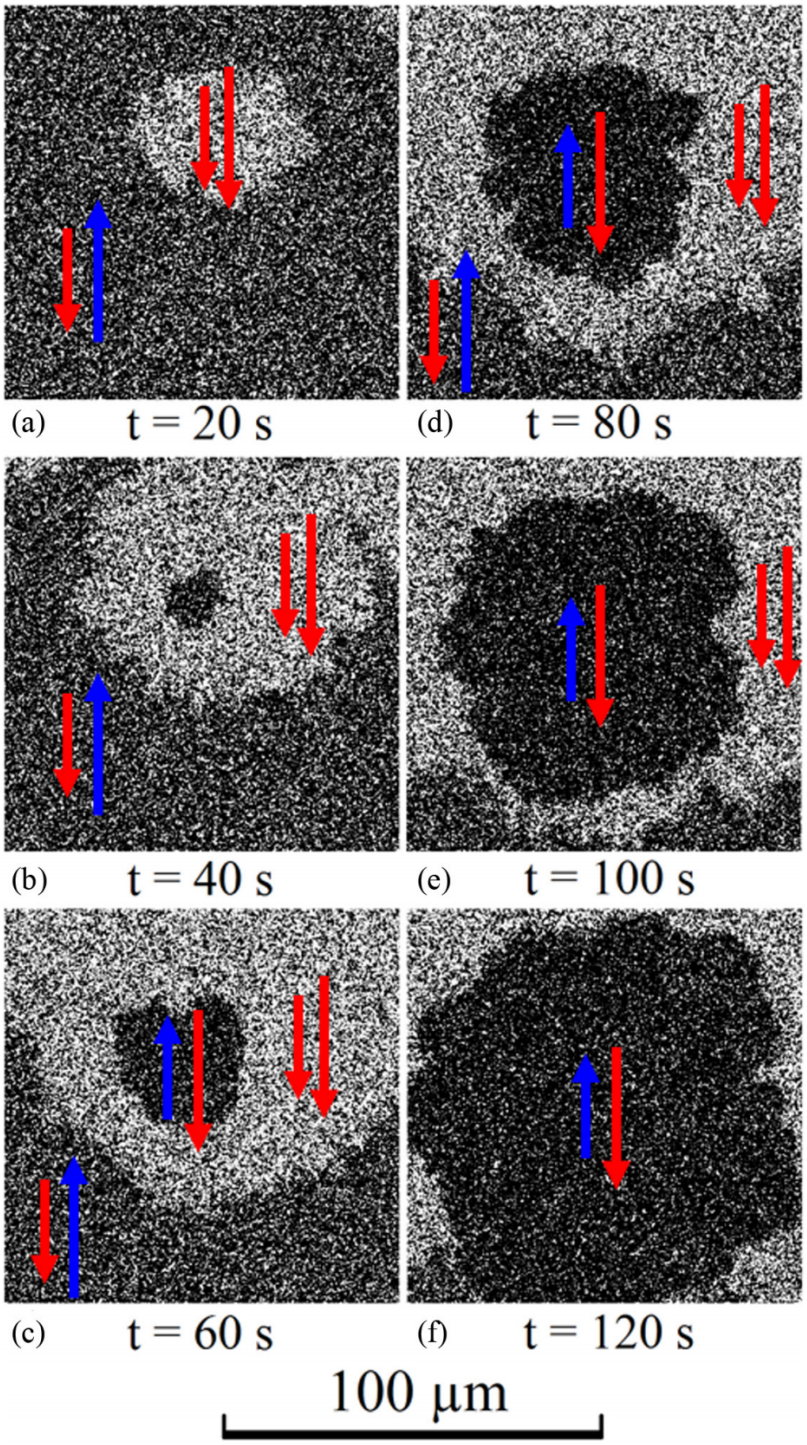

Figure 6.11: Domain wall movements in the Pt(3.2) / Co(1) / Ir(1.4) / Co(9) / Pt(3) multilayer film at room temperature with an applied field of -600 Oe. Photographs taken with a time interval of 20 seconds. The light, mid and dark grey colours represent P^- $\downarrow\downarrow$, AP^+ $\downarrow\uparrow$ and AP^- $\uparrow\downarrow$ domains, respectively. The greyscale contrast may not be very clear on the printed version of this thesis.

The movement of magnetic domains were recorded when the magnetic field was fixed between AP^+-P^- and P^--AP^-, shown in Figure 6.11. These images were taken 20 seconds apart and clearly show a two-step process: while the initial state was almost entirely AP^+ (mid grey $\downarrow\uparrow$), nucleation happened and a P^- domain (light grey $\downarrow\downarrow$) spread slowly. Then the AP^- domain (dark grey, $\uparrow\downarrow$) nucleated from within P^- and gradually spread. After 120 seconds the majority of the view was covered by the AP^- domain.

This non-monotonic magnetisation relaxation can be explained qualitatively by a one-dimensional two-spin model, that is, the two Co layers are regarded as two single marco spins. By taking into account Zeeman energy, exchange coupling and magneto-crystalline anisotropy, it is found that the system needs to go through a higher energy barrier for an AP^--AP^+ transition, compared to an AP^--P^--AP^+ two-step transition. The modelled relaxation curve of the two-step transition resembles the existing experimental results. This model has general suitability for all antiferromagnetically coupled systems with out-of-plane anisotropy.

In summary, this project reports non-monotonic magnetic relaxation in a perpendicular synthetic ferrimagnetic system using MOKE projection microscopy, SQUID and the low temperature focused MOKE probe. A two-spin model was developed that qualitatively matches the experimental data. As the same relaxation pattern is observed in several samples of different thickness, and the model is suitable for any out-of-plane multi-layer structure with antiferromagnetic coupling, it is possible that this non-monotonic relaxation is a general feature in most antiferromagnetically coupled systems with perpendicular magnetic anisotropy.

CHAPTER 7

LOW ENERGY ELECTRON MICROSCOPY STUDY OF METAL STRUCTURES

This chapter describes the study of Pt nanowires and oxygen-free tungsten surfaces using low energy electron microscopy (LEEM). LEEM is an *in situ* surface analysis technique that observes real-time dynamics of material surface manipulation with nm-scale spatial resolution, during procedures such as heating, cooling, exposure to gas, and material deposition [185, 186]. The initial plan of this project was to grow $L1_0$-FePt films using MBE, and examine the film quality *in situ* using spin-polarised LEEM (a LEEM with extra magnetisation resolution), and *ex situ* using the MOKE probe. $L1_0$-FePt is of strong interest in the surface science community, as the main candidate material for heat-assisted magnetic recording (HAMR) [187, 188]. However, a few difficulties were encountered during this progress, and the project tilted towards Pt nanowire formation and Pt droplet movements on Si substrate. In the meanwhile a new approach was discovered to make oxygen-free W(110) surface at reduced temperatures. These topics are illustrated in the following sections.

7.1 Low Energy Electron Microscopy

LEEM is a surface analysis technique invented by Ernst Bauer in 1962 [189]. Real-time LEEM images are formed by elastically-backscattered low-energy electrons from the surface of a crystalline material. The incident electrons have kinetic energy of only 0 - 50 eV, so the de Brogile wavelength is a few Å, comparable with the atomic spacing in solids. The reflection of low energy electrons is mainly sensitive to the surface of the

material, a consequence of short inelastic electron mean-free-path in solids [190].

The LEEM system used this experiment is a custom-made Specs P90 aberration-

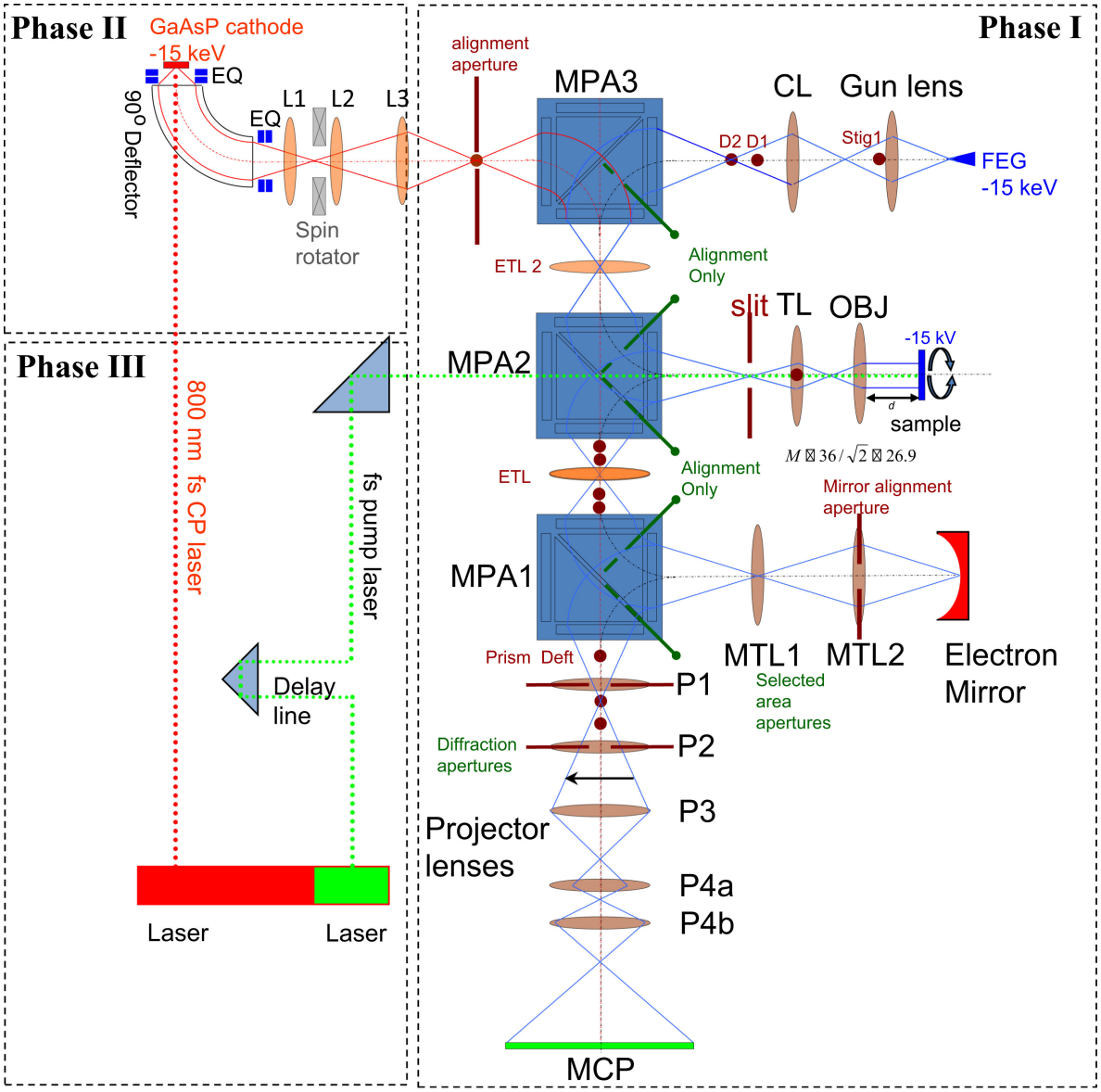

Figure 7.1: Schematic diagram of the AC-LEEM at Chongqing University. Phase I is the current AC-LEEM, Phase II is a spin-polarised electron gun system under development, and Phase III is a femtosecond laser system under development. Abbreviations are listed as follow. FEG: field emission gun, D: deflector, Stig: stigmator, CL: condenser lens, MPA: magnetic prism array, ETL: electrostatic transfer lens, MTL: magnetic transfer lens, TL: transfer lens, P: projector lens. Figure adapted from ref.[16].

corrected (AC) LEEM at Chongqing University, China, with a lateral resolution of 1.8 nm. Detailed design and commissioning of this AC-LEEM have been published elsewhere [16]. The schematic diagram of this AC-LEEM is shown in Figure 7.1. Note that the actual setup used was only in phase I of this figure. High energy electrons of -15 keV are generated at a cold field emission gun (FEG) and deflected by 90° anticlockwise using a magnetic prism array (MPA 3). After another 90° deflection from MPA 2, the beam passes though an objective lens. The sample sits on a cathode with high voltage applied close to FEG, to decelerate the electron beam to less than 50 eV before hitting the sample. The beam reflected from the sample is then deflected downwards by MPA 2 again, and redirected by MPA 1 to the aberration-correction column, which consists of an electron mirror and associated transfer optics to compensate chromatic and spherical aberrations of the objective lens [191]. The beam then returns from the electron mirror, gets deflected by 90° again through MPA 1, and finally enters the projection column, which can selectively display a real-space or reciprocal-space image (diffraction pattern) onto the micro channel plate (MCP). Phase II and phase III of this LEEM system, used for ultrafast spin-polarised detection, were still under construction.

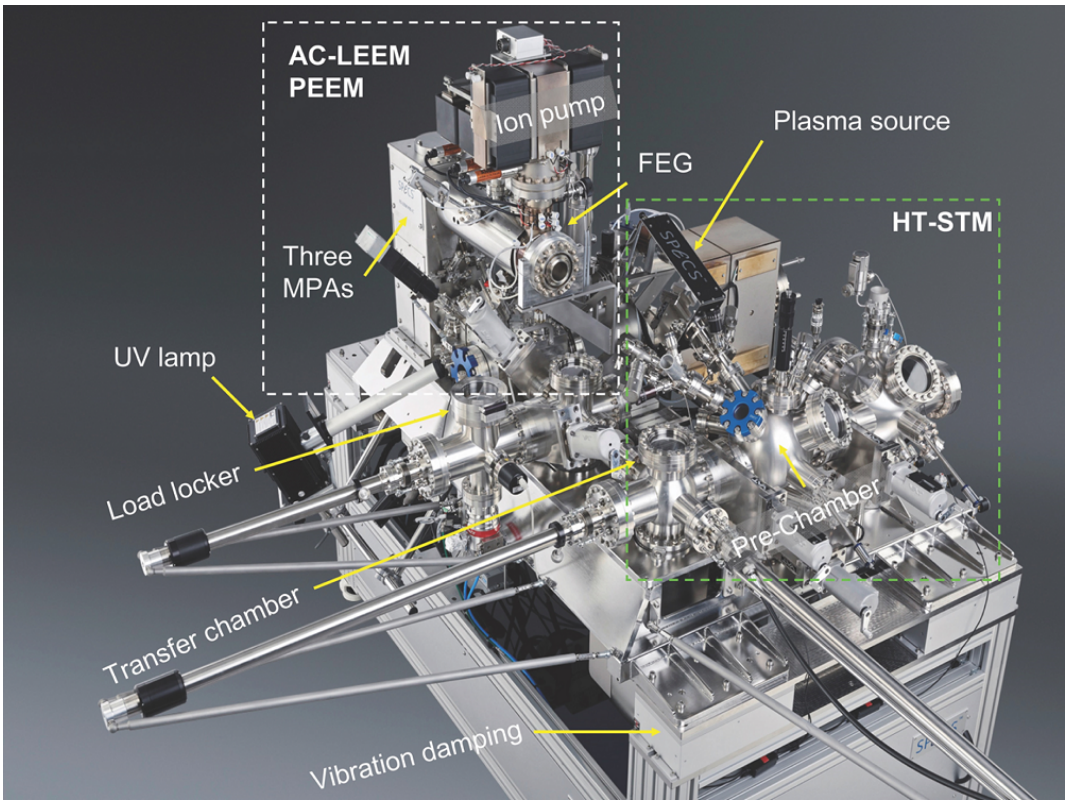

Figure 7.2: Photograph of the AC-LEEM/PEEM/HT-STM platform at Chongqing University. Figure adapted from ref.[16].

A photograph of the AC-LEEM platform is shown in Figure 7.2. There are six MBE sources in the LEEM chamber for material deposition. A mercury-vapour ultraviolet lamp is available for photoelectron emission microscopy (PEEM). There is a high-temperature scanning tunnelling microscopy (HT-STM) chamber connected to the LEEM chamber through a preparation chamber and transfer chamber, all of which are under UHV conditions. Temperatures in various chambers can measured by an optical pyrometer.

7.2 $L1_0$-FePt Heat-assisted Magnetic Recording

It has been illustrated in Chapter 6 that $L1_0$-FePt is an out-of-plane ferromagnetic material for spin injection into semiconductors. On of top that, $L1_0$-FePt is also a promising candidate material for heat-assisted magnetic recording (HAMR), a new high-density magnetic storage technology, which may supersede the current mainstream perpendicular magnetic recording (PMR) [192, 193]. HAMR uses a laser confined to less than 50 nm width, well below the diffraction limit, which heats a small area of recording media to close to T_C to write data, and then rapidly cool it to ensure long-term data retention. In this way it has potential to reach 5 Tbpsi (terabits per inch squared) areal recording density.

Conventional PMR uses only a perpendicular magnetic field to write on the recording media that consist countless magnetic grains. These grains differ slightly in properties such as areal size, height, and magnetic anisotropy. Each bit of information is stored on multiple neighbouring grains. The perpendicular writing field is confined to 60 nm width to write the designated bits and avoid the neighbouring bits, and therefore the recording density of PMR is mainly restricted by the field areal size and gradient [192]. High areal-density information technology also requires smaller media grains which ultimately has lower thermal stability. To protect bit switching from thermal fluctuations media grains need high magnetic anisotropy. Due to the limitation in the writing head technology, further reducing the areal size of the writing field will simultaneously reduce the field magnitude, which eventually may fail to switch the magnetisation of media grains. This trilemma of areal density, writability and thermal stability is the major obstacle against further development of PMR [194].

One of the possible solutions to break the PMR trilemma is HAMR, which records infor-

mation at a high temperature around 450 °C when the material's anisotropy is small, but stores information at room temperature when the anisotropy returns to a large value. The writing at high temperature is performed by a near-field transducer (NFT), utilising the near-field optics technique to focus the laser to far below the diffraction limit [195]. The bit size in HAMR is determined by two factors: the confined laser spot size, and the thermal gradient of the material. Among all the HAMR recoding materials, both research and commercialisation efforts have been focused on the $L1_0$-FePt ferromagnetic alloy. A schematic diagram of the FePt-HAMR system is shown in Figure 7.3. The $L1_0$-FePt film consists of nano-grains with a distribution in size and Curie temperature (T_C), due to variations in the stoichiometry and local ordering, as is shown in Figure 7.3(b).

Despite the commercial significance of $L1_0$-FePt, its growth dynamics especially the formation mechanism of nano-grains are not yet well understood. It is therefore interesting to investigate the growth and surface formation of $L1_0$-FePt thin films under LEEM. Growth of $L1_0$-FePt films was anticipated using *in situ* MBE co-evaporation in the Chongqing AC-LEEM. Unfortunately, this project was not successful for the following reasons. First, most substrates suitable for the $L1_0$-FePt growth are insulating oxides, such as MgO, $SrTiO_3$, and $LaAlO_3$, because of the matching cubic lattice parameters

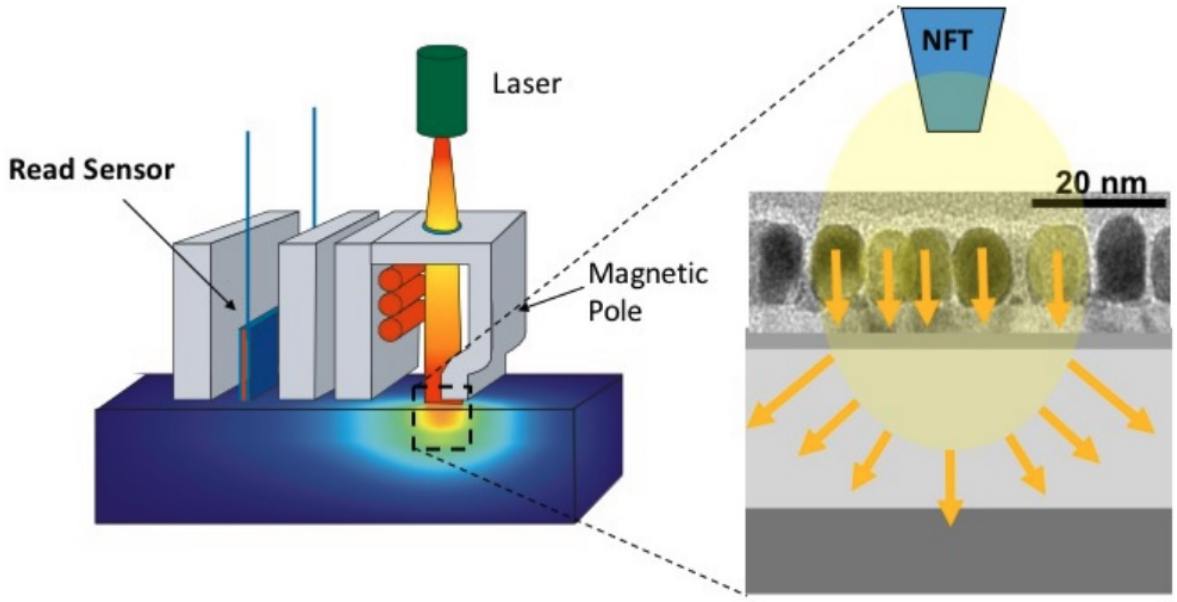

Figure 7.3: Left: schematic of HAMR. Right: close-up schematic of the NFT coupling to the $L1_0$-FePt granular media layer. Figure adapted from ref.[17].

with $L1_0$-FePt [196]. In order to obtain a LEEM image, the substrate must be conductive or semi-conductive to work as a cathode in the electron beam path. Secondly, the deposition rate of different sources in the LEEM was not calibrated, and it was difficult to grow at the 1:1 ratio between Fe and Pt. During the calibrations of Fe and Pt on W(110) and Si(100) substrates, a new approach of cleaning the W(110) surface was found, and the Pt-Si dynamics on Si(100) was investigated. The results are illustrated in following sections.

7.3 W(110) Surface Cleaning with Reduced Temperatures

Tungsten is a popular substrate material for surface science [197, 198, 199]. Single crystal tungsten has a high melting point and strong resistance to alloying with the overlayer, making it a promising candidate to support film growth at elevated temperatures [200, 201]. Ferromagnet (FM) / W(110) bilayer heterostructures have been a popular system in the field of magnetism, where Fe, Co, Ni or Cr was put on W(110) to investigate the dependence of structural and magnetic properties of the films on their thickness and growth temperature, especially in the ultrathin regime [202, 203, 204, 205, 206]. Although much effort has been put into the study of FM / W(110) structures, the preparation procedure of W(110) surfaces has varied little. Since W(110) often has carbon and oxygen contaminations on the surface, conventionally the substrate is first exposed to O_2 to clean up carbon contaminates, and then repeatedly flashed up to 2100 K to remove oxygen [199, 200, 201]. This elevated temperature is not applicable in many film deposition systems.

Here, a new approach is demonstrated to achieve an oxygen-free clean W(110) surface with reduced temperatures. By repeated flashing at 1800 K followed by Ar^+ ion milling and flashing at only 1300 K, an oxygen-free clean W(110) surface of more than 50 μm in lateral size is obtained. This finding is observed using LEEM and PEEM, and verified using micro low energy electron diffraction (μLEED).These results pave the way towards the *in situ* study of oxygen-free W(110) at a more instrument-friendly temperature.

The sample preparation and surface verification were performed in the Chongqing AC-LEEM. The single-crystal W(110) substrate used was 1.5 mm in thickness and 6.4×6.4

mm^2 in surface size, with 0.1 degree miscut and less than 10 nm surface roughness. The substrate was first cleaned by dry N_2 before loading into the preparation chamber. Afterwards it was degassed at 1000 K in the preparation chamber till the chamber pressure was less than 3×10^{-10} mbar. The substrate was then flashed to 1800 K ten times to further remove contaminates such as carbon, while oxygen remained on the surface. The sample was transferred under UHV to the LEEM chamber to verify the surface structure using PEEM/LEEM, then back to the preparation chamber for further treatments. To generate an oxygen-free W(110) area on the surface, the substrate was Ar^+ ion sputtered (300 V, 0.5 μA) at room temperature for one minute, and then flashed at 1300 K twice. The sample was then transferred to the LEEM chamber again to observe its surface. The substrate temperature was monitored by an optical pyrometer during the whole process.

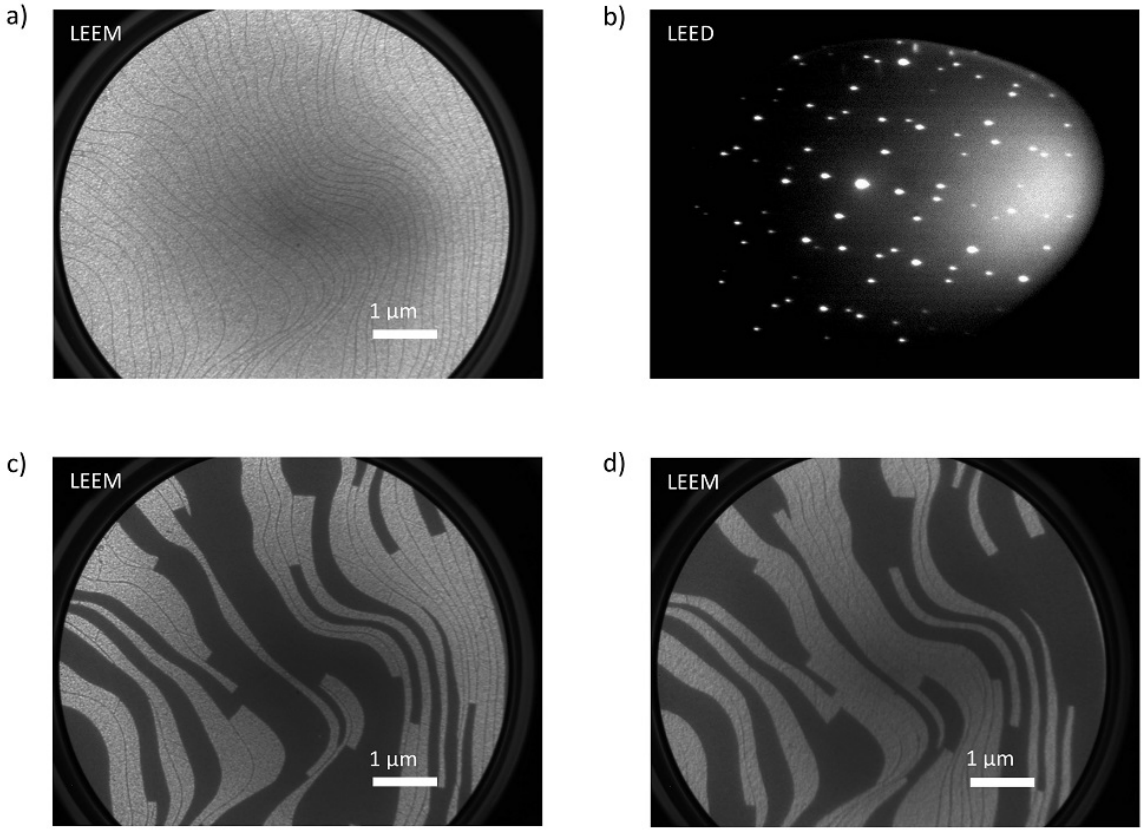

Figure 7.4: LEEM/LEED images of the oxygen-covered W(100) surface. (a) Bright-field LEEM at 14 eV with 7 μm field-of-view (FOV). (b) LEED pattern at 24 eV. (c,d) Dark-field LEEM images from two half-order LEED spots at 14 eV with 7 μm FOV, showing reversed bright/dark contrast.

After the 1800 K flashes, the W(110) surface appeared uniform under PEEM with a field-of-view (FOV) of 100 μm (not shown here), indicating a uniform oxygen distribution on the surface. This was followed by the bright-field LEEM imaging with a FOV of 7 μm, shown in Figure 7.4(a). The atomic steps of W-O with around 200 nm step size proves the surface is atomically flat at least on a 7 μm lateral scale. Unless otherwise specified all LEEM FOVs are 7 μm. Figure 7.4(b) shows the corresponding 24 eV LEED pattern of the O-W surface. By analysis in LEEDpat4 (FHI, Berlin), this pattern is confirmed as a superposition of (1×1), (1×2) and (2×1) phases. The first phase is from the oxygen-free W(110), while the latter two are common oxidised W(110) surface phases with 109.5° rotation [199, 200]. The high brightness on the right of this figure is due to the reflection of secondary electrons. Figure 7.4(c) and 7.4(d) show the dark-field LEEM images at 14 eV based on two half-order LEED spots nearest to the (0,0) spot. The reversed bright and dark contrast originates from (1×2) and (2×1) reconstructions respectively. These results show the W(110) surface is uniformly covered by oxygen without other contaminates.

Figure 7.5 shows the PEEM image of the W(110) surface after ion sputtering and 1300 K flashing. A 50 μm bright area was found in the middle of the 100 μm view. Figure 7.5(b,c) respectively show the 44 eV μLEED pattern of the bright and dark areas of the PEEM image. The bright area has a clear (1×1) pattern, indicating the presence of clean oxygen-free W(110). Meanwhile the surrounding dark area still shows the (2×1) O-W pattern, indicating the the presence of oxides. Figure 7.5(d) shows the bright-field LEEM image of oxygen-free area. The atomic steps indicates the surface is atomically flat.

In summary, this project demonstrates a new approach to acquire an oxygen-free W(110) single crystal surface at reduced temperatures. The whole procedure involves repeated flashing at 1800 K, ion sputtering and flashing again at 1300 K. The maximum temperature in this process is 1800 K, considerably lower than the standard W(110) preparation method (2100 K). It should be noted that most LEEM experiments, such as thickness-dependent magnetisation and growth mode of FM/W(110) heterostructures [202, 203, 204, 205, 206], focus on a lateral size of less than 10 μm. In this case, although the oxygen-free area after the new W(110) treatment is only 50 μm in lateral size, and most other parts of the surface still have oxygen coverage, this small area will be adequate to accommodate most LEEM research on W(110).

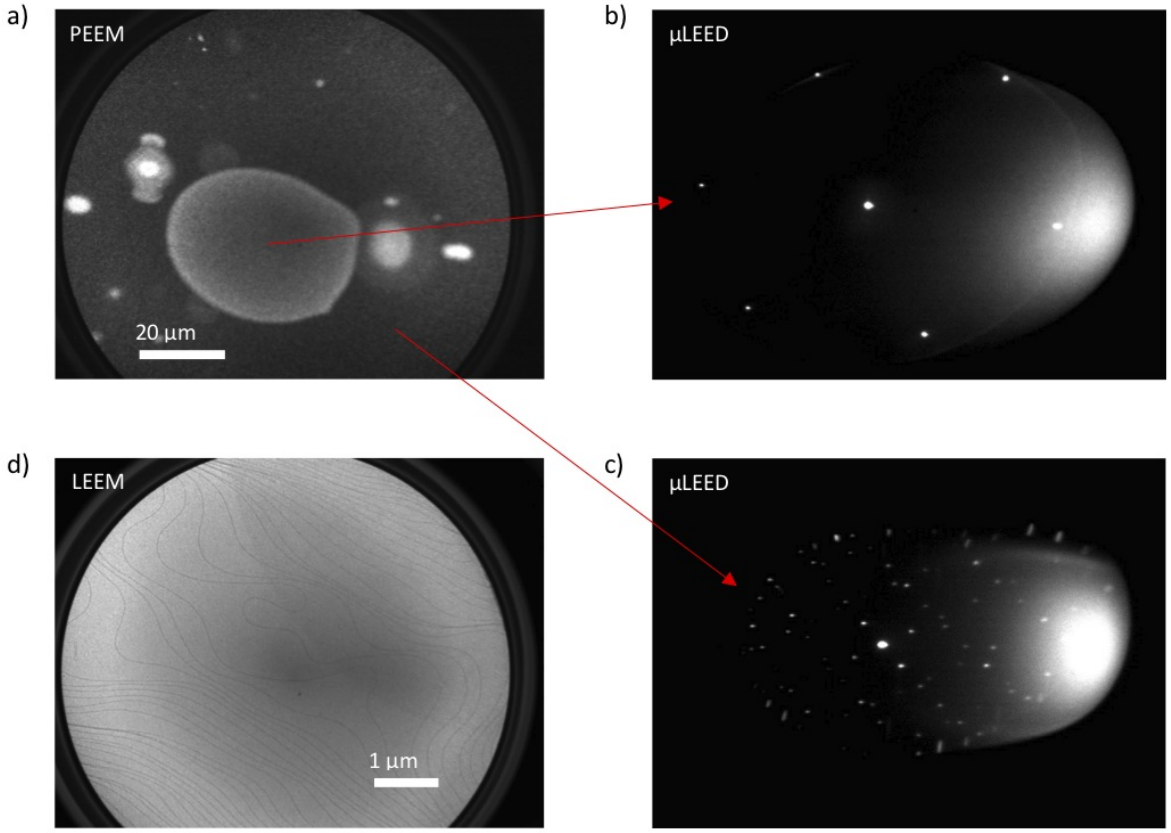

Figure 7.5: PEEM/LEEM/LEED images of the W(100) surface after ion sputtering and 1300 K flashing. (a) PEEM image with 100 µm FOV. (b,c) µLEED patterns of the areas shown under PEEM. (d) Bright-field LEEM image of the middle area at 16 eV.

7.4 Pt-Si Surface Dynamics on Si(100)

7.4.1 Pt-Si Dynamics: Background

Silicides are widely used as building blocks of microelectronic devices. When silicides are used as an electronic contact, the silicide/silicon interface is mechanically and chemically robust, and a Schottky barrier of specific height can be formed by selecting the silicide metal [207, 208]. Silicide nanowires (NWs) have attracted great attention for industry applications [209]. Some rare-earth NWs with regular shapes of only a few nm wide and hundreds of nm long are conductive on Si, making them potential candidates as nanoscale wiring materials [210, 211, 212]. However, rare-earth NWs are chemically active and can easily oxidise, and therefore researchers have moved effort towards the

Pt-Si NW system, as Pt is chemically inert. Lim *et al* demonstrated that Pt forms self-assembled Pt_2Si NWs on Si(110) and the NW conductivity is twice as much as bulk Pt_2Si [213]. Pt nanowire arrays may also work as chemical reaction catalysts, making use of their large surface area [214]. Despite intensive research on Pt-Si NWs, their formation dynamics have rarely been reported. In the meanwhile, it has been found that a thin layer of Pt on Si(100) can form Pt-Si liquid droplets above 950 °C, and the surface droplets can migrate along the atomic step edges or the local temperature gradient [215, 216, 217]. This temperature is higher than the formation temperature of NWs, and the transition dynamics from NWs to droplets has not been heavily investigated.

Here, the formation and transition dynamics of Pt-Si NWs and droplets on Si(100) substrates are reported. As the temperature goes up, Pt first grows as NWs with the length increasing on both sides, and then NWs shrink into Pt-Si islands. A higher temperature gives each island a small mobility, and then islands become droplets migrating the on the Si(100) surface, with small droplets colliding to form larger ones. Eventually, at the highest temperature, Pt-Si eutectic droplets evaporate, and a clean Pt-free Si(100) surface is recovered.

7.4.2 Pt-Si Dynamics: Nanowires

This experiment was conducted in the AC-LEEM suite in Chongqing. The Si(100) substrate has a lateral dimension of 6.4×6.4 mm^2, with 0.1 degree miscut and less than 10 nm surface roughness. The substrate was first sonicated in acetone, and then cleaned by dry N_2 before loading into the preparation chamber. Afterwards this Si substrate was degassed overnight at 500 °C, and flashed a few times at 1200 °C, until clean (1×2)Si and (2×1)Si LEED patterns and sharp atomic steps are observed in the LEEM chamber. After these steps, the Si(100) surface should be clean and atomically flat. Next, in the LEEM chamber with a base pressure of 5×10^{-10} mbar, Pt was evaporated from a Pt rod source (4N purity) onto the substrate by electron beam bombardment, with an evaporation power of 30 W and a flux of 35 nA. The chamber pressure during the growth was kept at 1.3×10^{-9} mbar, and the substrate temperature was kept at 100 °C for better alloying between Si and Pt. After 4 hours of deposition, the sample temperature was quickly ramped up to 600 °C. Then the temperature was adjusted in small steps, finally up to 720 °C. LEEM and LEED were constantly used to observe the surface dynamics during the deposition and the temperature rise.

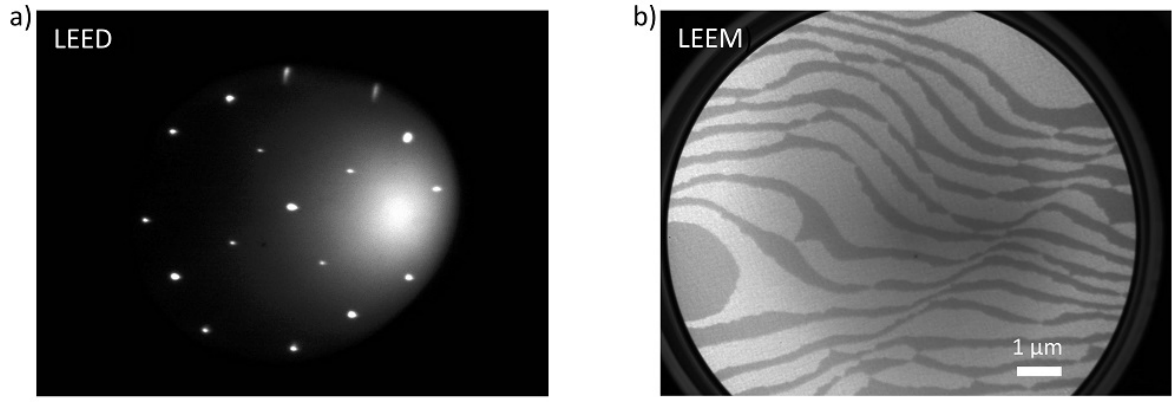

Figure 7.6: LEED/LEEM images of the Si(100) surface after degassing and flashing at 1200 °C. (a) LEED pattern at 17 eV. (b) Bright-field LEEM image at 2 eV with a tilted beam, showing (2 × 1) and (1 × 2) Si(100) domains. The FOV is 10 µm.

Figure 7.6 shows the LEED and bright-field LEEM images of the Si(100) surface after the overnight degassing and flashing. Clear (1×2) and (2×1) Si(100) phases are visible in the LEED pattern at 17 eV, and no extra diffraction spots can be seen. By tilting the electron beam slightly, bright and dark contrast is visible in the 10-µm-FOV LEEM LEEM image at 17 eV, corresponding to (1 × 2) and (2 × 1) Si(100) domains. Unless otherwise specified all LEEM FOVs in this section are 10 µm. These results indicate the Si(100) substrate is clean and atomically flat.

The bright-field LEEM image was monitored while Pt was deposited on Si(100) at 100 °C. It was found after several trials that a slightly elevated temperature such as 100 °C can increase the growth rate of Pt on Si(100), compared to the room temperature condition. This is possibly due to more active alloying between Pt and Si at 100 °C [208]. During the initial phase of the deposition, the LEEM image became gradually poorly defined, and after 30 minutes it completely disappeared. The LEED pattern also disappeared at this point, indicating Pt was successfully deposited on Si(100), and the Pt-covered surface has no well-defined lattice structure. No LEEM image or LEED pattern were visible during the rest of the 4-hour growth.

At this point, the substrate temperature was quickly ramped to 650°C and gradually increased by a step size of less than 20°C. At 720°C, NWs started growing along the [011] and $[0\bar{1}1]$ crystallographic directions of Si(100). A live movie was recorded during this process with 0.5 second time interval, and some snapshots are shown in Figure 7.7.

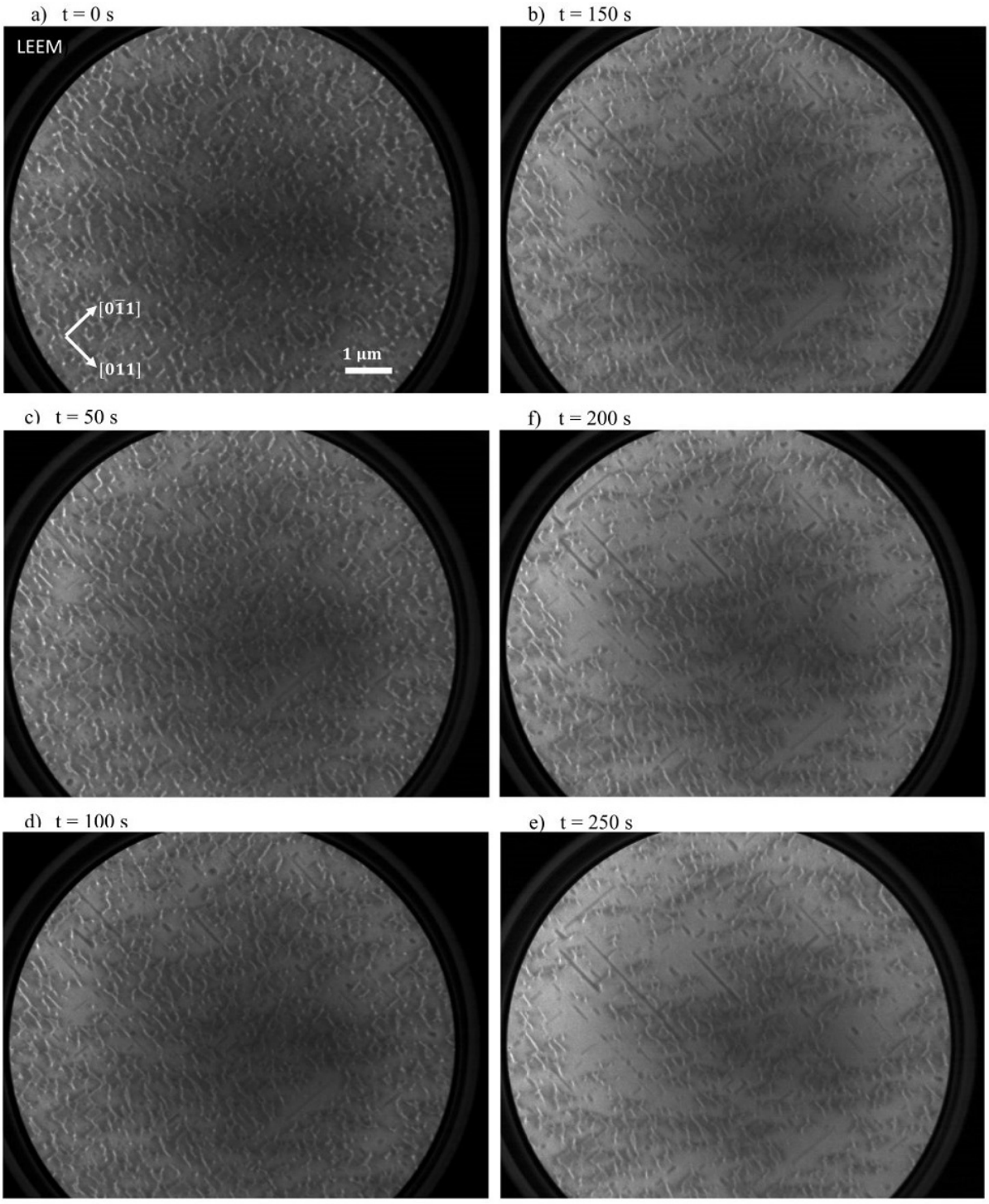
a) t = 0 s
LEEM
[0$\bar{1}$1]
[011]
1 µm
b) t = 150 s
c) t = 50 s
f) t = 200 s
d) t = 100 s
e) t = 250 s

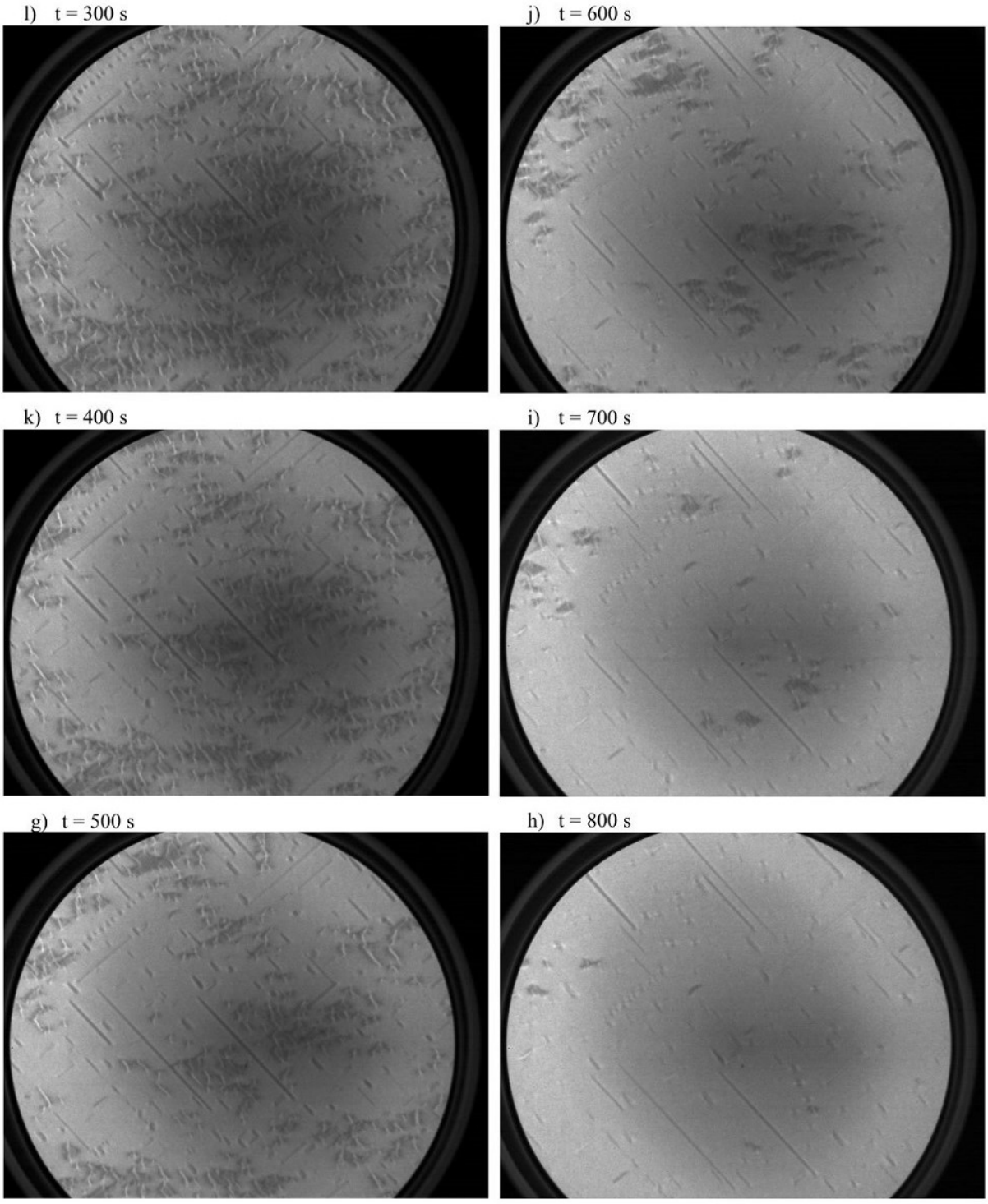

Figure 7.7: Bright-field LEEM images showing the formation of Pt-Si NWs on Si(100), with 10 μm FOV at 720°C. (a)-(g) were recorded with a time interval of 50 seconds, and (g)-(l) with an interval of 100 seconds. The view had a small lateral drift induced by the high temperature of the chamber.

The FOV was 10 μm and the electron beam energy was 7 eV. At $t = 0$ s the view contained many rough areas and no NW could be seen. At $t = 50$ s some NWs became visible along the [011] and [$0\bar{1}1$] crystallographic directions, and the surrounding part of the NWs showed smoothness with brighter colour compared to the rest of the Si(100) surface. As time went by, NWs continued growing from both ends, and the bright smooth area kept expanding from the location of NWs. At $t = 500$ s most NWs had reached their maximum lengths. The longest NW observed in this experiment was 500 nm long. The widths of most NWs were about 40 nm. The widths and lengths obtained here are the same orders of magnitude as in previous studies [209, 218]. One possible reason to explain this relationship between the bright/dark area and NW locations is that, NWs have a higher percentage of the Pt element, so nearby Pt atoms flow to NWs when they are self-assembled. As a result, the surrounding area contains a low percentage of Pt, which shows bright colour and smooth texture. During $t = 500$ - 600 s, most NWs along [$0\bar{1}1$] disappeared unexpectedly. Detailed movie clips show that these NWs turned bright gradually, so their colour contrast to the surrounding area became minimal. The mechanism behind this phenomenon is not yet understood. At $t = 800$ s it was obvious NWs along [$0\bar{1}1$] were more populated and most long NWs were along this direction. It is possible that the directional temperature gradient plays a role in NW formation, resulting in the difference between the [011] and [$0\bar{1}1$] direction. It should also be noted that, repeated measurements confirm NWs can self-assemble from 705°C, but the growth rate is substantially slower, so the live recording was made at 720°C.

LEED and dark-field LEEM imaging were applied to further investigate the structure and composition of the Pt-Si(100) surface. These results are shown in Figure 7.8. The LEED pattern of the whole FOV shows a $c(4 \times 6)$ reconstruction, indicating the main alloying composition of this Pt-Si(100) surface is Pt_2Si [219, 220]. It has been reported that the background phase of Pt-Si NWs is Pt_2Si, and that the surface reconstruction pattern is a superposition of $c(4\times6)$ and $c(4\times2)$ [218]. However, as the $c(4\times2)$ pattern is fully included in $c(4 \times 6)$, here it is not possible to directly distinguish $c(4 \times 2)$ from $c(4 \times 6)$. To further verify the LEED pattern, dark-field LEEM was used based on two spots: A and B in Figure 7.8(a), which are present in $c(4 \times 6)$ but not in $c(4 \times 2)$. The dark-field LEEM images (Figure 7.8(b)(c)) show reversed bright and dark contrast, indicating $c(4\times6)$ is the dominate phase of the Pt-Si(100) surface. The spatial distribution of bright/dark contrast does not seem to relate to the distribution or directions of NWs.

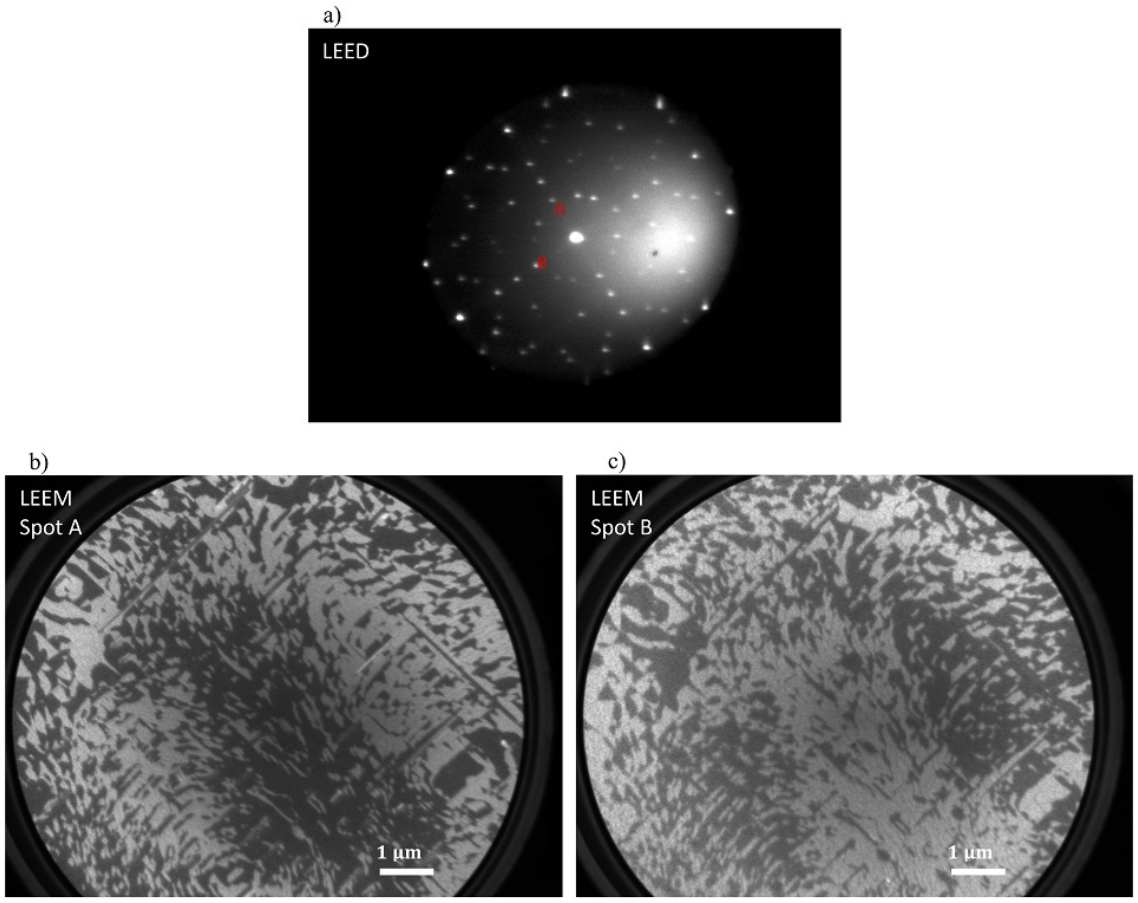

Figure 7.8: LEED and dark-field LEEM images of the Si(100) surface with Pt-Si NWs. (a) LEED pattern at 14 eV. showing $c(4 \times 6)$ phase. (b,c) Dark-field LEEM images at 4 eV, from spot A and B in the LEED pattern respectively.

To further investigate the chemical composition and phase of each individual NW, µLEED of 270 nm aperture diameter was performed on a few NWs. Due to the difference between the aperture size (270 nm) and the NW width (40 nm), the µLEED results may have substantial contributions from both the NW itself and its surrounding area. The µLEED patterns at 14 eV on 4 NWs are shown in Fiugre 7.9. NWs in (a) and (b) are along the [011] direction, and (c) and (d) are along the $[0\bar{1}1]$ direction. It can be seen that all 4 µLEED patterns resemble a $c(4 \times 6)$ reconstruction. The bright streaks across the (0,0) spot are due to the three-dimensional continuous profile of each NW, and, as NWs are orthogonal in real space, the streaks in reciprocal space are also orthogonal between (a,b) and (c,d). By moving the aperture slightly away from the NWs, the bright streaks disappeared and the rest of the patterns stayed intact. This indicates the surrounding area of NWs were mainly composed of Pt_2Si, with $c(4 \times 6)$

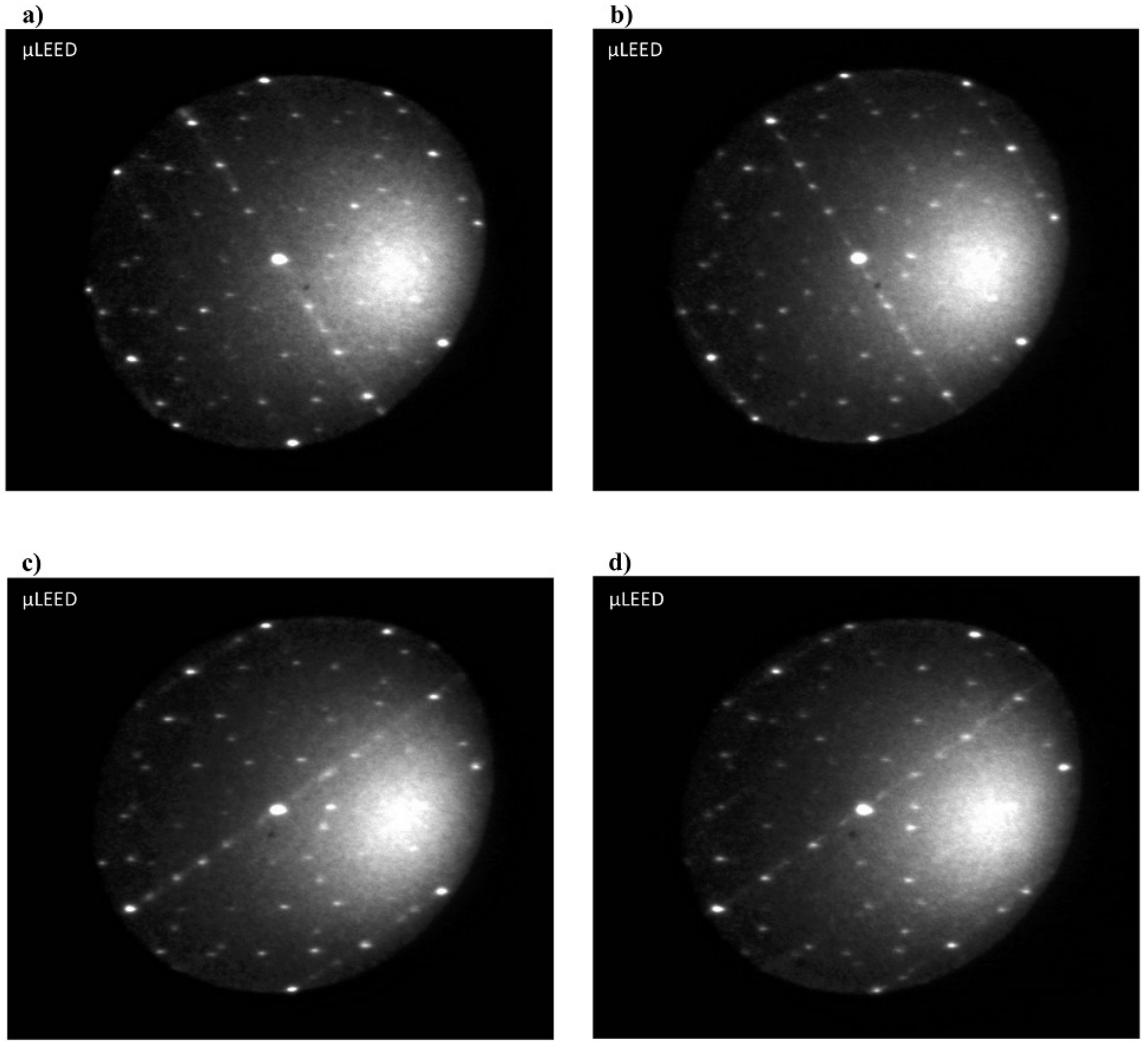

Figure 7.9: μLEED patterns at 14 eV on 4 Pt-Si NWs. NWs are along the [011] direction in (a) and (b), and along [0$\bar{1}$1] in (c) and (d).

reconstruction.

7.4.3 Pt-Si Dynamics: Droplets

Next, the substrate temperature was further elevated to verify the finding about Pt-Si eutectic droplets reported in previous publications [215, 216, 217]. The behaviour of liquid metal droplets at nanoscale has been a topic of interest to scientists, as eutectic droplets are commonly used as a seed for semiconductor NW growth in a vapour-liquid-solid (VLS) growth scheme [221, 222]. The growth rate is generally slow for a solid material by directly deposition of vapour phase onto a solid substrate. The VLS mech-

anism can overcome this problem by depositing an extra material on the substrate, which forms a catalyst liquid alloy and absorbs deposited vapour to supersaturation level. The new solid material will then grow from these seed spots at a liquid-solid interface. [223, 224].

One of the earliest direct observations of Pt-Si liquid droplets was done by Yang *et al* in 2004 using ultraviolet PEEM [215]. They found that Pt-Si islands on Si(100) substrates transform into a micro-sized Si-rich liquid phase below the melting temperature of the bulk Pt-Si alloy. The microdroplets move from cold to hot areas on the substrate surface following the temperature gradient, and grow in size through coalescence. They proposed that the migration mechanism is a dissolution-diffusion-deposition Si flow, that is, Si on the substrate dissolutes into the droplet, diffuse on the surface, and finally deposits at another part of the substrate surface dependent on the temperature gradient. The same mechanism was also discovered in the motion of Ga droplets on the GaAs surface [225]. Yang *et al* found the migration speed of an individual Pt-Si droplet is only related to the temperature and independent of the droplet size, providing the droplet has fulfilled the minimum size requirement, usually about 2 μm, to initialise the movement. Following this research, in 2007 Sutter's group published two articles on Pt-Si microdroplets using slightly-tilted bright-field LEEM with 10 nm lateral resolution [216, 217]. They discovered the interplay between the surface steps of Si(100) and the motion of droplets in various sizes. In short, large droplets with a diameter of more than a few μm migrate along the temperature gradient as discovered earlier, but when a Pt-Si droplet is smaller than a few hundreds of nm, it is constrained to move along an atomic monolayer step edge. In addition, a few atomic steps can be bunched at a large droplet, and dragged along the droplet migration before eventually depinning. Following these results, Sutter *et al* proposed using designed surface steps to manipulate motion of eutectic alloy droplets, which will help the patterning self-assembled NWs.

To investigate the Pt-Si droplet dynamics on Si(100) substrates at high temperatures, the NW formation experiment was conducted again using the Chongqing AC-LEEM, which showed visible NWs at 720°C. At this point, the substrate temperature was further raised in steps of less than 20°C, and bright-field LEEM at 9 eV was used monitor the surface change. The results are shown in Figure 7.10. At 770°C NWs began shrinking at both ends, and at 810°C most NWs in the view had transformed into islands. Then at 860°C some islands became mobile droplets and ran in small circles around

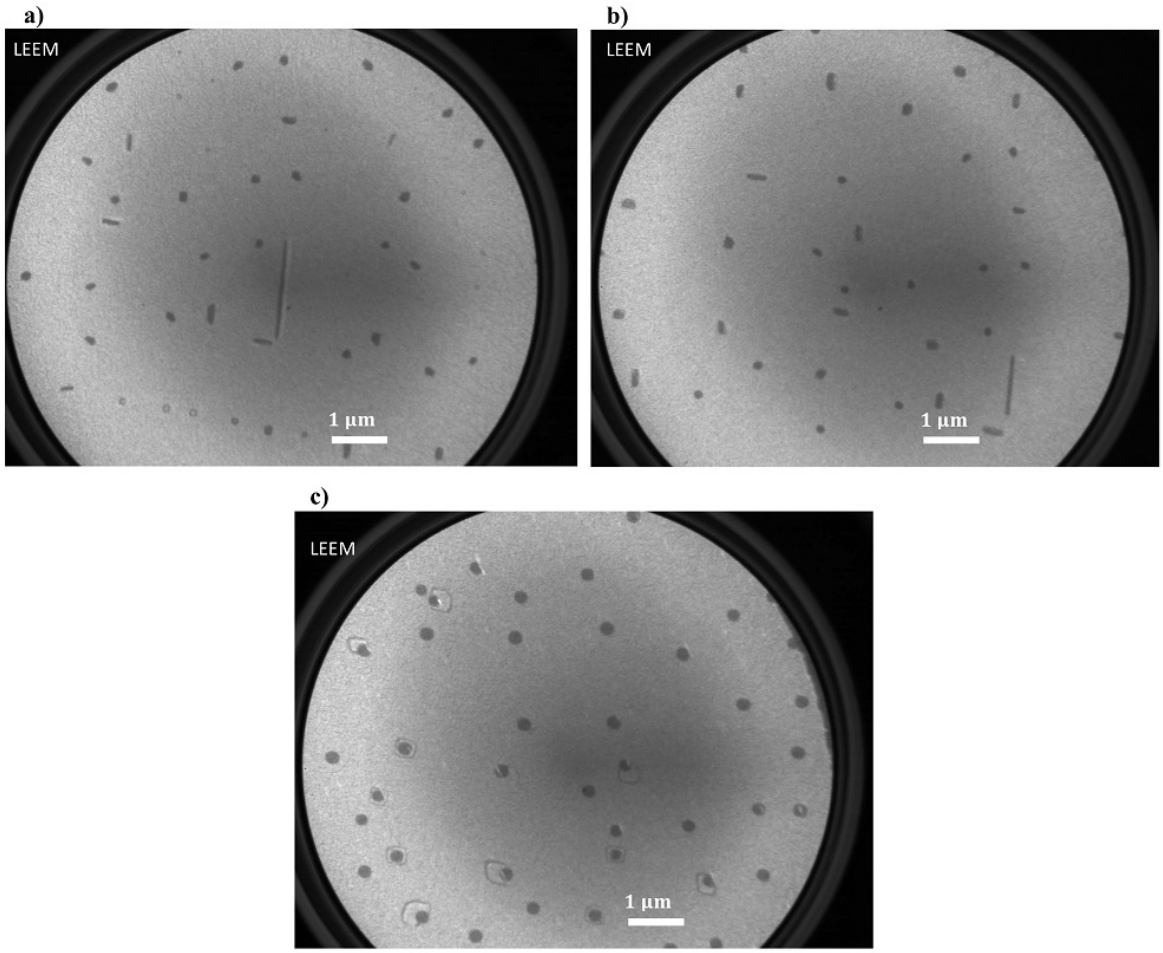

Figure 7.10: Bright-field LEEM images with 10 µm FOV at 9 eV on the Pt-Si(100) surface, taken at the following temperatures: (a) 770 °C, (b) 810 °C, and (c) 860 °C.

their original locations. A tail was left on the substrate surface when droplets went by, which can be explained by the dissolution-diffusion-deposition model, as Si was etched away from the substrate and then redeposited along the migration route.

Next, after the substrate temperature rose to 1040 °C, Pt-Si droplets and Si(100) atomic steps were observed to quickly migrate. A live video was recorded using slightly-tilted bright-field LEEM at 2 eV with 10 µm FOV, and snapshots with 50 seconds interval are displayed in Figure 7.11. The atomic steps flowed in a direction marked in red in the figure. At $t = 0$ s a high population of droplets existed, and as time went by, small droplets either evaporated due to the hot surface, or were swallowed by large droplets. Five droplets in the view are marked: D1 - D5. D1 and D2 are larger than 500 nm in diameter, while D3, D4 and D5 are between 100 nm and 500 nm in diameter.

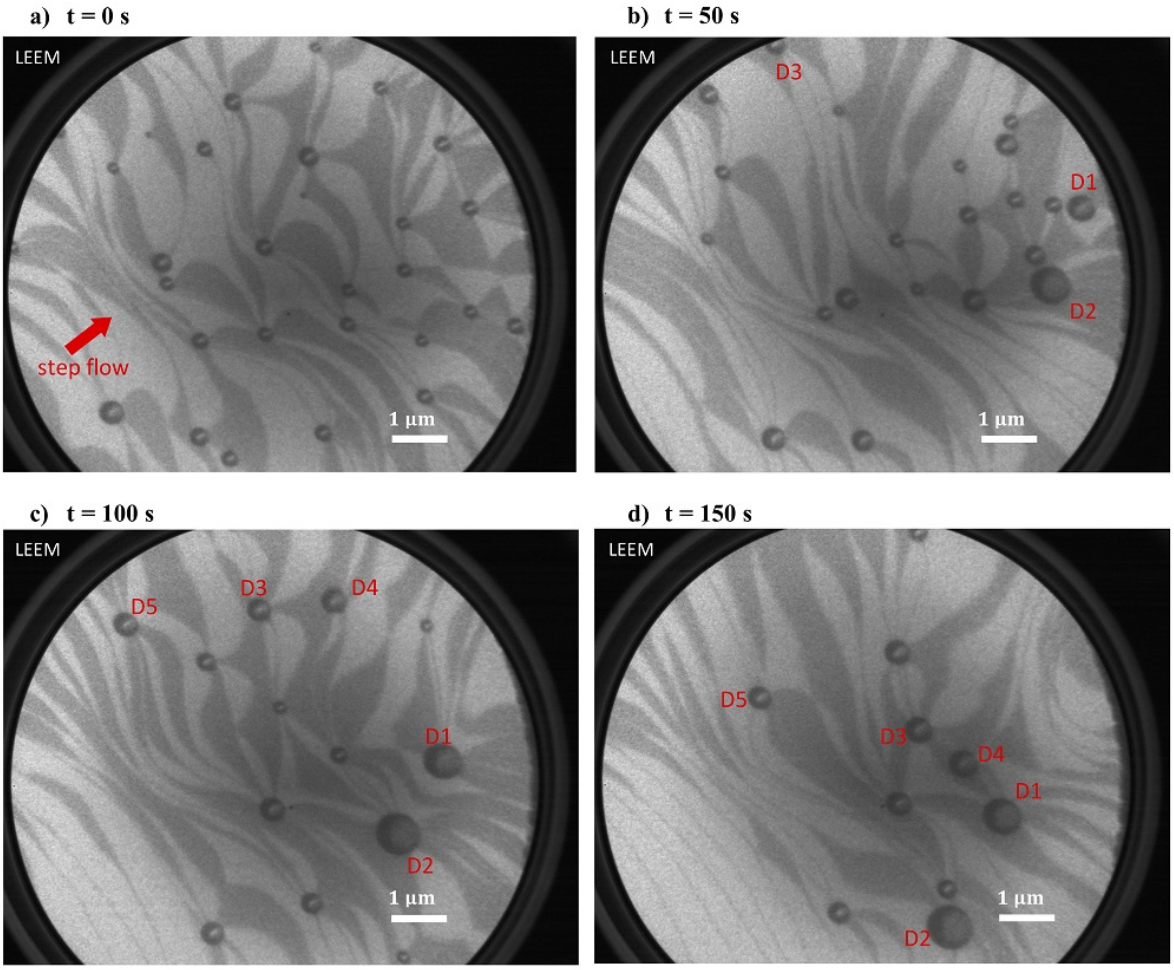

Figure 7.11: Slightly-tilted bright-field LEEM images showing the Pt-Si droplets on Si(100) at 1040°C. The FOV is 10 µm the electron energy is 2 eV. Time interval is 50 seconds.

Droplets smaller than 100 nm tended to evaporate quickly at the current temperature. It can be found that D1 and D2 migrated in the same direction towards lower left in the view, roughly opposite the direction of the atomic step flow. D3, D4 and D5 which were smaller flowed along the step edges perpendicular to the step flow. As the local temperature distribution is unknown, it is difficult to compare the directions of D1/D2 migration with the thermal gradient. It may be possible that these two droplets' migrated from cold to hot areas following the local temperature difference, and at the same time the gravity of the droplets played a role since the sample surface was perpendicular to the ground. Many surface steps were pinned together by some droplets, and the nodes were dragged along the droplets' migration. The view of the microscope was then adjusted to follow the movement of D1 and D2. The directions of both droplets' migration and the step flow did not alter significantly during this tracking that lasted

a few minutes, and the droplets' sizes did not change much either. Then after flashing multiple times to 1200°C, clear (2×1) and (1×2) LEED patterns were recovered, indicating all Pt atoms were evaporated away, and clean, flat Si(100) surface was obtained.

7.4.4 Pt-Si Dynamics: Summary and Discussion

In summary, temperature-dependent surface dynamics of the Pt-Si alloy on Si(100) substrates was demonstrated using LEEM and LEED techniques. As the temperature went up, Pt on Si first formed into NWs at 700 °C, then islands at 800 °C, and finally eutectic droplets at 1000 °C. NWs grown at 700 °C have an average width of 40 nm, and the maximum length observed was 500 nm. A spatial variation in brightness related to the NW distribution was observed under the bright-field LEEM, which may be explained by the variation of Pt coverage on the surface. A $c(4 \times 6)$ reconstruction was observed on the Si surface coexisting with the NWs, indicating the surface alloy was Pt_2Si. Migration of Pt-Si droplets formed on Si(100) was influenced by both the temperature gradient and atomic surface steps, that is, small droplets (less than 500 nm in diameter) tended to move along monolayer step edges, and large droplets (500 nm or more in diameter) migrated along the thermal gradient. Large droplets can be formed by coalescence of small ones, and, the smallest droplets (less than 200 nm in diameter) may quickly disappear due to evaporation. This research provides useful insight into the growth dynamics of nanostructures on Si, which may be applied in the nanoelectronic systems that contain NWs. Finally, regarding large droplets, it is interesting to wonder what factors can contribute to their movements once the thermal gradient is removed. One possible factor is the crystallographic axis, which determines the motion of Ga droplets on GaAs surfaces [225]. Further work should focus on eliminating the spatial thermal distribution in the substrate by carefully tuning the LEEM instrumentation, and then exploring the migration of Pt-Si droplets with respect to non-thermal factors.

CHAPTER 8

SUMMARY AND OUTLOOK

8.1 Research Summary

This thesis illustrates the study of magnetic topological insulator (MTI) films, ferromagnet/semiconductor heterostrctures, and some non-magnetic surface science systems, using magneto-optic Kerr effect (MOKE), low energy electron microscopy (LEEM), and various other techniques.

MOKE

The detailed design and construction of the low temperature polar MOKE microscope are demonstrated in Chapter 3. Instead of using a cold-finger and a transparent window, in this microscope all optical components are assembled into a stand-alone probe, which is compatible with non-optical cryostat systems. This MOKE probe has a base temperature of 1.6 K and is equipped with a 9 T superconducting magnet. Polarisation modulation at 100 kHz is sustained by employing a photoelastic modulator. A two-dimensional scanning experiment on a $[CoFeB/Pt]_n$ micro-pattern confirms the lateral resolution reaches mircon level, and the magnetisation sensitivity is 10 μrad (Kerr angle). Measurements on the (Ga,Mn)(As,P) films and micro-devices prove the electrical transport capability of the MOKE probe. Although this probe is outperformed by other world-class MOKE systems, such as the Regensburg MOKE, in both the sensitivity and spatial resolution, the successful execution of this instrument shows the practicability of constructing low temperature optical systems for users of common non-optical cryostats. Regarding future use of the MOKE probe, an air conditioner will help stablise the optical components against temperature-variant drift, and using solid-immersion lens and special cryogenic objectives may help reduce the focal spot

size to sub-micron level.

Topological Insulators

Chapter 4 and Chapter 5 present detailed structural, electrical and optical studies of various TI systems: single-doped Cr:Sb_2Te_3, co-doped (Cr,V):Sb_2Te_3, EuS/Bi_2Se_3 bilayer, and most importantly, [Cr:Sb_2Te_3/Dy:Bi_2Te_3]$_{10}$ superlattices. A good agreement is found between the optical and electrical results of the Cr:Sb_2Te_3 films with various doping concentrations. Compared to Cr:Sb_2Te_3, (Cr,V):Sb_2Te_3, the simultaneous MOKE and transport study reveals the presence of a secondary ferromagnetic phase, resulting in a combined effect of anomalous magneto-resistance (AMR) and weak antilocalisation (WAL) above the Curie temperature. X-ray diffraction (XRD) confirms the secondary phase is the ferromagnetic Cr_2Te_3. MOKE is also used to confirm the origin of the out-of-plane magnetisation in EuS/Bi_2Se_3, a ferromagnet/TI heterostructure. The MOKE signal of EuS/Bi_2Se_3 disappears above 16 K, matching the Curie temperature of pure EuS with in-plane anisotropy. In the meanwhile, the MOKE signal from pure EuS is significantly smaller than the bilayer. Since single-layer Bi_2Se_3 is known to be non-magnetic, one can conclude that the out-of-plane anisotropy in EuS/Bi_2Se_3 originates from interface coupling.

Unexpected exchange bias is discovered in the ferromagnet/paramagnet [Cr:Sb_2Te_3 / Dy:Bi_2Te_3]$_{10}$ TI superlattice film. The ordered crystal structure of the film with smooth interfaces is confirmed by TEM and XRD. Using both MOKE and electrical transport techniques, out-of-plane ferromagnetism is found in the film up to 150 K, and exchange bias is found up to 100 K. The existence of exchange bias in this TI superlattice is unexpected, since this phenomenon is mostly seen in FM/AFM heterostructures, due to the pinning effect at the interface. DFT calculations reveal antiferromagnetic ordering in the Dy-doped layer in close proximity to the Cr-doped layer. When the Cr-doped layers exhibit ferromagnetic ordering at low temperatures, the Dy atoms in the nearest atomic layer to Cr tend to align their spins parallel to Cr, and the next Dy layer tend to align anti-parallel to both Cr and the first Dy. This study demonstrates the proximity induced antiferromagnetic order in rare-earth doped TI films. Moreover, since the [Cr:Sb_2Te_3/Dy:Bi_2Te_3]$_{10}$ superlattice has a high exchange bias field of up to 0.15 T at 10 K, its strong tolerance to stray fields may favour industrial magnetic applications.

Ferromagnet/semicondutor Spin Transport

Chapter 6 demonstrates the growth and MOKE characterisation of ferromagnet / semiconductor heterostructures. Inspired by the Fe/GaAs and FeCo/GaAs spin transport devices from Crooker *et al.* and Kotissek *et al.* [14, 15], the initial plan of the PhD project was to grow different ferromagnet/semiconductor bilayer films with perpendicular magnetisation, and to explore the spin injection and transport property of the bilayer devices. Three material systems are featured in this chapter: $L1_0$-FePt/MgO, $L1_0$-FePt/MgO/GaAs, and $[Co/Pt]_n$/GaAs. $L1_0$-FePt is found to establish strong perpendicular anisotropy on MgO substrates at a growth temperature of over 500 °C. However, when the same growth condition is used for FePt/MgO/GaAs with a 2-nm MgO tunnel barrier, the magnetic easy axis is no longer out of plane, and the interfaces at FePt/MgO and MgO/GaAs are rough with reduced crystallinity, as is shown under the transmission electron microscope (TEM). Alternatively, $[Co/Pt]_n$ was grown on GaAs using magnetron sputtering. Even though strong perpendicular magnetic anisotropy is found in some samples, the magnetisation is independent of the crystal orientation of GaAs. This may indicate the growth is not epitaxial, and the spins may experience strong scattering at the interfaces before reaching GaAs. The above experiments demonstrate the difficulty to engineer an efficient ferromagnet/semiconductor spin transport heterostructure.

LEEM Surface Science

The $L1_0$-FePt alloy is not only a source material for spin injection into GaAs, but also the main candidate medium for the heat-assisted magnetic recording (HAMR) technology. The initial research plan regarding HAMR was to investigate the detailed surface dynamics of $L1_0$-FePt using LEEM. However, the co-evaporation of the LEEM platform was not functional, and therefore the project developed into surface studies of W(110) and Pt/Si(100) at high temperatures, as is illustrated in Chapter 7. By repeated flashing and Ar^+ ion sputtering with a maximum sample temperature of 1800 K, it is possible to acquire a clean, oxygen-free surface on W(110) single-crystal substrates with a lateral size of 50 μm. This lateral size is adequate to accommodate most LEEM experiments, such as the thickness-dependent magnetisation study of Fe/W. 1800 K is considerably lower than in the standard procedure for W(110) surface cleaning (2100 K), making the clean W(110) surface more accessible for LEEM users. The next experiment shows the temperature-dependent dynamics of the Pt-Si alloy on Si(100) substrates. As temper-

ature increases, Pt on Si(100) transforms from self-assembled nanowires (NWs) at 700 °C, through islands at 800 °C, and finally to eutectic droplets at 1000 °C. Above 1000 °C, droplets migrate long the thermal gradient, and small droplets collide to form large ones. In the future, it will be interesting to try eliminating the thermal gradient of the substrate surface, and to investigate if the Pt-Si droplets migrate along the crystallographic axis of Si(100).

In summary, most projects listed in the thesis fall into the spectrum of spintronics, aiming to utilise spin as an extra degree of freedom to store and process information in microelectronic systems. Compared to Si-based devices which are facing the end of Moore's Law [226], spintronic devices may have the advantages of fast response, low power consumption, low heat dissipation and compact size [42]. This thesis has provided insights of various spintronic materials and instruments, aiming to contribute to the future low-dissipation spintronic industry.

8.2 Future Work

Spin Hall Effect

The MOKE microscope is capable of mapping spin distributions with μm resolution, making it a suitable tool to directly image accumulations of opposite spins in a material due to the spin Hall effect (SHE). MOKE has been used to successfully observe SHE in GaAs and Ge [22, 24], due to the long spin diffusion length on the edges of semiconductors. However, the situation of imaging SHE in heavy metals is less clear. While there was a research group showing MOKE-resolved SHE on Pt and W [227], other groups disagreed on the results and suggested the false MOKE signal came from reflectivity changes induced by electric current heating [228, 229]. After carefully eliminating the heating effect, two more groups have recently claimed they detected SHE not only in Pt, but also in $(Bi,Sb)_2(Te,Se)_3$ TI materials [230, 231]. It can be concluded that there are not yet abundant proofs for the optical visualisation of SHE in heavy metals and TIs. Since both the heating effect and spin diffusion are dependent on temperature, in the future, it will be interesting to further investigate this topic, by employing a temperature-variant MOKE measurement scheme.

Rare-earth-doped Topological Insulators

Although exchange bias is unambiguously confirmed in $[Cr:Sb_2Te_3/Dy:Bi_2Te_3]_{10}$ superlattice films, the physical origin of this effect is not yet completely clear. Results obtained from the DFT calculation are still preliminary, and further simulations should be conducted involving van der Waals force and temperature variance. Also, since the proximity-induced antiferromagnetic ordering is an interface effect, it may be interesting to grow more superlattice films with reduced thickness-per-layer, to suppress bulk contribution in MOKE and transport measurements. Moreover, the Curie temperature of the $[Cr:Sb_2Te_3/Dy:Bi_2Te_3]_{10}$ superlattice (150 K) is much higher than that of $Cr:Sb_2Te_3$ single-doped films (80 K) with the same Cr concentration, indicating magnetic ordering at elevated temperatures through the modulation of Dy-doped layers. The increased Curie temperature is common in proximity-coupled MTI/AFM systems [232]. Similar results have been reported on $Cr:(Bi,Sb)_2Te_3$(MTI) / CrSb(AFM) heterostructures, which see a T_C increment from 40 K to 90 K compared to the single-doped MTI film [124]. It will be interesting to engineer various Cr:TI/Dy:TI heterostructures with larger Cr concentrations, and to explore possible QAHE above mK regime, and ferromagnetic ordering in TIs at room temperature.

Skyrmions

Magnetic skyrmions are topologically-protected, swirl-shaped spin configurations [233, 234, 235]. Nanoscale skyrmions can be created, moved and annihilated with limited energy consumption, making them suitable for information storage and logic applications [236]. Recently, researchers discovered skyrmions in FM/MTI heterostructures, that is, the NiFe/$Cr:Sb_2Te_3$ bilayer system using XMCD-PEEM [237]. Since skyrmions were not observed in FM/undoped-TI, and even in FM/MTI they were found only below the Curie temperature of the MTI layer, researchers attributed this effect to spin-polarised TI surface states, although its physical origin is not completely clear. Another way to directly record skyrmion dynamics is using spin-polarised LEEM, due to its capability to quantify three-dimensional spin textures with nm-sized lateral resolution [238, 239]. Once the spin-polarised LEEM in Chongqing is executed, it will be worth investigating magnetic domain and skyrmion dynamics of various materials, including NiFe/$Cr:Sb_2Te_3$ heterostructures.

BIBLIOGRAPHY

[1] Y. Fan, K. J. Smith, G. Lüpke, A. T. Hanbicki, R. Goswami, C. H. Li, H. B. Zhao, and B. T. Jonker, Nature Nanotechnology **8**, 438 (2013).

[2] S. O. Valenzuela, J. Wunderlich, C. H. Back, and T. Jungwirth, Reviews of Modern Physics **87**, 1213 (2017).

[3] X. Kou, Y. Fan, and K. L. Wang, Journal of Physics and Chemistry of Solids pp. 1–22 (2017).

[4] X. L. Qi and S. C. Zhang, Physics Today **63**, 33 (2010).

[5] Y. L. Chen, J. G. Analytis, Z. K. Liu, K. Igarashi, X. L. Qi, S. K. Mo, R. G. Moore, D. H. Lu, M. Hashimoto, T. Sasagawa, et al., Science **329**, 659 (2010).

[6] C.-Z. Chang, J. Zhang, X. Feng, J. Shen, Z. Zhang, M. Guo, K. Li, Y. Ou, P. Wei, L.-L. Wang, et al., Science **340**, 167 (2013).

[7] R. O. M. Aboljadayel, Ph.D. thesis, University of Cambridge (2018).

[8] M. Yasaka, The Rigaku Journal **26**, 1 (1978).

[9] T. Kogure, in *Developments in Clay Science* (Springer, 2013), pp. 275–317.

[10] L. Flajšman, M. Urbánek, V. Křižáková, M. Vaňatka, I. Turčan, and T. Šikola, Review of Scientific Instruments **87**, 053704 (2016).

[11] M. Buchner, Ph.D. thesis, University of Regensburg (2017).

[12] T. Hesjedal, Physica Status Solidi (a) p. 1800726 (2019).

[13] S. Harrison, L. J. Collins-McIntyre, P. Schönherr, A. Vailionis, V. Srot, P. A. van Aken, A. Kellock, A. Pushp, S. Parkin, J. Harris, et al., Scientific Reports **5**, 15767 (2015).

[14] S. A. Crooker, M. Furis, X. Lou, C. Adelmann, D. L. Smith, C. J. Palmstrøm, and P. A. Crowell, Science **309**, 2191 (2005).

[15] P. Kotissek, M. Bailleul, M. Sperl, A. Spitzer, D. Schuh, W. Wegscheider, C. H. Back, and G. Bayreuther, Nature Physics **3**, 872 (2007).

[16] W. Wan, L. Yu, L. Zhu, X. Yang, Z. Wei, J. Z. Liu, J. Feng, K. Kunze, O. Schaff, R. Tromp, et al., Ultramicroscopy **174**, 89 (2017).

[17] Helmholtz-Zentrum Dresden Rossendorf, URL `https://www.hzdr.de/db/Cms?pOid=48583&pNid=0`.

[18] P. N. Argyres, Physical Review **97**, 334 (1955).

[19] Z. Q. Qiu and S. D. Bader, J. Magn. Magn. Mater. **200**, 664 (1999).

[20] S. D. Bader, Journal of Magnetism and Magnetic Materials **100**, 440 (1991).

[21] J. McCord, Journal of Physics D: Applied Physics **48**, 333001 (2015).

[22] Y. K. Kato, R. C. Myers, A. C. Gossard, and D. D. Awschalom, Science **306**, 1910 (2004).

[23] C. Stamm, C. Murer, M. Berritta, J. Feng, M. Gabureac, P. M. Oppeneer, and P. Gambardella, Physical Review Letters **119**, 087203 (2017).

[24] F. Bottegoni, C. Zucchetti, S. Dal Conte, J. Frigerio, E. Carpene, C. Vergnaud, M. Jamet, G. Isella, F. Ciccacci, G. Cerullo, et al., Physical Review Letters **118**, 167402 (2017).

[25] C. Gong, L. Li, Z. Li, H. Ji, A. Stern, Y. Xia, T. Cao, W. Bao, C. Wang, Y. Wang, et al., Nature **546**, 265 (2017).

[26] B. Huang, G. Clark, E. Navarro-Moratalla, D. R. Klein, R. Cheng, K. L. Seyler, D. Zhong, E. Schmidgall, M. A. McGuire, D. H. Cobden, et al., Nature **546**, 270 (2017).

[27] D. A. Allwood, G. Xiong, M. D. Cooke, C. C. Faulkner, D. Atkinson, N. Vernier, and R. P. Cowburn, Science **296**, 2003 (2002).

[28] E. Jiménez, N. Mikuszeit, J. L. F. Cuñado, P. Perna, J. Pedrosa, D. Maccariello, C. Rodrigo, M. A. Niño, A. Bollero, J. Camarero, et al., Review of Scientific Instruments **85**, 053904 (2014).

[29] F. Radu and H. Zabel, in *Magnetic Heterostructures* (Springer, 2008), pp. 97–184.

[30] P. K. Manna and S. M. Yusuf, Physics Reports **535**, 61 (2014).

[31] C. Binek, Physical Review B **70**, 014421 (2004).

[32] M. Gibert, P. Zubko, R. Scherwitzl, J. Íñiguez, and J. M. Triscone, Nature Materials **11**, 195 (2012).

[33] J. W. Cai, K. Liu, and C. L. Chien, Physical Review B **60**, 72 (1999).

[34] A. R. Ball, A. J. Leenaers, P. J. Van Der Zaag, K. A. Shaw, B. Singer, D. M. Lind, H. Frederikze, and M. T. Rekveldt, Applied Physics Letters **69**, 1489 (1996).

[35] P. Z. Si, D. Li, J. W. Lee, C. J. Choi, Z. D. Zhang, D. Y. Geng, and E. Brück, Applied Physics Letters **87**, 1 (2005).

[36] C. Gatel, E. Snoeck, V. Serin, and A. R. Fert, European Physical Journal B **45**, 157 (2005).

[37] J. Sort, A. Popa, B. Rodmacq, and B. Dieny, Physical Review B **70**, 174431 (2004).

[38] C. Binek, S. Polisetty, X. He, and A. Berger, Physical Review Letters **96**, 067201 (2006).

[39] D. Navas, J. Torrejon, F. Béron, C. Redondo, F. Batallan, B. P. Toperverg, A. Devishvili, B. Sierra, F. Castaño, K. R. Pirota, et al., New Journal of Physics **14**, 0 (2012).

[40] W. H. Meiklejohn and C. P. Bean, Physical Review **102**, 1413 (1956).

[41] B. Dieny, V. S. Speriosu, S. S. Parkin, B. A. Gurney, D. R. Wilhoit, and D. Mauri, Physical Review B **43**, 1297 (1991).

[42] I. Žutić, J. Fabian, and S. Das Sarma, Reviews of Modern Physics **76**, 323 (2004).

[43] R. L. Stamps, Journal of Physics D: Applied Physics **3**, 444 (2000).

[44] M. Kiwi, Journal of Magnetism and Magnetic Materials **234**, 584 (2001).

[45] E. H. Hall, American Journal of Mathematics **2**, 287 (1879).

[46] E. H. Hall, Proceedings of the Physical Society of London **4**, 325 (1880).

[47] N. Nagaosa, J. Sinova, S. Onoda, A. H. MacDonald, and N. P. Ong, Reviews of Modern Physics **82**, 1539 (2010).

[48] M. I. Dyakonov and V. I. Perel, Physics Letters **35**, 459 (1971).

[49] K. von Klitzing, G. Dorda, and M. Pepper, Physical Review Letters **45**, 494 (1980).

[50] K. S. Novoselov, A. K. Geim, S. V. Morozov, D. Jiang, M. I. Katsnelson, I. V. Grigorieva, S. V. Dubonos, and A. A. Firsov, Nature **438**, 197 (2005).

[51] Y. Zhang, Y. W. Tan, H. L. Stormer, and P. Kim, Nature **438**, 201 (2005).

[52] M. J. Allen, V. C. Tung, and R. B. Kaner, Chemical Reviews **110**, 132 (2009).

[53] C. L. Kane and E. J. Mele, Physical Review Letters **95**, 226801 (2005).

[54] C. L. Kane and E. J. Mele, Physical Review Letters **95**, 146802 (2005).

[55] M. V. Berry, Proceedings of the Royal Society of London **392**, 45 (1984).

[56] M. König, L. W. Molenkamp, X.-l. Qi, and S.-C. Zhang, Science **318**, 766 (2007).

[57] B. A. Bernevig, T. L. Hughes, and S. C. Zhang, Science **206**, 1757 (2007).

[58] L. Fu, C. L. Kane, and E. J. Mele, Physical Review Letters **98**, 106803 (2007).

[59] H. Zhang, C. X. Liu, X. L. Qi, X. Dai, Z. Fang, and S. C. Zhang, Nature Physics **5**, 438 (2009).

[60] R. Yu, W. Zhang, H.-j. Zhang, S.-C. Zhang, X. Dai, and Z. Fang, Science **329**, 61 (2010).

[61] X. L. Qi and S. C. Zhang, Reviews of Modern Physics **83**, 1057 (2011).

[62] C. Z. Chang, W. Zhao, D. Y. Kim, H. Zhang, B. A. Assaf, D. Heiman, S. C. Zhang, C. Liu, M. H. Chan, and J. S. Moodera, Nature Materials **14**, 473 (2015).

[63] X. Kou, S. T. Guo, Y. Fan, L. Pan, M. Lang, Y. Jiang, Q. Shao, T. Nie, K. Murata, J. Tang, et al., Physical Review Letters **113**, 137201 (2014).

[64] J. G. Checkelsky, R. Yoshimi, A. Tsukazaki, K. S. Takahashi, Y. Kozuka, J. Falson, M. Kawasaki, and Y. Tokura, Nature Physics **10**, 731 (2014).

[65] L. J. Collins-Mcintyre, S. E. Harrison, P. Schönherr, N. J. Steinke, C. J. Kinane, T. R. Charlton, D. Alba-Veneroa, A. Pushp, A. J. Kellock, S. S. Parkin, et al., Epl **107** (2014).

[66] M. Mogi, R. Yoshimi, A. Tsukazaki, K. Yasuda, Y. Kozuka, K. S. Takahashi, M. Kawasaki, and Y. Tokura, Applied Physics Letters **107**, 182401 (2015).

[67] Y. Ou, C. Liu, G. Jiang, Y. Feng, D. Zhao, W. Wu, X. X. Wang, W. Li, C. Song, L. L. Wang, et al., Advanced Materials **30**, 1703062 (2018).

[68] L. J. Collins-Mcintyre, L. B. Duffy, A. Singh, N. J. Steinke, C. J. Kinane, T. R. Charlton, A. Pushp, A. J. Kellock, S. S. Parkin, S. N. Holmes, et al., EPL **115**, 27006 (2016).

[69] I. Lee, C. K. Kim, J. Lee, S. J. L. Billinge, R. Zhong, J. A. Schneeloch, T. Liu, T. Valla, J. M. Tranquada, G. Gu, et al., Proceedings of the National Academy of Sciences **112**, 1316 (2015).

[70] R. Dingle, H. L. Störmer, A. C. Gossard, and W. Wiegmann, Applied Physics Letters **33**, 665 (1978).

[71] H. L. Störmer, A. Pinczuk, A. C. Gossard, and W. Wiegmann, Applied Physics Letters **38**, 691 (1981).

[72] A. Y. Cho and J. R. Arthur, Progress in Solid-State Chemistry **10**, 157 (1975).

[73] J. R. Arthur, Journal of Applied Physics **39**, 4032 (1968).

[74] M. A. Herman and H. Sitter, *Molecular Beam epitaxy: fundamentals and current status* (Springer, 2012).

[75] P. J. Kelly and R. D. Arnell, Vacuum **56**, 159 (2000).

[76] B. E. Warren, *X-ray Diffraction* (Courier Corporation, 1990).

[77] D. B. Williams and C. B. Carter, in *Transmission Electron Microscopy* (Springer, 1996), pp. 3–17.

[78] J.Kerr, Proceedings of the Royal Society of London **25**, 447 (1876).

[79] R. Carey and B. W. Thomas, Journal of Physics D: Applied Physics **7**, 2362 (1974).

[80] H. Ding, S. Pütter, H. Oepen, and J. Kirschner, Physical Review B **63**, 134425 (2001).

[81] M. Buchner, P. Högl, S. Putz, M. Gmitra, S. Günther, M. A. Schoen, M. Kronseder, D. Schuh, D. Bougeard, J. Fabian, et al., Physical Review Letters **117**, 157202 (2016).

[82] M. Buchner, T. Kuczmik, M. Oltscher, M. Ciorga, T. Korn, J. Loher, D. Schuh, C. Schüller, D. Bougeard, D. Weiss, et al., Physical Review B **95**, 035304 (2017).

[83] K. Sato, Japanese Journal of Applied Physics **20**, 2403 (1981).

[84] S. Polisetty, J. Scheffler, S. Sahoo, Y. Wang, T. Mukherjee, X. He, and C. Binek, Review of Scientific Instruments **79**, 055107 (2008).

[85] E. Hecht and A. Zajac, *Optics* (2002).

[86] Y. Zhu, Z. Zhang, B. Ma, and Q. Y. Jin, Journal of Applied Physics **111**, 07C106 (2012).

[87] S. B. Wu, X. F. Yang, S. Chen, and T. Zhu, Journal of Applied Physics **113**, 17C119 (2013).

[88] K. W. Edmonds, P. Bogusławski, K. Y. Wang, R. P. Campion, S. N. Novikov, N. R. S. Farley, B. L. Gallagher, C. T. Foxon, M. Sawicki, T. Dietl, et al., Physical Review Letters **92**, 037201 (2004).

[89] T. Jungwirth, K. Y. Wang, J. Mašek, K. W. Edmonds, J. König, J. Sinova, M. Polini, N. A. Goncharuk, A. H. MacDonald, M. Sawicki, et al., Physical Review B **72**, 165204 (2005).

[90] M. Wang, R. P. Campion, A. W. Rushforth, K. W. Edmonds, C. T. Foxon, and B. L. Gallagher, Applied Physics Letters **93**, 8 (2008).

[91] A. W. Rushforth, M. Wang, N. R. Farley, R. P. Campion, K. W. Edmonds, C. R. Staddon, C. T. Foxon, and B. L. Gallagher, Journal of Applied Physics **104**, 073908 (2008).

[92] A. Lemàtre, A. Miard, L. Travers, O. Mauguin, L. Largeau, C. Gourdon, V. Jeudy, M. Tran, and J. M. George, Applied Physics Letters **93** (2008).

[93] D. Fang, H. Kurebayashi, J. Wunderlich, K. Výborný, L. P. Zârbo, R. P. Campion, A. Casiraghi, B. L. Gallagher, T. Jungwirth, and A. J. Ferguson, Nature Nanotechnology **6**, 413 (2011).

[94] E. De Ranieri, P. E. Roy, D. Fang, E. K. Vehsthedt, A. C. Irvine, D. Heiss, A. Casiraghi, R. P. Campion, B. L. Gallagher, T. Jungwirth, et al., Nature Materials **12**, 808 (2013).

[95] A. Casiraghi, A. W. Rushforth, M. Wang, N. R. Farley, P. Wadley, J. L. Hall, C. R. Staddon, K. W. Edmonds, R. P. Campion, C. T. Foxon, et al., Applied Physics Letters **97**, 95 (2010).

[96] J. M. Coey, *Magnetism and Magnetic Materials* (Cambridge University Press, 2010).

[97] D. A. Allwood, G. Xiong, M. D. Cooke, and R. P. Cowburn, Journal of Physics D: Applied Physics **36**, 2175 (2003).

[98] J. Kim, K. Lee, T. Takabatake, H. Kim, M. Kim, and M.-H. Jung, Scientific Reports **5**, 10309 (2015).

[99] S.-W. Kim and M.-H. Jung, Applied Physics Letters **112**, 202401 (2018).

[100] A. Shikin, D. Estyunin, Y. I. Surnin, A. Koroleva, E. Shevchenko, K. Kokh, O. Tereshchenko, S. Kumar, E. Schwier, K. Shimada, et al., Scientific Reports **9**, 4813 (2019).

[101] T. Chen, W. Liu, F. Zheng, M. Gao, X. Pan, G. van der Laan, X. Wang, Q. Zhang, F. Song, B. Wang, et al., Advanced Materials **27**, 4823 (2015).

[102] C. Yue, Y. Xu, Z. Song, H. Weng, Y.-M. Lu, C. Fang, and X. Dai, Nature Physics **15**, 577 (2019).

[103] S. Li, S. Harrison, Y. Huo, A. Pushp, H. Yuan, B. Zhou, A. Kellock, S. Parkin, Y.-L. Chen, T. Hesjedal, et al., Applied Physics Letters **102**, 242412 (2013).

[104] A. Figueroa, G. Van Der Laan, S. Harrison, G. Cibin, and T. Hesjedal, Scientific Reports **6**, 22935 (2016).

[105] A. Figueroa, S. Harrison, L. Collins-McIntyre, G. van der Laan, and T. Hesjedal, Physica Status Solidi (RRL)–Rapid Research Letters **10**, 467 (2016).

[106] S. Pokrzywnicki, Journal of Alloys and Compounds **225**, 163 (1995).

[107] P. Haazen, J.-B. Laloë, T. Nummy, H. Swagten, P. Jarillo-Herrero, D. Heiman, and J. Moodera, Applied Physics Letters **100**, 082404 (2012).

[108] S. Dhar, O. Brandt, M. Ramsteiner, V. Sapega, and K. Ploog, Physical Review Letters **94**, 037205 (2005).

[109] V. Kachkanov, M. Wallace, G. van der Laan, S. Dhesi, S. Cavill, Y. Fujiwara, and K. O'donnell, Scientific Reports **2**, 969 (2012).

[110] Y. Chen, J. G. Analytis, J.-H. Chu, Z. Liu, S.-K. Mo, X.-L. Qi, H. Zhang, D. Lu, X. Dai, Z. Fang, et al., Science **325**, 178 (2009).

[111] C.-Z. Chang, P. Tang, Y.-L. Wang, X. Feng, K. Li, Z. Zhang, Y. Wang, L.-L. Wang, X. Chen, C. Liu, et al., Physical review letters **112**, 056801 (2014).

[112] A. Figueroa, A. A. Baker, S. Harrison, K. Kummer, G. van der Laan, and T. Hesjedal, Journal of Magnetism and Magnetic Materials **422**, 93 (2017).

[113] L. Duffy, N.-J. Steinke, J. Krieger, A. Figueroa, K. Kummer, T. Lancaster, S. Giblin, F. Pratt, S. Blundell, T. Prokscha, et al., Physical Review B **97**, 174427 (2018).

[114] A. Singh, V. S. Kamboj, J. Liu, J. Llandro, L. B. Duffy, S. P. Senanayak, H. E. Beere, A. Ionescu, D. A. Ritchie, T. Hesjedal, et al., Sci. Rep. **8**, 17024 (2018).

[115] L. Duffy, A. Frisk, D. Burn, N.-J. Steinke, J. Herrero-Martin, A. Ernst, G. van der Laan, and T. Hesjedal, Physical Review Materials **2**, 054201 (2018).

[116] D. Das, K. Malik, A. K. Deb, S. Dhara, S. Bandyopadhyay, and A. Banerjee, Journal of Applied Physics **118**, 045102 (2015).

[117] K. Olejnik, P. Wadley, J. Haigh, K. Edmonds, R. Campion, A. Rushforth, B. Gallagher, C. Foxon, T. Jungwirth, J. Wunderlich, et al., Physical Review B **81**, 104402 (2010).

[118] J. P. Perdew, J. A. Chevary, S. H. Vosko, K. A. Jackson, M. R. Pederson, D. J. Singh, and C. Fiolhais, Physical Review B **46**, 6671 (1992).

[119] G. Kresse and J. Hafner, Journal of Physics: Condensed Matter **6**, 8245 (1994).

[120] G. Kresse and J. Furthmüller, Physical review B **54**, 11169 (1996).

[121] J. Perdew, K. Burke, and M. Ernzerhof, Physical Review Letters **80**, 891 (1998).

[122] B. Y. Yavorsky, N. Hinsche, I. Mertig, and P. Zahn, Physical Review B **84**, 165208 (2011).

[123] D. J. Tozer and N. C. Handy, The Journal of chemical physics **109**, 10180 (1998).

[124] Q. L. He, X. Kou, A. J. Grutter, G. Yin, L. Pan, X. Che, Y. Liu, T. Nie, B. Zhang, S. M. Disseler, et al., Nature Materials **16**, 94 (2017).

[125] L. Šmejkal, Y. Mokrousov, B. Yan, and A. H. MacDonald, Nature Physics **14**, 242 (2018).

[126] Q. L. He, G. Yin, A. J. Grutter, L. Pan, X. Che, G. Yu, D. A. Gilbert, S. M. Disseler, Y. Liu, P. Shafer, et al., Nature Communications **9**, 2767 (2018).

[127] Q. L. He, G. Yin, L. Yu, A. J. Grutter, L. Pan, C.-Z. Chen, X. Che, G. Yu, B. Zhang, Q. Shao, et al., Physical Review Letters **121**, 096802 (2018).

[128] Q. I. Yang, M. Dolev, L. Zhang, J. Zhao, A. D. Fried, E. Schemm, M. Liu, A. Palevski, A. F. Marshall, S. H. Risbud, et al., Physical Review B **88**, 081407 (2013).

[129] M. Lang, M. Montazeri, M. C. Onbasli, X. Kou, Y. Fan, P. Upadhyaya, K. Yao, F. Liu, Y. Jiang, W. Jiang, et al., Nano Letters **14**, 3459 (2014).

[130] A. L. Yeats, P. J. Mintun, Y. Pan, A. Richardella, B. B. Buckley, N. Samarth, and D. D. Awschalom, Proc. Natl. Acad. Sci. U.S.A. **114**, 10379 (2017).

[131] K. Yasuda, R. Wakatsuki, T. Morimoto, R. Yoshimi, A. Tsukazaki, K. S. Takahashi, M. Ezawa, M. Kawasaki, N. Nagaosa, and Y. Tokura, Nature Physics **12**, 555 (2016).

[132] J. Matsuno, N. Ogawa, K. Yasuda, F. Kagawa, W. Koshibae, N. Nagaosa, Y. Tokura, and M. Kawasaki, Science Advance **2**, 1600304 (2016).

[133] Y. Ohuchi, J. Matsuno, N. Ogawa, Y. Kozuka, M. Uchida, Y. Tokura, and M. Kawasaki, Nature Communications **9**, 213 (2018).

[134] W. Thomson, Proceedings of the Royal Society of London pp. 546–550 (1857).

[135] T. McGuire and R. Potter, IEEE Transactions on Magnetics **11**, 1018 (1975).

[136] C. Chang, M. Liu, Z. Zhang, Y. Wang, K. He, and Q. Xue, Science China Physics, Mechanics & Astronomy **59**, 637501 (2016).

[137] V. S. Kamboj, A. Singh, T. Ferrus, H. E. Beere, L. B. Duffy, T. Hesjedal, C. H. Barnes, and D. A. Ritchie, ACS Photonics **4**, 2711 (2017).

[138] L. B. Duffy, A. I. Figueroa, G. van der Laan, and T. Hesjedal, Physical Review Materials **1**, 064409 (2017).

[139] A. Roy, S. Guchhait, R. Dey, T. Pramanik, C. C. Hsieh, A. Rai, and S. K. Banerjee, ACS Nano **9**, 3772 (2015).

[140] H. T. He, G. Wang, T. Zhang, I. K. Sou, G. K. Wong, J. N. Wang, H. Z. Lu, S. Q. Shen, and F. C. Zhang, Physical Review Letters **106**, 166805 (2011).

[141] G. Bergmann, Solid State Communications **42**, 815 (1982).

[142] Y. S. Kim, M. Brahlek, N. Bansal, E. Edrey, G. A. Kapilevich, K. Iida, M. Tanimura, Y. Horibe, S.-W. Cheong, and S. Oh, Physical Review B **84**, 073109 (2011).

[143] M. Liu, C.-Z. Chang, Z. Zhang, Y. Zhang, W. Ruan, K. He, L.-l. Wang, X. Chen, J.-F. Jia, S.-C. Zhang, et al., Physical Review B **83**, 165440 (2011).

[144] D. Kim, P. Syers, M. S. Fuhrer, J. Paglione, and N. P. Butch, Nature Communications **4**, 2040 (2013).

[145] S. Hikami, A. I. Larkin, and Y. Nagaoka, Progress of Theoretical Physics **63**, 707 (1980).

[146] M. Liu, J. Zhang, C. Z. Chang, Z. Zhang, X. Feng, K. Li, K. He, L. L. Wang, X. Chen, X. Dai, et al., Physical Review Letters **108**, 036805 (2012).

[147] P. Wei, F. Katmis, B. A. Assaf, H. Steinberg, P. Jarillo-Herrero, D. Heiman, and J. S. Moodera, Physical Review Letters **110**, 186807 (2013).

[148] A. Mauger and C. Godart, Physics Reports **141**, 51 (1986).

[149] C. Lee, F. Katmis, P. Jarillo-Herrero, J. S. Moodera, and N. Gedik, Nature communications **7**, 12014 (2016).

[150] F. Katmis, V. Lauter, F. S. Nogueira, B. A. Assaf, M. E. Jamer, P. Wei, B. Satpati, J. W. Freeland, I. Eremin, D. Heiman, et al., Nature **533**, 513 (2016).

[151] P. Chuang, S. C. Ho, L. W. Smith, F. Sfigakis, M. Pepper, C. H. Chen, J. C. Fan, J. P. Griffiths, I. Farrer, H. E. Beere, et al., Nature Nanotechnology **10**, 35 (2015).

[152] E. I. Rashba, Physical Review B **62**, R16 267 (2000).

[153] R. I. Dzhioev, K. V. Kavokin, V. L. Korenev, M. V. Lazarev, B. Y. Meltser, M. N. Stepanova, B. P. Zakharchenya, D. Gammon, and D. S. Katzer, Physical Review B **66**, 245204 (2002).

[154] M. Furis, D. L. Smith, S. A. Crooker, and J. L. Reno, Applied Physics Letters **89**, 102102 (2006).

[155] N. Gerhardt, S. Hövel, C. Brenner, M. Hofmann, F.-Y. Lo, D. Reuter, A. Wieck, E. Schuster, W. Keune, and K. Westerholt, Applied Physics Letters **87**, 032502 (2005).

[156] A. Sinsarp, T. Manago, F. Takano, and H. Akinaga, Japanese Journal of Applied Physics **46**, L4 (2006).

[157] C. Adelmann, J. Hilton, B. Schultz, S. McKernan, C. Palmstrøm, X. Lou, H.-S. Chiang, and P. Crowell, Applied Physics Letters **89**, 112511 (2006).

[158] J. Bae, K.-H. Kim, J.-M. Han, H. Cheol Koo, B.-C. Min, H.-j. Kim, J. Chang, S. Hee Han, and S. Ho Lim, Applied Physics Letters **102**, 062412 (2013).

[159] S. G. Bhat and P. A. Kumar, Scientific Reports **4**, 5588 (2014).

[160] D. Sander, S. Valenzuela, D. Makarov, C. Marrows, E. Fullerton, P. Fischer, J. McCord, P. Vavassori, S. Mangin, P. Pirro, et al., Journal of Physics D: Applied Physics **50**, 363001 (2017).

[161] R. Ohsugi, J. Shiogai, Y. Kunihashi, M. Kohda, H. Sanada, T. Seki, M. Mizuguchi, H. Gotoh, K. Takanashi, and J. Nitta, Journal of Physics D: Applied Physics **48**, 164003 (2015).

[162] M. Tran, H. Jaffrès, C. Deranlot, J. M. George, A. Fert, A. Miard, and A. Lemaître, Physical Review Letters **102**, 036601 (2009).

[163] M. Kohda, A. Ohtsu, T. Seki, A. Fujita, J. Nitta, S. Mitani, and K. Takanashi, Japanese Journal of Applied Physics **47**, 3269 (2008).

[164] Y. K. Takahashi, K. Hono, T. Shima, and K. Takanashi, Journal of Magnetism and Magnetic Materials **267**, 248 (2003).

[165] J. B. Staunton, S. Ostanin, S. S. Razee, B. Gyorffy, L. Szunyogh, B. Ginatempo, and E. Bruno, Journal of Physics: Condensed Matter **16**, S5623 (2004).

[166] M. Rennhofer, M. Kozlowski, B. Laenens, B. Sepiol, R. Kozubski, D. Smeets, and A. Vantomme, Intermetallics **18**, 2069 (2010).

[167] F. Albertini, L. Nasi, F. Casoli, S. Fabbrici, P. Luches, A. Rota, and S. Valeri, Journal of Magnetism and Magnetic Materials **316**, 158 (2007).

[168] T. Bublat and D. Goll, Journal of Applied Physics **108**, 113910 (2010).

[169] R. Ohsugi, M. Kohda, T. Seki, A. Ohtsu, M. Mizuguchi, K. Takanashi, and J. Nitta, Japanese Journal of Applied Physics **51**, 02BM05 (2012).

[170] J. B. Laloë, A. Ionescu, S. Easton, N. J. Steinke, T. J. Hayward, H. Kurebayashi, J. A. Bland, T. R. Charlton, R. M. Dalgliesh, and S. Langridge, Applied Physics Letters **93**, 012505 (2008).

[171] S. H. Shim, H. J. Kim, H. C. Koo, Y. H. Lee, and J. Chang, Applied Physics Letters **107**, 102407 (2015).

[172] C. J. Lin, G. L. Gorman, C. H. Lee, R. F. Farrow, M. E. E, H. V. Do, N. H, and C. J. Chien, Journal of Magnetism and Magnetic Materials **93**, 194 (1991).

[173] N. Nakajima, T. Koide, T. Shidara, H. Miyauchi, H. Fukutani, A. Fujimori, K. Iio, T. Katayama, M. Nývlt, and Y. Suzuki, Physical Review Letters **81**, 5229 (1998).

[174] S. J. Yun, S. H. Lim, and S. R. Lee, AIP Advances **6**, 025112 (2016).

[175] P. Pirro, A. Hamadeh, M. Lavanant-Jambert, T. Meyer, B. Tao, E. Rosario, Y. Lu, M. Hehn, S. Mangin, and S. Petit Watelot, Journal of Magnetism and Magnetic Materials **432**, 260 (2017).

[176] O. Koplak, A. Talantsev, Y. Lu, A. Hamadeh, P. Pirro, T. Hauet, R. Morgunov, and S. Mangin, Journal of Magnetism and Magnetic Materials **433**, 91 (2017).

[177] P. J. Chen, M. Zhu, S. Tibus, T. Dyer, J. Piccirillo, B. Ocker, and R. D. Shull, Journal of Physics D: Applied Physics **50**, 025006 (2017).

[178] R. Ranjbar, K. Suzuki, A. Sugihara, T. Miyazaki, Y. Ando, and S. Mizukami, Materials **8**, 6531 (2015).

[179] P. Gargiani, R. Cuadrado, H. Vasili, M. Pruneda, and M. Valvidares, Nature Communications **8**, 699 (2017).

[180] G. M. Choi, I. J. Shin, B. C. Min, and K. H. Shin, Journal of Applied Physics **108** (2010).

[181] T. Devolder, J. V. Kim, F. Garcia-Sanchez, J. Swerts, W. Kim, S. Couet, G. Kar, and A. Furnemont, Physical Review B **93**, 024420 (2016).

[182] S. Parkin and S.-H. Yang, Nature Nanotechnology **10**, 195 (2015).

[183] T. Fache, H. S. Tarazona, J. Liu, G. L'Vova, M. J. Applegate, J. C. Rojas-Sanchez, S. Petit-Watelot, C. V. Landauro, J. Quispe-Marcatoma, R. Morgunov, et al., Physical Review B **98**, 064410 (2018).

[184] B. M. AlQassem, B. A. Hamad, J. M. Khalifeh, and C. Demangeat, European Physical Journal B **62**, 433 (2008).

[185] E. Bauer, Reports on Progress in Physics **57**, 895 (1994).

[186] M. Altman, Journal of Physics: Condensed Matter **22**, 084017 (2010).

[187] D. Weller, O. Mosendz, G. Parker, S. Pisana, and T. S. Santos, Physica Status Solidi (A) Applications and Materials Science **210**, 1245 (2013).

[188] D. Weller, G. Parker, O. Mosendz, A. Lyberatos, D. Mitin, N. Y. Safonova, and M. Albrecht, Journal of Vacuum Science & Technology B, Nanotechnology and Microelectronics: Materials, Processing, Measurement, and Phenomena **34**, 060801 (2016).

[189] E. Bauer, in *Proceedings of the Fifth International Congress on Electron Microscopy* (1962), vol. 1, pp. 11–12.

[190] A. Zangwill, *Physics at Surfaces* (Cambridge University Press, 1988).

[191] R. M. Tromp, J. B. Hannon, W. Wan, A. Berghaus, and O. Schaff, Ultramicroscopy **127**, 25 (2013).

[192] M. Kief and R. Victora, MRS Bulletin **43**, 87 (2018).

[193] K. Hono, Y. Takahashi, G. Ju, J.-U. Thiele, A. Ajan, X. Yang, R. Ruiz, and L. Wan, MRS Bulletin **43**, 93 (2018).

[194] R. F. Evans, R. W. Chantrell, U. Nowak, A. Lyberatos, and H. J. Richter, Applied Physics Letters **100**, 10 (2012).

[195] E. Betzig and J. K. Trautman, Science **257**, 189 (1992).

[196] K. F. Dong, H. H. Li, and J. S. Chen, Journal of Applied Physics **113** (2013).

[197] J. Eisinger, The Journal of Chemical Physics **30**, 412 (1959).

[198] E. Bauer and T. Engel, Surface Science **71**, 695 (1978).

[199] P. K. Wu, M. C. Tringides, and M. G. Legally, Physical Review B **39**, 7595 (1989).

[200] N. Stojić, T. O. Menteş, N. Binggeli, M. A. Niño, A. Locatelli, and E. Bauer, Physical Review B **81**, 115437 (2010).

[201] T. Giela, D. Wilgocka-Ślęzak, M. Ślęzak, N. Spiridis, and J. Korecki, Applied Surface Science **425**, 314 (2017).

[202] Y. Li and K. Baberschke, Physical Review Letters **68**, 1208 (1992).

[203] F. Gerhardter, Y. Li, and K. Baberschke, Physical Review B **47**, 11204 (1993).

[204] R. Zdyb and E. Bauer, Physical Review Letters **88**, 166403 (2002).

[205] B. Santos, J. Puerta, J. Cerda, R. Stumpf, K. von Bergmann, R. Wiesendanger, M. Bode, K. McCarty, and J. de la Figuera, New Journal of Physics **10**, 013005 (2008).

[206] B. Santos, M. Rybicki, I. Zasada, E. Starodub, K. F. McCarty, J. I. Cerda, J. M. Puerta, and J. De La Figuera, Physical Review B **93**, 195423 (2016).

[207] A. H. Reader and J. P. W. B. Duchateau, Reports on Progress in Physics **56**, 1397 (1993).

[208] P. A. Bennett, Z. He, D. J. Smith, and F. M. Ross, Thin Solid Films **519**, 8434 (2011).

[209] D. K. Lim, S. S. Bae, J. Choi, D. Lee, D. E. Sung, S. Kim, J. K. Kim, H. W. Yeom, and H. Lee, Journal of Chemical Physics **128** (2008).

[210] J. Nogami, B. Z. Liu, M. V. Katkov, C. Ohbuchi, and N. O. Birge, Physical Review B **63**, 233305 (2001).

[211] D. Lee and S. Kim, Applied Physics Letters **82**, 2619 (2003).

[212] C. Preinesberger, G. Pruskil, S. K. Becker, M. Dähne, D. V. Vyalikh, S. L. Molodtsov, C. Laubschat, and F. Schiller, Applied Physics Letters **87**, 2003 (2005).

[213] D. K. Lim, O. Kubo, Y. Shingaya, T. Nakayama, Y. H. Kim, J. Y. Lee, M. Aono, H. Lee, D. Lee, and S. Kim, Applied Physics Letters **92**, 2006 (2008).

[214] Z. Yan, B. Li, D. Yang, and J. Ma, Chinese Journal of Catalysis **34**, 1471 (2013).

[215] W.-C. Yang, H. Ade, and R. Nemanich, Physical Review B **69**, 045421 (2004).

[216] P. Sutter, P. A. Bennett, J. I. Flege, and E. Sutter, Physical Review Letters **99**, 125504 (2007).

[217] P. A. Bennett, J. Chobanian, J. I. Flege, E. Sutter, and P. Sutter, Physical Review B **76**, 125410 (2007).

[218] D. K. Lim, D. Lee, H. Lee, S.-S. Bae, J. Choi, S. Kim, C. Ji, R. Ragan, D. A. Ohlberg, Y. A. Chang, et al., Nanotechnology **18**, 095706 (2007).

[219] D. Choi, J. Jung, D. Shin, M. Yoon, W. Cho, J. Kim, K. Chae, K. Jeong, and C. Whang, Surface Science **505**, L222 (2002).

[220] C. Ji, R. Ragan, S. Kim, Y. Chang, Y. Chen, D. Ohlberg, and R. S. Williams, Applied Physics A **80**, 1301 (2005).

[221] R. S. Wagner and W. C. Ellis, Applied Physics Letters **4**, 89 (1964).

[222] Y. Wu and P. Yang, Journal of the American Chemical Society **123**, 3165 (2001).

[223] Y. Homma, P. Finnie, and T. Ogino, Applied Physics Letters **74**, 815 (1999).

[224] J. B. Hannon, S. Kodambaka, F. M. Ross, and R. M. Tromp, Nature **440**, 69 (2006).

[225] J. Tersoff, D. E. Jesson, and W. X. Wang, Science **324**, 236 (2009).

[226] M. M. Waldrop, Nature News **530**, 144 (2016).

[227] O. van 't Erve, A. Hanbicki, K. McCreary, C. Li, and B. Jonker, Applied Physics Letters **104**, 172402 (2014).

[228] P. Riego, S. Vélez, J. M. Gomez-Perez, J. A. Arregi, L. E. Hueso, F. Casanova, and A. Berger, Applied Physics Letters **109**, 172402 (2016).

[229] Y. Su, H. Wang, J. Li, C. Tian, R. Wu, X. Jin, and Y. Shen, Applied Physics Letters **110**, 042401 (2017).

[230] P. Seifert, K. Vaklinova, S. Ganichev, K. Kern, M. Burghard, and A. W. Holleitner, Nature Communications **9**, 331 (2018).

[231] Y. Liu, J. Besbas, Y. Wang, P. He, M. Chen, D. Zhu, Y. Wu, J. M. Lee, L. Wang, J. Moon, et al., Nature Communications **9**, 2492 (2018).

[232] K. Lenz, S. Zander, and W. Kuch, Physical Review Letters **98**, 237201 (2007).

[233] S. Mühlbauer, B. Binz, F. Jonietz, C. Pfleiderer, A. Rosch, A. Neubauer, R. Georgii, and P. Böni, Science **323**, 915 (2009).

[234] X. Yu, Y. Onose, N. Kanazawa, J. Park, J. Han, Y. Matsui, N. Nagaosa, and Y. Tokura, Nature **465**, 901 (2010).

[235] S. Heinze, K. Von Bergmann, M. Menzel, J. Brede, A. Kubetzka, R. Wiesendanger, G. Bihlmayer, and S. Blügel, Nature Physics **7**, 713 (2011).

[236] A. Fert, N. Reyren, and V. Cros, Nature Reviews Materials **2**, 17031 (2017).

[237] S. Zhang, F. Kronast, G. van der Laan, and T. Hesjedal, Nano Letters **18**, 1057 (2018).

[238] G. Chen, A. Mascaraque, A. T. N'Diaye, and A. K. Schmid, Applied Physics Letters **106**, 242404 (2015).

[239] W. Jiang, G. Chen, K. Liu, J. Zang, S. G. te Velthuis, and A. Hoffmann, Physics Reports **704**, 1 (2017).